Characterization of SRF Cavity Materials with Radioactive Beam Based Techniques for Gradient Enhancement

by

Md Asaduzzaman
B.Sc., Jahangirnagar University, Dhaka-1342, Bangladesh
M.S., Jahangirnagar University, Dhaka-1342, Bangladesh

A Dissertation Submitted in Partial Fulfillment of the
Requirements for the Degree of

DOCTOR OF PHILOSOPHY

in the Department of Physics and Astronomy

We acknowledge and respect the Lək̓ʷəŋən (Songhees and Xʷsepsəm/Esquimalt) Peoples on whose territory the university stands, and the Lək̓ʷəŋən and W̱SÁNEĆ Peoples whose historical relationships with the land continue to this day.

Characterization of SRF Cavity Materials with Radioactive Beam Based Techniques for Gradient Enhancement

by

Md Asaduzzaman
B.Sc., Jahangirnagar University, Dhaka-1342, Bangladesh
M.S., Jahangirnagar University, Dhaka-1342, Bangladesh

Supervisory Committee

Prof. Tobias Junginger, Co-Supervisor
(Department of Physics and Astronomy)

Prof. Bob Laxdal, Co-Supervisor
(Department of Physics and Astronomy)

Prof. Andrew MacFarlane, Outside Member
(Department of Chemistry, University of British Columbia)

Dr. Ryan M. L. McFadden, Outside Member
(TRIUMF)

Abstract

Superconducting radio frequency (SRF) cavities accelerate charged particle beams by transferring radio frequency (RF) energy. When operated near resonance, the applied RF power generates strong electromagnetic fields, with the electric field driving beam acceleration and the accompanying magnetic field running along the cavity surface. If this magnetic field becomes too large, the superconductor quenches, transitioning to the normal state and dissipating the stored energy. State-of-the-art Nb cavities are limited by their superheating field (B_{sh}), which defines the maximum sustainable surface field in the superconductor's Meissner state [1, 2]. Since applied magnetic field (B_0) scales with the accelerating gradient (E_{acc}) (i.e., the energy gain per unit length), increasing the B_{sh} limit allows a given beam energy to be achieved with a shorter linear accelerator, thereby reducing both the overall length and cost.

Coating Nb with thin superconducting layers of larger penetration depth λ than Nb, with or without insulating spacers (i.e., forming superconductor-superconductor (SS) or superconductor-insulator-superconductor (SIS) heterostructures), can enhance the attainable E_{acc} by sustaining the Meissner state beyond each layer's B_{sh}, supported by reduced surface currents and interfacial barriers. To investigate how these coatings modify local magnetic behavior, "exotic" ion-implanted β-detected spin spectroscopies (i.e., muon spin rotation (μSR), low energy muon spin rotation (LE-μSR) and β-detected nuclear magnetic resonance (βNMR)) were used to probe the internal fields within such heterostructures.

Previous μSR studies have indicated the presence of an interface barrier to flux penetration at the boundary between two superconductors, while low-temperature baking (LTB) treatments showed apparent increases in the vortex penetration field ($\mu_0 H_{\mathrm{vp}}$) where surface pinning effects could not be excluded. Motivated by these findings, μSR measurements were performed on Nb_3Sn(2 μm)/Nb and LTB-treated

Nb samples to distinguish between interface-barrier and pinning contributions. Using thin Ag foils as energy moderators for the implanted muon spin probes, depth profiling in the 10 µm-100 µm range of an SS bilayer revealed a $\mu_0 H_{\mathrm{vp}}$ consistent with Nb's metastable superheating field ($\mu_0 H_{\mathrm{sh}}$), indicating a surface barrier that delays flux entry. In contrast, the LTB-treated Nb exhibited a $\mu_0 H_{\mathrm{vp}}$ close to the lower critical field lower critical field ($\mu_0 H_{\mathrm{c1}}$) of Nb, with values increasing with implantation depth, provides clear evidence for surface-localized flux pinning.

Further optimization of multilayer coatings requires understanding how layer thickness influences screening currents. To this end, LE-μSR measurements probe nanoscale (depths $\lesssim$150 nm) Meissner screening in $Nb_{1-x}Ti_xN(x\ \mathrm{nm})$/Nb bilayers with surface-layer thicknesses x = 50, 80, and 160 in applied fields of $\leq$ 25 mT. The results confirm strong current suppression in the surface layer, consistent with theoretical predictions, and reveal bipartite field profiles well described by London theory. The extracted penetration depth $\lambda_{Nb_{1-x}Ti_xN}$ agrees with bulk values, establishing the optimal coating thickness for maximizing the vortex penetration field. These findings emphasize the importance of multilayered superconducting/insulating stacks for achieving the highest E_{acc}.

To further investigate multilayer enhancement mechanisms, the superconducting and normal-state properties of a thin-film $Nb_{0.75}Ti_{0.25}N$(91 nm) in a $Nb_{0.75}Ti_{0.25}N$ (91 nm)/AlN(4 nm)/Nb SIS heterostructure were studied using βNMR in the vortex state. Resonance spectra displayed broad, symmetric lineshapes at all temperatures, with additional broadening below critical temperature (T_{c}) ~15 K, yielding penetration depth (λ) and upper critical field (B_{c2}) values consistent with literature. Spin-lattice relaxation (SLR) data exhibited metallic Korringa behavior at low temperatures, modified below T_{c} by a Hebel-Slichter peak characterized by a superconducting gap and modest Dynes-like broadening, confirming the superconductor's strong-coupling behaviour. Possible sources of high-T SLR dynamics

are suggested.

Finally, this characterization of the superconducting layer in the SIS heterostructure establishes a foundation for future studies of the Meissner–vortex phase transition to directly test field enhancement. The high-parallel-field βNMR spectrometer [3] has been upgraded for such transition measurements, increasing the maximum B_0 from 24 mT to ~200 mT (comparable to the lower critical field (B_{c1}) of Nb) parallel to the sample surface, enabling investigations under realistic SRF cavity conditions.

Table of Contents

List of Tables

List of Figures

Symbols

Acronyms

3D three-dimensional 155

AC alternating current 52

AFM atomic force microscopy 103

ALCR avoided level-crossing resonance 170

ALD atomic layer deposition 149, 171

BCP buffered chemical polishing 102, 112, 113, 126, 127, 137, 148

BCS Bardeen-Cooper-Schrieffer vi, x, xvi, 10, 15–19, 21, 32, 35, 38–41, 138, 153, 158, 159, 162, 167, 176

BL Bean-Livingston xix, xxii, 2, 29, 31, 32, 42, 45, 52, 107, 110, 118, 127, 140

βNMR β-detected nuclear magnetic resonance iii–v, vii, x, xii, xxv, xxvi, li, lii, 3, 4, 57–60, 67, 81–92, 94, 145, 146, 152, 158, 161, 163, 165–168, 170, 177, 182–185, 190

BPP Bloembergen-Purcell-Pound 158, 160, 168, 169

CCD charge-coupled device 86, 87

CGS centimetre-gram-second system of units 181

CMMS Centre for Molecular and Materials Science 97

CW continuous wave 90, 152

DC direct current 34, 52, 55, 110, 115, 126

DOS density of states xvi, 18–21, 158, 159, 164, 173, 174

EDX energy dispersive X-ray spectroscopy xliii, 103, 191–193

EFGs electric field gradients 58, 91, 150

EM electromagnetic 33, 34, 38, 57, 119

EP electropolishing 112, 113, 126

FCC face-centred cubic xl, 164, 173

FLL flux-line lattice 151, 170, 183, 185

FWHM full width at half maximum 80, 150, 152

GIXRD Grazing incidence x-ray diffraction xl, 171–173

GL Ginzburg-Landau xi, xv, xvii, xviii, 11–15, 17, 22–27, 30, 32, 43, 45, 138, 139, 145, 153, 162, 166

GUI graphical user interface 87

HFQS high field Q slope 112, 113

HPCVD hybrid physical chemical vapour deposition 110

HV high-voltage xxv, 86

ISAC isotope separator and accelerator 83–85, 146

JLab Thomas Jefferson National Accelerator Facility 127

LE-μSR low energy muon spin rotation iii, iv, vii, viii, x, xxvi, xxxiii, xxxv, li, lii, 3, 4, 57–60, 67, 78, 80–82, 91–93, 96, 112, 113, 121, 122, 124, 125, 127, 131, 134, 136, 137, 140, 141, 145, 162, 182, 183, 187, 190

LTB low-temperature baking iii, iv, xxx, xxxi, 2, 4, 40, 45, 95–97, 102–104, 106–110, 112–116, 182, 183

MCP multi-channel plate 80

MFM Magnetic force microscopy 3, 122

MP mechanical polishing 126

μSR muon spin rotation iii, vii, x, xxvi, xxvii, xxix, xxx, li, lii, 3, 4, 24, 53, 57–60, 67, 71, 72, 74, 80, 89, 91–93, 96–99, 101–103, 105–107, 110, 116, 145, 182, 187, 190

NMR nuclear magnetic resonance vii, xiii, xxxvii, 57, 60, 88, 90, 145, 148, 150, 154–156, 159–162, 164, 165, 170

PCT point contact tunneling xlii, 149, 161, 166, 167, 173, 174, 177

PSI Paul Scherrer Institute xxiv, 78, 79, 122

QPR quadrupole resonator 55, 56

RF radio frequency iii, xxiii, xxvi, 1, 2, 30, 33–36, 38–41, 55, 56, 60, 87–89, 91, 115, 116, 143, 147, 148, 184, 186

RIB radioactive ion beam xxv, 84, 86

RRR residual-resistivity ratio xlii, 102, 103, 148, 191, 192

SEM scanning electron microscope xliii, 103, 191–193

SIMS secondary ion mass spectrometry xliii, 103, 191–193

SIS superconductor-insulator-superconductor iii–v, xx, 2–4, 42–45, 53, 55, 56, 111, 118, 145, 146, 167, 170, 183–186

SLR spin-lattice relaxation iv, ix, xiii, xxxviii, xxxix, 63, 65, 88–90, 146–148, 155–158, 160–163, 165, 166, 168–170, 183, 185

SQUID superconducting quantum interference device 3, 52, 53

SRF superconducting radio frequency iii, v, vii, x, xx, xxi, xxxi, liii, 1, 30, 33–43, 46, 51, 52, 54–56, 59, 73, 95, 96, 101, 108, 110, 112, 115–118, 126, 143, 145, 167, 170, 173, 182, 186, 191, 192

SRIM Stopping and Range of Ions in Matter xxviii, xxxvii, 92, 98, 100, 146, 147

SS superconductor-superconductor iii, iv, xxi, xxii, xxxii, xxxiii, xxxvi, 2, 3, 45–53, 96, 97, 102, 107–113, 115, 118–121, 124–131, 136, 138–140, 182–184

STM scanning tunnelling microscopy 3, 122

TEM transmission electron microscopy 135

TF-μSR transverse field muon spin rotation xxiv, 67, 72, 73, 77, 78

TOF time-of-flight 80

UHV ultra-high vacuum xxv, 80, 85–87

VSM vibrating sample magnetometer 149, 172, 184–186

WHH Werthamer-Helfand-Hohenberg 28, 153, 177

XPS x-ray photoelectron spectroscopy 149

XRR x-ray reflection xxxix, 171, 172

ZF-μSR zero field muon spin rotation xxiv, 67, 72–75, 78

Acknowledgements

First and foremost, I am profoundly grateful to Allah (SWT)—the GOD the Almighty, the Most Gracious, and the Most Merciful—for His infinite blessings and boundless mercy. It is through His will that I exist, and by His grace, I have been granted the strength, knowledge, and perseverance to complete this journey.

I extend my heartfelt appreciation to my primary supervisor, Tobias Junginger, for his exceptional mentorship, support, and invaluable insights, which have profoundly shaped my research and the completion of this thesis. From my first year of graduate studies, his guidance, generosity with time, and belief in my potential have been deeply inspiring, helping me develop as an independent researcher and complete this work. I am sincerely honored to work under his supervision.

I am equally thankful to my co-supervisor, Robert Laxdal, for his critical feedback, valuable suggestions, and kind support, especially in helping me settle into my work at TRIUMF. I also extend my sincere thanks to my committee members, Dr. Andrew MacFarlane and Dr. Ryan M. L. McFadden, for their thoughtful comments and valuable guidance, which have greatly contributed to shaping this research.

My deepest appreciation goes to Dr. R. M. L. McFadden for his invaluable technical discussions, constructive criticism, and expertise, which have greatly enriched my understanding of experimental methods and data analysis. His mentorship and guidance have been instrumental throughout my research. He generously shared the first Python scripts that motivated me to develop custom code for my data-fitting models, as well as the LaTeX templates that supported my manuscripts preparation.

I am sincerely grateful to my colleagues and collaborators at TRIUMF, including E. Theong, P. Kolb, Z. Yao, M. Abbaslou, D. Lang, J. Keir, S. Bruckner, P. D. Zilwa and many others, for their continual support and collaboration. In particular, I owe special thanks to E. Theong for his generous time, technical

assistance, and insightful discussions, which have been invaluable throughout my graduate studies. I also wish to acknowledge R. M. L. McFadden, T. Junginger, E. Theong, A. MacFarlane, S. Dunsiger, G. Morris, V. Karner, J. Ticknor, D. Fujimoto, I. McKenzie, D. Arseneau, B. Hitti, R. Li, R. Abasalti, and D. Vyas for their assistance during the βNMR experiments. I am especially thankful for the hands-on guidance and discussions provided by R. M. L. McFadden, A. MacFarlane, E. Theong, S. Dunsiger, D. Fujimoto, G. Morris, V. Karner, and J. Ticknor during βNMR beamtime. I further acknowledge R. M. L. McFadden, E. Theong, and T. Junginger for taking experimental shifts; B. Laxdal for his support; and G. Morris, D. Arseneau, D. Vyas, and B. Hitti for their technical assistance during the μSR experiments.

I gratefully acknowledge A.-M. Valente-Feliciano and D. R. Beverstock from Jefferson Lab (Newport News, VA, USA) for thin film coating of LE-μSR samples, and Y. Kalboussi and T. Proslier from CEA Paris-Saclay University (Paris, France) for coating βNMR samples. I also thank the LE-μSR support staff—T. Prokscha, A. Suter, and Z. Salman—for their essential contributions to LE-μSR experiment.

On a personal note, I am forever indebted to my mother, for her unconditional love, care, countless sacrifices, and plenty of prayers, and to my father, for his hard work, perseverance, unwavering support and constant encouragement. My deepest gratitude goes to my wife, Farhana Firdaus, for her enduring love, patience, support and encouragement throughout this journey—her companionship and belief in me have been a source of strength and balance throughout the challenges of this path. I am also profoundly thankful to my brother, Md Aminul Islam, for his constant encouragement and for supporting and taking care of our parents in my absence.

Finally, I extend my heartfelt thanks to my extended family, friends, and well-wishers whose encouragement, kindness, and good wishes have provided me with strength and motivation throughout this endeavor.

Preface

The research presented in this thesis is the result of a broad collaborative effort involving multiple research groups from the University of Victoria, TRIUMF, and several international institutions. The experiments performed used radioactive beam–based techniques that require access to large accelerator facilities, where beam time is both highly competitive and limited. The μSR and βNMR measurements were carried out at TRIUMF in Vancouver, Canada, while the LE-μSR experiments were conducted at PSI, CERN, in Switzerland. Each experiment required a successful research proposal and formal beam-time approval from the respective facility. Once scheduled, the measurements were conducted in continuous, round-the-clock shifts over one- to two-week periods, typically several times per year. Responsibilities were shared among collaborators/coauthors to ensure efficient and reliable data acquisition. These efforts culminated in three peer-reviewed publications. My principal contributions include data analysis and manuscript preparation for all three studies, with specific details for each experiment outlined below.

Chapter 5 is primarily based on the publication:

- M. Asaduzzaman, R. M. L. McFadden, E. Thoeng, R. E. Laxdal, and T. Junginger, "Measurements of the first-flux-penetration field in surface-treated and coated Nb: distinguishing between near-surface pinning and an interface energy barrier", Supercond. Sci. Technol. **37**, 085006 (2024)

The original research proposal and progress reports were prepared by Dr. Tobias Junginger, who also designed the experiments. The samples were prepared through a multi-step synthesis procedure by collaborators from TRIUMF and Cornell University (New York, USA). I contributed to the experimental planning and actively participated in the beamtime shifts during data collection. The data analysis code was developed jointly by Dr. Ryan M. L. McFadden and me, and I performed all

data analysis. The manuscript was co-written by Dr. Junginger, Dr. Ryan M. L. McFadden, and me, with the initial draft written by me. The other coauthors took experimental shifts and supported the experiment. All co-authors contributed to the interpretation of the results and the final revision of the manuscript.

Chapter 6 is based on the publication:

- M. Asaduzzaman, R. M. L. McFadden, A.-M. Valente-Feliciano, D. R. Beverstock, A. Suter, Z. Salman, T. Prokscha, and T. Junginger, "Evidence for current suppression in superconductor–superconductor bilayers", Supercond. Sci. Technol. **37**, 025002 (2023)

The original research proposal and experimental design were developed by Dr. Tobias Junginger. Sample synthesis was performed in multiple stages by collaborators from TRIUMF and the SRF Institute at Thomas Jefferson National Accelerator Facility (Virginia, USA). Code development was conducted by Dr. Ryan M. L. McFadden and I, while I was responsible for all data analysis. The manuscript was co-written by Dr. Junginger, Dr. Ryan M. L. McFadden, and me, with the first draft prepared by me. The other coauthors assisted in performing the experiments. All co-authors participated in result interpretation, discussions, and manuscript revisions.

Chapter 7 is based on the publication:

- M. Asaduzzaman, R. M. L. McFadden, E. Thoeng, Y. Kalboussi, I. Curci, T. Proslier, S. R. Dunsiger, W. Andrew MacFarlane, G. D. Morris, R. Li, J. O. Ticknor, R. E. Laxdal, and T. Junginger, "Superconducting properties of thin film $Nb_{1-x}Ti_xN$ studied via the NMR of implanted ^{8}Li", J. Phys.: Condens. Matter **37**, 395701 (2025)

The original research proposal was written by me, serving as the principal investigator. The sample preparation involved a multi-step synthesis process carried out by collaborators from TRIUMF and IRFU at CEA Paris-Saclay University (Paris,

France). I designed the experiments in consultation with Dr. Ryan M. L. McFadden and Dr. Tobias Junginger, and actively participated in the beamtime to perform the measurements. I developed the analysis code and carried out all data processing and interpretation. The manuscript was co-written by Dr. Ryan M. L. McFadden and me, with the initial draft authored by me. The other coauthors either helped prepare the sample, took experimental shifts, or provided support during beamtime. All co-authors contributed to the interpretation of the results and the final revision of the manuscript.

Each of the aforementioned works are published open access under a Creative Commons Attribution 4.0 License. They are reproduced here with minor editorial modifications to ensure the clarity and consistency of the overall thesis structure. Figures from other works are also included in this thesis, with permission for reproduction granted by their respective publishers.

Chapter 1

Introduction

This thesis explores superconducting coating on Nb, both with and without alternating insulating layers, aimed at increasing the maximum applied magnetic field (B_0) under which Nb's Meissner state can be sustained—an essential parameter for advancing superconducting radio frequency (SRF) cavity performance. SRF cavities, which serve as microwave-frequency electrodynamic resonators, accelerate charged particles via the electric field established when radio frequency (RF) power is applied near resonance. The axial electric field drives acceleration, while the associated B_0 extends along the cavity surface. Since B_0 scales with the accelerating gradient (E_{acc}), which determines the energy imparted per unit length, increasing this limit is critical for improving accelerator efficiency. Once B_0 exceeds a critical threshold, the superconductor quenches—transitioning from Meissner to normal state—leading to energy dissipation and degradation of cavity performance.

Nb is the material of choice for SRF cavities due to its favorable superconducting properties, including the highest critical temperature (T_{c}) among elemental metals of 9.2 K and the highest lower critical field (B_{c1}) of $\simeq$ 170 mT of all superconductors [7, 8]. These properties are vital for maintaining stable superconductivity in the presence of magnetic fields, a requirement in the operation of particle accelerators. Despite this, practical breakdown fields in Nb cavities typically occur around ~80 mT to 100 mT [2, 8–10], significantly below the theoretical B_{c1}. In pursuit of higher performance and delayed quench (superconducting break-

down field) onset, various low-temperature heat treatments—commonly referred to as low-temperature baking (LTB)—have been developed, wherein Nb cavities are baked at around 120 °C in vacuum or low-pressure gas atmospheres modifying the composition and structure of the Nb at the inner surface of the cavity where flux penetration starts [11–16]. Such treatments have enabled $E_{\mathrm{acc}} \sim 50\,\mathrm{MV\,m^{-1}}$, corresponding to a $B_0 \sim 200\,\mathrm{mT}$ in TESLA-shaped cavities [17].[1] Achieving further advancements with "bulk" Nb technology faces intrinsic limitations, as the surface screening current density, $J_0 \propto B_0$, approaches the depairing current density (J_{d})—the fundamental limit of superfluid stability. This threshold corresponds to the superheating field (B_{sh}) (i.e., $J_{\mathrm{d}} \propto B_{\mathrm{sh}}$), which defines the ultimate field limit under RF conditions beyond which the Meissner state becomes unstable. Crossing this limit initiates vortex penetration, dissipation, and ultimately the quenching of superconductivity.

A promising route to overcome the limitations of bulk Nb involves coating Nb with other thin superconducting layers—either alone (superconductor-superconductor (SS) structures [18, 19]) or interleaved with insulating layers (superconductor-insulator-superconductor (SIS) heterostructures [18, 20–22]). These coatings are designed with materials possessing a longer magnetic penetration depth (λ), than their Nb "substrate," which are predicted to suppress surface screening currents and thereby help sustain the Meissner state beyond the B_{sh} of each individual layer. In coated superconducting heterostructures, the vortex penetration field in the substrate layer is enhanced by a reduction in screening currents, which arises from a compensating "counter-current"[2] induced in the underlying substrate. Furthermore, an interfacial energy barrier analogous to the Bean-Livingston (BL) barrier [24] forms at the material junction, helping to inhibit vortex penetration into the bulk. SIS heterostructures provide an even more robust defense against flux entry; in these systems, the inclusion of insulating layers does not impede the

[1] This is an elliptical 9-cell cavity shape is designed for TeV Superconducting Linear Accelerators (TESLA) [17].
[2] This is a counterflow current generated by the substrate in a multilayer superconductor [18, 19, 22, 23].

propagation of vortices from the surface into the underlying Nb substrate.

To study the behavior of such layered superconducting systems, a variety of experimental techniques can be employed to probe local magnetic-field distributions, visualize vortex structures, examine flux penetration, and determine penetration depth. Magneto-optical imaging [25–29] enables real-time visualization of flux dynamics and trapping with micrometer-scale spatial resolution, while Bitter decoration [30–34] provides sub-micrometer imaging of vortices on the sample surface. Techniques such as scanning superconducting quantum interference device (SQUID) microscopy [35], scanning tunnelling microscopy (STM) [36–38] and scanning Hall-probe microscopy [39, 40] offer local magnetic-field mapping with micrometer-scale lateral resolution. Similarly, Magnetic force microscopy (MFM) [41–43] provides surface-sensitive measurements with high lateral resolution and has been employed to extract penetration depth. Furthermore, combined MFM and SQUID susceptometry [44, 45] enables simultaneous determination of penetration depth and pinning forces. In contrast, bulk-sensitive techniques such as macroscopic magnetization measurements [46–48] and neutron scattering [49] provide averaged superconducting properties over the entire sample volume. Despite their success in characterizing superconductors, these methods typically offer either high-resolution surface information or bulk-averaged responses, and thus lack true depth-resolved capability essential for investigating layered heterostructures such as SS and SIS systems.

For investigations requiring depth resolution, the superconducting behaviour of coated Nb is examined using depth-resolved techniques such as muon spin rotation (μSR), low energy muon spin rotation (LE-μSR), and β-detected nuclear magnetic resonance (βNMR), which utilize implanted radioactive probes to measure the local electromagnetic environment within the sample. These methods are especially suited for studying field penetration, Meissner screening profiles, and superconducting properties in both bulk and multilayer systems. Specifically,

μSR measurements of the first flux penetration field in Nb_3Sn-coated Nb and LTB-treated Nb provided evidence for an interface barrier. The suppression of Meissner currents in the surface layers was observed via LE-μSR by measuring nanoscale (depths $\lesssim$150 nm) screening profiles in 50 nm, 80 nm, and 160 nm $Nb_{1-x}Ti_xN$ on Nb samples under applied fields of $\leq$ 25 mT. Finally, the superconducting and normal-state properties of a thin-film $Nb_{0.75}Ti_{0.25}N$ in a SIS $Nb_{0.75}Ti_{0.25}N$(91 nm) /AlN(4 nm)/Nb heterostructure were characterized using βNMR in the vortex state for future Meissner-vortex transition measurements.

In order to interpret the experimental observations and guide the selection of appropriate measurement techniques, the remainder of this dissertation is organized as follows. Chapters 2 and 3 present the theoretical framework of superconductivity, including both conventional bulk superconductivity and extensions relevant to heterostructured systems. Building on that foundation, the Chapter 4 details the experimental methods, with each technique chosen based on its sensitivity to key superconducting properties and its relevance to the specific questions addressed. The Chapters 5 to 7 present the experimental investigations carried out using above techniques. Finally, Chapter 8 summarizes the key findings and outlines directions for future research.

Chapter 2

Basics of superconductivity

Superconductivity is a remarkable physical phenomenon observed in certain electrically conductive materials at extremely low temperatures, characterized by zero electrical resistance and unique magnetic properties. When cooled below a critical temperature (T_c), these materials undergo an electronic phase transition into a superconducting state.

2.1 Meissner effect

One of the most striking and defining properties of superconductors is the Meissner effect, discovered by Meissner et al. in 1933 [50]. Upon entering the superconducting state, a material expels magnetic fields from its interior, creating a state of perfect diamagnetism. This magnetic field exclusion is not merely a consequence of zero resistance, but rather a fundamental property of the superconducting phase itself. While both superconductors and ordinary diamagnetic materials oppose applied magnetic fields, they do so in fundamentally different ways. In ordinary diamagnets, such as bismuth, weakly induced currents oppose changes in the applied field, but the material still permits partial penetration of magnetic flux into its bulk. In contrast, superconductors exhibit perfect diamagnetism,[1] actively expelling magnetic flux from their interior below T_c, regardless of its initial state,

[1] For comparison, bismuth has one of the largest diamagnetic susceptibilities among non-superconductors, yet its response is still about 10^4 times weaker than the perfect diamagnetism of a superconductor.

as illustrated in Figure 2.1. As a result, cooling an ordinary diamagnetic material has no effect on any magnetic flux already present, whereas a superconductor will expel the field upon entering the superconducting state. This perfect diamagnetic response is what sets the Meissner effect — and thus superconductivity — apart from conventional diamagnetic behaviour.

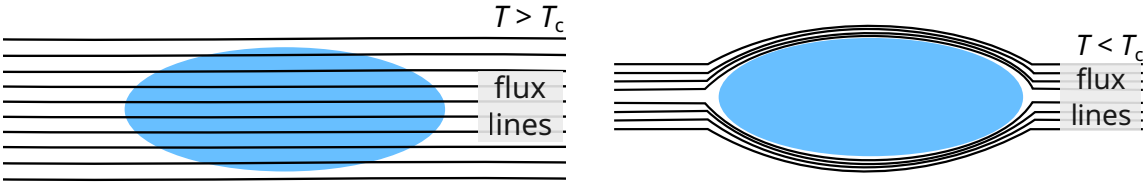

(a) Normal state (b) Meissner state

Figure 2.1: Ellipsoidal samples in different states. (a) Normal state: Magnetic flux lines pass through the superconductor, and (b) Meissner state: flux lines expel from the interior of the superconductor.

Based on the discovery of the Meissner effect, the London brothers proposed a theoretical framework to describe how magnetic fields behave inside superconductors, including how they are expelled near the surface [51]. Their model provides quantitative estimates for the penetration depth of magnetic fields into a superconductor, forming the foundation of the London equations, which we describe below.

2.2 London model

In order to derive London equations [51], the relevant Maxwell's equation is:

$$\nabla \times \mathbf{E} = -\frac{1}{c}\frac{\partial \mathbf{B}}{\partial t}, \tag{2.1}$$

where ∇ represents the three-dimensional gradient operator, $\mathbf{E}$ is the electric field, $\mathbf{B}$ is the magnetic field, and c is the speed of light. According to the classical Drude model of electrical conductivity, which describes charge transport in metals, conduction electrons experience resistance due to scattering. In contrast,

in a superconducting metal, superconducting electrons move without resistance. Consequently, their equation of motion in an electric field contains no friction term:

$$m\frac{\mathrm{d}\mathbf{v_s}}{\mathrm{d}t} = -e\mathbf{E}, \tag{2.2}$$

where $\mathbf{v_s}$ is the velocity of the superconducting electrons and m and e are their mass and charge, respectively. Given a density n_s of superconducting electrons per unit volume, the resulting supercurrent density $\mathbf{J_s}$ is:

$$\mathbf{J_s} = -n_\mathrm{s} e \mathbf{v_s}. \tag{2.3}$$

Substituting Equation (2.3) into Equation (2.2), leads directly to the first London equation:

$$\frac{\mathrm{d}\mathbf{J_s}}{\mathrm{d}t} = \left(\frac{n_\mathrm{s}e^2}{m}\right)\mathbf{E}. \tag{2.4}$$

Taking the curl on both sides of Equation (2.4) and substituting Equation (2.1) yields the second London equation:

$$\frac{m}{n_\mathrm{s}e^2}\left(\boldsymbol{\nabla}\times\frac{\mathrm{d}\mathbf{J_s}}{\mathrm{d}t}\right) = \boldsymbol{\nabla}\times\mathbf{E} \tag{2.5}$$

$$\frac{mc}{n_\mathrm{s}e^2}\left(\boldsymbol{\nabla}\times\frac{\mathrm{d}\mathbf{J_s}}{\mathrm{d}t}\right) + \frac{\mathrm{d}\mathbf{B}}{\mathrm{d}t} = 0 \tag{2.6}$$

$$\frac{\mathrm{d}}{\mathrm{d}t}\left(\boldsymbol{\nabla}\times\mathbf{J_s} + \frac{n_\mathrm{s}e^2}{mc}\mathbf{B}\right) = 0. \tag{2.7}$$

To account for the magnetic flux expulsion from a superconducting body, the Londons postulated that:

$$\left(\boldsymbol{\nabla}\times\mathbf{J_s} + \frac{n_\mathrm{s}e^2}{mc}\mathbf{B}\right) = 0, \tag{2.8}$$

which is consistent with Equation (2.7). Recalling the fourth Maxwell equation (for time-independent fields):

$$\mathbf{J_s} = \frac{c}{4\pi}\left(\boldsymbol{\nabla} \times \mathbf{B}\right), \tag{2.9}$$

substituting Equation (2.9) into Equation (2.8) produces:

$$(\boldsymbol{\nabla} \times \boldsymbol{\nabla} \times \mathbf{B}) + \frac{4\pi n_s e^2}{mc^2}\mathbf{B} = 0, \tag{2.10}$$

$$\boldsymbol{\nabla}(\boldsymbol{\nabla} \cdot \mathbf{B}) - \boldsymbol{\nabla}^2\mathbf{B} + \frac{4\pi n_s e^2}{mc^2}\mathbf{B} = 0 \tag{2.11}$$

$$\nabla^2\mathbf{B} = \frac{1}{\lambda_L^2}\mathbf{B}, \tag{2.12}$$

where

$$\frac{1}{\lambda_L^2} = \frac{4\pi n_s e^2}{mc^2}. \tag{2.13}$$

At vacuum-superconductor interface, the solution of Equation (2.12) is given by:

$$B(z) = B_0 \times \begin{cases} 1, & z < 0, \\ \exp\left(-\dfrac{z}{\lambda_L}\right), & z \geq 0, \end{cases} \tag{2.14}$$

where B_0 is the magnitude of the external applied field, z is the length below the surface and the quantity λ_L is known as the London penetration depth [51]. The behaviour of Equation (2.14) is shown in Figure 2.2. The most important consequence of Equation (2.9) and Equation (2.12) is that a static magnetic field is screened from the interior of a bulk superconductor over a characteristic length scale λ_L. As one approaches the critical temperature T_c, $n_s \to 0$ continuously as $T \to T_c$, and, as a consequence of Equation (2.14), $\lambda(T)$ diverges toward infinity. Equation (2.14) is true for $T = 0$, Gorter and Casimir found that good agreement

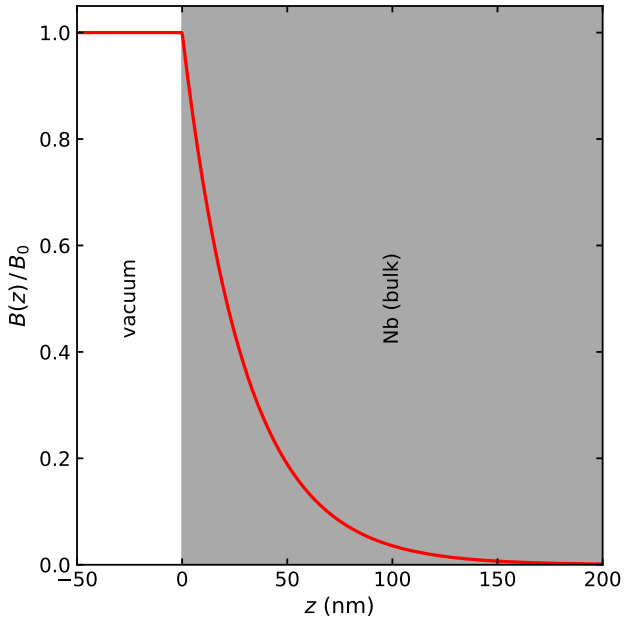

Figure 2.2: Exponential decay of magnetic field $B(z)$ screening inside a superconductor as a function of depth z from the surface, normalized to the applied field B_0. The decay follows the London model described by Equation (2.14), with London penetration depth (λ_L) of 30 nm, indicating the characteristic length over which the field decreases to $1/e$ of B_0.

with early experiments could be obtained if one assumes, what is known as the "two-fluid" model [52]. The model assumes that the total current in the superconductor below the critical temperature T_c is the sum of two components (electron fluids), one of normal electrons and one of superconducting electrons:

$$n_s(T) = n_n \left[1 - \left(\frac{T}{T_c} \right)^2 \right]. \tag{2.15}$$

Here, n_n is the density of normal conducting electrons. Empirically, the T-dependence of λ_L follows:

$$\lambda_L(T) \approx \lambda_L(0\,\mathrm{K}) / \sqrt{1 - (T/T_c)^n}, \tag{2.16}$$

where the exponent $n = 2 - 4$ and 0 K penetration depth is defined as:

$$\lambda_{\mathrm{L}}(0\,\mathrm{K}) = \sqrt{\frac{mc^2}{4\pi n_{\mathrm{s}} e^2}}. \tag{2.17}$$

In many conventional superconductors, $n = 4$, which is consistent with the two-fluid model of Gorter and Casimir;[2] however, the behaviour isn't universal.

Alternatively, for some superconductors $n = 2$ gives much better agreement with the data. Interestingly, the use of $n = 2$ in Equation (2.16) gives an excellent analytic approximation of λ_{L}'s T-dependence derived from Bardeen-Cooper-Schrieffer (BCS) theory — a microscopic model of superconductivity [53]. The behaviour of both $n = 2$ and 4 in Equation (2.16) are plotted in Figure 2.3.

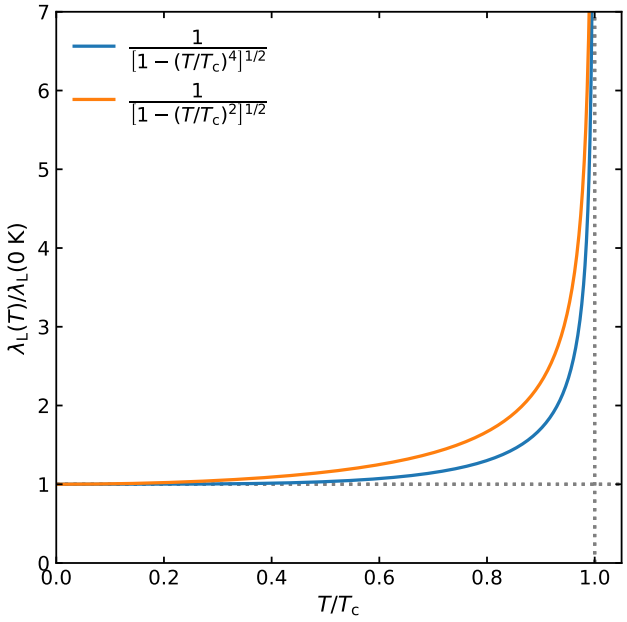

Figure 2.3: Temperature dependence of the London penetration depth $\lambda_{\mathrm{L}}(T)$ calculated using Equation (2.16) with both $n = 2$ and $n = 4$. The values of λ_{L} remain constant near $T = 0$ K and diverges as T approaches T_{c}.

While the London model effectively describes the electromagnetic response of superconductors, particularly the expulsion of magnetic fields (the Meissner

[2]This could be derived by substituting Equation (2.15) in Equation (2.13).

effect), it does not account for the thermodynamic or spatially varying properties of the superconducting state near the transition temperature.

2.3 Ginzburg-Landau theory

To address the shortcomings of London theory, the Ginzburg-Landau (GL) theory was proposed by Vitaly Ginzburg and Lev Landau in 1950 [54] as a phenomenological framework providing a macroscopic description of superconductivity. GL theory extends the London model by introducing a macroscopic complex order parameter $\psi(\hat{\mathbf{r}})$ for the low T "ordered" state of the electrons (i.e., the superfluid electrons), which represents the collective behaviour of the superconducting electron pairs. This order parameter varies smoothly in space and is particularly sensitive near the T_c, where the superconducting state emerges. Under conditions of small variations in $\psi(\hat{\mathbf{r}})$ near T_c and in the absence of a magnetic field, the free energy density of the superconducting state, F_s, can be expanded as a power series in $|\psi(\hat{\mathbf{r}})|^2$, relative to the normal-state free energy density F_n:

$$F_s = F_n + \alpha(T)|\psi(\hat{\mathbf{r}})|^2 + \frac{\beta(T)}{2}|\psi(\hat{\mathbf{r}})|^4 + ..., \tag{2.18}$$

here $\alpha(T)$ and $\beta(T)$ are material dependent phenomenological parameters. While Equation (2.18) is strictly valid only for temperatures $T \simeq T_c$, the expansion contains only even powers of the order parameter, ensuring stability both at the transition and in the superconducting state. For $T \geq T_c$ the free energy F_s must have a minimum at $\psi = 0$, while stability of the superconducting state requires $\beta(T) > 0$ so that F_s admits a minimum at finite $|\psi|$. Consequently, the change in free energy density ΔF:

$$\Delta F = F_s - F_n = \alpha(T)|\psi(\hat{\mathbf{r}})|^2 + \frac{\beta(T)}{2}|\psi(\hat{\mathbf{r}})|^4 + ..., \tag{2.19}$$

is contingent only on the sign of $\alpha(T)$. In the normal-conducting phase ($T > T_c$), $\alpha(T) > 0$, leading to the minimum at $\psi(\hat{\mathbf{r}}) = 0$ (see, Figure 2.4). Conversely, in the superconducting phase ($T < T_c$), $\alpha(T) < 0$, resulting in the minimum at:

$$|\psi(\hat{\mathbf{r}})|^2 = -\frac{\alpha}{\beta}. \tag{2.20}$$

Thus, $\alpha(T)$ must necessarily change its sign at T_c.

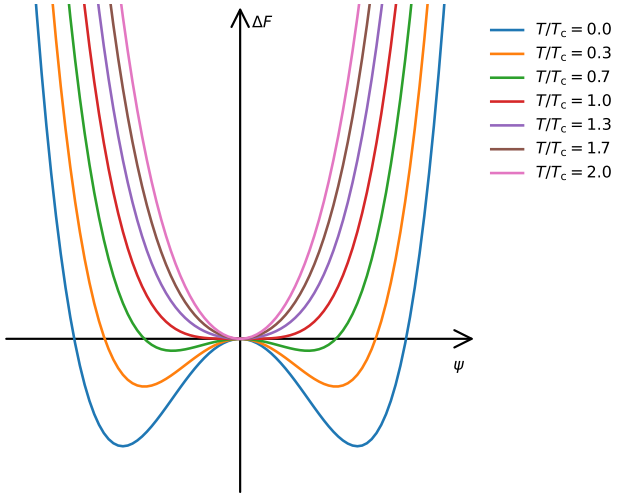

Figure 2.4: GL free energy functions plotted as a function of the order parameter ψ for temperatures above and below the critical temperature, T_c. For $T > T_c$ ($\alpha > 0$), the free energy exhibits a single minimum at $\psi = 0$, corresponding to the normal state. For $T < T_c$ ($\alpha < 0$), the free energy develops a double-well structure, with minima at nonzero values of ψ, representing the emergence of the superconducting state. For simplicity, ψ is assumed to be real in this plot.

To account for spatial variations of the order parameter—such as those introduced by surfaces or interfaces—and the presence of a magnetic field, the free energy density expansion in Equation (2.18) must be generalized. The resulting GL free energy density takes the form [55]:

$$F_s = F_n + \alpha(T)|\psi(\hat{\mathbf{r}})|^2 + \frac{\beta(T)}{2}|\psi(\hat{\mathbf{r}})|^4 + \frac{1}{2m^*}|(-i\hbar\nabla - e^*\mathbf{A})\psi(\hat{\mathbf{r}})|^2 + \frac{B^2}{2\mu_0}, \tag{2.21}$$

where $m^* = 2m$, $e^* = \pm 2e$ with their hole(electron) counterparts m and $\pm e$ and $\mathbf{A}$ represents the vector potential describing the currents (hence magnetic field) in

the superconductor—the kinetic energy of a charged particle in a magnetic field. The last term is the energy density of the magnetic field inside the superconductor. Minimizing the free energy with respect to $\psi(\hat{\mathbf{r}})$ yields the condition that $\psi(\hat{\mathbf{r}}) \to 0$ as $T \to T_c$, and $|\psi(\hat{\mathbf{r}})|^2 = n_\mathrm{s}(\hat{\mathbf{r}})$, identifying the order parameter magnitude with the local superconducting carrier density. The following definition of the GL penetration depth is obtained:

$$\lambda_\mathrm{GL} = \sqrt{\frac{m^* c^2}{4\pi|\psi(r)|^2 e^{*2}}}, \tag{2.22}$$

$$= \sqrt{\frac{m^* c^2}{4\pi n_\mathrm{s} e^{*2}}} \simeq \lambda_\mathrm{L}. \tag{2.23}$$

Expressing the density of superconducting carriers in terms of the equilibrium value of the order parameter i.e., Equation (2.20), which is applicable far from an interface it is found that Equation (2.22) agrees with the definition of λ_L in Equations (2.13) and (2.17).

In addition to identifying λ_L, GL theory introduces another fundamental length scale, the coherence length ξ_GL, which emerges when minimizing the free energy with respect to a spatially varying ψ in the absence of an external magnetic field. This characteristic length defines the spatial scale over which variations in the magnitude of the order parameter, or equivalently the density of superconducting electrons, occur:

$$\xi_\mathrm{GL}(T) = \sqrt{-\frac{\hbar}{2m\alpha(T)}}, \tag{2.24}$$

where $\alpha(T)$ is a temperature-dependent coefficient in the series expansion of the free energy.

To classify different types of superconductors, the GL theory defines a dimen-

sionless parameter κ, known as the GL parameter, which is the ratio of the λ_L to the ξ_{GL}:

$$\kappa = \frac{\lambda_L}{\xi_{GL}}. \tag{2.25}$$

This parameter plays a crucial role in determining the magnetic behaviour of super-

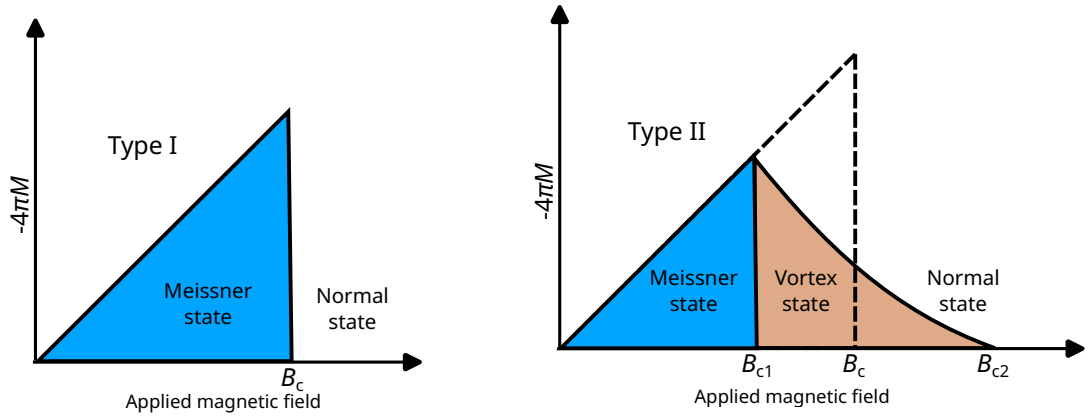

(a) type-I (b) type-II

Figure 2.5: Magnetization ($-4\pi M$) as a function of applied magnetic field for (a) type-I and (b) type-II superconductors. (a) A type-I superconductor exhibits a complete Meissner state up to the thermodynamic critical field B_c, above which it undergoes a first-order transition to the normal state. (b) A type-II superconductor is characterized by two critical fields: the lower critical field B_{c1}, at which magnetic flux begins to penetrate the material in the form of quantized vortices (vortex or mixed state), and the upper critical field B_{c2}, beyond which superconductivity is destroyed and the material becomes normal. The region between B_{c1} and B_{c2} corresponds to the vortex state, where the superconductor partially expels the magnetic field while allowing quantized flux lines to penetrate. The dashed line marks the B_c.

conductors. Seven years after Ginzburg and Landau's publication, Abrikosov [56] demonstrated that κ governs the transition between type-I and type-II behaviour through the sign of the surface (interface) energy separating normal and superconducting regions. For small κ, this energy is positive, making it energetically unfavorable for magnetic flux to penetrate, resulting in complete flux expulsion (type-I behaviour). For κ values above a certain critical value, the interface energy becomes negative, and above a lower critical field (B_{c1}), it is favorable for magnetic flux to enter the material as quantized vortices where superconductivity is locally

suppressed—characteristic of type-II superconductors:

$$\kappa < \frac{1}{\sqrt{2}} \rightarrow \text{type-I}, \tag{2.26}$$

$$\kappa > \frac{1}{\sqrt{2}} \rightarrow \text{type-II}. \tag{2.27}$$

This distinction is illustrated in Figure 2.5, in type-I superconductors, the applied magnetic field is completely expelled from the bulk (the Meissner state) up to a thermodynamic critical field thermodynamic critical field (B_c), beyond which superconductivity is abruptly destroyed. In contrast, type-II superconductors exhibit a completely different magnetic response: above a lower critical field B_{c1}, magnetic flux begins to penetrate the material in the form of quantized vortices—regions where superconductivity is locally suppressed and magnetic flux lines pass through. In many cases, these vortices arrange themselves in a regular lattice, forming what is known as the mixed or vortex state. This state persists until an upper critical field (B_{c2}), above which the material transitions fully into the normal (non-superconducting) state. The field distribution within the vortex state is further described in Section 2.5.2.

2.4 BCS theory

Despite the success of GL theory in describing the macroscopic behaviour of superconductors, it does not address the microscopic mechanism underlying the formation of the superconducting state. This fundamental question was resolved by the development of the Bardeen-Cooper-Schrieffer (BCS) theory in 1957 [57, 58], which remains the most successful and widely accepted microscopic explanation of conventional superconductivity.[3] BCS theory offers a quantum mechanical

[3]The term "conventional superconductors" refers to materials whose superconducting properties are well described by the BCS theory, where electron pairing arises from electron-phonon interactions. In contrast, "unconventional superconductors"—such as cuprates, iron-based, or heavy-fermion systems—exhibit pairing mechanisms that deviate from the BCS framework and are often not mediated by phonons.

explanation for superconductivity by describing how conduction electrons form bound pairs, known as "Cooper pairs." Rather than presenting full derivations of the BCS formalism, the following discussion outlines the central concepts and physical insights that form the foundation of the theory. For readers interested in a more detailed treatment, comprehensive discussions can be found in Refs. [55, 59].

The concept of Cooper pairs was first introduced by L. Cooper in 1956 [60], who showed that in the presence of an attractive interaction, even an infinitesimal one, electrons near the Fermi surface—the boundary between occupied and unoccupied electronic states at zero temperature—can pair up. In a crystalline lattice, this attraction arises from an interaction mediated by phonons (or lattice vibrations). As a negatively charged electron moves through an arrangement of positively charged ions, it distorts the lattice structure, creating a region of excess positive charge. This distortion then attracts a second electron with opposite spin and momentum, resulting in the formation of a Cooper pair. Electrons are fermions and obey the Pauli exclusion principle, but Cooper pairs act as composite bosons and can occupy the same quantum state. Once paired, these electrons act collectively as a single quantum state and can move through the lattice without resistance. This collective, resistance-free motion of Cooper pairs is what gives rise to the superconducting state.

At the microscopic level, the Fermi-Dirac distribution function describes the probability of occupation of electronic states at a given energy E and temperature T, and is given by:

$$f(E) = \frac{1}{\exp\left((E - E_{\mathrm{F}})/k_{\mathrm{B}}T\right) + 1}, \tag{2.28}$$

where $f(E)$ is the probability of occupancy for energy state E, E_{F} is the Fermi energy (i.e., the energy level of the highest occupied state at absolute zero T), and k_{B} is the Boltzmann constant. At $T \to 0$ all states with energies $E < E_{\mathrm{F}}$ are fully

occupied, while states with $E > E_F$, are empty.

At absolute zero, when two electrons are added to the Fermi sea—the collection of all occupied electronic states up to the Fermi energy—they interact via phonon-mediated coupling to form a Cooper pair. In a typical electron-electron interaction, Coulomb repulsion would prevent pairing, but within a crystal lattice, this repulsion is overcome through the exchange of lattice vibrations (phonons). The exchanged particle in this interaction is a virtual phonon (a transient lattice vibration that mediates an interaction between electrons without being a real, propagating excitation). Unlike real phonon exchange, which would result in a dissipative process transferring energy to the lattice and generating resistance, the virtual phonon exchange allows for the formation of Cooper pairs without dissipation. The characteristic length over which these pairs interact is defined as the BCS coherence length, ξ_0.[4] When the electrons form a singlet state with zero total momentum, they behave as bosons, and the Cooper pairs collectively form a coherent superconducting state described by a single macroscopic wavefunction.

This bound electron state is energetically favored below T_c, but not all electrons in the Fermi sea can pair up. Only electrons within a narrow energy range (on the order of meV) around E_F, specifically within the range $E_F \pm \hbar\omega$ (where ω is the cutoff frequency associated with the maximum phonon energy), contribute to superconductivity. This implies that only a small fraction of the Fermi sea is involved in the superconducting state. The energy of the bound system yields [61, 62]:

$$E_{pair} = 2E_F - \Delta, \tag{2.29}$$

where Δ is the energy gap in the superconducting state between the paired electron state and the non-interacting state. In the weak coupling limit (i.e., $\Delta \ll \hbar\omega$), BCS theory establishes a relationship between Δ at absolute zero and T_c, with the ratio

[4] For a "pure" superconductor (i.e., one where its electron mean free path $\ell \gg \xi_0$) near T_c, ξ_0 is related to the GL coherence length at 0 K by $\xi_{GL}(0\,\mathrm{K}) \simeq 0.74\xi_0$. In the opposite limit (i.e., the "dirty" limit where $\ell \ll \xi_0$), the relation becomes $\xi_{GL}(0\,\mathrm{K}) \simeq 0.855\sqrt{\xi_0 \ell}$ [55].

being approximately constant. This ratio is given by [57, 58]:

$$\frac{\Delta(0\,\mathrm{K})}{k_\mathrm{B}T_\mathrm{c}} = 1.764. \tag{2.30}$$

The magnitude of Δ depends on the strength of the electron-phonon interaction and therefore varies for different materials. Additionally, its value varies with temperature: as T increases from absolute zero to T_c, the gap gradually decreases, and then rapidly approaches zero near T_c. While BCS theory provides no analytic expression for Δ (i.e., it must be computed numerically), an excellent approximation takes the form [63]:

$$\Delta(T) = \Delta(0\,\mathrm{K}) \tanh\left(1.82\left(1.018\left(\frac{T_c}{T} - 1\right)\right)^{0.51}\right) \tag{2.31}$$

where $\Delta(0\,\mathrm{K})$ energy gap at $T = 0\,\mathrm{K}$. An even simpler approximate expression that works well for many superconductors follows [64]:

$$\Delta(T) \approx \Delta(0\,\mathrm{K})\sqrt{\cos\left(\frac{\pi t^2}{2}\right)}, \tag{2.32}$$

where $t = T/T_\mathrm{c}$. Equations (2.31) and (2.32) are compared with the numerical results of BCS theory calculated by Mühlschlegel [65], as shown in Figure 2.6. The approximations closely reproduce the numerical BCS solution across the full temperature range, confirming their validity for conventional superconductors.

The formation of the energy gap significantly alters the density of states (DOS), $N(E)$, which represents the number of available states at a particular energy level for electrons. The gap introduces singularities at the energy levels corresponding to the gap edges. Since Cooper pairs follow the Bose-Einstein distribution, an effectively infinite number of pairs can occupy the same energy level. As a result,

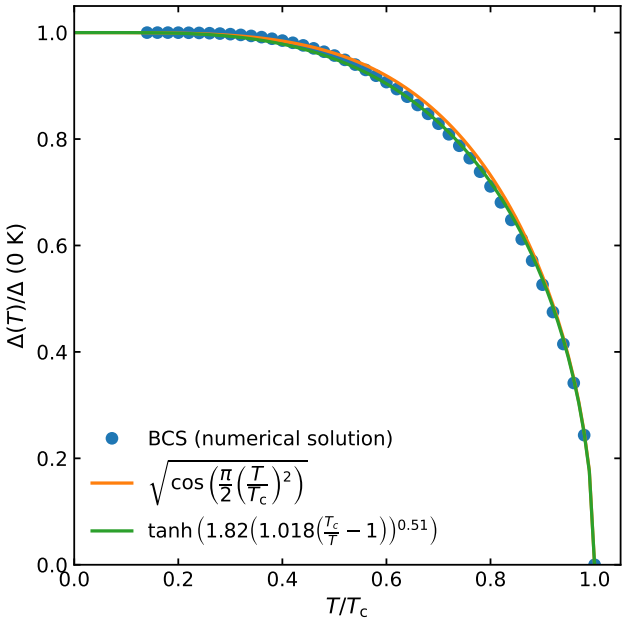

Figure 2.6: Temperature dependence of the normalized energy gap $\Delta(T)/\Delta(0\,\mathrm{K})$ obtained using Equations (2.31) and (2.32), compared with the numerical BCS result [65]. Near absolute zero, all the Δ remains nearly constant, reflecting the stability of the superconducting state at low temperatures. As the temperature approaches the critical temperature T_c, $\Delta(T)$ decreases rapidly, eventually vanishing at $T = T_c$, marking the transition to the normal state. Both analytic forms follow the BCS curve closely, with only subtle deviations near T_c.

the DOS in the superconducting state N_s takes the form:

$$N_s(E) = \begin{cases} N_n(0)\mathrm{Re}\left(\dfrac{|E|}{\sqrt{|E|^2 - \Delta^2}}\right), & \text{for } E > \Delta, \\ 0, & \text{for } E < \Delta, \end{cases} \tag{2.33}$$

where $N_n(0)$ is the DOS in the normal conducting state. In Equation (2.33) the singularities arise when $E = \Delta$, marking the energy gap edges as seen in Figure 2.7. These singularities indicate a sharp change in the DOS near the gap, which plays a crucial role in the superconducting behaviour. In practice, it is crucial to consider *modifications* to the energy gap, which can result from imperfections in the crystal structure and the finite lifetimes of quasiparticles (collective excitation that behave like particles and represent the effective low-energy degrees of freedom in a many-

body system). These factors contribute to the broadening of the singularities in the DOS, ultimately reducing their height. When the singularities are smeared out at $E = \Delta$, subgap states with finite DOS appear at energies below Δ. Such a situation is often described by the phenomenological Dynes formula [66, 67]:

$$N_{\mathrm{s}}(E) = \begin{cases} N_{\mathrm{n}}(0)\mathrm{Re}\left(\dfrac{E - i\Gamma_{\mathrm{D}}}{\sqrt{(E - i\Gamma_{\mathrm{D}})^2 - \Delta^2}}\right), & \text{for } E > \Delta, \\ 0, & \text{for } E < \Delta, \end{cases} \tag{2.34}$$

where Γ_{D} is a broadening term (in other words, a damping parameter) which accounts for the finite lifetime of quasiparticles. The characteristic features of Equation (2.34) with finite quasiparticles lifetime (i.e., $\Gamma_{\mathrm{D}} = 0.1\Delta(0\,\mathrm{K})$ and $0.2\Delta(0\,\mathrm{K})$) are plotted in Figure 2.7. This quantity is measured more or less directly in tunneling experiments, and such data motivated the development of the phenomenology.

2.5 Critical magnetic fields

As discussed in Sections 2.1 and 2.2, in the Meissner state the applied magnetic field (induction) B_0 is screened by $1/e$ over the λ_{L}. However, there is a limit of B_0 below which the sample remains a superconductor, above that limit it turns into normal conductor. The transition to the normal state can be analyzed using thermodynamic principles. In exploring the critical magnetic field of superconductors, our attention turns to the "Gibbs free energy"[5] to compare the magnetic contributions in both phases under the same applied magnetic field.

2.5.1 Thermodynamic critical field B_{c}

For the simplest case of a type-I superconductor at temperature T and in the absence of an applied magnetic field (i.e., $B_0 = 0$), a superconducting specimen

[5] A thermodynamic potential used to compare the stability of the superconducting and normal states in an external magnetic field in a situation of constant external pressure (typically 1 atm).

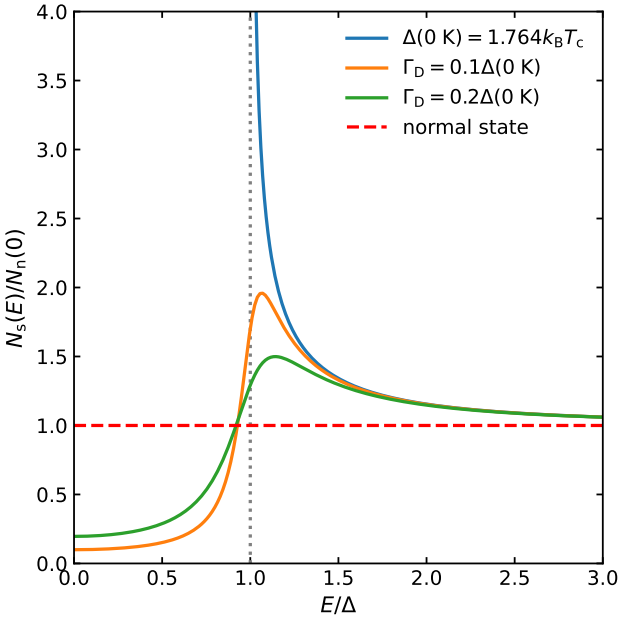

Figure 2.7: Superconducting DOS $N_s(E)$ compared to the normal state $N_n(0)$. The superconducting DOS is shown using the BCS model (Equation (2.33)) with a zero-temperature gap $\Delta(0\,\mathrm{K}) = 1.764 k_B T_c$, as well as the Dynes broadening model (Equation (2.34)) with broadening parameters $\Gamma_D = 0.1\Delta(0\,\mathrm{K})$ and $0.2\Delta(0\,\mathrm{K})$, represented by the solid coloured lines. The red dashed line denotes the normal state DOS. In the ideal BCS case, a divergence in the DOS occurs at $E = \Delta$ (indicated by the vertical dotted line). For $E/\Delta \gg 1$, the superconducting DOS approaches the normal state value.

possesses a Gibbs free energy per unit volume represented by F_s, while the normal conducting state exhibits F_n (as considered in Section 2.3). Upon applying an external magnetic field, B_0, parallel to its surface, it develops a magnetization, M. The alteration in free energy per unit volume is consequently influenced by this magnetic field:

$$\begin{aligned} \Delta F(B_0) &= F_s(T, B_0) - F_s(T, 0), \\ &= -\int_0^{B_0} M\, dB. \end{aligned} \tag{2.35}$$

Given that a superconductor behaves as an ideal diamagnet, its $M = H_0 =$

$-B_0/\mu 0$, whereas in the normal state, is negligible (see Figure 2.5), therefore:

$$\Delta F(B_0) = F_{\mathrm{s}}(T, B_0) - F_{\mathrm{s}}(T, 0) = \frac{B_0^2}{2\mu_0}. \tag{2.36}$$

Thus, a superconductor will be in superconducting state up to maximum magnetic field strength called critical field B_{c}. When $B_0 = B_{\mathrm{c}}$ at a specific temperature $T < T_{\mathrm{c}}$, the free energy takes the form:

$$F_{\mathrm{s}}(T, B_c) - F_{\mathrm{s}}(T, 0) = \frac{B_{\mathrm{c}}^2}{2\mu_0}. \tag{2.37}$$

At B_{c} the free energy density in the superconducting F_{s} and normal state F_{n} are equal which yields:

$$B_{\mathrm{c}} = \sqrt{2\mu_0 \left[F_{\mathrm{n}}(T) - F_{\mathrm{s}}(T, 0)\right]}. \tag{2.38}$$

The B_{c} using GL theory takes the form [55]:

$$B_{\mathrm{c}}(T) = \frac{\Phi_0}{2\sqrt{2}\pi\xi_{\mathrm{GL}}(T)\lambda_{\mathrm{GL}}(T)}, \tag{2.39}$$

where $\Phi_0 = h/2e = 2.068 \times 10^{-15}$ Wb.[6] At temperatures below T_{c}, $B_{\mathrm{c}}(T)$ exhibits an approximate temperature dependence, often well-described by a parabolic relationship given by [55]:

$$B_{\mathrm{c}}(T) = B_{\mathrm{c}}(0\,\mathrm{K}) \left[1 - \left(\frac{T}{T_{\mathrm{c}}}\right)^2\right]. \tag{2.40}$$

Here, $B_{\mathrm{c}}(0\,\mathrm{K})$ is the critical field at $T = 0\,\mathrm{K}$ and $B_{\mathrm{c}}(T)$ represents the maximum field that the Meissner state can sustain for type-I superconductors (see Figure 2.5a). When the applied field strength exceeds this critical value, superconductivity abruptly ceases. In contrast, type-II superconductors exhibit both a lower crit-

[6]The smallest amount of magnetic flux that can penetrate a superconductor is one flux quantum, $\Phi_0 = h/2e$, which corresponds to the magnetic flux associated with a Cooper pair carrying charge $2e$.

ical field B_{c1} and an upper critical field B_{c2} (see Figure 2.5b), which are discussed below.

2.5.2 Lower and upper critical fields B_{c1} and B_{c2}

In type-II superconductors, the Meissner state becomes energetically unfavorable in the presence of external magnetic fields that exceed the lower critical field, denoted as B_{c1}. While a Type-II superconductor exhibits ideal diamagnetism below this threshold (see Figure 2.5b), at higher fields a regular array of flux tubes, termed vortices (see Figure 2.8), allows the partial penetration of the magnetic field into the superconductor. In the simple GL [54] model, each vortex, as illustrated in Figure 2.8, carries a quantized magnetic flux Φ_0 and has a normal-conducting core covering an area of approximately $\pi\xi_{GL}^2/2$ [2]. Inside these "tubules," the order parameter, $\psi(\hat{\mathbf{r}})$, diminishes to zero along the radial axis of each flux tube, with the magnetic field associated with the vortex reaching its maximum at the core center and decaying exponentially outward over the London penetration depth λ_L. Within these normal conducting "cores," there exist shielding currents that rotate in the opposite direction to the diamagnetic surface current. This partial flux penetration is referred to as the "vortex state" or, given the coexistence of superconducting and normal conducting regions, the "mixed state". In this state, the vortices form a lattice whose spacing is determined by the applied field B_0, leading to increasingly dense vortex packing as B_0 increases.

As a consequence of the spatial variation of magnetic flux lines in the vortex state, the magnetic field distribution $p(B)$ exhibits several key characteristics, including a sharp cutoff at low fields, which results from the *minimum* of the field distribution B_{min} (located at the corners of Wigner-Seitz [68] unit cells[7] centered on the vortices), a sharp peak B_{peak} arising from the *saddle point* between two adjacent vortices, and a long tail stemming from the region around the vortex

[7]This is the region of space around a lattice point that contains all points closer to it than to any other lattice point.

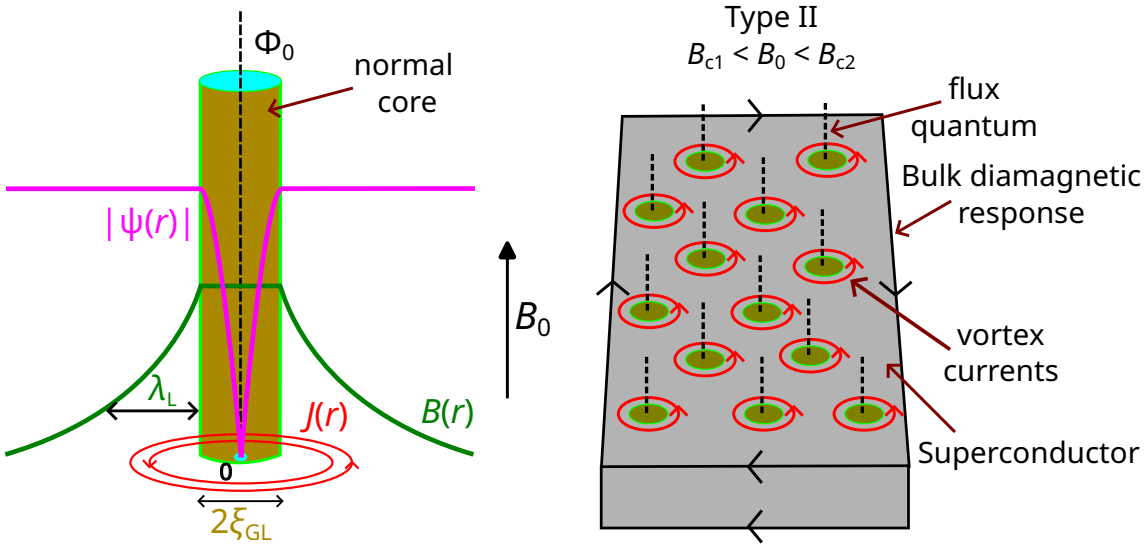

(a) Single vortex (b) Mixed state

Figure 2.8: (a) Illustration of a single vortex in a type-II superconductor, highlighting the normal core, quantized magnetic flux, GL coherence length ξ_{GL}, London penetration depth λ_{L}, and the circulating vortex current $J(r)$. (b) Mixed-state representation showing an array of vortices within the superconducting phase, with the diamagnetic response and quantized flux in each vortex core. The interplay between vortex currents and the surrounding superconducting regions reflects the mixed-state behaviour characteristic of type-II superconductors.

core, with the high-field cutoff dictated by the *maximum* of the field B_{max} at the center of the core [69]. The field distribution of this state, simulated using the models described in Refs. [70–73], is shown in Figure 2.9. Note that $p(B)$ can be experimentally measured using techniques like muon spin rotation (μSR) [74–76]. The variance, $\sigma^2 = \langle (B - \langle B \rangle)^2 \rangle$, of the field distribution is related to λ_{L}. In an isotropic, extreme type-II superconductor with $\kappa \geq 70$ and within the field range $0.13/\kappa^2 \ll b \ll 1$, where $b = B_0/B_{\mathrm{c2}}$, this relationship is often expressed as [74]:

$$\sigma_{\mathrm{sc}}^2(T) = 0.00371 \frac{\Phi_0^2}{\lambda_{\mathrm{L}}^4(T)}. \tag{2.41}$$

This formula demonstrates how the spatial variation of the magnetic field in the vortex state is tied to the material's superconducting properties, particularly to λ_{L}. Thus, B_{c1} marks the boundary between a complete Meissner state, where

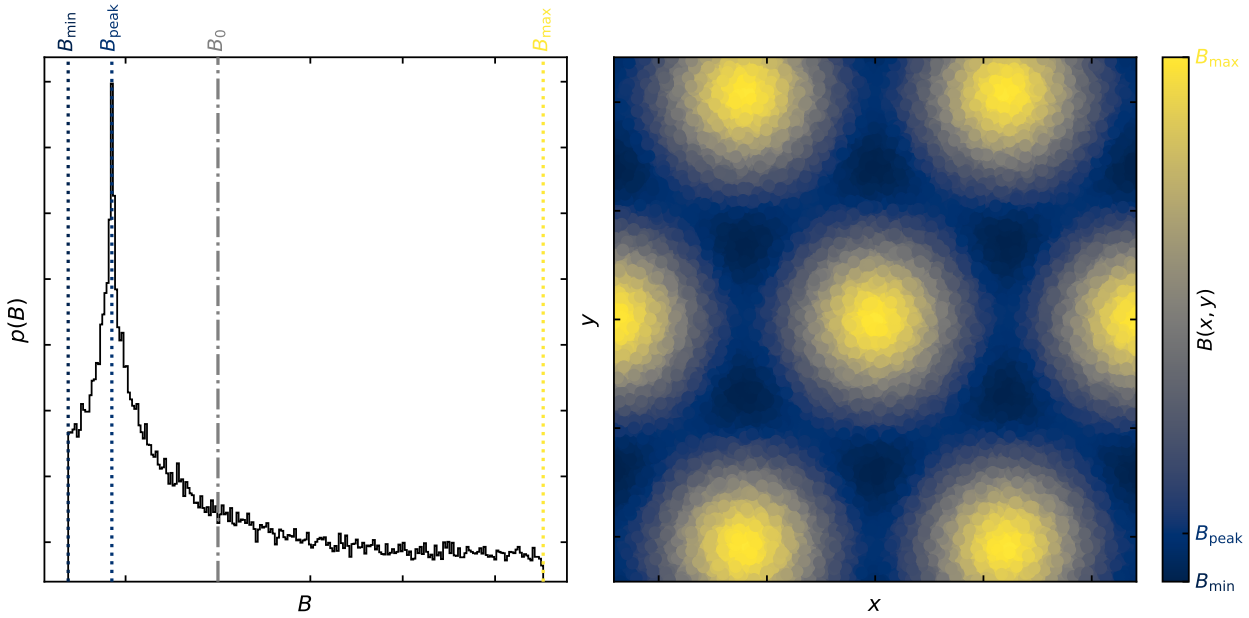

Figure 2.9: Simulated magnetic field distribution of a triangular superconducting vortex lattice based on the modified London model with a Gaussian cutoff, calculated using reciprocal-space summation [72, 73, 77]. Here, B_0 denotes the applied (average) magnetic field corresponding to the mean flux density in the lattice, B_{min} is the lowest local field occurring midway between vortices, B_{peak} represents the most probable field value in the field distribution $p(B)$, and B_{max} is the maximum field found at the vortex cores. (Left) Magnetic field distribution $p(B)$ computed from Monte Carlo sampling of spatial points uniformly distributed within the vortex lattice unit cell, illustrating the characteristic field broadening due to the flux line lattice. (Right) Contour plot of the spatial variation in the magnetic field $B(x, y)$ over several vortex lattice unit cells, showing periodic field modulation around vortex cores.

the magnetic flux is fully expelled except within a few λ of the free surface, and the onset of vortex formation, where quantized flux lines begin to penetrate the superconductor, forming the characteristic field distribution $p(B)$ described above. At this point, the Gibbs free energy is the same whether a vortex is inside or outside the superconductor. By solving the GL equations for a single vortex, one obtains the characteristic expression [55]:

$$B_{c1} \approx \frac{\Phi_0}{4\pi\lambda_L^2} \ln \kappa, \tag{2.42}$$

$$= \frac{B_c}{\sqrt{2}\kappa} \ln \kappa. \tag{2.43}$$

A more general formula for B_{c1} was first derived by Abrikosov [56] through the solution of the GL equations for the cylindrically symmetric scenario, which represents an isolated flux tube, in the case where $\kappa \gg 1$ B_{c1} has the form:

$$B_{c1} = \frac{\Phi_0}{4\pi\lambda_L^2} \left(\ln \kappa + \alpha\right), \tag{2.44}$$

where the additional term $\alpha = 0.08$. A close examination of the precise GL expressions introduces $\alpha = 0.497$ to the B_{c1} [78, 79], which supersedes Abrikosov's earlier approximation. Both $\alpha = 0.08$ and 0.497 are valid only when $k \gg 1$, and do not hold true for $\kappa \to 1/\sqrt{2}$. Therefore, numerical solutions of the GL theory (i.e., Equation (2.21) given the condition when magnetic flux first enters) are required, which were computed over the range of $1/\sqrt{2} < \kappa < \infty$ [80, 81] and showed agreement with the Abrikosov formula at $\kappa \gg 1$ but they deviated at $\kappa \sim 1/\sqrt{2}$ (see Figure 2.10).

An accurate approximation (to within 1 %) for the κ-dependent numeric coefficient was proposed by Brandt [82], which is valid for $1/\sqrt{2} < \kappa < \infty$, where:

$$\alpha = \frac{1}{2} + \frac{1 + \ln 2}{2\kappa - \sqrt{2} + 2}. \tag{2.45}$$

This convenient expression, when used with Equation (2.44), provides excellent agreement with the B_{c1} values derived from numerical solutions to the GL differential equations reported by Harden et al. [80] and Neumann et al. [81], as shown in Figure 2.10. The temperature dependence of the B_{c1} aligns closely with B_c, following an expression akin to Equation (2.40).

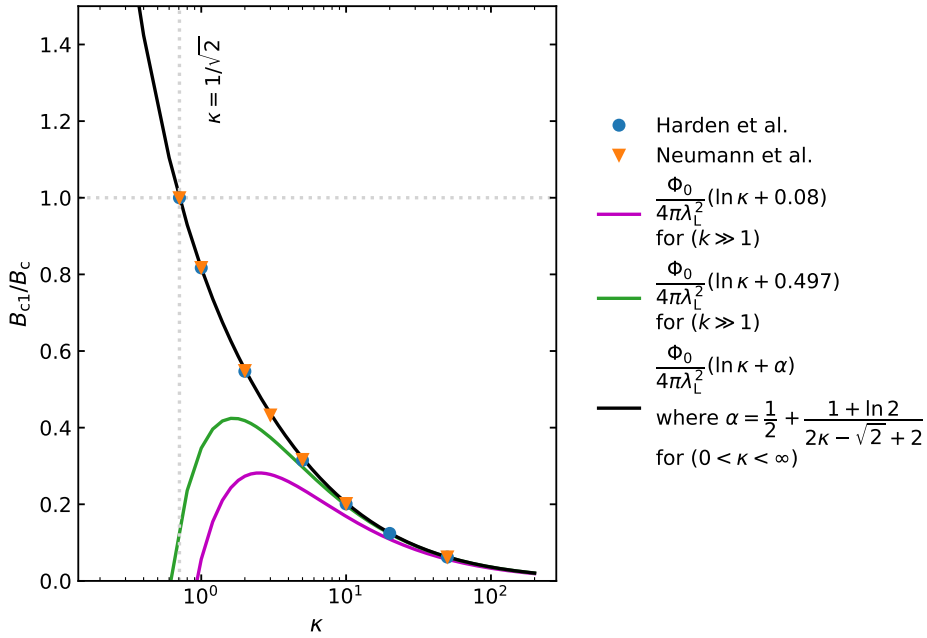

Figure 2.10: Dependence of the lower critical field B_{c1} (normalized by the B_c) on the GL parameter κ. Equation (2.44) with $\alpha = 0.08$ and $\alpha = 0.497$ are shown as purple and green solid lines, respectively, highlighting their deviations from the numerical simulations of Harden et al. [80], Neumann et al. [81], represented by • and ▼. In contrast, Equation (2.45) exhibits excellent agreement with the numerical data and remains valid across the full range of κ that corresponds to type-II superconductivity (i.e., $1/\sqrt{2} \leq \kappa \leq \infty$).

As the magnetic field surpasses B_{c1}, the cores gather closer, increasing the average flux density in the superconductor, as each core carrying a fixed flux amount. With sufficiently high magnetic fields, these cores merge, bringing the combined flux density of the cores and the surface current closer to the flux density of B_0. This critical point, where the flux density aligns with the B_0, marks the transition of the material into the normal state and is termed the upper critical field, B_{c2}. At 0 K, the B_{c2} is defined as follows:

$$B_{c2}(0\,\mathrm{K}) = \frac{\Phi_0}{2\pi\xi_{GL}^2}, \tag{2.46}$$

$$= \frac{4\pi\lambda_L^2 B_c^2}{\Phi_0}, \tag{2.47}$$

$$= \sqrt{2}\kappa B_c, \tag{2.48}$$

The T dependence of B_{c2} can be approximated using Werthamer-Helfand-Hohenberg (WHH) theory, which, while not yielding a closed-form analytical solution, in its simplest form it can be accurately approximated by the expression [83]:

$$B_{c2}(T) = \frac{B_{c2}(0\,\mathrm{K})}{0.693} \cdot h^*(t)\,, \tag{2.49}$$

where $t = \dfrac{T}{T_c}$ and

$$h^*(t) = (1-t) - C_1(1-t)^2 - C_2(1-t)^4\,, \tag{2.50}$$

with $C_1 = 0.153$ and $C_2 = 0.152$. The functional form of Equation (2.49) plotted in Figure 2.11.

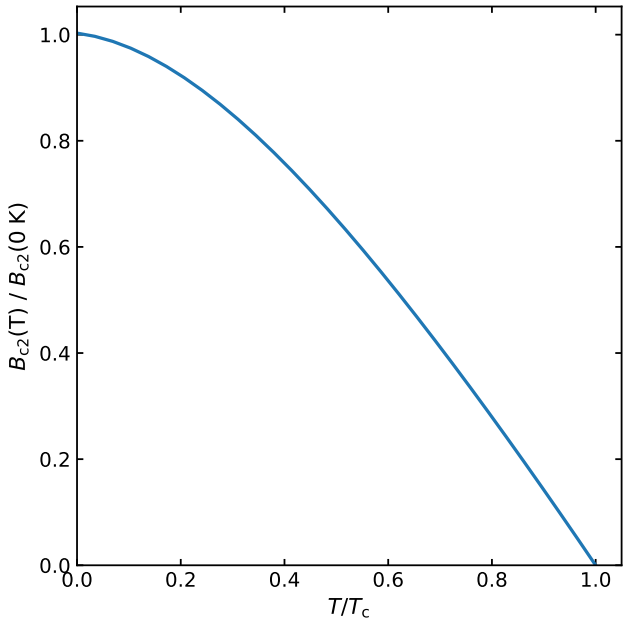

Figure 2.11: The upper critical field $B_{c2}(T)$ (nomalized to $B_{c2}(0\,\mathrm{K})$) as a function of reduced temperature T/T_c. The solid curve depict the temperature dependence of B_{c2} based on Equation (2.49).

2.5.3 Superheating field B_{sh}

Recall that although the lower critical field B_{c1} represents the field at which it becomes energetically favorable for flux to enter the bulk of a type-II superconductor,

the Meissner state can be sustained exceeding B_{c1}—a metastable non-equilibrium state that decays toward thermal equilibrium at a finite kinetic rate. This delay is due to the presence of an energy *barrier* associated with the nucleation of vortices at the superconductor's surface. This phenomenon, initially explored by Bean-Livingston (BL) [24] in 1965 with London theory for type-II superconductors, is termed the BL barrier. As a result of this barrier, a superconductor can maintain its perfect diamagnetism in magnetic field exceeding B_{c1} until this barrier is surpassed. Consequently, the state remains metastable up to a field value above B_{c1}, known as the superheating field B_{sh}, beyond which the barrier vanishes, and vortices can spontaneously penetrate the material, causing a "quench" via the sudden penetration of vortices. The superheating field (B_{sh}) therefore defines the theoretical magnetic field limit for sustaining a metastable Meissner state in type-II superconductors.

The physical mechanism underlying this barrier originates from the interaction between vortices at a superconductor's surface. On a perfectly smooth superconductor containing an isolated vortex parallel to its surface and located at a distance x from the surface, two competing forces arise. An attractive force is produced by a surface screening current, which opposes the external magnetic field and can be equivalently represented by an "image vortex" located outside the surface.[8] Simultaneously, a repulsive force acts on the vortex due to the applied magnetic field itself, aligned with the vortex's magnetic field. The competition between these forces determines whether a vortex can escape the surface and penetrate into the supercondcutor. The total energy $E(x)$ of an isolated flux thread near the surface can be quantitatively expressed by [24]:

$$E(x) = \epsilon - \left(\frac{\Phi_0}{4\pi\lambda_L}\right)^2 K_0(2x/\lambda_L) + \frac{\Phi_0}{4\pi} B_0 \exp\left(-x/\lambda_L\right), \tag{2.51}$$

[8]The method of images involves removing material boundaries and extending the system to all space, then introducing one or more fictitious image vortices to satisfy boundary conditions. These images exert forces on real vortices, influencing their dynamics near interfaces.

where ϵ represents the energy per unit length of an individual flux thread, observed far from the surface, and is approximately equivalent to:

$$\epsilon = \left(\frac{\Phi_0}{4\pi\lambda_\mathrm{L}}\right)^2 \ln\left(\lambda_\mathrm{L}/\xi_\mathrm{GL}\right), \tag{2.52}$$

and K_0 is the modified Bessel function of the second kind. Using the definition of B_{c1} from Equation (2.43), Equation (2.52) becomes:

$$\epsilon = \frac{\Phi_0}{4\pi} B_{\mathrm{c1}}. \tag{2.53}$$

The second term in Equation (2.51) represents the attractive force exerted on the surface by the flux thread (i.e., between the vortex and its image), whereas the final term accounts for the repulsive force acting on the vortex due to the external field B_0, decaying exponentially with increasing distance from the surface.

Figure 2.12 shows the energy barrier for vortex entry near the surface of a type-II superconductor for increasing applied fields. At $B_0 = 0$, the vortex is attracted to the surface but cannot enter. For $B_0 < B_{\mathrm{c1}}$, vortices are energetically unfavorable inside the superconductor. In the regime $B_0 < B_{\mathrm{c1}} < B_{\mathrm{sh}}$, the vortex entry becomes energetically favorable, but a surface barrier still inhibits penetration. The barrier height decreases with increasing B_0 and vanishes when $B_0 = B_{\mathrm{sh}}$, allowing unhindered vortex penetration.[9] Note that thermal fluctuations capable of activating vortices over the surface barrier in conventional superconductors are negligible for two main reasons. First, the condensation energy within a coherence volume $F\xi_{\mathrm{GL}}^3$ greatly exceeds the thermal energy $k_\mathrm{B}T$ [86]. Here, F is the condensation energy density, ξ_{GL} is the GL coherence length, k_B is the Boltzmann constant, and T is the temperature. Because each Cooper pair overlaps

[9]For superconducting radio frequency (SRF) cavities, the persistence of the metastable Meissner state under strong radio frequency (RF) fields depends on the vortex core formation time τ_v relative to the RF period (i.e., inverse of RF frequency ν) [84, 85]. The core forms within $\tau_\mathrm{v} \sim \xi_{\mathrm{GL}}/v_\mathrm{d} \simeq (v_\mathrm{F}/\pi v_\mathrm{d})\,\hbar/\Delta$, where v_d and v_F are the vortex terminal velocity and the Fermi velocity, respectively. For Nb, $\tau_\mathrm{v} \sim 2\times10^{-12}\,\mathrm{s} - 4\times10^{-12}\,\mathrm{s}$, giving $\nu\tau_\mathrm{v} \sim 10^{-2} - 10^{-3}$ at GHz frequencies [85]. Thus, once B_0 exceeds B_{sh}, vortex penetration occurs almost instantaneously.

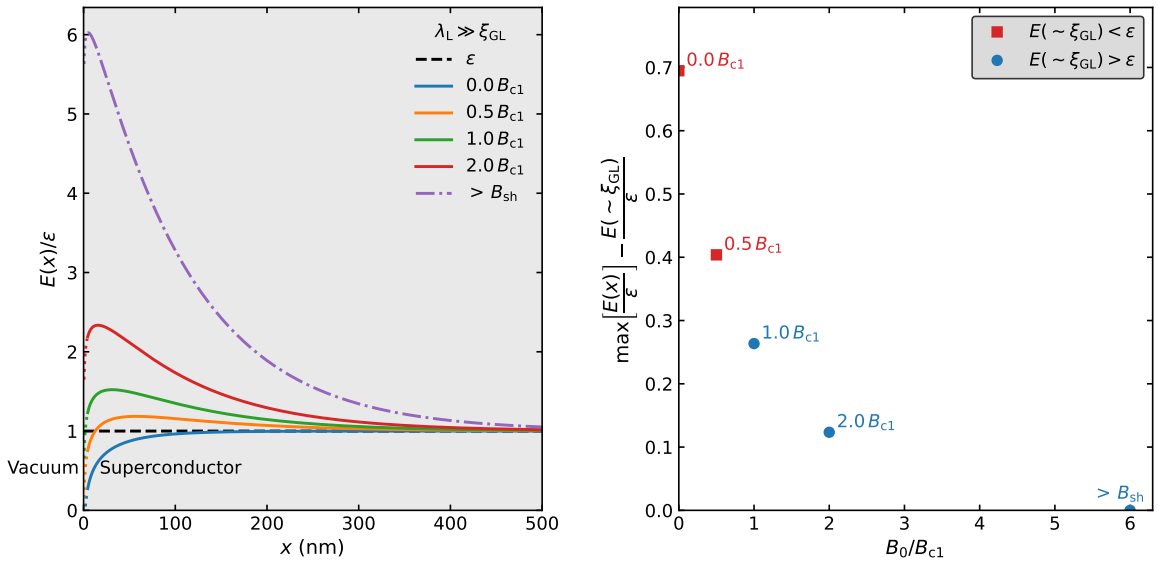

(a) (b)

Figure 2.12: (a) Energy profile of a magnetic flux line near the vacuum-superconductor interface as a function of distance x from the surface, based on Equation (2.51), illustrating the BL barrier for $\lambda_L \gg \xi_{GL}$ under various applied fields B_0. The blue curve shows $B_0 = 0$ ($B_0 < B_{c1}$) where the vortex is fully repelled. The solid orange, green, and red curves are representative of when $B_{c1} < B_0 < B_{sh}$, where vortex penetration is energetically favorable but still blocked by the surface barrier. The dotted-dashed curve corresponds to $B_0 > B_{sh}$, where the barrier disappears, allowing unhindered vortex entry. (b) Maximum barrier height, expressed as $\max\left[\frac{E(x)}{\epsilon}\right] - \frac{E(\sim\xi_{GL})}{\epsilon}$, plotted against normalized field B_0/B_{c1}, showing the barrier decreases with increasing B_0 and vanishes above B_{sh}. For $B_0 < B_{c1}$, the energy is $E(\sim\xi_{GL}) < \epsilon$, indicating vortex repulsion (filled squares), while for $B_0 > B_{c1}$, vortices are energetically favorable but still face the barrier (filled circles) until B_{sh} is reached.

with roughly 10^6 neighbors, the system behaves as a mean-field model (i.e., each pair experiences only the average occupancy of other pairs), thereby strongly suppressing thermal fluctuations of the order parameter [87]. Second, the energy barrier for vortex nucleation is itself immense when compared to the available thermal energy k_BT. The energy per unit length of a vortex line integrated over a coherence length ξ_{GL}, is $E_v = \epsilon\xi_{GL}$, (ϵ is given by Equation (2.52)) which gives a ratio with thermal energy of $E_v/k_BT \approx 1.4(T_c/T)(E_F/\Delta)^2$, where E_F is the Fermi energy and Δ is the superconducting gap [86]. Since $\Delta \ll E_F$, the vortex-nucleation barrier is enormously larger than k_BT, rendering thermally activated

flux penetration effectively impossible [86]. Consequently, the Meissner state remains kinetically stable up to the B_{sh}.

Building on these considerations of vortex penetration and the stability of the Meissner state, the validity of Equation (2.51) is confined to the regime where $\lambda_{\mathrm{L}} \gg \xi_{\mathrm{GL}}$ and $x \gg \xi_{\mathrm{GL}}$. Near the surface, when $x \approx \xi_{\mathrm{GL}}$, the model predicts an unphysical divergence due to the behaviour of the Bessel function K_0. To ensure physical accuracy, the force must vanish smoothly at the surface, requiring a modification of the expression in this limit. Additionally, Equation (2.51) faces two key limitations [88]: (i) for $\lambda_{\mathrm{L}} \approx \xi_{\mathrm{GL}}$, B_{sh} becomes sensitive to ξ_{GL}, reducing the model's reliability; and (ii) it neglects the suppression of Cooper pair density near the surface, an aspect not considered in the BL framework, thus limiting its applicability to regions $x \gg \xi_{\mathrm{GL}}$. These considerations do not undermine the utility of the BL framework, but highlight the contexts in which caution is required.

The value of the B_{sh} relies on T-dependent material characteristics, such as λ_{L} and ξ_{GL}. A numerical solution of the GL equations based on linear stability analysis provides a rigorous evaluation of the B_{sh} within GL theory for both $\kappa < \kappa_{\mathrm{c}}$ and $\kappa > \kappa_{\mathrm{c}}$, where the (critical) value is $\kappa_{\mathrm{c}} = 1.1495$ [89]. This approach yields numerical results with an accuracy within $\sim$1 % of the full GL solutions. The resulting expressions for B_{sh} take the form:

$$B_{\mathrm{sh}} \approx B_{\mathrm{c}} \begin{cases} 2^{-1/4}\kappa^{-1/2}\dfrac{1 + 4.6825120\kappa + 3.3478315\kappa^2}{1 + 4.0195994\kappa + 1.0005712\kappa^2}, & \text{for } \kappa < \kappa_{\mathrm{c}}, \\ \dfrac{\sqrt{20}}{6} + \dfrac{0.54476}{\sqrt{\kappa}}, & \text{for } \kappa > \kappa_{\mathrm{c}}. \end{cases} \tag{2.54}$$

It is important to note that the GL theory is strictly valid at $T \simeq T_{\mathrm{c}}$, whereas superconducting cavities typically operate at much lower temperatures $T \ll T_{\mathrm{c}}$, where the GL formalism breaks down. Accurate determination of the B_{sh} at low-temperature (i.e., $T \ll T_{\mathrm{c}}$) regime requires solving the full BCS or Eilenberger

equations [90, 91], which are valid at all T, must be treated numerically or via approximation due to a lack of analytical solutions. This microscopic approach enables reliable calculation of B_{sh} at $T \ll T_{\mathrm{c}}$. In particular, for a clean superconductor in the limit $\kappa \to \infty$ as $T \to 0$, the expression for the B_{sh} is given by [92, 93]:

$$B_{\mathrm{sh}} \simeq 0.84 B_{\mathrm{c}}. \tag{2.55}$$

This result is particularly relevant for emerging SRF materials such as Nb_3Sn and $Nb_{1-x}Ti_xN$ [94], which possess significantly larger κ values than pure Nb and are being investigated for their potential to withstand higher fields. The (emperical) quadratic temperature dependence of the thermodynamic critical field (i.e., Equation (2.40)) provides a good approximation for B_{sh} [95].

2.6 Radiofrequency supercoductivity

Thus far, our discussion of superconductivity has focused exclusively on the phenomenon's behaviour under DC fields; however, the SRF cavities that motivate this work exclusively under RF fields. While the concepts introduced so far are suitable for this regime, several aspects specific to cavity operation in the GHz range are discussed below. The characteristic response time of conduction electrons and the superconducting condensate is orders of magnitude shorter than the period of the applied RF field, ensuring that both metallic and superconducting responses effectively follow the RF oscillations in real time [86].

As noted in Chapter 1, SRF cavities are key components in modern particle accelerators, designed to accelerate charged particle beams by converting RF power into electromagnetic (EM) fields. When driven near their resonant frequency, the cavity supports standing electromagnetic waves, with the electric field oriented along the beam axis to accelerate particles. The accompanying magnetic field oscillates perpendicular to the electric field and runs parallel to the cavity surface,

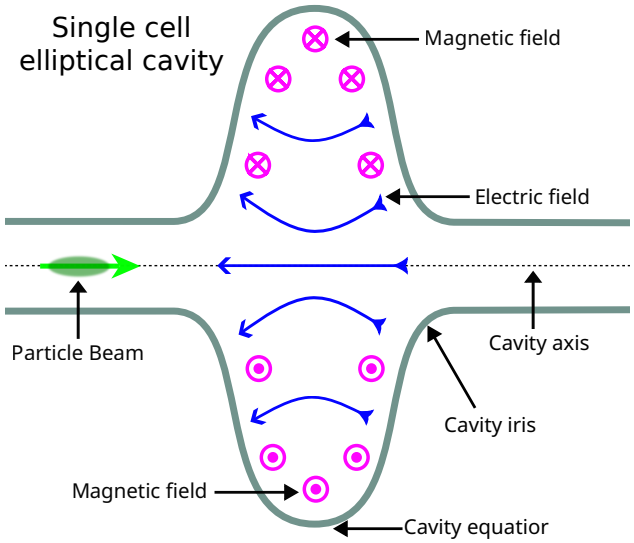

Figure 2.13: Schematic of a single-cell elliptical SRF cavity, illustrating the fundamental mode's electromagnetic field distribution. The oscillating electric field (blue lines) peaks near the iris and drives particle acceleration, while the magnetic field (magenta loops) reaches its maximum near the cavity equator. The particle beam is represented by green bunches traveling along the cavity axis. The surface magnetic field at the equator is a key factor limiting the cavity's accelerating gradient.

as required by Maxwell's equations. The typical distributions of the electric and magnetic fields in a single-cell $\beta = 1$ cavity are illustrated in Figure 2.13, where $\beta = v/c$ with v being the particle velocity and c the speed of light. In such cavities, the electric field peaks near the iris, while the magnetic field reaches its maximum near the cavity equator. The accelerating performance of an SRF cavity is limited by the maximum surface fields that can be sustained without causing a breakdown of superconductivity. When the surface magnetic field surpasses the material's critical threshold, the cavity undergoes a quench, transitioning to the normal conducting state and dissipating the stored energy.

In addition to magnetic breakdown, the efficiency of SRF cavities is also fundamentally limited by surface resistance, which governs the quality factor (Q_0) of the "resonator." Although superconductors exhibit zero direct current (DC) resistance, SRF cavities remain dissipative under RF fields, because normal electrons, which are always thermally excited, are driven by the alternating EM fields even

at cryogenic temperatures, resulting in a finite surface resistance [1, 96]. The performance of an SRF cavity is primarily characterized by two key figures of merit: Q_0 and the accelerating gradient (E_{acc}), which are discussed below.

Q_0 is the ratio of the stored energy to the energy dissipated in the cavity in a radian of the RF cycle [1, 10]:

$$Q_0 = \frac{\omega U}{P_{\mathrm{d}}}, \tag{2.56}$$

where ω is the angular frequency of the accelerating mode and P_{d} is the dissipated power in the cavity walls. Expressing U and P_{d} in terms of magnetic fields, Equation (2.56) can be as [1, 10]:

$$Q_0 = \frac{\omega \mu_0 \int_V |\mathbf{H}|^2 \mathrm{d}V}{R_{\mathrm{s}} \oint_A |\mathbf{H}|^2 \mathrm{d}A}, \tag{2.57}$$

where μ_0 is the vacuum magnetic permeability, $\mathbf{H}$ is the magnetic field, V is the cavity volume, A is the surface area, and R_{s} is the surface resistance. R_{s} is typically decomposed into two contributions:

$$R_{\mathrm{s}} = R_{\mathrm{BCS}}(T) + R_{\mathrm{res}}, \tag{2.58}$$

where $R_{\mathrm{BCS}}(T)$ is the T-dependent component described by BCS theory [96]:

$$R_{\mathrm{BCS}}(T) = \frac{A_0 \omega^2}{T} \exp\left(-\frac{\Delta}{k_{\mathrm{B}} T}\right), \tag{2.59}$$

where A_0 is a material-dependent factor related to purity and electron mean free path, Δ is the superconducting energy gap, and k_{B} is the Boltzmann constant. R_{BCS} arises from the RF excitation of thermally activated quasiparticles and decreases exponentially with decreasing temperature, making high-T_{c} materials particularly attractive for RF applications. The second term, R_{res}, known as the residual resistance, is largely T-independent and not yet fully understood. It is commonly attributed to extrinsic sources such as surface roughness, impurities, defects, or

trapped magnetic flux during cooldown [1, 2, 96, 97]. Equation (2.57) may also be expressed as:

$$Q_0 = \frac{G}{R_s}, \tag{2.60}$$

where G is the geometry factor and is defined as:

$$G = \frac{\omega\mu_0 \int_V |\mathbf{H}|^2 \mathrm{d}V}{\oint_A |\mathbf{H}|^2 \mathrm{d}A}, \tag{2.61}$$

which is determined only by the shape of the cavity.

E_{acc} quantifies the energy gain per unit length experienced by a charged particle traversing an SRF cavity. It is defined as [10]:

$$E_{\mathrm{acc}} = \frac{V_c}{L}, \tag{2.62}$$

where V_c is the accelerating voltage, obtained by integrating the electric field along the particle's trajectory through the cavity, and L is the effective cavity length. For example, a TESLA-type cavity consists of 9 cells, giving $L = 9\lambda/2$ for $\beta = 1$. Here, λ denotes the RF wavelength corresponding to the cavity's resonance frequency.

In practice, Q_0 is often observed to be a function of E_{acc}, as shown in Figure 2.14. While achieving both high Q_0 and high E_{acc} is essential for the optimal performance of SRF cavities—minimizing RF power dissipation and enabling compact accelerator designs—this thesis focuses exclusively on increasing the E_{acc}. A higher E_{acc} reduces the length required to achieve a target beam energy, thereby decreasing the overall size and cost of the accelerator system.

A fundamental challenge in pushing E_{acc} to higher values lies in avoiding quenches, wherein a loss of superconductivity due to excessive surface magnetic field transpires (see Figure 2.14). The maximum achievable E_{acc} is ultimately limited by the magnetic field that the cavity can sustain in the Meissner state (i.e., B_{sh}) [1]. Thus, the central objective of this thesis is to investigate and extend this

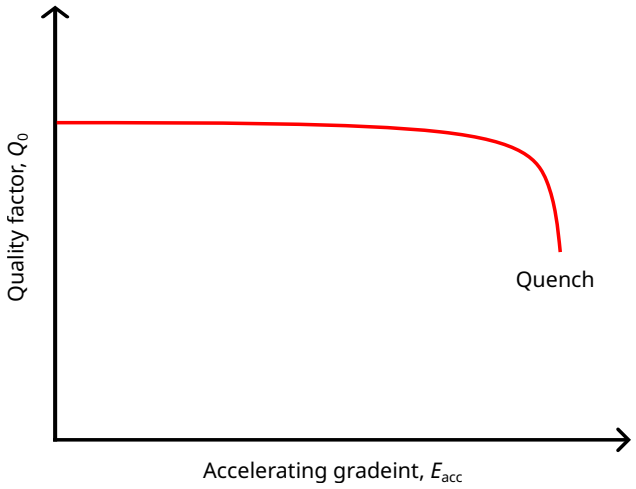

Figure 2.14: Sketch of an SRF cavity's quality factor Q_0 as a function of its accelerating gradient E_{acc}. In the ideal case, Q_0 remains relatively constant up to a certain gradient, beyond which it drops sharply due to a quench, where the superconducting cavity material transitions from the superconducting to the normal conducting state. Achieving high Q_0 at elevated E_{acc} is essential for efficient SRF cavity operation, enabling reduced cryogenic load and compact accelerator design. The quench point defines the maximum sustainable field before energy dissipation becomes prohibitive.

limit by exploring the underlying mechanisms that constrain surface field stability, with the goal of enabling SRF cavities to operate at higher accelerating gradients.

Chapter 3

Materials for SRF cavities

A superconducting material intended for superconducting radio frequency (SRF) cavity applications must exhibit superior electromagnetic (EM) performance along with favorable physical and chemical surface properties.[1] The foremost requirement is a large superheating field (B_{sh}), as this determines the maximum accelerating gradient (E_{acc}) achievable before magnetic flux penetration occurs, as discussed in Section 2.6. Equally important is a high critical temperature (T_{c}), which allows operation at elevated cryogenic temperatures, reduces the Bardeen-Cooper-Schrieffer (BCS) surface resistance exponentially, and consequently lowers the refrigeration power demand (see Section 2.6).

The high quality factor (Q_0) required for efficient SRF operation arises from the need to minimize the surface resistance R_{s}, which depends strongly on the superconducting energy gap Δ and the material's purity and surface quality. Recall from Section 2.6, a larger Δ suppresses thermally excited quasiparticles, lowering the BCS contribution to R_{s}, while impurities, roughness, and trapped magnetic flux increase the temperature-independent residual resistance R_{res}. Achieving a low R_{s} therefore requires materials with long electron mean free paths, minimal impurities,

[1] Typical elliptical SRF cavities, such as the 1.3 GHz nine-cell type used in electron linacs, are about 1 m long with a cell aperture of roughly 70 mm. Designed for particles moving nearly at the speed of light ($\beta = v/c \approx 1$ defines the ratio of the particle velocity v to the speed of light in vacuum c), these cavities operate in the π-mode, where adjacent cells are phase-shifted by 180° to maximize acceleration. The cell-to-cell spacing is $\beta\lambda/2$, and the overall cavity diameter is typically $\sim 0.9\lambda$, where λ is the radio frequency (RF) wavelength. Operated within a cryomodule weighing several hundred kilograms, the cavities are cooled by superfluid helium at about 2 K—the lowest practical temperature of pumped liquid ^{4}He [2, 17].

and atomically smooth, defect-free surfaces. Good thermal conductivity is also essential, as it enables efficient heat removal from localized hotspots and stabilizes the cavity against thermal runaway under high RF power [94, 97].

From a materials engineering perspective, the superconductor must be chemically and mechanically stable under repeated thermal cycling to cryogenic temperatures, resistant to oxidation and contamination, and capable of being fabricated into high-purity, uniform films or bulk structures with reproducible surface treatments. Compatibility with established cavity manufacturing processes—such as forming, welding, and polishing—is equally important for practical integration into accelerator systems [1, 94, 96].

Overall, an ideal SRF material should possess a high T_c, large B_{sh}, a wide superconducting gap Δ, low R_s, excellent thermal conductivity, and robust surface and mechanical stability [1, 96]. These combined characteristics enable high accelerating gradients, low cryogenic losses, and reliable long-term performance under intense RF fields, making them essential benchmarks for modern superconducting materials.

3.1 Current materials and their limitations

In view of the criteria discussed in the previous section, the selection of bulk Nb as the standard material for SRF cavities was a natural choice. A comparison of key superconducting parameters for Nb and other candidate SRF materials is summarized in Table 3.1.

Although the BCS surface resistance R_{BCS} decreases exponentially with increasing T_c, suggesting that materials with higher T_c could offer better SRF performance, Nb remains the most practical and reliable choice. Despite its modest critical temperature of $T_c = 9.2\,\mathrm{K}$ compared to other superconductors with higher T_c (i.e., $\geq 16\,\mathrm{K}$) such as Nb_3Sn, $Nb_{1-x}Ti_xN$, or MgB_2, it uniquely satisfies both the fundamental and technological requirements for SRF applications. Its combination

Table 3.1: Comparison of key superconducting material parameters relevant to SRF applications, including the critical temperature T_c, thermodynamic critical field B_c, lower and upper critical fields (B_{c1} and B_{c2}), superheating field B_{sh}, magnetic penetration depth λ, superconducting energy gap Δ, and BCS coherence length ξ_0. For MgB_2, two distinct superconducting gaps are listed due to its multi-band nature. Reported values are based on Refs. [94, 98–101].

Material	T_c (K)	B_c (mT)	B_{c1} (mT)	B_{c2} (mT)	B_{sh} (mT)	λ (nm)	Δ (meV)	ξ_0(nm)
Nb	9.2	200	180	280	240	29	1.5	40
Nb_3Sn	18	540	30	28000	425	~100	3.1	~5
$Nb_{1-x}Ti_xN$	17.3	500	30	15000	440	150-200	2.8	~2.5
NbN	16	230	20	15000	214	200-350	2.6	~3
MgB_2	40	430	30	3500-60000	170	185	2.3 /7.2	5

the highest lower critical field (B_{c1}) of all superconductors with a large B_{sh}, low surface resistance, and excellent thermal conductivity ensures efficient operation with minimal RF losses [96].

While Nb's favorable superconducting properties have established it as the standard material for SRF cavities, its performance remains constrained by both fundamental and practical limits [18, 20]. The primary objective of this thesis is to increase the achievable E_{acc}, which is ultimately constrained by the theoretical magnetic field limit that a superconductor can sustain in the Meissner state, defined by the B_{sh}, as discussed in Section 2.6. Although low-temperature baking (LTB) treatments have significantly enhanced the performance of Nb-based SRF cavities, the achieved fields still fall short of Nb's theoretical limit [11–14] (i.e., an E_{acc} of approximately 50 MV m^{-1}) corresponding to an applied magnetic field (B_0) of about 200 mT in TESLA-shaped cavities (as defined in Chapter 1). Further improvements with bulk Nb are intrinsically limited by the onset of vortex penetration and quenching, as the surface current density approaches the depairing current density (J_d), which is $\propto B_{sh}$, as discussed in Chapter 1. The LTB process modifies the near-surface region of Nb by diffusing native oxygen—the oxygen from the metal's natural surface oxide layer—into the metal, forming a "dirty" layer that suppresses hydride precipitation and alters the vacancy structure [11]. This effect

reduces the concentration of free hydrogen accumulated during prior chemical treatments, thereby mitigating the formation of nanoscale niobium hydrides—the primary cause of superconducting quench around 100 mT—and improving both Meissner-state stability and overall cavity performance [10, 102]. Ultimately, the remaining discrepancy between experimental and theoretical field limits arises from the onset of vortex penetration and associated dissipation mechanisms, which become significant well below B_{sh} in practical systems.

3.2 Materials other than Nb

To overcome the intrinsic performance limits of bulk Nb, one promising direction involves adopting alternative superconducting materials with higher superheating fields B_{sh}. Compounds such as Nb_3Sn, $Nb_{1-x}Ti_xN$, NbN, and MgB_2 are prime candidates to surpass the established bulk Nb technology (see Table 3.1). However, their B_{c1} values are lower than that of Nb, rendering the Meissner state more vulnerable to vortex penetration. These materials also exhibit greater sensitivity to surface defects due to their relatively short BCS coherence lengths ($\lesssim$5 nm), which are approximately an order of magnitude smaller than that of Nb. The level of research maturity (e.g., characterization of each material's intrinsic properties, challenges of integrating them into cavity structures, etc.) across these alternative materials varies significantly, in part because their application in SRF cavities requires the development of advanced thin-film deposition techniques on suitable substrates. Currently, none of these materials surpass Nb in terms of RF performance (i.e., $E_{\mathrm{acc}} \gtrsim 50\,\mathrm{MV\,m^{-1}}$ while maintaining $Q_0 \sim 10^{10}$) in accelerator environments. Among them, bulk Nb_3Sn (i.e., when the material's thickness is far greater than its magnetic penetration depth) is the most advanced and is closest to becoming a viable alternative for SRF cavities; its recent progress is summarized below.

Nb_3Sn cavity performance has advanced significantly over the past decades. Us-

ing the maximum E_{acc} at $Q_0 > 10^{10}$ and 4.4 K, as a benchmark, the E_{acc} of a Nb_3Sn cavity has improved from approximately 5 MV m^{-1} in the 1990s [103] to around 24 MV m^{-1} by 2021 [104], enabled by sustained progress in material development, cavity preparation, and coating techniques [105–112]. Despite continued development through 2024 [113–118], this value remains below 24 MV m^{-1}, falling short of the ~50 MV m^{-1} achieved by the best bulk Nb cavities [14–16]. Experimental investigations indicate that this performance ceiling in Nb_3Sn cavities is primarily caused by surface defects, such as grain boundaries, roughness, or inhomogeneities, which can locally suppress the surface barrier and enable premature magnetic flux entry [119, 120].

Although the Bean-Livingston (BL) surface barrier can delay vortex penetration, it is highly sensitive to imperfections. At typical cavity operating temperatures ($T \lesssim 4$ K), even minimal vortex entry can trigger thermomagnetic flux avalanches, leading to sudden and irreversible quenching [18, 22, 23]. Thus, while these alternative materials like Nb_3Sn are promising, their implementation is fundamentally constrained by vortex instability under realistic SRF operating conditions.

3.3 Multilayer structure for SRF cavities

To mitigate the limitations, in particular premature flux penetration of both bulk Nb and its higher-B_{sh} alternatives, a compelling solution was first proposed by Gurevich [20]. The concepts involves coating Nb with a superconducting material that has a penetration depth $\lambda > \lambda_{\mathrm{Nb}}$ and $B_{\mathrm{sh}} > B_{\mathrm{sh}}^{\mathrm{Nb}}$, such as Nb_3Sn or $Nb_{1-x}Ti_xN$, so as to enhance the vortex penetration field [20]. This approach involves constructing a cavity with several thin superconducting and insulating layers, with the simplest configuration being a single superconducting layer and an insulating layer on superconducting Nb substrate, known as a superconductor-insulator-superconductor (SIS) structure (see Figure 3.1).

The key principle behind this approach lies in the absence of thermodynamically

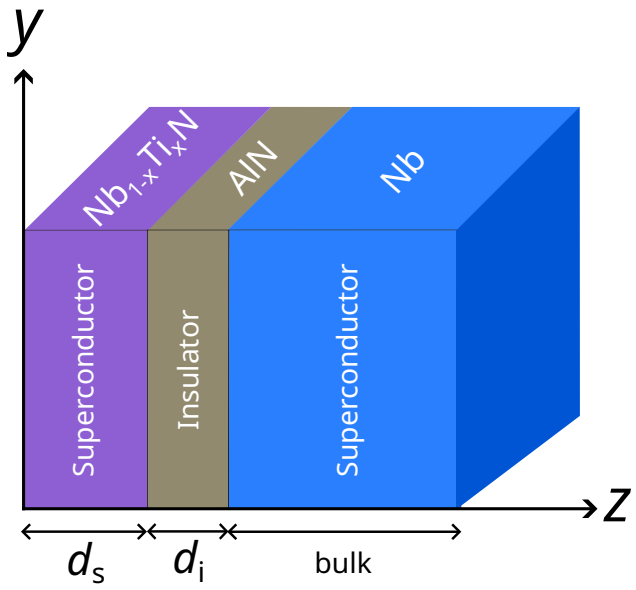

Figure 3.1: Schematic of the SIS heterostructure, illustrating a surface layer of thickness d_s and an insulating layer of thickness d_i deposited on a bulk superconductor. For SRF applications, a common example of such a structure consists of a thin $Nb_{1-x}Ti_xN$ surface layer deposited on a thin AlN insulating layer atop a bulk Nb substrate.

stable parallel vortices within a decoupled superconducting surface (s) layer when its thickness d_s becomes greater than the layer's screening length λ_s (i.e., $d_s < \lambda_s$). The inclusion of an intermediate insulating layer prevents the formation of the vortex and if the layer is thick enough it suppresses Josephson coupling between the surface layer and the underlying superconducting substrate, thereby effectively decoupling the screening currents. This configuration ensures that the magnetic field $B(z)$ at the interface with the bulk Nb substrate remains below its B_{c1} of $\simeq 170\,\mathrm{mT}$ [7, 8]. Under these conditions, the effective B_{c1} for vortex penetration in a thin surface-layer is substantially enhanced and approximated by [121, 122]:[2]

$$B_{c1} = \frac{2\Phi_0}{\pi d_s^2}\left[\ln\left(\frac{d_s}{\xi_{GL}} - 0.007\right)\right], \quad d_s < \lambda_s, \tag{3.1}$$

where Φ_0 is the flux quantum and ξ_{GL} is the Ginzburg-Landau (GL) coherence

[2]This expression assumes vortex penetration from both sides of the film and is therefore not strictly applicable to the single-sided geometry relevant for SRF cavities. It remains useful, however, as a qualitative indication that the effective B_{c1} increases with decreasing film thickness.

length. For a stack of n superconducting films with total thickness $nd_s \gg \lambda_s$, the maximum screenable field is limited by the B_{sh} of the surface-layers. As described by Equation (2.55) for a type-II superconductor (i.e., $k \gg 1$), the $B_{sh} \propto B_c$, where B_c is the thermodynamic critical field. Since B_c of the potential surface-material nearly twice that of Nb (see Table 3.1), the achievable B_{sh} in an SIS multilayer can significantly exceed Nb's intrinsic value. Note that, a direct application of Equation (2.55) to multilayer coatings is invalid, as field amplitudes differ across each superconducting layer due to screening. Instead, the vortex penetration field must be derived by evaluating the net force on a vortex within this layered structure [18].

Furthermore, in such an SIS heterostructure the current distribution within each layer is influenced not only by the intrinsic properties of the individual materials, but also by the electromagnetic interaction with adjacent layers, the latter being governed by boundary and continuity conditions at the interfaces [18, 19, 22]. In particular, the Meissner screening current density (J) in the surface-layer is reduced when its magnetic penetration depth λ_s is greater than in the substrate (sub) layer (i.e, $\lambda_s > \lambda_{sub}$). This suppression arises because J is proportional to the spatial derivative of the magnetic field, and a larger penetration depth leads to weaker field attenuation in the surface layer. Consequently, the theoretical field limit can be enhanced, as it depends directly on the magnitude of J. This relationship can be understood quantitatively through the connection between the thermodynamic critical field B_c and J_d, expressed as [123]:[3]

$$J_d = B_c/\mu_0\lambda. \tag{3.2}$$

Since $B_{sh} \propto B_c$, based on the relation in Equation (2.55), suppressing the Meissner current through appropriate material design leads to an effective enhancement of

[3]This form applies in the limit of zero temperature and represents the condition at which superconductivity breaks down, either due to an applied magnetic field exceeding B_c or a current exceeding J_c.

the vortex penetration field. This provides a significant advantage over traditional homogeneous superconducting cavities when it comes to extending the theoretical field limit. The presence of an insulating layer plays a critical role in decoupling adjacent superconducting layers. Moreover, the insulating layer serves a dual purpose: it not only inhibits vortex entry but also suppresses vortex-related dissipation by eliminating the dissipative vortex core within the insulating region [18, 21].

However, a simplified variant of the SIS structure omits the insulating interlayer, yielding the superconductor-superconductor (SS) bilayer configuration. Such a model was proposed by Kubo [18, 19] as a model for LTB Nb, as illustrated in Figure 3.2. Like SIS structures, SS bilayers with a surface layer of larger penetration depth than the substrate (i.e., $\lambda_s > \lambda_{sub}$) suppress vortex entry via two mechanisms [18, 21, 22]: enhanced surface vortex penetration field due to reduced Meissner current, and an interface energy barrier analogous to the BL barrier [24]. This barrier, arising from interactions with "image" vortices,[4] repels real vortices toward the high-penetration depth (λ) layer, stabilizing the Meissner state up to the substrate's B_{sh} [18]. Unlike SIS structures, SS bilayers suppress flux nucleation in the substrate solely through superconducting interface effects.

To understand vortex penetration in SS structures, it is essential to examine the fundamental mechanism by which vortices enter a superconductor. As discussed in Section 2.5.3, vortex entry is governed by the balance of forces acting on a vortex near the surface. Consider an extreme type-II superconductor with penetration depth λ and GL coherence length ξ, and a vortex carrying a flux quantum $\Phi_0 = 2.07 \times 10^{-15}$ Wb located at $(y, z) = (0, \xi)$ in Figure 3.2b. The vortex experiences a Lorentz force from the Meissner current induced by an external applied magnetic

[4]The method of images involves removing material boundaries and extending the system to all space, then introducing one or more fictitious image vortices to satisfy boundary conditions. These images exert forces on real vortices, influencing their dynamics near interfaces.

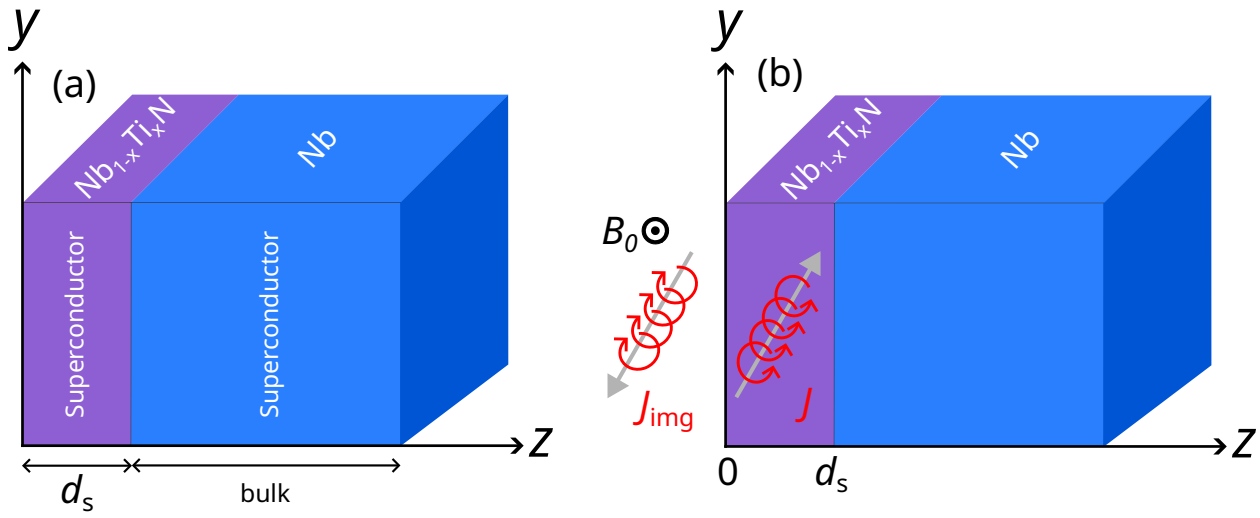

Figure 3.2: Schematic illustration of SS heterostructure used for SRF applications. A typical configuration consists of a thin $Nb_{1-x}Ti_xN$ surface layer of thickness d_s deposited on a bulk Nb substrate. (a) Cross-sectional view of the SS structure. (b) Configuration under an applied field B_0 parallel to x-axis, a vortex in the surface layer and its image antivortex, carrying screening currents J and J_{img} parallel to y-axis.

field B_0, given by [18]:

$$\mathbf{F}_M(\xi) = \mathbf{J}(\xi) \times \Phi_0 \hat{\mathbf{x}} = \Phi_0 J(0) \hat{\mathbf{z}}, \tag{3.3}$$

where $\mathbf{J}(\xi = 0) = J(0)\hat{\mathbf{y}}$ is the surface screening current density. Simultaneously, a repulsive force arises from an image antivortex[5] located at $(0, -\xi)$, constructed using the method of images to satisfy boundary conditions at the superconductor surface [18]:[6]

$$\mathbf{F}_B(\xi) = \mathbf{J}_{img}(\xi) \times \Phi_0 \hat{\mathbf{x}} \tag{3.4}$$

$$= -\frac{\Phi_0^2}{4\pi\mu_0\lambda^2\xi}\hat{\mathbf{z}}, \tag{3.5}$$

where $\mathbf{J}_{img}(\xi) = J_{img}(\xi)\hat{\mathbf{y}} = -\left(\Phi_0/(2\pi\mu_0\lambda^2 \cdot 2\xi)\right)\hat{\mathbf{y}}$ is the current circulating the image antivortex for $z < \lambda$ [18]. Writing out the "balancing" requirement for

[5]Required to ensure that the normal component of the current density at the vacuum-superconductor boundary is 0.
[6]When considering vortex at the surface (i.e., $x = \xi_0$) and $\xi_0 \ll d_s$.

Equations (3.3) and (3.5) yields:

$$\mathbf{F}_{\mathrm{M}}(\xi) + \mathbf{F}_{\mathrm{B}}(\xi) = 0, \tag{3.6}$$

$$J(0)\hat{\mathbf{z}} = \frac{\Phi_0^2}{4\pi\mu_0\lambda^2\xi}\hat{\mathbf{z}}, \tag{3.7}$$

which is the maximum screening current density at $z = \xi$ under which $|\mathbf{F}_{\mathrm{M}}(\xi)| > |\mathbf{F}_{\mathrm{B}}(\xi)|$. By solving the relation between applied field B_0 and screening current density J differential equation in the London model, following the boundary[7] and continuity conditions[8] in an SS heterostructure, the field distribution $B(z)$ yields [18]:

$$B(z) = B_0 \times \begin{cases} \dfrac{\cosh\left(\dfrac{d_{\mathrm{s}} - z}{\lambda_{\mathrm{s}}}\right) + \left(\dfrac{\lambda_{\mathrm{sub}}}{\lambda_{\mathrm{s}}}\right)\sinh\left(\dfrac{d_{\mathrm{s}} - z}{\lambda_{\mathrm{s}}}\right)}{\cosh\left(\dfrac{d_{\mathrm{s}}}{\lambda_{\mathrm{s}}}\right) + \left(\dfrac{\lambda_{\mathrm{sub}}}{\lambda_{\mathrm{s}}}\right)\sinh\left(\dfrac{d_{\mathrm{s}}}{\lambda_{\mathrm{s}}}\right)}, & 0 \le z < d_{\mathrm{s}}, \\ \dfrac{\exp\left(-\dfrac{z - d_{\mathrm{s}}}{\lambda_{\mathrm{sub}}}\right)}{\cosh\left(\dfrac{d_{\mathrm{s}}}{\lambda_{\mathrm{s}}}\right) + \left(\dfrac{\lambda_{\mathrm{sub}}}{\lambda_{\mathrm{s}}}\right)\sinh\left(\dfrac{d_{\mathrm{s}}}{\lambda_{\mathrm{s}}}\right)}, & d_{\mathrm{s}} \le z \le \infty, \end{cases} \tag{3.8}$$

where z is the depth below the surface, d_{s} is the thickness of the surface layer, λ_{s} and λ_{sub} are the penetration depths of the surface and substrate layers, respectively. Using the definition of current density:

$$J(z) = -\frac{1}{\mu_0}\frac{\mathrm{d}B(z)}{\mathrm{d}z}, \tag{3.9}$$

[7]This is, zero current normal to the boundaries at $z = 0$ and $z = d_{\mathrm{s}}$ in an SS structure.
[8]That is, both $J(z)$ and its derivative must vary continuously across $z = d_{\mathrm{S}}$.

Equation (3.8) implies a spatially-dependent $J(z)$ of:

$$J(z) = \frac{B_0}{\mu_0} \times \begin{cases} \left(\frac{1}{\lambda_s}\right) \dfrac{\cosh\left(\frac{d_s - z}{\lambda_s}\right) + \left(\frac{\lambda_{sub}}{\lambda_s}\right) \sinh\left(\frac{d_s - z}{\lambda_s}\right)}{\cosh\left(\frac{d_s}{\lambda_s}\right) + \left(\frac{\lambda_{sub}}{\lambda_s}\right) \sinh\left(\frac{d_s}{\lambda_s}\right)}, & 0 \leq z < d_s, \\ \left(\frac{1}{\lambda_{sub}}\right) \dfrac{\exp\left(-\frac{z - d_s}{\lambda_{sub}}\right)}{\cosh\left(\frac{d_s}{\lambda_s}\right) + \left(\frac{\lambda_{sub}}{\lambda_s}\right) \sinh\left(\frac{d_s}{\lambda_s}\right)}, & d_s \leq z \leq \infty. \end{cases} \tag{3.10}$$

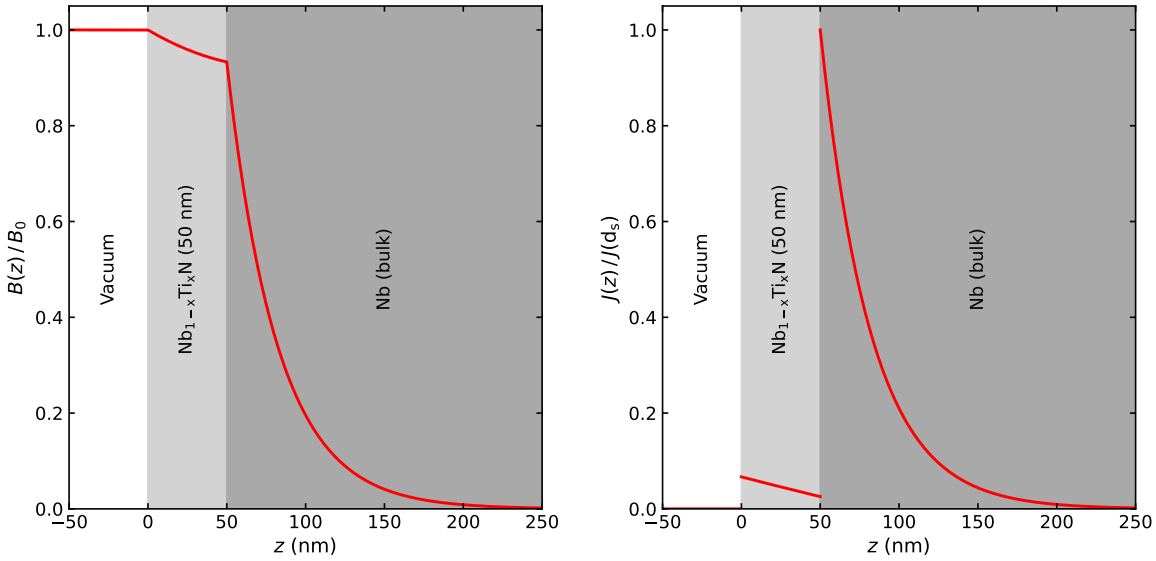

(a) Normalized magnetic field screening profile $B(z)/B_0$ as a function of a depth z below the sample surface.

(b) Normalized screening current density profile $J(z)/J(d_s)$ as a function of a depth z below the sample surface

Figure 3.3: (a) Magnetic field screening profile $B(z)$ normalized to the applied field B_0, and (b) current density screening profile $J(z)$ normalized to the current density at the SS interface $J(d_s)$. The curves are calculated using Equations (3.8) and (3.10), with parameters $d_s = 50\,\text{nm}$, $\lambda_s = 200\,\text{nm}$, and $\lambda_{sub} = 40\,\text{nm}$. The magnetic field profile exhibits continuity across the structure's interfaces and boundaries, whereas the current density profile is discontinuous.

The magnetic field $B(z)$ and current density $J(z)$ profiles for an SS structure are shown in Figure 3.3. According to Equation (3.10), the current distribution is modified across adjacent materials due to their differing λ, resulting in the

suppression of the Meissner screening current in the surface layer [18, 22]. At the vacuum-superconductor interface, $J(0)$, is given by:

$$J(0) = \gamma_1 \left(\frac{B_0}{\mu_0 \lambda_s} \right), \tag{3.11}$$

where the factor

$$\gamma_1 \equiv \frac{\sinh\left(\frac{d_s}{\lambda_s}\right) + \left(\frac{\lambda_{sub}}{\lambda_s}\right)\cosh\left(\frac{d_s}{\lambda_s}\right)}{\cosh\left(\frac{d_s}{\lambda_s}\right) + \left(\frac{\lambda_{sub}}{\lambda_s}\right)\sinh\left(\frac{d_s}{\lambda_s}\right)}, \tag{3.12}$$

encapsulates the combined effects of the superconducting film thickness d_s the penetration depths λ_s of the film, and λ_{sub} of the substrate.

As shown in Figure 3.3, the current density profile exhibits sharp maxima at the material interfaces, with $J(0)$ representing the peak within the superconducting film. These interface value is encoded in γ_1. This quantity is crucial for evaluating field limits and stability criteria in SS structures and will be further analyzed below. In the same way, the current density at the SS interface (i.e., $x \to d_s$) may be written as:

$$J(d_s) = \gamma_2 \left(\frac{B_0}{\mu_0 \lambda_{sub}} \right), \tag{3.13}$$

where the analogous constant is:

$$\gamma_2 \equiv \frac{1}{\cosh\left(\frac{d_s}{\lambda_s}\right) + \left(\frac{\lambda_{sub}}{\lambda_s}\right)\sinh\left(\frac{d_s}{\lambda_s}\right)}. \tag{3.14}$$

These current densities must remain below the respective depairing limits of the surface layer and the substrate, denoted by $B^s_{sh}/\mu_0\lambda_s$ and $B^{sub}_{sh}/\mu_0\lambda_{sub}$, where B^s_{sh} and B^{sub}_{sh} are the superheating fields of the surface and substrate layers, respectively [18]. Therefore, any improvement the substrate gains is primarily attributed to the fact that the surface layer offers some screening of B_0 over a distance d_s

according to Equation (3.8). The maximum field $B_{\max}$ under which the *entire* SS structure remains in the Meissner state necessitates optimizing d_s so as to *simultaneously* increase the B_0 for the surface and suppress the screening field at the buried SS interface. This requirement is expressed by [18]:

$$B_{\max} = \min\left\{\frac{B_{sh}^{s}}{\gamma_1}, \frac{B_{sh}^{sub}}{\gamma_2}\right\}. \tag{3.15}$$

Equation (3.15) indicates $B_{\max}$ is a function of d_s which reaches it's maximal value when the below condition satisfied:

$$\frac{B_{sh}^{s}}{\gamma_1} = \frac{B_{max}^{sub}}{\gamma_2}. \tag{3.16}$$

The corresponding thickness d_S^{opt} that achieves this condition takes the form [18]:

$$d_s^{opt} = \lambda_s \log\left[\frac{\lambda_s B_{sh}^{s}}{(\lambda_s + \lambda_{sub})\, B_{sh}^{sub}} + \sqrt{\left(\frac{\lambda_s B_{sh}^{s}}{(\lambda_s + \lambda_{sub}) B_{sh}^{sub}}\right)^2 + \left(\frac{\lambda_s - \lambda_{sub}}{\lambda_s + \lambda_{sub}}\right)}\right], \tag{3.17}$$

with the corresponding field value B_{max}^{opt} given by:

$$B_{max}^{opt} = \sqrt{\left(B_{sh}^{s}\right)^2 + \left(1 - \frac{\lambda_{sub}^2}{\lambda_s^2}\right)\left(B_{sh}^{sub}\right)^2}. \tag{3.18}$$

B_{max}^{opt} as a function of the d_s is plotted in the Figure 3.4, showing how small changes to d_s can give rise to a B_{max}^{opt} that exceeds the B_{sh} of both the surface and substrate layers. This model predicts not only an enhanced vortex penetration field, but also the emergence of an interface energy barrier in SS bilayers. The force acting on a vortex in an SS bilayer can be calculated using the method of images, extending the approach in Equation (3.5) to include an infinite series of image vortices that satisfy the boundary conditions at both interfaces. More precisely,

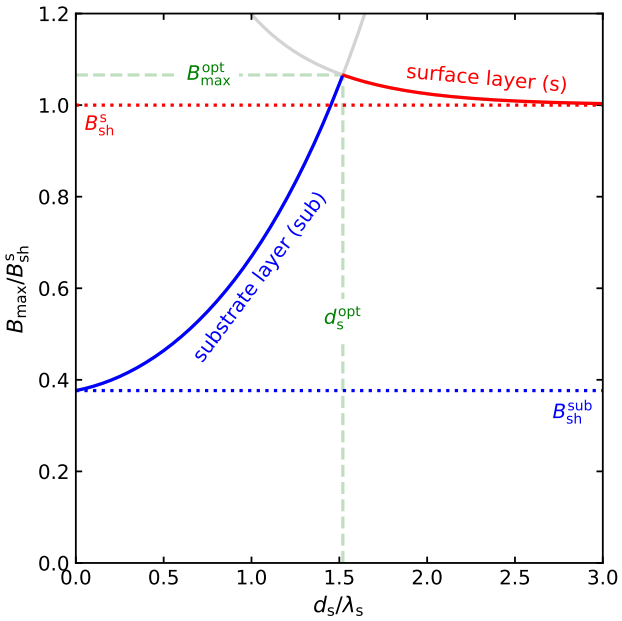

Figure 3.4: Maximum field B_{max}, normalized to the surface superheating field B^s_{sh}, plotted as a function of the normalized surface layer thickness d_s/λ_s, using Equation (3.18). Colored solid curves correspond to B_{max} in different layers, while the horizontal dotted lines indicate the superheating fields of the surface B^s_{sh} and substrate B^{sub}_{sh} layers, respectively. The optimal field B^{opt}_{max} is achieved by tuning d_s indicated by the intersection of horizontal and vertical dashed lines. Notably, this value exceeds both superheating field limits.

this can be expressed as [18]:

$$\mathbf{F}_B(z) = -\frac{\Phi_0^2}{4\pi\mu_0\lambda_s^2}\left[-\frac{1}{z} + \sum_{n=1}^{\infty}(-1)^n\left(\frac{\lambda_s^2-\lambda_{sub}^2}{\lambda_s^2+\lambda_{sub}^2}\right)^n\left(\frac{1}{nd_s-z}-\frac{1}{nd_s+z}\right)\right]\hat{\mathbf{z}}. \quad (3.19)$$

The resulting force profile is shown in Figure 3.5. The appearance of an additional barrier at the SS interface for $\lambda_s > \lambda_{sub}$ indicates a potential mechanism for inhibiting vortex entry, thereby raising the onset of vortex penetration in SS bilayers. Experimental validation of this effect is crucial to assess its impact on the performance of practical SRF cavity structures.

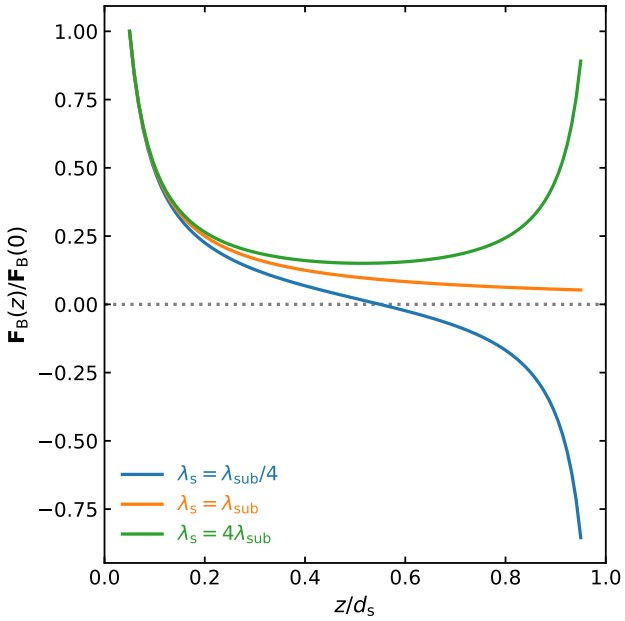

Figure 3.5: Normalized vortex interaction force $\mathbf{F}_B(z)$ as a function of vortex position z normalized to surface layer thickness d_s in a superconducting bilayer. The force is normalized to its value near $z \simeq 0$, corresponding to the conventional BL barrier (i.e., $\mathbf{F}_B(0) \simeq \mathbf{F}_{BL}$) at the vacuum-superconductor interface. A secondary barrier appears near the SS boundary at $z \simeq d_s$ when $\lambda_s > \lambda_{sub}$, providing additional resistance to vortex entry. This feature is absent in homogeneous superconductors where ($\lambda_s = \lambda_{sub}$). A short-distance cutoff of $d_s/20$ is applied to regularize the singular behavior at the interfaces, i.e., at the vacuum or substrate boundary.

3.4 Performance of multilayers

Multilayer coatings for SRF cavities remain an active area of research and development. Experimental demonstrations of such coatings (with or without insulating layers) have shown promising results over the years. The effective first penetration field of the Nb layer is enhanced in studies of single and multiple stacks of NbN(25 nm-200 nm)/MgO(15 nm) deposited on Nb($\geq$250 nm) thin films, characterized using direct current (DC) superconducting quantum interference device (SQUID) and third-harmonic alternating current (AC) susceptibility measurements [124–127]. A similar delay in magnetic field penetration beyond Nb's B_{c1} has been observed for NbN(30 nm-50 nm)/MgO(15 nm)/Nb(250 nm-600 nm)/MgO [128] and for MgB_2(100 nm-200 nm) coated on ellipsoidal Nb [129],

both using SQUID magnetometry. In the latter case, the vortex penetration field increased from approximately 210 mT for uncoated Nb to about 270 mT for Nb coated with a ~200 nm MgB_2 layer which is 28 % increase.

Thickness-dependent increases in the lower critical field of MgB_2 thin films have also been reported for MgB_2(40 nm-100 nm)/Al_2O_3 [130] and MgB_2(100 nm-300 nm) grown on SiC and MgO substrates [131], again using SQUID magnetometry. Furthermore, delayed vortex entry—up to the B_{sh} of Nb—has been observed in first-flux-penetration measurements using muon spin rotation (μSR) for MgB_2 and Nb_3Sn layers of 50 nm-2000 nm on Nb [132, 133], with the latter study [133] suggesting the presence of an SS barrier in an SS Nb_3Sn/Nb sample. However, further experimental verification is required to conclusively establish the existence of such an SS barrier.

Building upon the progress made with SS multilayer coatings, recent studies have explored the potential of SIS heterostructures to further enhance the field limits of superconducting surfaces. Hall probe measurements on flat SIS samples consisting of NbTiN(83 nm-400 nm)/AlN(10 nm)/Nb demonstrated a 25 % increase in the first magnetic penetration field [134]. Similarly, $Nb_{0.75}Ti_{0.25}N$/AlN/Nb ellipsoids investigated in Ref. [135] exhibited an enhancement in the vortex penetration field (B_{vp}) of about 15 mT, corresponding to an 8 % improvement. Although this enhancement is roughly four times smaller than that achieved for SS MgB_2(100 nm-200 nm)/Nb ellipsoids [129], the presence of the insulating layer in SIS structures offers a key advantage—robust protection against vortex penetration even in the presence of surface imperfections (see Section 3.3).

In the latter study, the magnetic response of superconducting ellipsoidal samples was measured using SQUID magnetometry to assess the effectiveness of the SIS coating. Two configurations were compared: a bare Nb ellipsoid and one coated with $Nb_{0.75}Ti_{0.25}N$(43 nm) and AlN(10 nm). In the Meissner state, the magnetic

The raw data of Figure 3.6 were kindly provided by Kalboussi [48] and replotted here in the author's style.

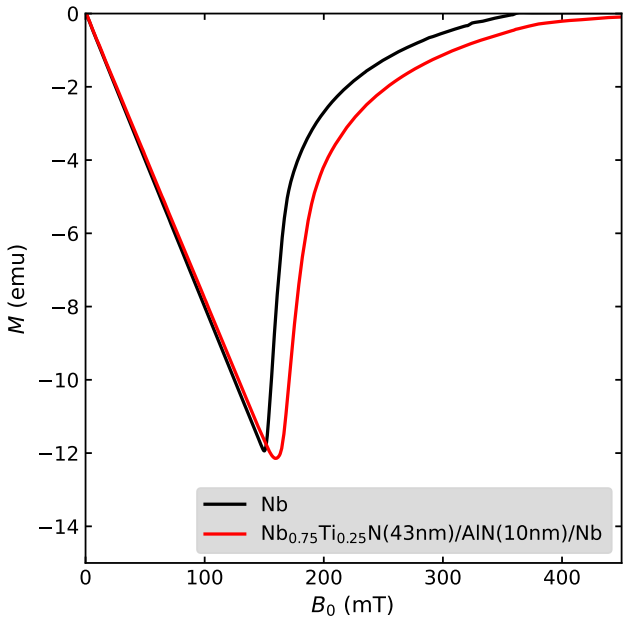

Figure 3.6: Magnetization M, curves as a function of B_0 for ellipsoidal-shaped superconducting samples measured at 2 K [48]. The B_0 was oriented parallel to the sample's longest semi-axis. The black curve represents the bare Nb sample, while the red curve corresponds to the sample after being coated with $Nb_{0.75}Ti_{0.25}N$(43 nm)/AlN(10 nm) multilayers. Both curves exhibit an initial linear region, characteristic of perfect diamagnetism in the Meissner state. The point of deviation from linearity marks the field of first flux penetration, vortex penetration field (B_{vp}). The coated sample shows a higher B_{vp} compared to the bare one, indicating improved flux exclusion capability due to the multilayer coating.

moment decreases linearly with increasing applied field B_0, reflecting ideal diamagnetic screening. This linearity persists up to the vortex penetration field B_{vp}, beyond which the response becomes nonlinear as flux begins to enter. For the bare ellipsoid, B_{vp} was observed at 148.3 mT, increasing to 159.6 mT with the multilayer coating. After accounting for demagnetization effects using the ellipsoidal geometry factor N [136], the corrected values are 170.4 mT and 183.5 mT, respectively, indicating a 13.4 mT enhancement due to the coating. This improvement is significant for SRF applications, corresponding to an estimated gain of about 5 MV m^{-1} in accelerating gradient (E_{acc}) for a TESLA-shaped cavity (as defined in Chapter 1).

The raw data of Figure 3.7 were kindly provided by Kalboussi [48] and replotted here in the author's style.

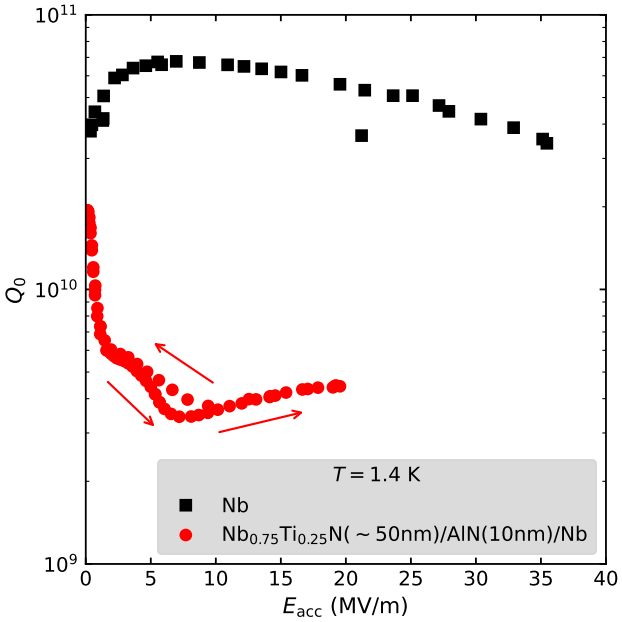

Figure 3.7: RF measurements of the cavity quality factor Q_0 as a function of accelerating gradient E_{acc} at 1.4 K, comparing the performance of a multilayer-coated cavity ($Nb_{0.75}Ti_{0.25}N$(~50 nm) /AlN(10 nm)/Nb, red circles) with a baseline (bare Nb cavity, black squares) [48]. The multilayer-coated sample shows reduced performance relative to the baseline.

Complementing the results from DC magnetization studies, several investigations have examined the RF performance of SIS multilayers. In quadrupole resonator (QPR) measurements, NbTiN(75 nm)/AlN(15 nm) coatings on bulk Nb showed that the maximum field in the Meissner state was limited by a magnetic quench near 20 mT—approximately corresponding to the B_{c1} of NbTiN—indicating early flux penetration [137]. A similar limitation was observed in NbTiN(180 nm-197 nm)/AlN(8 nm-35 nm)/Nb(3000 nm-4000 nm) multilayers deposited on Cu QPRs, which exhibited quench fields around 35 mT [138]. Further insight into the RF performance in a practical SRF cavity was obtained by measuring the Q_0 of a 1.3 GHz Nb cavity as a function of E_{acc} at 1.4 K, before and after applying a $Nb_{0.75}Ti_{0.25}N$ (~50 nm)/AlN(10 nm) coating. As shown in Figure 3.7, the coated cavity exhibited a notable degradation in Q_0 across the entire E_{acc} range.

The observed degradation in 1.3 GHz $Nb_{0.75}Ti_{0.25}N$(~50 nm)/AlN(10 nm)/Nb cavity is likely caused by premature vortex dissipation in the $Nb_{0.75}Ti_{0.25}N$ layer

under RF excitation. This may have been exacerbated by film delamination resulting from suboptimal annealing conditions, where inadequate vacuum control compromised the film's integrity [48]. This is despite the effective suppression of Meissner screening currents that would otherwise shield the underlying Nb up to its B_{sh}. While bulk magnetization measurements such as those in Figure 3.6 reveal the overall magnetic behavior of the multilayer, they lack the spatial resolution needed to pinpoint layer-specific vortex penetration. Taken together, the 1.3 GHz cavity results and earlier QPR studies highlight a persistent challenge in SIS multilayers—namely, their experimental performance continues to fall short of theoretical expectations and remains below the established benchmarks of bulk Nb cavities.

To address this limitation, a depth-resolved measure of subsurface fields under conditions that mimic those inside an SRF cavity, where B_0 is parallel to the cavity walls are essential. Such measurements have recently become feasible using "exotic" ion-implanted β-detected spin spectroscopies that employ implanted radioactive spin probes [3]. In such methods, the energy of the implanted probe dictates the characteristic depth at which it stops below a sample's surface, wherein it's spin interacts with the local (electro)magnetic environment and "communicates" a measurement of the fields via it's decay products.

To provide the necessary context for interpreting experiments using these techniques, their underlying principles, operational mechanisms, and capabilities are presented in the next chapter.

Chapter 4

Experimental details

4.1 Introduction

This thesis employs β-detected implanted spin spectroscopies including muon spin rotation (μSR) [139, 140] low energy muon spin rotation (LE-μSR) [141], and β-detected nuclear magnetic resonance (βNMR) [142]. These techniques are highly effective for studying the electromagnetic (EM) properties of materials making them well suited for the study of superconducting materials. Although they share conceptual similarities with conventional nuclear magnetic resonance (NMR), their detection mechanisms and sensitivity to local magnetic environments differ fundamentally.

While conventional NMR is well-suited for bulk materials, as it typically requires $\sim 10^{17}$ probe nuclei to generate measurable signals, its application to thin films, multilayers, or depth-dependent analyses is limited due to the smaller number of spins in these regions. In contrast, methods like μSR, LE-μSR, and βNMR detect their NMR signal via high-energy β-decay products, overcoming this sensitivity limitation and extending the scope of magnetic and electronic structure studies. Each operates on the same underlying principles: a beam of highly polarized spins is implanted into a sample of interest—almost invariably normal to its surface—and their spin-polarization is monitored through the anisotropic β-emissions from the decay of the radioactive spin probes. While both μSR and LE-μSR techniques

employ positively charged muons μ^+ as the probe, βNMR experiment generally utilizes ^{8}Li nuclei as probes. Table 4.1 outlines some fundamental properties of μ^+ and ^{8}Li. Note that, these experiments can only be performed at dedicated spectrometers installed at the end of accelerator beamlines.

Table 4.1: The fundamental properties of μ^+ and ^{8}Li. The columns contain each probe's nuclear spin I, radioactive lifetime τ, gyromagnetic ratio $\gamma/2\pi$, and, quadrupole moment Q [142–144].

Probe	I	τ (s)	$\gamma/2\pi$ (MHz T^{-1})	Q (mb)
μ^+	1/2	2.2×10^{-6}	135.54	0
^{8}Li	2	1.21	6.302	31.4

μSR, LE-μSR, and βNMR are complementary techniques; however, they differ in several key aspects. These differences arise primarily from their distinct probe lifetimes, as summarized in Table 4.1, which make each technique sensitive to phenomena on different timescales. Moreover, while μSR and LE-μSR use spin-1/2 muons, which are pure magnetic probes, ^{8}Li βNMR is additionally sensitive to electric field gradients (EFGs) as a result of the probe's non-zero nuclear electric quadrupole moment.

Conventional μSR employs high-energy "surface" muons with a kinetic energy of approximately 4.1 MeV, corresponding to a stopping range of about 100 µm in Nb and its alloys [6, 132, 133]. This makes the technique particularly effective for probing bulk magnetic properties under magnetic fields applied parallel to the sample surface. In contrast, LE-μSR and βNMR operate with significantly lower implantation energies in the range of ~2 keV to 30 keV, resulting in implantation depths on the order of ~10 nm to 100 nm [4, 5, 101, 145]. In these methods, the implantation energy of the probe serves as a tunable and independent parameter, enabling depth-resolved measurements on the nanoscale—a length scale comparable to the London penetration depth (λ_L). These shallow depths render LE-μSR well-suited for depth-resolved investigations of magnetic screening under

surface-parallel fields,[1] while βNMR is especially advantageous for characterizing superconducting properties of Nb-based alloys in the presence of magnetic fields up to 9 T perpendicular to the sample surface.[2] Regarding field capabilities mimicking superconducting radio frequency (SRF) cavities, LE-μSR is currently limited to surface-parallel fields of about 30 mT [146], since low-momentum muons are readily deflected by the applied field. By contrast, a specialized high-parallel-field ($\|$) βNMR technique [3] now supports surface-parallel fields up to ~200 mT, approaching the lower critical field (B_{c1}) of Nb. Recent upgrades to the parallel-field βNMR spectrometer [3] have enabled these higher fields, allowing the emulation of SRF cavity operating conditions. As a result, this version ($\|$ field) of βNMR is uniquely suited for depth-resolved magnetic field profiling and for clearly identifying the Meissner-to-vortex transition [147] in both bare and coated Nb samples. A summary of these techniques specific features applicable for the study of SRF materials is given in Table 4.2.

Table 4.2: Measurement capabilities relevant to SRF studies using the μSR, LE-μSR, and βNMR techniques [139, 146, 148]. Here, B_0 represents the applied magnetic field, oriented either parallel ($\|$) or perpendicular ($\perp$) to the sample surface, E denotes the beam implantation energy, while $\langle z \rangle$ corresponds to the resulting mean implantation depth.

Techniques	B_0	E	$\langle z \rangle$	**Suitable to study/measure**
μSR (TRIUMF)	0 mT-300 mT $\|$	~4.1 MeV (fixed)	~100 μm (fixed)	Pinning strength, Field of first vortex penetration
LE-μSR(PSI)	0 mT-30 mT $\|$	~2 keV-30 keV	~10 nm-100 nm	Magnetic screening, Hydrogen diffusion, Magnetic impurities
βNMR* (TRIUMF)	0 T-9 T $\perp$	~2 keV-30 keV	~10 nm-100 nm	Penetration depth, Upper critical field, Superconducting gap
	0 mT-200 mT $\|$			Vortex penetration in the London layer, penetration depth

* In βNMR techniques, the applied field applied magnetic field (B_0) can be oriented either perpendicular ($\perp$) or parallel ($\|$) to the sample surface. The $\perp$ configuration, used in this thesis, does not represent the field orientation in an SRF cavity but is suitable for probing superconducting properties in the vortex state, particularly in Nb alloys such as $Nb_{1-x}Ti_xN$.

[1] In this standard geometry, the applied magnetic field is parallel to the sample surface and therefore orthogonal to the incident beam of charged probes. This configuration results in a Lorentz force that can deflect the beam, a consideration common to all charged-particle beam techniques, though the magnitude of the effect depends on the beam energy and mass.

[2] A perpendicular-field LE-μSR configuration also exists, though it is limited to applied fields of $B_0 \leq 300$ mT [146], and was not employed in this thesis.

The following sections provide a brief overview of the fundamental principles underlying the experiments presented in this thesis. The discussion begins with an introduction to NMR techniques, followed by a review of the basic features of β-decay, which form the conceptual foundation for spin-polarization–based methods. This is then extended to the specific methodologies of μSR, LE-μSR, and βNMR, including descriptions of implantation profiles and the data analysis procedures employed.

4.2 Basics of NMR

NMR is a sophisticated and powerful analytical technique used to study the magnetic properties of atomic nuclei[3] and their surrounding environment. It is primarily based on the principle that certain nuclei possess a property called "spin," which gives rise to a magnetic moment μ. When placed in an externally applied static magnetic field, nuclear magnetic moments align along the field in discrete orientations determined by their spin quantum number—for example, a spin-$1/2$ nucleus has two possible orientations, parallel or antiparallel to the field, resulting in two distinct spin states.[4] Transitions between these states are induced when the nuclei absorb and subsequently emit radio frequency (RF) radiation, forming the basis of NMR spectroscopy. After such excitations, the nuclear spin system does not remain in the perturbed state indefinitely and gradually returns to thermal equilibrium with its surrounding molecular environment. This return process, known as "relaxation," is governed by specific mechanisms that are crucial for interpreting the measurements. The detailed discussion that follows is inspired by the works of Kittel et al., Blundell and Cowan [62, 149, 150], which provide foundational insights into the principles and relaxation phenomena in NMR.

NMR is based on the fact that, under an externally applied magnetic field B_0,

[3] While the "N" in NMR refers to atomic nuclei, the underlying principles are equally applicable to any particle possessing both non-zero spin and a magnetic moment, such as the positive muon.

[4] More generally, a nucleus with spin I has $2I + 1$ possible spin states.

nuclear spins can occupy discrete quantum states. Consider a nucleus characterized by a magnetic moment μ and an angular momentum $\hbar I$, where I is the nuclear spin quantum number and $\hbar$ is the reduced Planck constant. These two quantities are aligned parallel to each other, and their relationship can be mathematically represented as:

$$\mu = \gamma \hbar I, \tag{4.1}$$

where γ is the gyromagnetic ratio that varies for different nuclei. The interaction energy E of the magnetic moment with the external field B_0 is then:

$$\begin{aligned} E &= -\mu B_0 \\ &= -\gamma \hbar I B_0. \end{aligned} \tag{4.2}$$

However, since the component of angular momentum along the direction of the field is quantized, the energy levels are expressed in terms of the magnetic quantum number m, which takes on $2I + 1$ discrete values from $+I$ to $-I$. Thus, the energy associated with each quantum state is:

$$E_m = -\gamma m \hbar B_0. \tag{4.3}$$

In the specific case of spin-1/2 nucleus, there are two energy levels for the $m = \pm 1/2$ states. The energy difference between these two levels, denoted as ΔE or the Zeeman energy, is represented by $\hbar\omega_0$ and can be expressed as:

$$\Delta E = \hbar\omega_0 = \gamma \hbar B_0, \tag{4.4}$$

where

$$\omega_0 = \gamma B_0, \tag{4.5}$$

is the resonance frequency, also known as the Larmor frequency.[5] This resonance condition is fundamental for magnetic resonance absorption.

[5] A quantum-mechanical description of spin precession, yielding an identical expression, is derived in Section 9.1.

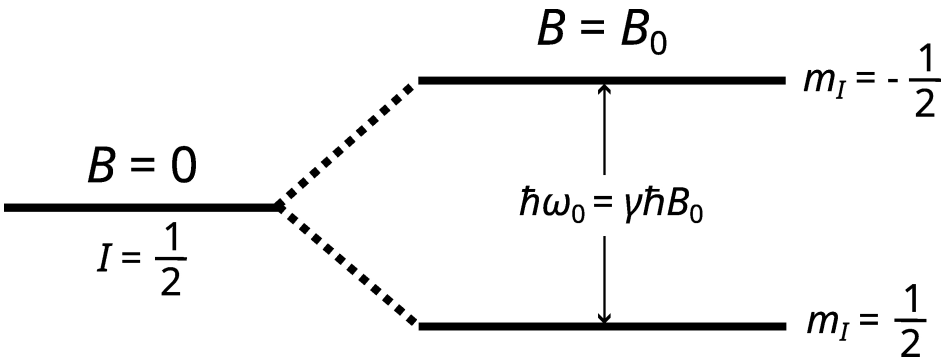

Figure 4.1: Energy level splitting for a nucleus with spin $I = \frac{1}{2}$ in a static magnetic field B_0. In the absence of an external field ($B = 0$), the two spin states are degenerate. When a magnetic field B_0 is applied, the degeneracy is lifted, resulting in two distinct energy levels corresponding to magnetic quantum numbers $m_I = \pm\frac{1}{2}$. The energy separation between these levels is $\hbar\omega_0 = \gamma\hbar B_0$, where γ is the gyromagnetic ratio and ω_0 is the Larmor frequency.

In addition to defining the energy level structure, the interaction between the nuclear magnetic moment $\boldsymbol{\mu}$ and the applied magnetic field $\mathbf{B_0}$ also governs the spin dynamics of the system. Specifically, in the presence of a static $\mathbf{B_0}$, $\boldsymbol{\mu}$ experiences a torque given by $\boldsymbol{\mu} \times \mathbf{B_0}$. According to the rotational analogue of Newton's Second Law, which states that the rate of change of angular momentum of a system is equal to the torque acting on the system, this relationship can be mathematically expressed as:

$$\hbar \frac{\mathrm{d}\mathbf{I}}{\mathrm{d}t} = \boldsymbol{\mu} \times \mathbf{B_0}. \tag{4.6}$$

Substituting the definition of $\boldsymbol{\mu}$ and applying Equation (4.1) in Equation (4.6), we obtain:

$$\frac{\mathrm{d}\boldsymbol{\mu}}{\mathrm{d}t} = \gamma \boldsymbol{\mu} \times \mathbf{B_0}. \tag{4.7}$$

For an assembly of nuclear spins, the magnetization vector $\mathbf{M}$ can be introduced, representing the total magnetic moment per unit volume (i.e., $\sum \boldsymbol{\mu_i}$). By summing the equations of motion for each spin (assuming they belong to the same species), we derive the equation of motion in terms of $\mathbf{M}$:

$$\frac{\mathrm{d}\mathbf{M}}{\mathrm{d}t} = \gamma \mathbf{M} \times \mathbf{B_0}. \tag{4.8}$$

This equation can be easily solved once the direction of $\mathbf{B_0}$ has been specified. Specifically, when $\mathbf{B_0} = B_0\hat{\boldsymbol{z}}$, the solution to Equation (4.8) is:

$$\begin{aligned} M_x &= 0, \\ M_y &= 0, \\ M_z &= M_0. \end{aligned} \tag{4.9}$$

For the simplest case, the magnetization of a system with $I = \frac{1}{2}$ is related to the state population difference $N_+ - N_-$ of the lower and upper levels, where N refers to a unit volume. The population ratio in thermal equilibrium is given by the Boltzmann factor of the energy difference $2\mu_0 B_0$:

$$\frac{N_-}{N_+} = \exp\left(\frac{-2\mu B_0}{k_B T}\right), \tag{4.10}$$

and the equilibrium magnetization is $M_0 = N\mu \tanh(\mu B/k_B T)$.

When the magnetization component M_z is not in thermal equilibrium, we suppose that it approaches equilibrium at a rate proportional to the departure from the equilibrium value of M_0:

$$\frac{\mathrm{d}M_z}{\mathrm{d}t} = \frac{M_0 - M_z}{T_1}. \tag{4.11}$$

This T_1 is the spin-lattice relaxation (SLR) time, quantifying the characteristic timescale of approach to equilibrium. In general, SLR involves an energy exchange between the spin system and its surrounding environment—often referred to as the "lattice." If an unmagnetized specimen is placed in a magnetic field $\mathbf{B_0} = B_0\hat{\boldsymbol{z}}$ at time $t = 0$, the magnetization increases from $M_z = 0$ to $M_z = M_0$. Considering Equation (4.11), the z component of Equation (4.8) is:

$$\frac{\mathrm{d}M_z}{\mathrm{d}t} = \gamma\left(\mathbf{M} \times \mathbf{B_0}\right)_z + \frac{M_0 - M_z}{T_1}, \tag{4.12}$$

where the additional term $\frac{M_0 - M_z}{T_1}$ arises from Equation (4.11), indicating that $\mathbf{M}$

not only precesses around the magnetic field but also relaxes to the equilibrium value $\mathbf{M_0}$.

While the magnetic field tends to align $\mathbf{B_0}$ with the z-axis, the x- and y-components, M_x and M_y, are not initially zero. Over time, M_x and M_y decay to zero due to the alignment of the magnetic field with the z-axis, as the transverse components are zero in thermal equilibrium. The transverse relaxation can be described by:

$$\begin{aligned} \frac{\mathrm{d}M_x}{\mathrm{d}t} &= \gamma \left(\mathbf{M} \times \mathbf{B_0}\right)_x - \frac{M_x}{T_2}, \\ \frac{\mathrm{d}M_y}{\mathrm{d}t} &= \gamma \left(\mathbf{M} \times \mathbf{B_0}\right)_y - \frac{M_y}{T_2}. \end{aligned} \tag{4.13}$$

Here, T_2 is known as the spin-spin relaxation time, which describes the decay of phase coherence among the probe nuclei. Typically, in solids, $T_2 \ll T_1$, while in liquids, $T_2 \approx T_1$. From Equation (4.13), it is evident that the magnetic energy remains unchanged as M_x or M_y changes, provided that $\mathbf{B_0}$ is along the z-axis. Together Equations (4.12) and (4.13) are referred to as the Bloch equations [151], which provide a macroscopic model describing the collective behavior of nuclei. Note, the magnetization in the transverse plane (i.e., Equation (4.13)), is often described using a complex representation in the x-y plane as:

$$M_{xy} = M_x(t) + iM_y(t), \tag{4.14}$$

which simplifies the mathematical treatment of precessional motion. The solutions to Equations (4.12) and (4.14) are given by:

$$M_z(t) = M_0 + (M_z(t=0) - M_0)\exp(-t/T_1) \tag{4.15}$$

$$M_{xy}(t) = M_{xy}(t=0)\exp(-t/T_2)\exp(-i\omega_0 t) \tag{4.16}$$

where ω_0 is given by Equation (4.5). The Bloch formalism thus describes both

longitudinal and transverse relaxation: the longitudinal (i.e., SLR) processes are experimentally examined in Chapter 7, while transverse relaxation is probed in Chapters 5 and 6. Specifically, Equation (4.16) shows that the transverse magnetization precesses at the Larmor frequency ω_0 with an exponential decay governed by T_2, reflecting the loss of spin phase coherence. In the special case $M_z(t = 0) = 0$ and $M_{xy}(t = 0) > 0$, the magnetization dynamics reduce to spin-precession at a frequency ω_0 that is damped by a factor $\exp(-t/T_2)$.

For more detailed microscopic descriptions, such as incorporating higher-order spin interactions, the density matrix formalism provides a broader framework [152, 153], though the essential physical picture remains consistent with the Bloch model. Importantly, the macroscopic magnetization vector **M** introduced here is itself a collective representation of the underlying microscopic spin polarizations, which are directly probed in the experimental techniques employed in this thesis. In particular, the spin polarization of radioactive nuclei produced via β-decay serves as a sensitive probe of local magnetic environments. The following section introduces the essential principles of β-decay.

4.3 Basic features of β-decay

β-decay is one among various types of radioactive decay processes, occurring when a nucleus undergoes a charge state transition between its nucleons (i.e., proton or neutron) to attain a more stable configuration. The process is accompanied by the emission of a β-particle, which can be either an electron (e^-) or a positron (e^+).

Formally, a progenitor nucleus X transforms into a progeny nucleus Y according to the following reactions for $\beta^\pm$-decay (i.e., $e^\pm$ emission):

$$\begin{aligned} {}^{A}_{Z}\mathrm{X} &\longrightarrow {}^{A}_{Z-1}\mathrm{Y} + \mathrm{e}^+ + \nu_\mathrm{e}\,, \\ {}^{A}_{Z}\mathrm{X} &\longrightarrow {}^{A}_{Z+1}\mathrm{Y} + \mathrm{e}^- + \bar{\nu}_\mathrm{e}\,, \end{aligned} \tag{4.17}$$

where A and Z are the mass and atomic numbers of the progenitor nucleus,

respectively, and ν_e and $\bar{\nu}_e$ represent the electron neutrino and antineutrino. The specific type of β-decay that an isotope undergoes depends on its neutron-to-proton ratio: neutron-rich nuclei undergo β^--decay, while neutron-poor nuclei undergo β^+-decay. A related process, known as "electron capture," occurs in proton-rich nuclei when an inner orbital electron is absorbed by the nucleus, converting a proton into a neutron. During β-decay, several quantities are conserved, including mass number, electric charge, and lepton number. The emission of a neutrino or antineutrino ensures lepton number conservation, making β-decay a three-body process. The total energy released in the decay—equal to the difference in rest-mass energy between the progenitor and progeny nuclei—is shared among the emitted particles. As a result, the β-particles exhibit a continuous energy spectrum, ranging from zero up to a maximum (endpoint) energy determined by the available decay energy. The recoil energy of the progeny nucleus, though finite, is typically negligible.

The mechanism of β-decay is governed by the weak interaction, one of the four fundamental forces. Unlike electromagnetism, gravity, and the strong interaction, where parity (mirror symmetry) is conserved, the weak interaction exhibits maximal parity violation. In physical terms, a parity transformation inverts spatial coordinates, making "left" and "right" indistinguishable if parity is conserved. In weak processes, however, this symmetry is broken, and handedness becomes a physically meaningful property. The idea that weak interactions might violate parity was first proposed by Lee et al. [154] and confirmed the following year in two landmark experiments: the measurement of anisotropic β-emissions in the decay of polarized ^{60}Co nuclei by Wu et al. [155], and the measurement of asymmetric positron emissions from spin-polarized μ^+ decay by Garwin et al. [156], the latter exploiting the natural polarization of μ^+ from π^+ decay. The practical consequence of this discovery is that for an ensemble of spin-polarized nuclei or particles, β-particle emission direction is probabilistically correlated with the progenitor's spin

orientation at the moment of decay. This principle forms the foundation of μSR and its complementary technique, βNMR, which are discussed in detail below.

4.4 μSR

μSR is a versatile spectroscopic technique that probes local magnetic environments in materials by tracking the time evolution of the spin polarization of implanted muons. In this section, we first introduce the fundamental properties of the muon relevant to μSR, followed by the basic principles of the technique. We then describe the characteristic depolarization functions for zero field muon spin rotation (ZF-μSR) and transverse field muon spin rotation (TF-μSR) configurations, which form the foundation for analyzing subsurface magnetic field distributions in superconductors and related systems.

4.4.1 Properties of muon

In μSR and LE-μSR, the probe is the muon, an unstable spin-$\frac{1}{2}$ lepton with a mean lifetime of $2.197\,\mu\mathrm{s}$. It has a mass approximately 207 times that of the electron (or roughly $1/9$ the proton mass) and a gyromagnetic ratio of $\gamma_{\mu^+} = 2\pi \times 135.54\,\mathrm{MHz\,T^{-1}}$. Due to the asymmetric decay properties of the muon, the μ^+ is suitable as a sensitive probe of magnetic environment in the matter. Muons are created by the decay of charged pions, which are primarily produced by high energy protons colliding with nuclei like carbon or beryllium. The decay of pions that are produced in MeV energy proton-nucleon collisions are as follows:

$$\begin{aligned} \mathrm{p^+ + p^+ \longrightarrow p^+ + n^0 + \pi^+}, \\ \mathrm{p^+ + n^0 \longrightarrow n^0 + n^0 + \pi^+}, \end{aligned} \tag{4.18}$$

where p^+ is the proton, n^0 is the neutron, and π^+ is the positive pion, is a short lived meson (mean lifetime 26 ns) which decays into a positive muon (μ^+) and a muon neutrino (ν_μ):

$$\pi^+ \longrightarrow \mu^+ + \nu_\mu \,. \tag{4.19}$$

The decay of pions at rest (e.g., those stopped near the surface of the production target) is used to produce a fully polarized muon beam. Due to angular momentum conservation—manifested by the exclusively left-handed neutrinos—the resulting muons emerge with 100 % polarization. This resultant beam possesses a kinetic energy of 4.12 MeV and a corresponding momentum of 29.8 MeV/c (where c is speed of light in vacuum), with the spin of the μ^+ particle aligned antiparallel to its momentum. Muons generated in this manner are referred to as a "surface" muon beam.

Muons are unstable particles that decay into a positron (e^+), electron neutrino (ν_e), and, a muon antineutrino ($\bar{\nu}_\mu$) as follows:

$$\mu^+ \longrightarrow e^+ + \nu_e + \bar{\nu}_\mu \,. \tag{4.20}$$

This is a three-body decay as discussed in Section 4.3, so the total energy of the muon is shared among the positron and the two neutrinos. As a result, the kinetic energy of the emerging positron can vary continuously from nearly zero—if the neutrinos carry most of the energy—up to a maximum of 52.8 MeV, discussed below.

Due to the parity-violating nature of weak β-decay, the positron in a μ^+ decay is correlated with the direction of the muon's spin at the time of decay. This leads to an angular distribution $W(\theta)$ for the β-emission direction. As an example, for the decay of μ^+ described by Equation (4.20), $W(\theta)$ takes the form:

$$W(\theta) = 1 + a(E)P\frac{v}{c}\cos(\theta), \tag{4.21}$$

where θ is the angle between the spin polarization axis and the β-particle emission direction, v is the velocity of the β electrons, c is the speed of light (generally $v \approx c$),[6] P is the nuclear spin-polarization, and $a(E)$ is the energy-dependent decay asymmetry. The P is defined by:

$$P = \frac{1}{I} \sum_{m=-I}^{+I} p_m m, \tag{4.22}$$

where I is the nuclear spin quantum number, m is the nuclear magnetic quantum number and p_m is the population of the corresponding sublevel. For μ^+, which are produced highly polarized in pion decay, no external polarization procedure is required, so $P = 1$. The $a(E)$ is given by:

$$a(\epsilon) = \frac{2\epsilon - 1}{3 - 2\epsilon}, \tag{4.23}$$

with $\epsilon = E/E^{\mathrm{m}}$, where $E^{\mathrm{m}} = 52.83\,\mathrm{MeV}$ is the maximum energy of the emitted positron. Equation (4.21) is depicted in Figure 4.2 for a variety of positron energies. While the decay asymmetry is 1 at the maximal positron emission energy of 52.8 MeV, the angular distribution is isotropic ($a(E) = 0$) at half of that energy. When E is even smaller, $a(E)$ becomes negative (not shown in Figure 4.2). When sampling positron energies uniformly [157], $a(E)$ averages to $\bar{a}(E) = 1/3$.

The angular dependence of positron emission in μ^+ decay, described by Equation (4.21), motivates the use of a two-detector system with detectors positioned at 0° and 180° relative to each other. At these angles, the difference in emission probability is maximized, making the measurement most sensitive to the muon spin orientation. By forming the asymmetry of the counts measured in the two detectors, one can directly track the time evolution of the muon spin polarization. More formally, one can define the asymmetry spectrum $A(t)$ of the counts $N_\pm$

[6] The factor v/c arises because for relativistic β-electrons, the correlation is strongest when $v \approx c$; at lower velocities, the asymmetry is suppressed.

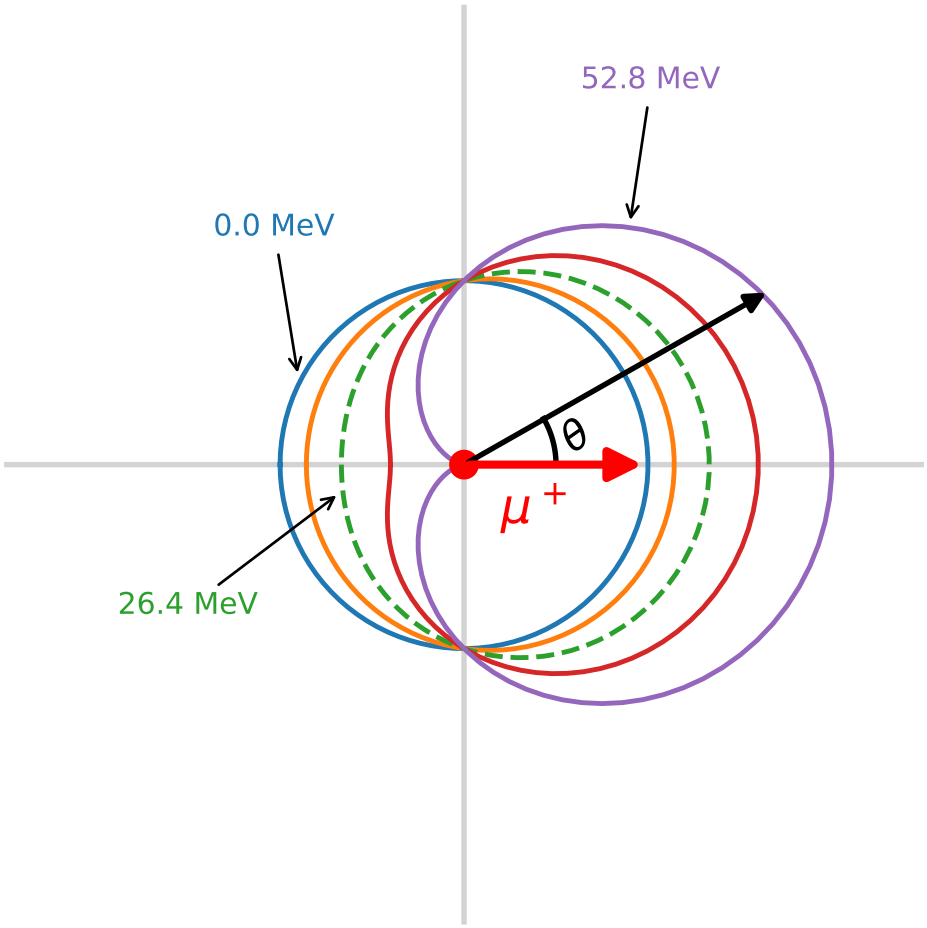

Figure 4.2: Angular probability distribution $W(\theta)$ of positrons emitted from a μ^+ decay, for positron energies between 0 MeV to 52.8 MeV, as described by Equation (4.21). The angle θ is defined between the muon spin direction at its instant of decay and the positron emission direction. The dashed green curve shows the average asymmetry $\bar{a}(E) = 1/3$ for this energy range.

measured by the two detectors as:

$$A(t) = A_0 P(t), \tag{4.24}$$

$$= \frac{[N_+(t) - N_{+,\mathrm{bg}}] - \alpha[N_-(t) - N_{-,\mathrm{bg}}]}{[N_+(t) - N_{+,\mathrm{bg}}] + \alpha[N_-(t) - N_{-,\mathrm{bg}}]}. \tag{4.25}$$

where $\alpha \equiv N_{+,0}/N_{-,0}$ is the balance parameter between the two detectors (e.g., detection efficiencies and solid-angle coverage) [158].[7] Here, A_0 is the initial

[7]This α depends on the detailed geometry of the experiment, it is not known a priori and is typically treated as a fit parameter in the analysis.

asymmetry, which is directly related to the theoretical asymmetry $a(E)$ in Equation (4.21) and $A_0P(t)$ is a function describing the time evolution of the muon spin polarization.

Thus, forming the asymmetry provides a direct measure of the muon spin dynamics. In this context, the time histogram of positron counts naturally extends the angular distribution in Equation (4.21) to the time domain and takes the form:

$$N_{\pm}(t) = N_{\pm,0} \exp(-t/\tau_\mu)[1 \pm A_0P(t)] + N_{\pm,\mathrm{bg}}, \tag{4.26}$$

where $N_{\pm,0}$ is a normalization constant, τ_μ is the μ^+ lifetime, $N_{\pm,\mathrm{bg}}$ is a contribution of uncorrelated background events. The empirically observed maximum A_0 typically lies between 0.2 to 0.3, lower than the theoretical 1/3, due to factors such as the finite solid angle covered by the detection geometry, the sensitivity/efficiency of the detectors, and positron absorption in the sample and surroundings. Through the use of two opposing detectors, Equation (4.25) provides $A(t)$ directly by canceling the lifetime factor $\exp(-t/\tau_\mu)$ that originates from Equation (4.26), yielding the time evolution of the muon-spin polarization $P(t)$. The measured $A(t)$ is influenced by both the static and dynamic characteristics of the local fields at the μ^+ stopping site, encompassing all relevant information regarding the magnetic interactions between the μ^+ spin and the host sample material.

4.4.2 Principle of the technique

The μSR technique is employed to investigate the local magnetic fields within a material. In this process, spin-polarized μ^+ are introduced into a sample, where their spins interact with the local electromagnetic environment. By leveraging the asymmetric decay of the muon, the time evolution of spin polarization is monitored. In the experiments performed in this thesis, the μ^+ are implanted into a sample one at a time using (quasi-)continuous beams.

At the beginning of a measurement, a single μ^+ enters into the spectrometer,

passing through a trigger detector that initiates the start of a high-precision timer (e.g., see Figure 4.3). The muon then stops in the sample in a very short time ($\approx 10^{-10}$ s) of the muon lifetime (2.2 µs) while retaining its polarization. In general, the muon's spin interacts with its local environment meaning, the spin precesses around the local magnetic field at the Larmor frequency ω_0 (i.e., Equation (4.5)), as does the preferential positron emission direction. The emitted positron is detected in one of the positron detectors surrounding the sample once the muon decays. Subsequently, the timer is stopped, and the decay event is recorded in a histogram. It is essential to measure the decay of numerous muons, often more than $\sim 10^6$, in order to derive the time evolution of muon spin polarization with sufficient statistical accuracy,[8] ensuring that even the small fraction of long-lived muons is adequately sampled and the resulting spin-precession signal can be reliably extracted.

During the measurement, a histogram of decay events as a function of time after the muon arrives in the sample is created for each detector recorded, as described in Section 4.3. In this thesis, the asymmetry $A(t)$ (i.e., Equation (4.25)) is evaluated in two distinct configurations:

- ZF-μSR: This is the fundamental technique for studying magnetic systems, where the absence of an external field leaves the system undisturbed and $P(t)$ reflects only the internal fields and their distribution.[9] In such experiments, the muon spin is usually antiparallel to the beam direction, its natural orientation.[10]

- TF-μSR: An external magnetic field is applied perpendicular to $P_\mu(0)$, allowing measurements of the internal magnetic field distribution and the behavior

[8] The relative statistical uncertainty follows Poisson statistics as $1/\sqrt{N(t)}$, where $N(t)$ is the number of decay events recorded at time t; increasing $N(t)$ reduces the fractional uncertainty.

[9] ZF measurements require active compensation of the Earth's and surrounding magnetic fields, typically to within ~ 2 µT.

[10] The ZF-μSR setup can be regarded as a special case of longitudinal-field μSR, where a field is applied along the initial muon spin direction. Longitudinal-field scans help distinguish static from fluctuating internal fields.

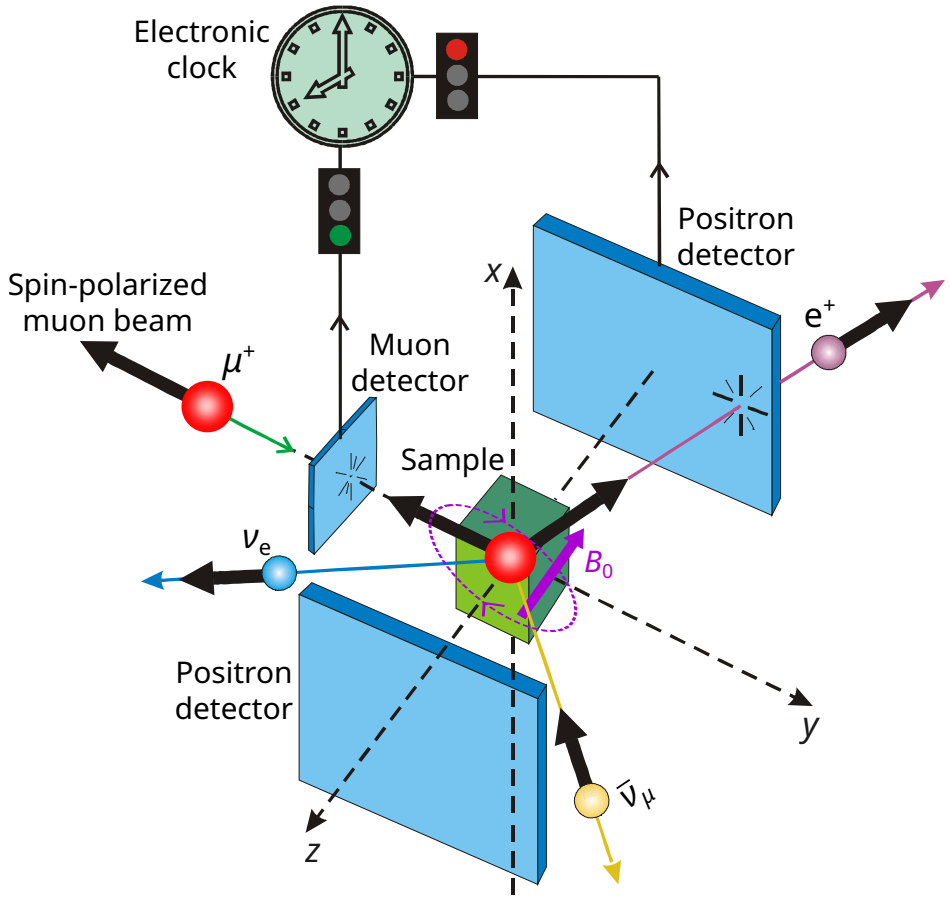

Figure 4.3: Sketch of a TF-μSR experiment setup. Muons are implanted with their spins initially aligned along the y-axis, antiparallel to the beam direction. While the external magnetic field B_0 is applied perpendicular to the muon spin direction (along the z-axis), parallel to the sample surface, and the positron detectors are placed in the yz plane. The muon spin precesses about the local magnetic field at its stopping site in the sample. Redrawn from Ref. [159].

of the local magnetic susceptibility.

By employing these two configurations, this thesis leverages the unique capabilities of ZF-μSR and TF-μSR to detect and characterize magnetic fields in SRF materials. ZF-μSR is employed to study the distributions of $P(t)$ in the absence of an external field, which is subsequently used in Chapter 5 to determine the field of first-flux-penetration in SRF samples. In contrast, TF-μSR is particularly relevant for investigating the field screening profile in Chapter 6, as the applied field B_0 is oriented parallel to the cavity surface, allowing precise measurement

of local magnetic field distributions. The depolarization of muons in these two configurations is discussed next.

ZF-μSR depolarization function

The depolarization of the μSR signal depends on the configuration and fluctuation rate of the internal field that is experienced by the muon. In ZF-μSR, the initial spin polarization of the muon beam is along the z-direction (Figure 4.4), and the polarization function is based on the assumption that the muon ensemble encounters a magnetic field distribution.

In general, the muon spin polarization's time evolution, $P_z(t)$, in the case that the distribution is static, is given by:

$$\begin{aligned} P_z(t) &= \cos^2\theta + \sin^2\theta\cos(\omega_0 t), \\ &= \cos^2\theta + \sin^2\theta\cos(\gamma_\mu B t), \end{aligned} \tag{4.27}$$

where θ denotes the relative angle between the spin polarization and the direction of the magnetic field, γ_μ is the gyromagnetic ratio of muon and $\boldsymbol{B} = |B|$.

When the muon ensemble encounters a non-uniform internal magnetic field, each muon does not experience the same field strength. The time evolution of the muon spin polarization is determined by averaging Equation (4.27) over the relevant magnetic field distribution [160]:

$$P(t) = \int\int\int P(\boldsymbol{B}) P_z(t) \mathrm{d}\boldsymbol{B}, \tag{4.28}$$

where $P(\boldsymbol{B})$ is the normalized probability distribution of magnetic field inside the sample. Within the sample, randomly oriented magnetic moments create a magnetic field distribution at each muon site. In the simplest case, $P(\boldsymbol{B})$ can be

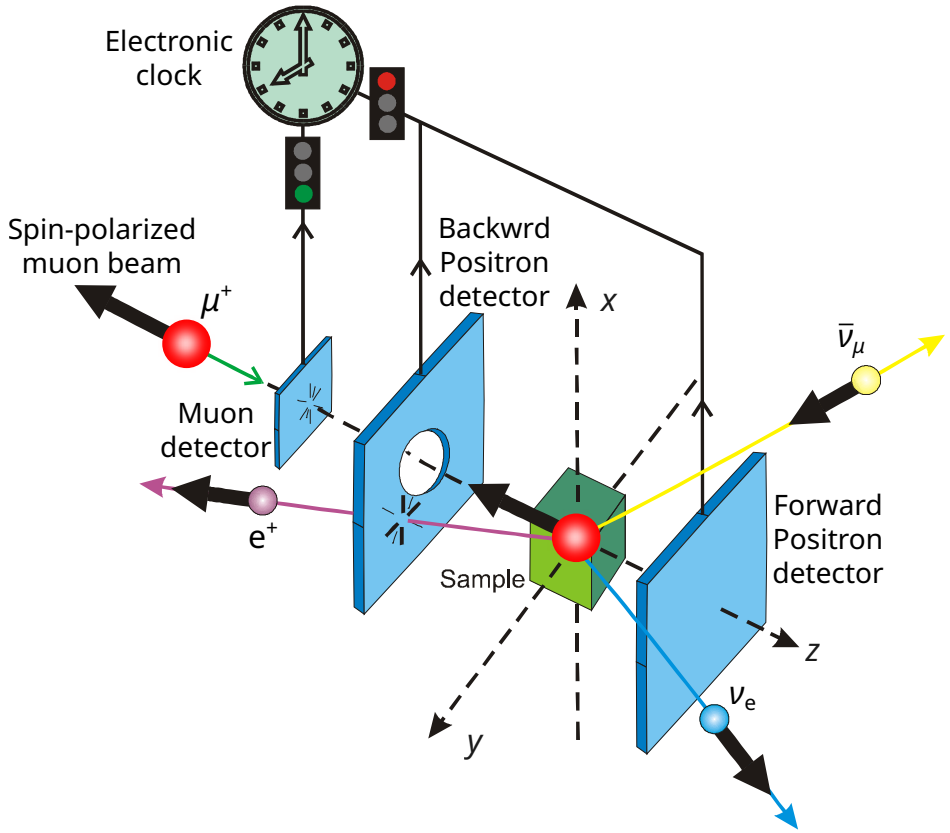

Figure 4.4: Sketch of a ZF-μSR experiment setup. The muon spin direction is antiparallel to the muon beam direction, which is parallel to the z axis. The detectors are placed in the yz plane along the beam direction. Redrawn from Ref. [159].

approximated by a three-dimensional Gaussian distribution:

$$P(B_i) = \frac{\gamma_\mu}{\sqrt{2\pi\sigma^2}} \exp\left(-\frac{\gamma_\mu^2 {B_i}^2}{2\sigma^2}\right), \qquad (i = x, y, z), \tag{4.29}$$

where σ/γ_μ is the width of the internal magnetic field distribution. By substituting $P(\boldsymbol{B})$ into Equation (4.28) and solving the integral, we obtain the so-called static Gaussian Kubo-Toyabe polarization function [161, 162]:

$$P_{\mathrm{ZF}}(t) = \frac{1}{3} + \frac{2}{3}(1 - \sigma^2 t^2) \exp\left(-\frac{1}{2}\sigma^2 t^2\right), \tag{4.30}$$

shows that a finite-width field distribution leads to muon spin depolarization.

This function exhibits Gaussian damping initially and recovers to $\frac{1}{3}$ of its initial value later on, with initial damping caused by x and y local field components perpendicular to the initial muon spin direction.

In many instances, the magnetic field sensed by the muon ensemble is not static, and stochastic (i.e., random) processes are responsible for the field fluctuation(s) that modulate the spin's time-evolution. These dynamic fields, resulting from fluctuations in either the local magnetic field or the muon's site (with a single fluctuation rate ν), contribute to the depolarization of the muon-spin ensemble. The polarization function under these dynamic conditions is derived assuming a stationary Gaussian-Markovian process, implying that the properties of the dynamic process are time-independent. More precisely, the probability of a future state is not influenced by its history, and the field distribution at any given moment is Gaussian.

Using the strong-collision model, the muon spin polarization for sudden changes in the internal field can be derived. In this model, initially, the muon ensemble evolves in a static field, but approximately after an average time of $\tau = 1/\nu$, the local field undergoes a discontinuous fluctuation, adopting a new value. The muon ensemble then precesses in this updated static configuration until the next discontinuous change occurs. This process, effectively resetting the muon precession, is mathematically addressed through dynamicization. In the dynamical case, the muon depolarization function $P_{\mathrm{D}}(t)$ is the sum of the depolarization functions corresponding to all configurations:

$$P_{\mathrm{D}}(t) = \sum_{k=0}^{\infty} G_k(t), \tag{4.31}$$

where $G_k(t)$ describe k number of field changes between instants 0 and t. This model assumes that the probability that the internal field fluctuates within the

interval $\in [0, t]$ is described by:

$$P(t) = \exp(-\nu t). \tag{4.32}$$

Therefore, in the absence of any fluctuation (i.e., $k = 0$) and for a static depolarization function (e.g., $P_{\mathrm{ZF}}(t)$ following Equation (4.32)), $G_k(t)$ yields:

$$\begin{aligned} G_0(t) &= P(t)P_{\mathrm{ZF}}(t), \\ &= \exp(-\nu t)P_{\mathrm{ZF}}(t). \end{aligned} \tag{4.33}$$

Given these hypotheses and using the recursive relation:

$$G_k(t) = \nu \int_0^t G_{k-1}(t - t')G_0(t')\mathrm{d}t', \tag{4.34}$$

upon combining Equations (4.31), (4.33) and (4.34) we can derive a polarization function P_{DGKT}:

$$P_{\mathrm{DGKT}} = P_{\mathrm{ZF}}(t)\exp(-\nu t) + \nu \int_0^t P_{\mathrm{D}}(t - t')P_{\mathrm{ZF}}(t')\exp(-\nu t')\mathrm{d}t'. \tag{4.35}$$

The integral equation relates the dynamic to the static polarization functions and is commonly referred to as the dynamic Kubo-Toyabe polarization function [162].

TF-μSR depolarization function

In the case of TF-μSR, a magnetic field B_0 is applied perpendicular to the initial muon spin direction, as shown in Figure 4.3. The components B_x and B_y are negligible compared to $B_z \approx B_0$ among the values of $\boldsymbol{B}$ with significant weight in the distribution. As a result, the muons perceive an effective field distribution mainly along the z-direction, causing muon spin precession in the xy-plane. The triple integral in Equation (4.28) reduces to a single integral, and the time evolution of the initial muon spin polarization monitored along the y-direction is given

by [146]:

$$P_{\mathrm{TF}} = \int P(B_z) \cos\left(\gamma_\mu B_z t + \phi\right) \mathrm{d}B_z. \tag{4.36}$$

where ϕ is the initial phase of the muon spin polarization. For a static Gaussian internal magnetic field distribution $P(B_z)$ can be expressed as:

$$P(B_z) = \frac{\gamma_\mu}{\sqrt{2\pi}\sigma} \exp\left(-\frac{\gamma_\mu^2 (B_z - B_0)^2}{2\sigma^2}\right). \tag{4.37}$$

By substituting $P(B_z)$ into Equation (4.36) and evaluating the integral, the transverse-field polarization function becomes:

$$P_{\mathrm{GTF}} = \exp\left(-\frac{\sigma^2 t^2}{2}\right) \cos\left(\gamma_\mu B_z t + \phi\right), \tag{4.38}$$

which features an oscillating component reflecting the muon spin precession about the applied magnetic field, along with a "damping" term accounting for depolarization at long times due to the field distribution. It is important to note that in this TF-μSR geometry, only the longitudinal component B_z contributes to damping of the transverse polarization, so the depolarization rate in this geometry is reduced relative to the ZF-μSR case by a factor of $1/\sqrt{2}$. Similar to the expression in Equation (4.35), the dynamic expression for Equation (4.38) can also be derived; however, this expression is not required for the analyses presented in this thesis, and the derivation is therefore omitted. Detailed discussions can be found in Refs. [146, 158].

4.4.3 LE-μSR

The LE-μSR experiments were conducted at the Paul Scherrer Institute (PSI)s Center for Neutron and Muon Sciences in Villigen, Switzerland. In these experiments, a "surface" muon beam with an initial energy of 4.1 MeV is moderated to approximately 15 eV, and subsequently accelerated to create a beam with adjustable

energy ranging from 2 keV to 30 keV. Importantly, the spin polarization of the muons remains intact during the moderation process, allowing for the generation of a 100 % spin-polarized μ^+ beam [163, 164]. Figure 4.5 Illustrates the schematic layout of the μE4 beamline.

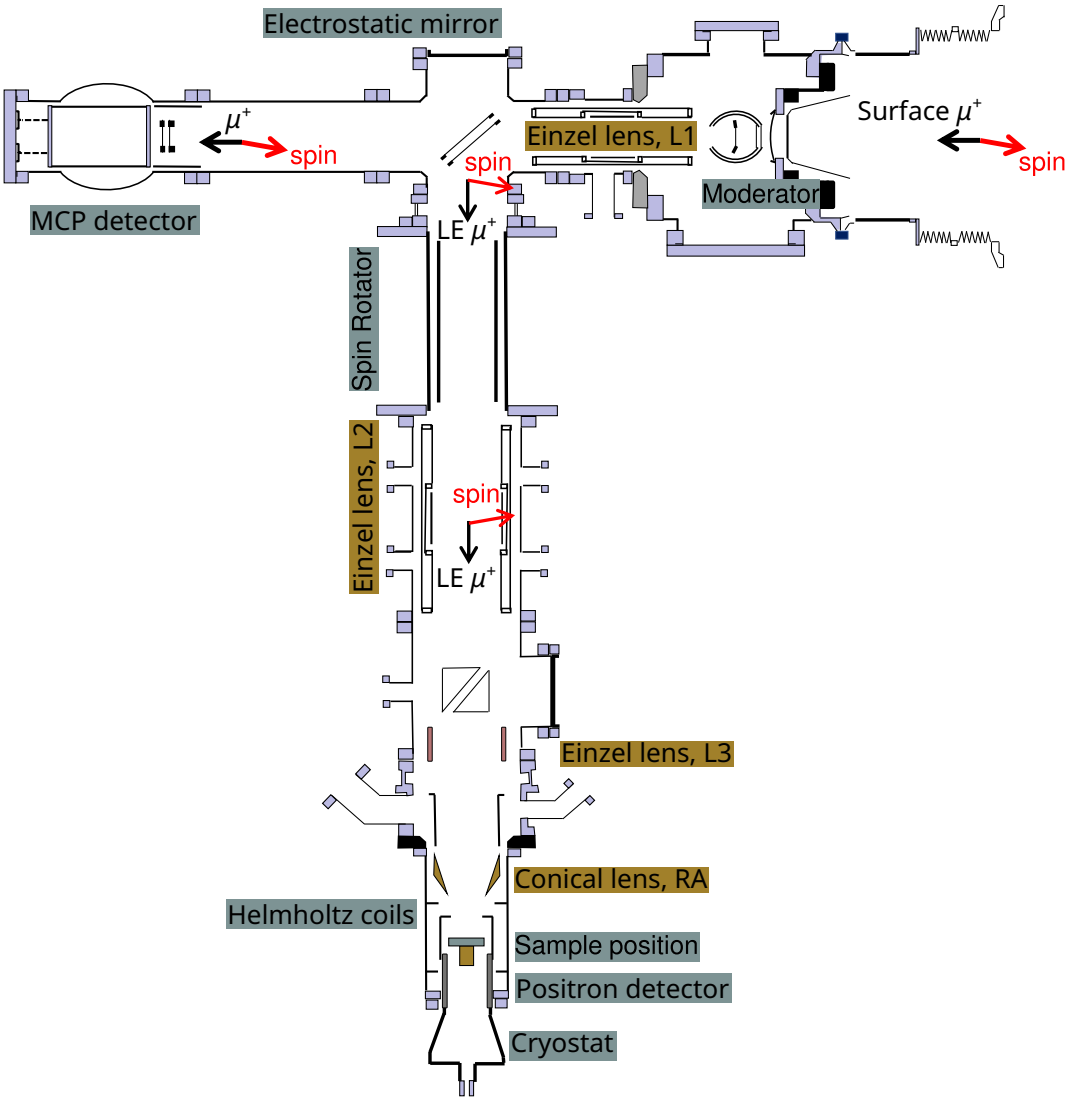

Figure 4.5: Schematic of the PSI low energy muon (LEM) beamline. A 4 MeV surface μ^+ beam is moderated to 15 eV using a 125 µm Ag foil coated with a 200 nm-300 nm solid Ar$-$N$_2$ layer. The moderated beam is re-accelerated to energies up to 20 keV and guided to the sample position via electrostatic elements, including a 45° electrostatic mirror and a spin rotator [165]. A thin carbon foil start detector measures the beam before implantation into the sample, which is mounted on a cryostat cold finger for depth-tunable implantation (0.5 nm to several 100 nm). Adapted from Ref. [166].

The following describes the key components of the beamline–from muon moderation and separation, to transport optics and energy selection–that together enable the delivery of a highly controlled, low-energy polarized muon beam to the sample. First, a "surface" muon beam traverses a moderator composed of a thin layer ($\sim$100 nm) of rare gas solid or solid nitrogen deposited on a 125 µm silver substrate [164, 167]. To prevent rapid deterioration of the moderator and enable the use of high voltages for beam transport, the LE-μSR muon beamline is maintained under ultra-high vacuum (UHV) conditions [168, 169]. This entails maintaining pressures of approximately 10^{-10} mbar in the moderator area and typically better than 10^{-8} mbar in the sample space. A *very* small fraction (10^{-5} to 10^{-4}) of the muons escape the moderator with a mean energy of about 15 eV and an energy spread full width at half maximum (FWHM) of around 20 eV. The majority of the beam exits the moderator target as fast (degraded but unmoderated) muons with an average energy of 500 keV and a similar FWHM. These fast muons are separated from the slow ones by an electrostatic mirror made of a fine wire grid, which deflects the low-energy muons by 90° while leaving their spin direction unchanged.

Following deflection, the muon spin and momentum directions become perpendicular. Fast muons remain unaffected by the electrostatic mirror and are monitored by a multi-channel plate (MCP) detector. Low-energy muons are distinctly identified through a time-of-flight (TOF) measurement between the start scintillator and the trigger detector. The trigger detector, consisting of an ultra-thin carbon foil (2.2 µg cm^{-2}), serves to establish the initial arrival time for incoming low-energy muons. As the muons pass through the foil, they emit on average three electrons, which are deflected by 90° and detected by a grid system to a MCP to provide the start signal for the μSR measurement. The detection efficiency of the trigger detector is approximately 80 %, ensuring the amount of material interacting with the muons and the consequent effects on the trajectory is minimal. The trigger de-

tector induces an energy loss of ∼1 keV for muon beam, with a (Gaussian) standard deviation of 450 eV. Upon passing the trigger detector, the μ^+ beam is focused on the sample using an Einzel lens (L3) and a conically shaped electrostatic lens. The final element, the ring anode (RA) labeled in Figure 4.5, serves to steer and focus the muons onto the sample.

The energy of the muon beam prior to implantation in the sample under investigation is accomplished using static electric fields in a two-step process. Initially, a high positive potential is applied to the moderator substrate to initiate downstream transport. Subsequently, the sample can be biased to further accelerate or decelerate the muons before implantation into the sample. The sample, affixed to a Ni-coated Al holder, is electrically insulated by a thick sapphire crystal and can be biased from −12.5 kV to 12.5 kV. The sapphire crystal also facilitates good thermal contact between the cold finger cryostat and the sample. The implantation energy of the muons at the sample is determined by the re-acceleration voltage applied to the moderated beam, corrected for the small energy loss incurred when passing through the thin carbon-foil trigger detector, and further adjusted by the bias voltage applied to the sample holder (which can be either positive or negative). Under typical operating conditions, this results in a tunable muon energy in the range of 2 keV to 30 keV. In the bottom of Figure 4.5 a small Helmholtz coil generates an external magnetic field of up to 30 mT, applied parallel to the sample surface and perpendicular to the beam direction.

4.5 βNMR

A βNMR experiment employs a beam of highly spin-polarized radioactive nuclei–typically $^8Li^+$–implanted into a sample. The technique closely parallels LE-μSR (see Section 4.4.2), since both methods infer the time evolution of a probe's spin polarization from the asymmetry in detected decay products and both employ implanted probes with tunable kinetic energies on the keV scale. Crucially, both

βNMR and LE-μSR require highly specialized infrastructure, making the facilities that host these experiments essentially world-unique. In addition, producing the probes differs: generating isotopically pure beams of short-lived radioisotopes such as ^{8}Li is more involved than producing muons, and isotopic purity alone is insufficient–the beams must also be prepared with the required spin polarization. Further elaboration on this technique will be provided in the subsequent discussion.

4.5.1 Properties of ^{8}Li

In complement to LE-μSR, βNMR also involves implanting a low-energy, radioactive isotope into the sample and monitoring the probe's spin-polarization via β-decay. At TRIUMF, β-NMR primarily employs the $^{8}_{3}$Li radioisotope due to its abundant availability from a host of production targets, making it one of the simplest to produce in the form of a high-intensity ion beam. Moreover, it has a relatively small mass facilitating efficient implantation at tunable depths, making it particularly suitable for probing thin films and near-surface regions. The $^{8}_{3}$Li β-decay scheme is:

$$\begin{aligned} {}^{8}_{3}\mathrm{Li} &\longrightarrow {}^{8}_{4}\mathrm{Be}^{*} + \bar{\nu}_{\mathrm{e}} + \mathrm{e}^{-}, \\ {}^{8}_{4}\mathrm{Be}^{*} &\longrightarrow 2\,\alpha\,, \end{aligned} \tag{4.39}$$

yielding ^{8}Be* in an excited state which subsequently decays with a short mean lifetime of 8.19×10^{-17} s into two α particles (see Equation (4.39)) [170], a negative β-particle (i.e., e^{-}), and an electron antineutriono, $\bar{\nu}_{\mathrm{e}}$. Because β decay is a three-body process (see Section 4.3), the emitted β-particles (e^{-} or e^{+}) exhibit a continuous energy spectrum ranging from 0 MeV to 13 MeV. In the case of ^{8}Li, the emitted e^{-} tends to be emitted opposite to the nuclear spin direction at the moment of decay. Consequently, the angular distribution of the emitted electrons can be expressed using Equations (4.21) and (4.22), which describe the general form of

anisotropic β emission from polarized nuclei.[11] For ^{8}Li, average $\bar{a}(E) = -1/3$, meaning that its decay electron is preferentially emitted in the direction opposite its spin-polarization.

In a βNMR experiment, a specific way to measure the asymmetry is using four-counter method,[12] which is proportional to the nuclear spin-polarization P:

$$A(t) \equiv \frac{r-1}{r+1} = A_0 P, \tag{4.40}$$

where

$$r \equiv \sqrt{\frac{\left(N_F^+/N_B^+\right)}{\left(N_F^-/N_B^-\right)}},$$

$N_B^\pm$ and $N_F^\pm$ are the beta decay electron events recorded in the forward (F) and backward (B) detectors for the positive (+) and negative (−) helicities,[13] and $A_0 \approx 0.1$ is a proportionality factor that depends on the experimental setup (e.g., detection geometry, probe β-decay properties, etc.).

4.5.2 βNMR facility at TRIUMF

At TRIUMF's isotope separator and accelerator (ISAC) facility [171], the process of generating isotopes involves bombarding the stable nuclei in a target material (typically SiC or Ta, depends on the desired isotope) with a 500 MeV proton beam [172], inducing various spallation reactions. For the production of ^{8}Li, a typical target comprises metallic Ta foils operated at temperatures exceeding 2000 K to facilitate isotope diffusion. The resulting isotopes then diffuse out of the target, where they must ionized and collected as an ion beam then purified to remove unwanted isobars. The diffusion proceeds from the target to a surface

[11] The ^{8}Li nuclei are spin-polarized in flight before entering the βNMR spectrometer,resulting in a non-thermal population of the magnetic sublevels with a preferential occupation of the highest magnetic sublevels (e.g., $m = +2$) (see Section 4.5.2).

[12] Forming the asymmetry in this manner has the advantage of implicitly removing select detection systematics (e.g., different detector efficiencies).

[13] These details have been discussed in Section 4.5.2.

ionization tube, where thermal ionization occurs–a particularly effective scheme for elements with low ionization energies, such as the alkalis. To ensure efficiency, the target is kept at a high positive voltage to expel any cations produced, which are then extracted to form a high-intensity beam. Before delivery to the experiment, the beam undergoes isotopic purification based on their mass-to-charge ratio (m/q) using a magnetic dipole mass separator. Since there are no stable species with a mass number of 8, isotopic purification for ^{8}Li is straightforward and obtaining a beam free of contaminants is routine. While the radioactive ion beam (RIB) produced at the ISAC facility is continuous, a pulsed beam can be generated with the assistance of an electrostatic kicker. The beam is then transported through a high-vacuum beamline ($\sim 10^{-6}$ Torr) using electrostatic optical elements to reach the experimental station.

It is important to note, however, that while this isotope production method provides a high-quality, isotopically pure ^{8}Li beam, it does not produce spin polarization. This stands in contrast to the case of muons, which are inherently produced with nearly 100 % spin polarization due to the parity-violating nature of pion decay (see Section 4.4.1). In βNMR, achieving nuclear polarization in the ^{8}Li probe requires additional beam preparation, involving three key steps: neutralization of the ^{8}Li^{+} ions, optical pumping of the neutralized atoms, and re-ionization of the beam, as outlined in Ref. [173]. These steps are briefly discussed below. Firstly, the ^{8}Li^{+} ions undergo neutralization, typically facilitated by a charge exchange cell filled with the key parameter is that the gas atoms must be more electropositive than Li (i.e., so the "pass" their valence electron to Li spontaneously). This neutralization is crucial since ^{8}Li polarization relies on the presence of an unpaired electron spin. Any remaining unneutralized ions are subsequently removed from the beam using electrostatic deflection plates. After neutralization, the hyperfine levels of ^{8}Li are manipulated through collinear pumping using a circularly polarized resonant laser

beam.[14] The sense of ^{8}Li beam's polarization, or helicity, is alternated by periodically inserting a half-wave plate into the laser beam's path. This procedure reduces systematic errors in the βNMR measurement.

Following optical pumping, ^{8}Li predominantly occupies states with a nuclear magnetic quantum number $m = \pm 2$, resulting in a high degree of spin polarization, typically reaching around ~70 % [173, 174]. Following polarization, the beam undergoes re-ionization upon passing through a He vapor cell. Once re-ionized, the polarized ^{8}Li ion beam is directed electrostatically towards either of the two βNMR spectrometers for implantation into a material under investigation. This re-ionization process typically operates with an efficiency of approximately 50 % [175]. Meanwhile, the remaining neutral fraction travels undeflected into a neutral beam monitor positioned outside the polarizer. This neutral beam serves as a sample-independent diagnostic tool for assessing the polarization process. In a βNMR spectrometer, the experimental asymmetry $A(t)$ is calculated from the emitted β-particle as described in Section 4.5.1.

4.5.3 βNMR spectrometer

At TRIUMF's ISAC-I facility, two spectrometers cover a broad range of magnetic field conditions: (1) a high-perpendicular (to the sample surface) field spectrometer for measurements at >0.5 T and (2) a high/low parallel (to the sample surface) field spectrometer providing fields in the range of 0 mT to 200 mT [3, 139, 176–179]. Both spectrometers operate under UHV conditions, with base pressures around $\sim 10^{-10}$ Torr each using He flow coldfinger cryostats for temperature control over a broad range (3.5 K to 317 K). In this UHV environment, gas molecules primarily interact with the chamber walls rather than with the beam or sample, improving ion beam transport efficiency and reducing contamination from the progressive

[14] A small longitudinal holding field applied along the polarizer section of the beamline leading to the spectrometers lifts the degeneracy of the magnetic hyperfine sublevels.

accumulation of surface adsorbates. Sample insertion and removal are performed via a vacuum load-lock chamber that is isolated from the main vacuum system by a gate valve. This configuration enables independent venting and pumping of the load-lock chamber, preserving the UHV conditions of the main spectrometer chamber. Each spectrometer is positioned on an electrically isolated HV platform,

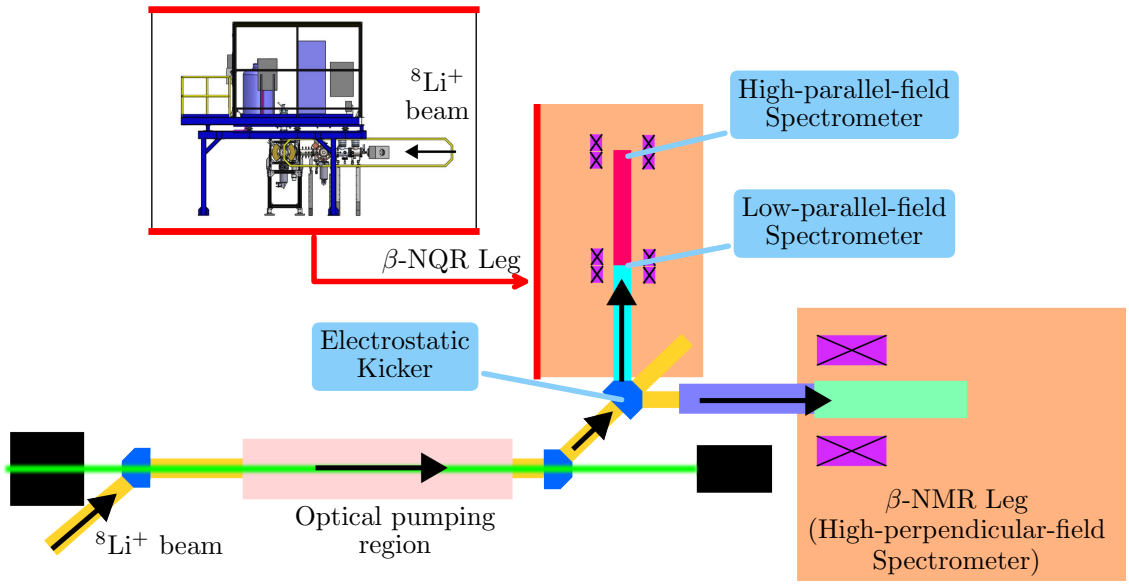

Figure 4.6: Beamline layout of the upgraded βNMR facility. The ^{8}Li$^+$ beam is spin-polarized in-flight (first neutralized with an alkali vapor cell and later re-ionized by a He vapor cell) using dedicated optical pumping infrastructure, allowing for routine operation. The fast electrostatic kicker enables the semi-simultaneous operation of two spectrometers (i.e., two experiments running at the same time off a single RIB). Both spectrometers are equipped with cold-finger UHV cryostats: at the βNMR leg, the spectrometer with a superconducting solenoid allows measurements at high magnetic fields (up to 9 T) perpendicular ($\perp$) to the sample surface, while the upgraded βNMR parallel-field spectrometer (in the image β-NQR Leg) enables measurements up to 200 mT parallel ($\parallel$) to the sample surface, just downstream of the existing low-parallel-field (0 mT to 24 mT) spectrometer. The inset shows a side view of the upgraded high-parallel-field beamline and the high-voltage (HV) platform above the beamline. Adapted from [3].

facilitating the deceleration of incoming positive ion beams by applying a positive bias. This capability enables quick switching between energies ranging from 0.1 keV to 30 keV, depending on the production target voltage. The spectrometers, equipped with charge-coupled device (CCD) cameras, use scintillating sapphire

substrates—particularly defective ones—for imaging the beam's location at the sample position.[15] Sapphire scintillates effectively under $^8Li^+$ irradiation, making it a robust and economical choice for beam imaging [180, 181]. The CCD graphical user interface (GUI) of *bccd*[16] assists in accurately overlaying sample and beamspot images, a feature especially vital for small sample analyses.

Although both spectrometer configurations are available at TRIUMF, this thesis exclusively utilizes the high-perpendicular-field βNMR setup. Accordingly, the following section focuses on the design and operational principles of this specific configuration.

High perpendicular-field spectrometer

Figure 4.7 illustrates a schematic of the high-field spectrometer. The setup features two plastic scintillators, named the forward and backward detectors, positioned in front of and behind the sample, whose function is to detect the outgoing β-particles emitted after the ^{8}Li β-decay. The sample is mounted on a UHV cold finger cryostat. The beam enters through a small aperture in the backward detector, and finally lands on the sample. The size of the beam spot on the sample, typically ranging from 1 mm to 2 mm (with beam intensities $\sim 10^7\,s^{-1}$ [3]), is primarily determined by the focusing electrostatic Einzel lenses, three adjustable collimating slits before the spectrometer, the applied magnetic field, and the beam energy. In particular, the Einzel lenses assists in tuning the $^8Li^+$ beam and focusing it under magnetic fields $\lesssim 1$ T.

The polarization is oriented along the beam axis, which is parallel to a high-homogeneity magnetic field (B_0 up to 9 T) produced by a superconducting solenoid. A small Helmholtz coil straddling the sample position applies an RF field $B_1(t)$ of up to 1 G in the horizontal transverse to B_0. The design of the cryostat, combined

[15] Defective sapphire (α-Al_2O_3) contains crystal imperfections that act as luminescent centers.
[16] This is an in-house open source software package available at https://pypi.org/project/bccd/.

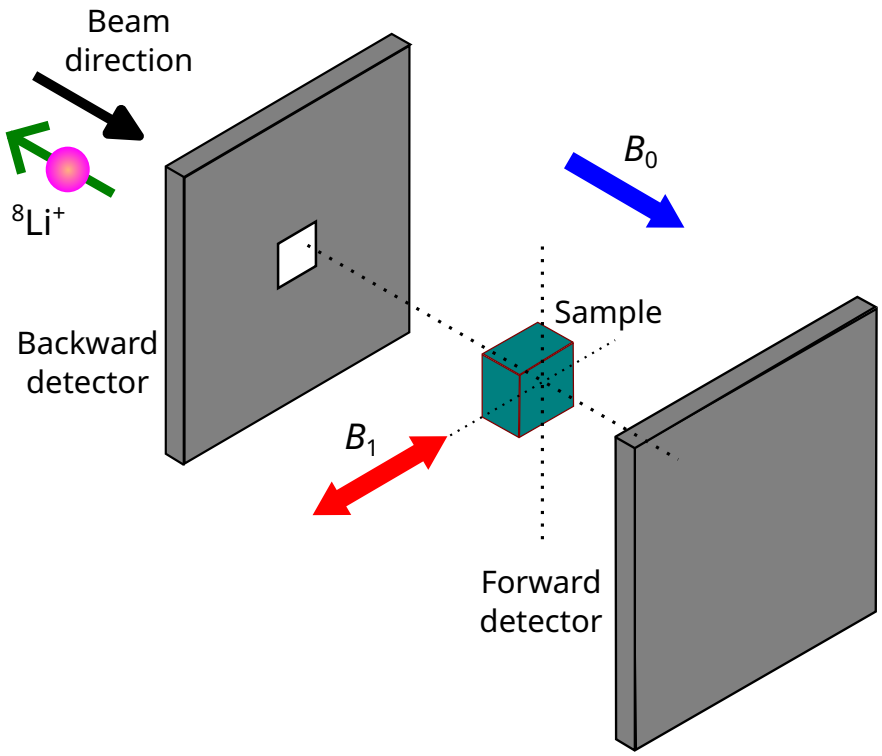

Figure 4.7: Schematic of the high-perpendicular-field spectrometer (i.e., βNMR). The applied magnetic field B_0 is perpendicular ($\perp$) to the sample surface, but parallel to the beam's momentum and polarization axis. The polarized $^8Li^+$ beam enters from the left side, passing through a small aperture in the upstream "Backward" scintillation detector and before being implanted in the sample. The other "Forward" detector is located downstream of the sample and is 180° opposite to the upstream detector. A transverse RF field $B_1 \sim 1$ G at frequency ω may be applied by a Helmholtz coil in the horizontal direction, perpendicular to both the beam and the applied field B_0.

with the split coil around the sample position, restricts a sample's lateral dimensions to 8×12 mm and a thickness of approximately 2 mm.

4.5.4 βNMR measurements

Spin lattice relaxation

As in conventional NMR, SLR in βNMR originates from time-dependent local magnetic field fluctuations at the Larmor frequency, which typically lies in the radiofrequency range. However, because the probe nuclei are radioactive, the

range of relaxation times that can be experimentally accessed is constrained by the nuclear lifetime, τ. In practice, reliable SLR time T_1 values can usually be measured between $10^{-2}\tau$ and $10^{2}\tau$ [182]. For very long T_1, the relaxation is so slow that only a nearly linear decay is observed within the experimental time window, and the relaxation rate becomes strongly coupled to the fitted initial polarization amplitude. Conversely, if the relaxation is much shorter than τ, most of the spin polarization is lost before the nuclei decay, leading to an apparent missing fraction or abrupt step in the measured asymmetry. These limitations define the practical dynamic window of βNMR as a local probe of magnetic fluctuations.

To access this relaxation behavior experimentally, the time dependence of the nuclear polarization of ^{8}Li is monitored through a spin-lattice relaxation measurement without applying the RF B_1 field. An electrostatic kicker is used to pulse the ion beam, with the probe polarization monitored both during and following the process.[17] The pulse's duration is short, typically a few radioactive lifetimes (e.g., 4 s for ^{8}Li), followed by a longer counting period of ~10 radioactive lifetimes (i.e., to allow all implanted nuclei to decay before the next beam pulse arrives). This cycle is repeated until sufficient (counting) statistics have accrued. During the pulse, the polarization (i.e., Equation (4.40)) relaxes towards a dynamic equilibrium, determined by the balance between the loss of polarization due to SLR and the continuous arrival of new polarized spins. After the pulse, the polarization decays to its thermal equilibrium value, which is effectively zero.

Independent of the form of the SLR function $f(t, t'; 1/T_1)$, where t is the decay time, t' is the arrival time, and $1/T_1$ is the relaxation rate, the average polarization follows [77]:

[17] Unlike in μSR, there is no direct analog to a muon counter; the technique does not associate individual ^{8}Li nuclei with single beta decays. Instead, the probe polarization is derived from the measured asymmetry in the beta emission, which provides an ensemble average.

$$P(t) = P_0 \begin{cases} \dfrac{\int_0^t \exp^{-(t-t')/\tau} f(t,t';1/T_1)dt'}{\int_0^t \exp^{(-t/\tau)}\, dt}, & t \leq t_\mathrm{p}, \\ \dfrac{\int_0^{t_\mathrm{p}} \exp^{-(t_\mathrm{p}-t')/\tau} f(t,t',1/T_1)dt'}{\int_0^{t_\mathrm{p}} \exp^{(-t/\tau)}\, dt}; & t > t_\mathrm{p}, \end{cases} \tag{4.41}$$

where P_0 is the initial nuclear spin polarization set by the optical pumping of ^{8}Li before implantation, t_p is the beam's pulse length and τ is the radioactive lifetime of ^{8}Li. In the simplest case of a single characteristic relaxation rate $1/T_1$, the SLR function as the form:

$$f(t,t';1/T_1) = A_0 e^{-\frac{1}{T_1}(t-t')}. \tag{4.42}$$

In the experiment, one measures the asymmetry $A(t)$ whose form follows Equations (4.40) and (4.41) due to its proportionality with the polarization $P(t)$.

Resonance

Unlike conventional NMR, βNMR experiments determine the resonance condition using a continuous wave (CW) approach. It provides a highly efficient means of obtaining resonance spectra with optimal counting statistics. This efficiency is particularly important in radioactive probe experiments, where beamtime is limited and statistical precision is at a premium. Under typical conditions, a resonance spectrum can be acquired in roughly half an hour, while systems exhibiting quadrupolar splitting may require longer accumulation times to resolve the full line shape. Despite these challenges, CW βNMR remains one of the most effective tools for extracting resonance frequencies and local magnetic environments on practical experimental timescales.

The spectral information obtained in this way reflects the microscopic interactions experienced by the implanted nuclei. The nuclear spin interacts with local magnetic fields through the Zeeman interaction, and their time-averages influ-

ence the resonance shift and lineshape. Moreover, due to ^{8}Li's non-zero nuclear quadrupole moment, our resonance spectrum can exhibit quadrupolar splitting from the interaction of the quadrupole moment with non-zero EFGs. In such cases, the peak splitting is determined by the nuclear quadrupole Hamiltonian. Additionally, the width and relative peak position of the spectra from a resonance measurement can also offer insights into the system's relaxation when the relaxation rate is comparable to or slower than the resonance frequency, while very fast relaxation can broaden these features beyond resolution.

Resonance measurements are acquired using a continuous ion beam implanted at a constant rate. Under these conditions, the polarization approaches a steady-state (i.e., a dynamic equilibrium) value given by Equation (4.41) with a $t_p = \infty$. A small transverse RF magnetic field B_1 stepped slowly through the ^{8}Li Larmor frequency. When the RF field matches ^{8}Li's resonance frequency ω_0, it causes the polarization to precess in a plane perpendicular to B_1. The rapid precession during a short integration time (typically 1 s) leads to a reduction in polarization, resulting in a decrease of the observed asymmetry. In resonance measurements, the off-resonance asymmetry value acts as the "baseline" for any signals in the spectrum.

4.6 Ion implantation in solids

As mentioned in Section 4.1, all three techniques (μSR, LE-μSR, and βNMR) involve implanting spin polarized probes (μ^+ or ^{8}Li$^+$) into a sample under investigation, where they come to rest at subsurface depths. At these depths, their interaction with the local magnetic environment provides microscopic information about the internal magnetic fields. In many cases, knowledge of this stopping depth is crucial to the interpretation of the measurements. While not directly available from these techniques, it is possible to simulate the implantation process and accurately predict this length scale. The method of calculation and estimation of the

stopping depths are briefly discussed below.

Ion implantation is a non-equilibrium process, analogous to semiconductor doping [183, 184], in which energetic ions are introduced into a solid. As ions traverse the host material, they lose energy through a stochastic sequence of collisions with electrons and nuclei until they come to rest. Because each ion follows an individual trajectory, the stopping depth is statistically distributed, producing a depth profile that can be characterized by two parameters: the projected range (mean stopping depth) and the straggle (standard deviation). These parameters provide a statistical description of where the implanted probes reside, summarizing the more complete stopping probability distribution that contains all depth-dependent information. In the context of μSR, LE-μSR, and βNMR, knowledge of such details allows for selective studies of surfaces, interfaces, and bulk regions.

The stochastic slowing-down of implanted probes charged particles in solids is accurately described using Monte Carlo simulations. These simulations are typically performed using the Stopping and Range of Ions in Matter (SRIM) [183] and TRIM.SP [184] codes. Both employ Monte Carlo algorithms based on the binary collision approximation and are well-established for predicting ion range distributions across various materials. They are routinely applied in depth-controlled experiments such as LE-μSR [145] and βNMR [185]. By specifying the probe's energy, charge, and mass, along with the target's density and chemical composition, implantation profiles can be reliably simulated.

SRIM is particularly well-suited for simulating the implantation of heavier light ions such as $^{8}\mathrm{Li}^{+}$ in βNMR experiments [101, 185], whereas TRIM.SP provides more accurate results for lighter, hydrogen-like projectiles such as μ^{+} at keV energies [145, 186]. In LE-μSR and βNMR, the probe implantation energy can be tuned continuously in the low-energy regime ($\leq$30 keV), providing nanometer-scale depth resolution. By contrast, in μSR, the μ^{+} beam energy is much higher (about 4.1 MeV), corresponding to stopping ranges of 0.1 mm to 1 mm in typical

solids. Such conditions are well suited for probing bulk properties of matter. For illustration, the stopping range of μ^+ in copper as a function of implantation energy is shown in Figure 4.8.[18]

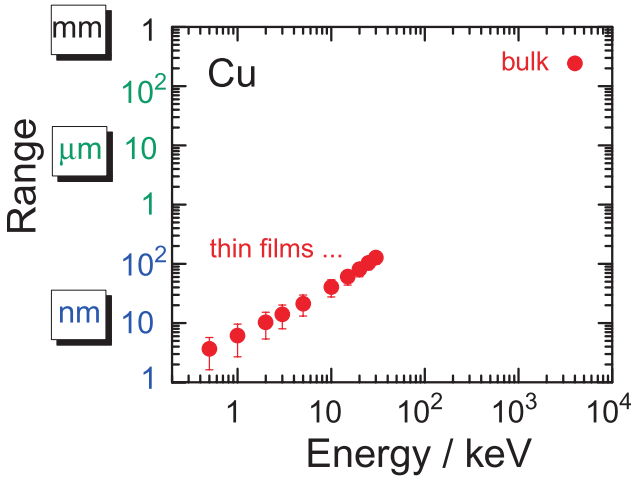

Figure 4.8: Predicted range of positive muons implanted in copper as a function of implantation energy. μSR employs μ^+ beams at about 4 MeV to probe bulk properties on millimeter length scales, whereas LE-μSR uses tunable low energies ($\leq$30 keV) for depth-resolved studies of thin films, multilayers, and nanometer-scale interfacial regions. Adapted from [192]. Copyright ©2004, Taylor & Francis.

Together, these simulation frameworks provide quantitative stopping profiles essential for connecting implantation depths to the measured local magnetic response in the spectroscopic measurements.

4.7 Data analysis

All μSR and LE-μSR data presented in Chapters 5 and 6 were initially analyzed using the dedicated software package `musrfit` [193], which is built on the ROOT [194] object-oriented data analysis framework developed at CERN for high-energy physics experiments and employs the `Minuit2` minimization rou-

[18] For μ^+ implantation at keV energies in Nb-containing compounds however, accurate modeling requires refinements to the electronic stopping cross section that governs energy loss of proton-like projectiles [187]. Earlier parameterizations [188–190] underestimated the stopping ranges of hydrogen isotopes in Nb, as reviewed in Ref. [145]. A revised Varelas-Biersack fit [191], constructed using the full set of available stopping data, corrected this discrepancy and now provides a reliable mapping between the probe's stopping distribution and the spatial regions probed in Nb [145].

tines for fitting data [195, 196]. Post-analysis of the parameters extracted from `musrfit` was carried out using custom fitting functions implemented in `Python`, with homemade scripts making extensive use of the `NumPy` [197], `SciPy` [198], and `iminuit` [199] libraries for statistical modeling and minimization. The βNMR data presented in Chapter 7 were analyzed separately using `Python` scripts incorporating the `mudpy`, `bdata`, and `bfit` libraries [200, 201], together with `iminuit` for fitting. In addition, many of the figures in this thesis were generated using `Matplotlib` [202].

Chapter 5

Measurements of the first-flux-penetration field in surface-treated and coated Nb: Distinguishing between near-surface pinning and an interface energy barrier

5.1 Introduction

A key technical application of the elemental type-II superconductor Nb is its use in superconducting radio frequency (SRF) cavities [1, 2, 203], which are utilized in particle accelerators across the globe. Crucial to their operation is maintaining Nb in its magnetic-flux-free Meissner state (i.e., to prevent dissipation caused by magnetic vortices), which generally restricts their use to surface magnetic fields up to the element's lower critical field ($\mu_0 H_{c1}$) $\approx$ 170 mT [47]. Such a limitation ultimately sets a ceiling for a cavity's maximum accelerating gradient (E_{acc}) (i.e., the achievable energy gain per unit length), which impacts design considerations for accelerating structures (e.g., size, operating temperature, etc.). Consequently, there is great interest in pushing SRF cavity operation up to Nb's so-called superheating field ($\mu_0 H_{sh}$) $\approx$ 240 mT [119, 133], where the Meissner state is preserved in a metastable configuration. Currently, the largest gradients are achieved by so-called low-temperature baking (LTB) surface treatments, wherein a Nb cavity is baked at temperatures on the order of ~120 °C either in vacuum [11, 14] or in a low-pressure gas atmosphere [12, 13]. Indeed, the best performing treatments have enabled cavities to achieve surface magnetic fields beyond $\mu_0 H_{c1}$ (with some even

approaching $\mu_0 H_{\mathrm{sh}}$) [14, 119, 204]; however, the underlying mechanism for this enhancement remains unclear.

The typical LTB treatment, involves vacuum annealing Nb at 120 °C for a duration up to 48 h [11]. Early measurements of this treatment's effect on Nb's Meissner response using low energy muon spin rotation (LE-μSR) [192, 205] showed a sharp discontinuity in the screening profile [206], which led to suggestions that LTB can be used to create an "effective" superconductor-superconductor (SS) bilayer [18]. Of particular interest for SRF applications is the case where a thin "dirty" layer resides atop a "clean" bulk (e.g., as a result of surface-localized inhomogeneous doping), as it offered several avenues for increasing the vortex penetration field ($\mu_0 H_{\mathrm{vp}}$) via a reduced current density at Nb's surface (e.g., following directly from the SS-like structure [18] or as a consequence of deformations found in the Meissner profile itself [207, 208]). While both theories [18] and measurements [206] have been presented that support the interpretation of a surface barrier originating from a "dirty" layer, other measurements [145] and analyses [209] contradict such views. To resolve this discrepancy, additional measurements using alternative approaches would be highly beneficial.

One such possibility is instead using techniques capable of identifying $\mu_0 H_{\mathrm{vp}}$ directly. This has been done, for example, using "bulk" muon spin rotation (μSR) [158, 210], which provides a local measurement of the magnetic field $\sim$100 µm below Nb's surface. Such studies have found $\mu_0 H_{\mathrm{vp}} \gtrsim \mu_0 H_{\mathrm{c1}}$ for both LTB and coated Nb [132], the latter yielding $\mu_0 H_{\mathrm{vp}} \approx \mu_0 H_{\mathrm{sh}}$ [133]. While this provided strong evidence that a surface energy barrier [24] was preventing flux nucleation in SS samples, some ambiguity in interpreting the enhancement from LTB remained. Specifically, subsequent magnetometry measurements on identically prepared samples showed no such enhancement [47], implying an accumulation of near-surface vortices caused by *pinning*. The discrepancy between μSR and magnetometry suggests that any pinning centers must be localized to depths less

than ~100 μm below Nb's surface.

To test these ideas, here we extend the "bulk" μSR approach used in related work [9, 132, 133] to provide *depth-resolved* measurements of $\mu_0 H_{vp}$ in both surface-treated and coated Nb. Specifically, we make use of thin Ag foils to moderate the implantation energy of the muon spin probes, providing spatial sensitivity to depths on the order of ~30 μm to ~100 μm. In the presence of surface energy barrier [24], $\mu_0 H_{vp}$ is expected to be depth-independent, whereas surface-localized pinning is anticipated to produce larger $\mu_0 H_{vp}$s deeper below the surface (see Figure 5.1). Using this approach, we find that $\mu_0 H_{vp}$ is depth-independent and close to Nb's $\mu_0 H_{sh}$ for a Nb sample coated with the A15 superconductor Nb_3Sn [211, 212], consistent with the energy barrier expected for the SS bilayer. Conversely, for Nb that has been surface-treated by LTB at 120 °C, the measured $\mu_0 H_{vp}$s are comparable to Nb's $\mu_0 H_{c1}$, but increase deeper below the surface, suggesting the presence of localized pinning near the surface that prevents detection by deeper implanted muons.

5.2 Experiment

μSR experiments were performed at TRIUMF's Centre for Molecular and Materials Science (CMMS) facility in Vancouver, Canada. Using the M20C beamline [139], a ~100 % spin-polarized ~4.1 MeV "surface" μ^+ beam was extracted, spin-rotated in flight, and delivered to the high-parallel-field (i.e., "HodgePodge") spectrometer equipped with a horizontal gas-flow cryostat and a low-background (i.e., Knight shift) insert [139]. A sketch of cryostat configuration is given in Figure 5.2. This setup is similar to that used in related experiments [9, 132, 133], with the external magnetic field parallel to each sample's surface (see Figure 5.1) and perpendicular to the implanted μ^+ spin direction. Notably, the present work also incorporates thin Ag foils (Goodfellow, 99.95 % purity, 10 μm to 30 μm thick) as part of the cryostat assembly, acting as energy moderators for the μ^+ beam. By varying

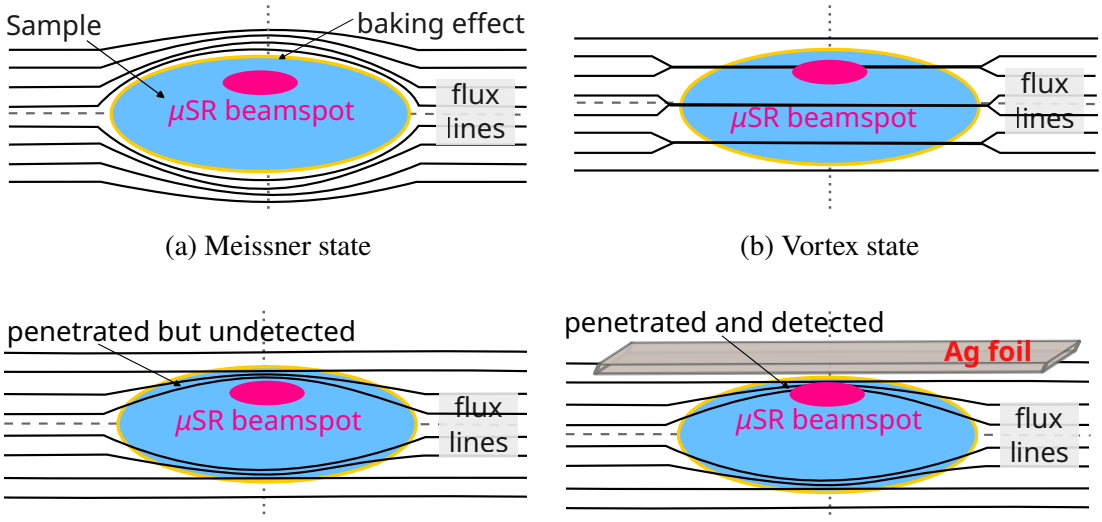

(a) Meissner state

(b) Vortex state

(c) Vortex state with (undetected) pinning

(d) Vortex state with (detected) pinning

Figure 5.1: Sketch of the present μSR experiment on superconducting Nb samples with ellipsoidal shape in an applied magnetic field parallel to the ellipsoid major axis (- - -), with the magnetic flux lines (—) also indicated. (**a**): In the Meissner state, complete flux expulsion from the ellipsoid's interior is achieved. Without any energy moderation for the μ^+ beam, the magnetic probes stop well-below the sample surface and experience no external contribution to their local field. (**b**): In the vortex state, some magnetic flux penetrates the sample as quantized fluxoids with a field-depended lattice arrangement, leading to a broad local field distribution samples by the μ^+ beamspot. (**c**): In the presence of strong near-surface pinning in the vortex state, fluxoid penetration is localized to the sample surface, which may go undetected by the implanted μ^+ at full beam energy. (**d**): Through the use of thin Ag foils as energy moderators for the μ^+ beam, the μ^+ probes stop closer to the surface, allowing for flux that is surface-pinned in the vortex state to be observed.

the thickness of the foils, the range of implanted μ^+ in the Nb samples can be controlled on the μm scale. Simulations of the moderating effect were performed using the Stopping and Range of Ions in Matter (SRIM) Monte Carlo code [183], which incorporated all major materials along the beam's path (e.g., muon counters, moderator foils, etc.—see Figure 5.2), as well as compound corrections [213] to the stopping powers (where appropriate). Typical μ^+ stopping profiles for this setup are shown in Figure 5.3, showing mean stopping ranges $\langle z \rangle$ between ~36 μm to ~108 μm for a Nb target, along with the width (i.e., standard deviation) σ_z of the stopping distributions.[1] Note that similar simulations for Nb_3Sn(2 μm)/Nb samples

[1]Note that the mean stopping depth $\langle z \rangle$ is often used as a proxy for the full μ^+ stopping distribution.

(not shown) yielded virtually identical results. In cases where a 60 μm Ag foil was used, a small fraction (~2 %) of the implanted probes stop in the inner μ^+ counter, located immediately upstream of the sample (see Figure 5.2).

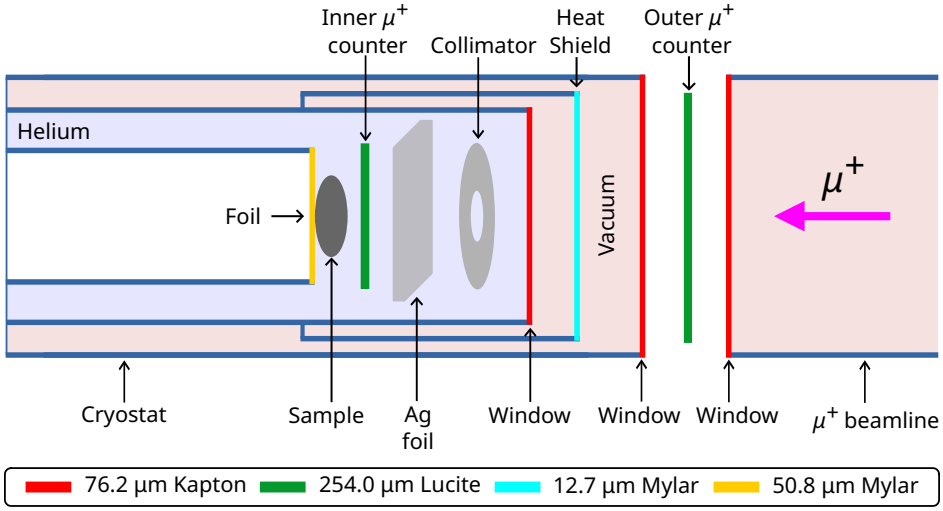

Figure 5.2: Schematic of the horizontal gas-flow cryostat and low-background (i.e., Knight shift) insert used with TRIUMF's high parallel-field (i.e., "HodgePodge") spectrometer [139]. The thin Ag foils used as μ^+ energy moderators are located between a 8 mm diameter beam collimator (also made of Ag) and the inner μ^+ counter.

In μSR, the implanted μ^+ spin probes (spin $S = 1/2$, gyromagnetic ratio $\gamma/(2\pi) = 135.54\,\mathrm{MHz\,T^{-1}}$, lifetime $\tau_\mu = 2.197\,\mu\mathrm{s}$) are sensitive to the local magnetic field at their stopping sites, with the temporal evolution of the ensemble's spin-polarization monitored via the anisotropic property of radioactive β-decay. Specifically, each μ^+ decay positron's emission direction is statistically correlated with the μ^+ spin direction at the moment of decay, providing an easy means of tracking spin-reorientation. Specifically, in a two-detector setup like that used here (see Figure 5.2), the recorded histogram of decay events takes the form of Equation (4.26), where $\pm$ denotes each detector, t is the time (in μs) after implantation, $N_{\pm,0}$ and $b_\pm$ denote the rate of "good" and "background" decay events, $P(t)$ is $P_\mu(t) \in [-1, +1]$ is the muon spin-polarization, and A_0 is a proportionality constant (~0.2 here). The most essential part of Equation (4.26) is $A_0 P_\mu(t)$ and it may be obtained directly by taking the *asymmetry* of two counters using Equa-

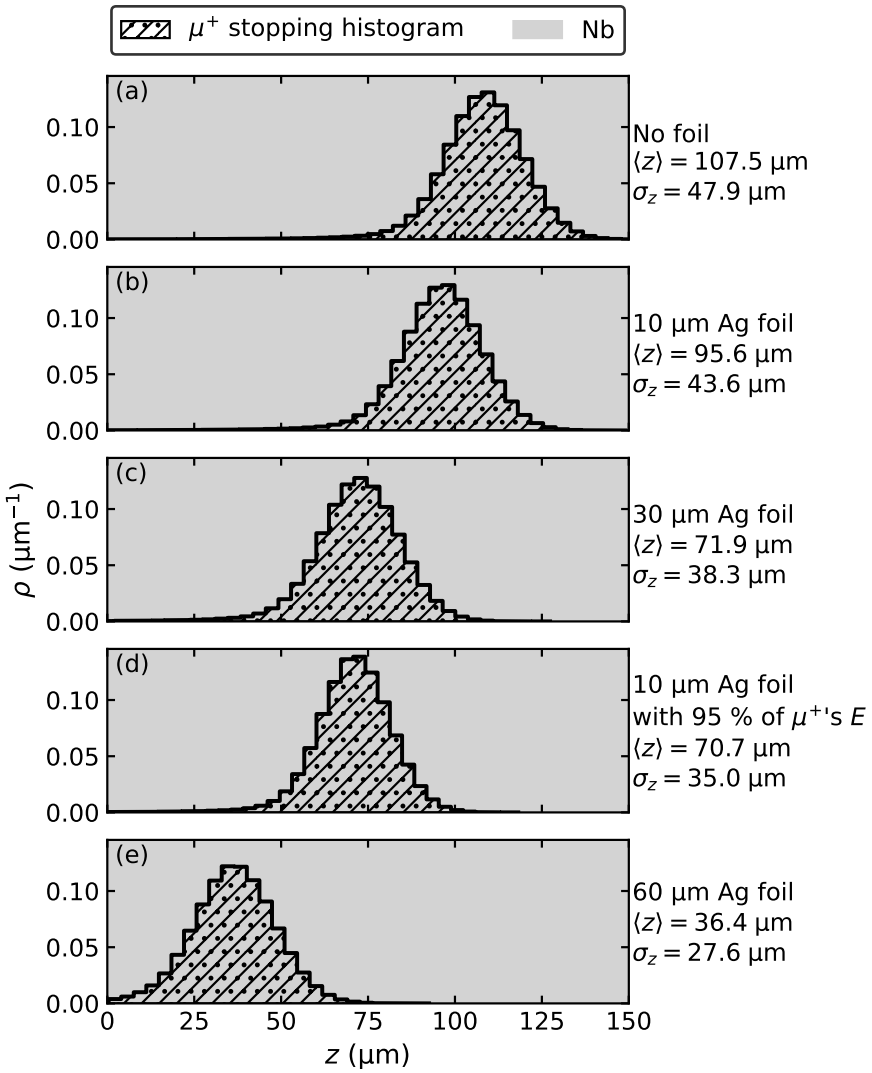

Figure 5.3: Simulated stopping profiles for ~4.1 MeV "surface" μ^+ implanted in Nb using the SRIM Monte Carlo code [183]. The profiles, represented here as histograms, were generated from 10^6 μ^+ projectiles and account for all materials in the beam's path prior to implantation (e.g., cryostat windows, μ^+ counters, moderating foils, etc. — see Figure 5.2). Using Ag foils of different thicknesses (indicated in each plot's inset), mean stopping depths $\langle z \rangle$ in the range of ~36 µm to ~108 µm are achieved. The width (i.e., standard deviation) σ_z of each stopping distribution is also indicated. Note that a reduced μ^+ implantation energy is used for panel (d), yielding a $\langle z \rangle$ comparable to using a thicker moderating foil, as shown in panel (c).

tion (4.25), where $\alpha \equiv N_{+,0}/N_{-,0}$ accounts for imperfections in the detector pair (e.g., different efficiencies, effective solid angles, etc.). Important for this work is the temporal evolution of $P_\mu(t)$, which contains all information about the local

magnetic environment below the sample's surface (i.e., at the μ^+ stopping site). Fortunately, $P_\mu(t)$ differs in each of Nb's superconducting states, allowing us to quantify their volume fraction for our set of measurement conditions.

For the simplest case of Nb's normal state, where magnetic flux penetrates the sample's surface freely, the μSR signal follows that of a typical transverse-field measurement i.e., Equation (4.38) [158], where t is the time after implantation, σ is the damping rate (from a Gaussian field distribution), applied magnetic field ($\mu_0 H_0$) is magnetic field at the μ^+ stopping site (dominated by the external applied field), and ϕ is a phase factor. In non-superconducting Nb, the term $\sigma \approx 0.5\,\mu\text{s}^{-1}$ [9, 132, 133], causing minimal damping. Conversely, in Nb's vortex state, where fluxoids form a periodic arrangement with a broad distribution [70, 82], σ is much larger and the signal is damped quickly (i.e., within the first $\sim$0.3 µs following implantation). In the opposite limit of Nb's Meissner state, where all magnetic flux is expelled from the sample's interior, the signal follows that of a so-called dynamic zero-field Kubo-Toyabe function [162] i.e., Equation (4.35), which is obtained from a static Kubo-Toyabe function by Equation (4.30) [161], where the local field is fluctuating (e.g., from stochastic site-to-site "hopping" of μ^+ [214]) at a rate ν, typically $\sim$0.7 μs^{-1} for SRF Nb [9, 215]. Note that both Equations (4.30) and (4.35) assume the local field distribution at the μ^+ stopping site to be Gaussian, in accord with related studies [9, 132, 133, 215].

For the present experiments, the μSR signal is, in general, described by a superposition of Equations (4.35) and (4.38), which may be written as:

$$P_\mu(t) = f_{\text{ZF}} P_{\text{DGKT}}(t) + (1 - f_{\text{ZF}}) \sum_i f_{\text{TF},i} P_{\text{GTF},i}(t), \tag{5.1}$$

where $f_{\text{ZF}} \in [0, 1]$ denotes the volume fraction of the zero-field component, which for superconducting Nb in an applied field corresponds to its Meissner state, and $f_{\text{TF},i} \in [0, 1]$ represents the individual transverse-field components (e.g., normal

state, vortex state, etc.), subject to the constraint that $\sum_i f_{\mathrm{TF},i} \equiv 1$. Examples of this type of composite signal are shown in Figure 5.4.

In order to identify the $\mu_0 H_{\mathrm{vp}}$ in each sample, the evolution of f_{ZF} in (monotonically increasing) magnetic fields $\mu_0 H_0$ up to ~260 mT was measured at the cryostat's base temperature ($T \approx 2.7$ K) following zero-field cooling. Any depth-dependence was inferred from repeat measurements using different moderator foil thicknesses (and μ^+ beam energies). Note that, to ensure the accuracy of the applied fields reported for all superconducting states (i.e., due to its geometric enhancement from flux-expulsion), all values were derived from field calibration measurements conducted above T_{c} (i.e., at $T \geq 10.5$ K for the LTB Nb and $T \geq 20$ K for the SS bilayer), where the μSR signal simply follows Equation (4.38). Specifically, they were corrected using [216]:

$$\mu_0 H_0 = \mu_0 H_0^{\mathrm{NS}} \times \frac{1}{1-N}, \tag{5.2}$$

where $\mu_0 H_0^{\mathrm{NS}}$ is the (measured) applied field in the normal state and $N \approx 0.13$ [132, 133] is the demagnetization factor for our samples (see Section 5.2.1).

5.2.1 Samples

The samples used in this study are identical to those employed in previous μSR measurements on the first-flux-penetration field [132, 133]. For completeness, we briefly restate their preparation details below.

Each Nb sample was cut from fine-grain Nb (Wah Chang Corporation) stock sheets with a residual-resistivity ratio (RRR) >150[2] and machined into prolate ellipsoids with a semi-major radius 22.9 mm and semi-minor radii 9.0 mm for the other axes. After machining, the samples underwent buffered chemical polishing (BCP) to remove the surface's topmost 100 µm of the material (see, e.g., [217]).

[2]The RRR of the Nb stock (> 150) is lower than that typically specified for TESLA [17] cavities (≥ 300). Possible contributions to the reduced RRR, including the role of interstitial and metallic impurities, are discussed in detail in Section 9.2.

For one of the samples, a typical LTB "recipe" was followed where, after degassing in vacuum at 800 °C for 4 h, the Nb ellipsoid was baked in vacuum at 120 °C for 48 h [11]. A complementary magnetostatic characterization of the LTB sample can also be found elsewhere [47]. Microstructure analysis was conducted on identically prepared flat "witness" samples using scanning electron microscope (SEM)/energy dispersive X-ray spectroscopy (EDX) and secondary ion mass spectrometry (SIMS). The SEM/EDX analysis revealed no unexpected features or contaminations beyond typical observations for high-RRR Nb exposed to air [218]. SIMS confirmed the expected increase in near-surface oxygen concentration following LTB for depths <20 nm, in accord with models for oxygen diffusion [219–221]. For another sample, a 2 µm Nb_3Sn surface coating was applied using a vapour diffusion [222, 223] procedure developed at Cornell University [106, 107]. SEM and atomic force microscopy (AFM) measurements on identically prepared "witness" samples revealed that the as-grown Nb_3Sn exhibits surface roughness comparable to their grain size, typically in the µm range [212]. Further tests on substrates prepared using different polishing techniques had no effect on the bilayer's surface roughness [224].

5.3 Results

Figure 5.4 depicts typical time-differential μSR data in one of our samples (LTB Nb [11]), showing the contrast in signals for different material states. In the normal state, where the local field at the μ^+ stopping sites is dominated by the (transverse) $\mu_0 H_0$, coherent spin-precession is observed with minimal damping, consistent with a narrow field distribution. By contrast, in the Meissner state, $\mu_0 H_0$ is completely screened[3] and the local field is dominated, in part, by Nb's 100 % abundant ^{93}Nb nuclear spins, resulting in the characteristic (dynamic) "zero-field"

[3] The range of implanted μ^+ greatly exceeds Nb's London penetration depth (~29 nm [145]), leading to the absence of magnetic flux density for depths greater than ~100 nm.

signal [162]. At applied fields just above the vortex penetration field $\mu_0 H_{\mathrm{vp}}$, a mixed signal with both zero- and transverse-field components is observed, the latter being strongly damped. As the field is further increased beyond $\mu_0 H_{\mathrm{vp}}$, the sample fully enters a vortex state, where the signal resembles that of the normal state, but the broad field distribution from the vortex lattice causes strong damping of the spin-polarization. Similar behavior is observed at other implantation ranges, as well as in the Nb_3Sn(2 μm)/Nb sample (not shown). In line with the experiment's description in Section 5.2, these observations can be quantified through fits to Equation (5.1), yielding good agreement with the data in all cases (typical reduced-$\chi^2 \approx 1.07$). A subset of the fit results are shown in Figure 5.4.

To aid in identifying $\mu_0 H_{\mathrm{vp}}$ and its depth-dependence, we plot the measured f_{ZF}s vs. $\mu_0 H_0$ for each Nb sample in Figure 5.5. The resulting "curves" all have a sigmoid-like shape, where $f_{\mathrm{ZF}} = 1$ for $\mu_0 H_0 < \mu_0 H_{\mathrm{vp}}$, with f_{ZF} decreasing rapidly towards zero once $\mu_0 H_0 \geq \mu_0 H_{\mathrm{vp}}$. This behavior is phenomenologically captured by a logistic function:

$$f_{\mathrm{ZF}}(\mu_0 H_0) \approx \frac{f_0}{\exp\left[-k\left(\mu_0 H_0 - \mu_0 H_{\mathrm{m}}\right)\right] + 1}, \tag{5.3}$$

where f_0 is the curve's height, k denotes the "steepness" of the transition, and $\mu_0 H_{\mathrm{m}}$ represents its midpoint. Fits of the measured volume fractions to Equation (5.3) are shown in Figure 5.5 as guides to the eye.

It is clear from Figure 5.5 that $\mu_0 H_{\mathrm{vp}}$'s depth-dependence is quite different for LTB and coated Nb. In the LTB sample, flux-penetration is detected just above Nb's $\mu_0 H_{\mathrm{c1}}$, with the onset pushed to higher $\mu_0 H_0$s for larger μ^+ ranges. Similarly, the field span of this "transition" (i.e., going from zero- to full-flux-penetration) also increases slightly deeper below the surface. By contrast, in the Nb_3Sn(2 μm)/Nb, first-flux-penetration onsets close to Nb's $\mu_0 H_{\mathrm{sh}}$, with this value and the transition's width both virtually unaffected by μ^+'s proximity to the sample's surface. Qualitatively, this disparity between the Nb treatments indicates

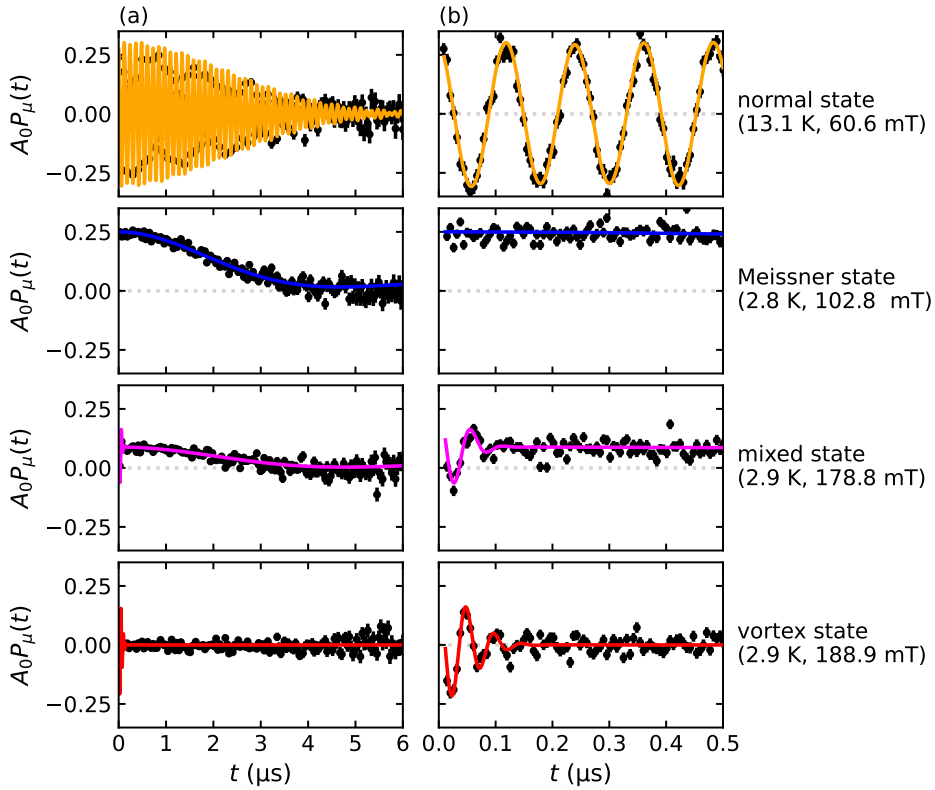

Figure 5.4: Typical μSR data in surface-treated Nb, illustrating the evolution with applied magnetic field $\mu_0 H_0$. Both panels **(a)** and **(b)** display the same dataset; however, **(b)** specifically represents the initial 0.5 μs. The temperature T and $\mu_0 H_0$ for each superconducting state are detailed in the panel's inset. The solid lines are fits to the data points using Equation (5.1). In the normal state, coherent spin-precession is observed with minimal damping, consistent with a narrow local field distribution. In the Meissner state, the applied field is completely screened and the local field is dominated by the host's ^{93}Nb nuclear spin, resulting in the characteristic (dynamic) "zero-field" signal. At fields just above the vortex penetration field, a mixed signal with both zero- and transverse-field components is observed, the latter being strongly damped. Finally, in the vortex state, the broad field distribution causes strong damping of the transverse-field response.

that different mechanisms are likely responsible for determining each sample's $\mu_0 H_{\mathrm{vp}}$.

To quantify these differences explicitly, we use a non-parametric approach to identify $\mu_0 H_{\mathrm{vp}}$ for each "curve" in Figure 5.5. Noting that each f_{ZF} has a statistical uncertainty of ∼4 % (determined from fitting), we define $\mu_0 H_{\mathrm{vp}}$ to correspond to the applied field where $f_{\mathrm{ZF}} \leq 0.96$ (i.e., the very onset of flux-penetration). Due to the finite "sampling" of our measurements, this field is estimated as midpoint

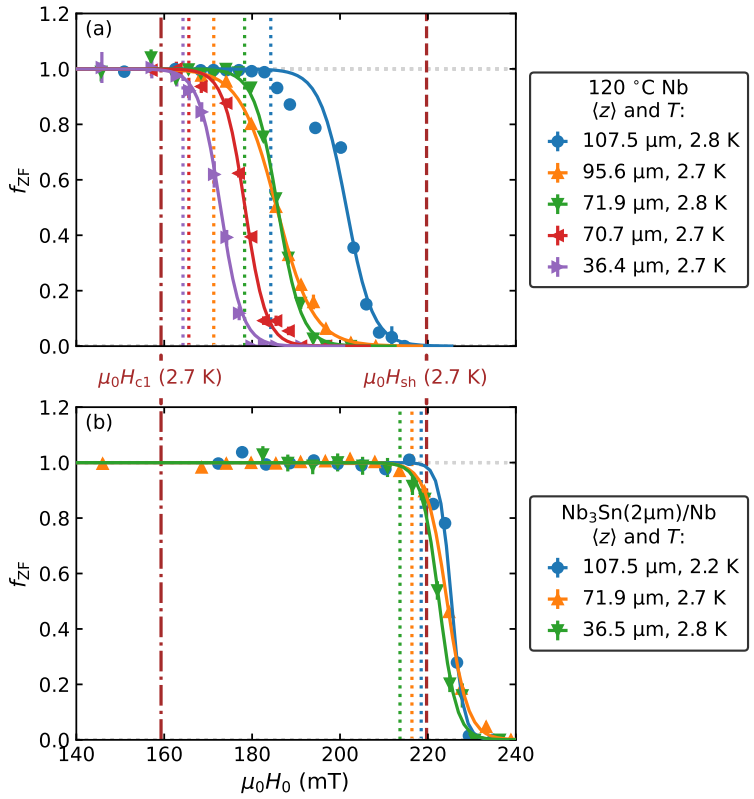

Figure 5.5: Volume fraction of the zero-field μSR signal f_{ZF} at different applied magnetic field $\mu_0 H_0$ and mean μ^+ implantation depths $\langle z \rangle$. The $\langle z \rangle$ and measurements temperature T are mentioned in the figure's inset. The solid colored lines denotes fits to a logistic function, intended to guide the eye. The $\mu_0 H_{vp}$ at each $\langle z \rangle$ are shown using colored dotted vertical lines. Vertical dotted-dashed and dashed brown lines are included to mark Nb's lower critical field $\mu_0 H_{c1}$ and superheating field $\mu_0 H_{sh}$ at 2.7 K. Note that Nb_3Sn has a considerably smaller $\mu_0 H_{c1} = 25.0(14)$ mT [119] compared to the fields shown here. **(a)**: In LTB Nb, the vortex penetration field $\mu_0 H_{vp}$ is comparable to $\mu_0 H_{c1}$, but shows a strong $\langle z \rangle$-dependence, increasing with increasing $\langle z \rangle$. **(b)**: In Nb_3Sn(2 µm)/Nb, $\mu_0 H_{vp}$ is $\langle z \rangle$-independent and close to $\mu_0 H_{sh}$.

between the pair of f_{ZF}s on either side of the threshold criteria.[4] These values are marked graphically in Figure 5.5 by vertical dotted colored lines. Similarly, we take the width of the zero- to full-flux-penetration "transition" Δ_{vp} to be the field range where $4\,\% \leq f_{ZF} \leq 96\,\%$. To correct for any influence from the finite span of the μ^+ stopping profile we additionally normalize the Δ_{vp}s by the width

[4]While simple, this approach introduces an additional systematic uncertainty to the assignment of $\mu_0 H_{vp}$. We estimate this quantity as one-sixth the distance between the field points, such that ±3 standard deviations covers the full span of the "uncertain" region with ~100 % probability.

σ_z of the implantation distribution, which varies for different beam implantation conditions (see Figure 5.3). For each of our samples, the dependence of both $\mu_0 H_{\rm vp}$ and $\Delta_{\rm vp}/\sigma_z$ on the implanted μ^+ range $\langle z \rangle$ is shown in Figure 5.6. For comparison, measured values for additional surface-treated samples [132, 133] have also been included.[5] Lastly, to facilitate comparison between the measured $\mu_0 H_{\rm vp}$s, we correct for minor temperature differences and extrapolate our values to 0 K using the empirical relation by Equation (2.40), but for $\mu_0 H_{\rm vp}(T)$, where T is the absolute temperature, $T_{\rm c} \approx 9.25$ K is Nb's critical temperature [7], and $\mu_0 H_{\rm vp}(0\,{\rm K})$ is the value at absolute zero.

5.4 Discussion

Consistent with our main observations in Figure 5.5 for the vortex penetration field, Figure 5.6(a) shows that $\mu_0 H_{\rm vp}$s in Nb_3Sn(2 μm)/Nb (extrapolated to 0 K) remain depth-independent with an average value of 234.5(35) mT, in excellent agreement with Nb's $\mu_0 H_{\rm sh}(0\,{\rm K}) \approx 240$ mT [119, 133]. That the flux penetration occurs in such close proximity to the superheating field is strong evidence for the presence of an interface barrier at the SS boundary, similar to a Bean-Livingston (BL) surface energy barrier [24], as anticipated by the theoretical framework for superconducting multilayers [18, 21]. Conversely, in LTB Nb the $\mu_0 H_{\rm vp}$s are much lower, remaining close to (but slightly above) $\mu_0 H_{\rm c1}$ for all measurements. In this case, however, a modest depth-dependence is observed, with $\mu_0 H_{\rm vp}$ increasing gradually with increasing $\langle z \rangle$. That these details coincide is significant, as it sets LTB apart from other surface treatments, where flux-penetration occurs at Nb's lower critical field. We note that, though small, the observation of such a depth-dependence is inconsistent with a surface energy barrier being solely responsible for pushing

[5] To ensure the self-consistency of our $\mu_0 H_{\rm vp}$ comparison in Figure 5.6, following the approach described in Section 5.2, we re-analyzed the raw μSR data for select samples originally reported in Refs. [132, 133]. As anticipated, our updated values are in good agreement with those in the original reports.

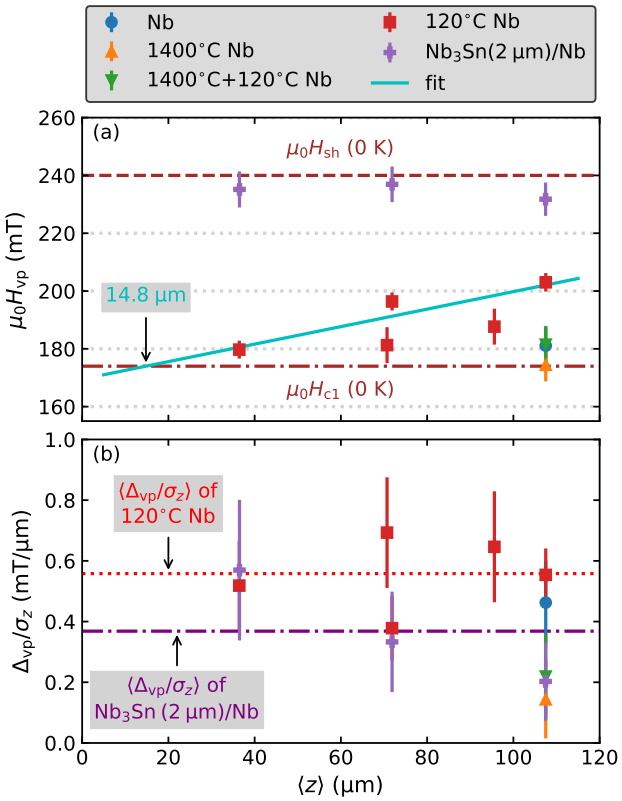

Figure 5.6: Summary of the first-flux penetration measurements at different mean μ^+ implantation depths $\langle z \rangle$ for LTB Nb and Nb_3Sn(2 µm)/Nb. For comparison, we include re-analyzed results for additional SRF Nb treatments (originally reported elsewhere [132, 133]). **(a)**: Measured vortex penetration fields $\mu_0 H_{vp}$. The horizontal dashed and dotted-dashed brown lines denote Nb's superheating field $\mu_0 H_{sh}$ and lower critical field $\mu_0 H_{c1}$, respectively. In Nb_3Sn(2 µm)/Nb, $\mu_0 H_{vp}$ is $\langle z \rangle$-independent and close to $\mu_0 H_{sh}$, whereas $\mu_0 H_{vp} \approx \mu_0 H_{c1}$ in LTB Nb, increasing modestly with increasing $\langle z \rangle$. The other surface-treatments have $\mu_0 H_{vp}$s that are similarly close to $\mu_0 H_{c1}$. The cyan color solid line represents the "straight line" fit applied to the LTB data, providing an estimate of the depth where $\mu_0 H_{vp} = \mu_0 H_{c1}$. **(b)**: Measured Meissner-vortex transition "widths" $\Delta\mu_0 H_{vp}$, divided by σ_z, confirm that the stopping distributions are not significantly different. The dotted and dash-dotted horizontal lines are the average values of Δ_{vp}/σ_z, $\langle \Delta_{vp}/\sigma_z \rangle$ for LTB and Nb_3Sn(2 µm)/Nb samples, respectively.

$\mu_0 H_{vp} > \mu_0 H_{c1}$.[6] An alternative possibility is the presence of pinnning centers localized near LTB Nb's surface, which has been suggested previously [47, 132]. In such a case, $\mu_0 H_{vp}$ closely approximates $\mu_0 H_{c1}$ due to the presence of pinning,

[6] A similar argument can be made for the Nb_3Sn(2 µm)/Nb sample (i.e., that flux pinning — particularly from the thin Nb_3Sn layer — may contribute to the increased $\mu_0 H_{vp}$ we observe). We point out, however, that the observed lack of depth-dependence in our data, along with the magnitude in which $\mu_0 H_{vp}$ exceeds Nb's $\mu_0 H_{c1}$, suggest that pinning is not the dominant mechanism for elevating the vortex penetration field in the SS bilayer.

which diminishes towards the sample's center, resulting in delayed flux penetration (i.e., the pinning centers act as supplemental flux "blockades," providing resistance to the free motion of the fluxoids, which would otherwise uniformly distribute throughout the sample) [132]. Independent of the mechanistic details, from our data we identify the length scale over which flux-penetration is retarded. Using a simple linear fit to the measured values, we find that $\mu_0 H_{\mathrm{vp}} \approx \mu_0 H_{\mathrm{c1}}$ at a mean depth of $\sim$14 µm, characterizing the distance in which it is delayed for our sample geometry. Note that, there is a significant proportion of muons that stop significantly closer to the surface at this average depth. We shall return the implications of this quantity later on.

Further insight into the flux-penetration mechanism for the LTB and SS samples can be gleaned from the (normalized) flux-entry "transition" widths $\Delta_{\mathrm{vp}}/\sigma_z$, which are shown in Figure 5.6(b). The span from first- to full-flux penetration provides a measure for the "haste" in which vortices nucleate through the probe μ^+ stopping depths where, in the presence of near-surface pinning, we expect that the Meissner-vortex transition becomes "extended" to a larger range of applied fields (i.e., the presence of pinning centers delays full-flux penetration). Thus, we suggest that $\Delta_{\mathrm{vp}}/\sigma_z$ serves as a proxy for each treatment's pinning strength. Indeed, we observe that the values for LTB Nb are all similar, which also suggests that the pinning strength appears to be depth-independent and exceeds the values of all other surface preparations shown in Figure 5.6. However, given the relatively large uncertainty in each measurement, drawing firm conclusions about treatment-specific differences is challenging. This is clear from their average values, which turned out to be 0.56(15) mT/µm (for LTB) and 0.37(18) mT/µm (for Nb_3Sn(2 µm)/Nb), respectively. Interestingly, both quantities are comparable to that of Nb in the absence of any treatment (0.46(14) mT/µm), which is larger than both the values obtained for 1400 °C annealing (0.14(13) mT/µm), as well as 1400 °C annealing + 120 °C LTB (0.22(14) mT/µm). We note that, in line with our expectations

for Δ_{vp}/σ_z, its value is minimized for the 1400 °C treatment, which is known to release virtually all pinning [132]. Thus, although not as conclusive as the $\mu_0 H_{vp}$ measurements, the large values for LTB insinuate that pinning is strongest for this treatment. With these results in mind, we will explore their implications in the remaining discussion.

First, we consider the SS bilayer Nb_3Sn(2 µm)/Nb, whose high $\mu_0 H_{vp}$ is favorable for technical applications requiring operation in a flux-free state (e.g., SRF cavities). In fact, direct current (DC) measurements of first-flux-penetration using a Hall probe magnetometer on a 1.3 GHz single-cell SRF cavity of similar composition are in good agreement with our result [119], with similar $\mu_0 H_{vp}$ values reported for surface coatings other than Nb_3Sn, such as hybrid physical chemical vapour deposition (HPCVD) MgB_2 [133]. The combination of our work and related studies [119, 132, 133] provides compelling evidence for the use of SS bilayers as an empirical means for increasing $\mu_0 H_{vp}$, consistent with earlier observations using μSR [132, 133]. For further insight into why such a treatment is so effective at enhancing $\mu_0 H_{vp}$, we must consider the theory of superconducting multilayers (see, e.g., [18]), which we shall briefly outline below.

In bilayer superconductors, by analogy with the BL barrier at the surface of "bulk" superconductors [24], the discontinuity in each material's (coupled) electromagnetic response at the SS interface is responsible for creating a second (subsurface) barrier that impedes flux penetration [21]. Specifically, electromagnetic continuity across the SS boundary creates a "coupling" between the layer's properties, leading to marked deviations from the lone material's native behavior when the surface layer penetration depth is larger than the substrate. Microscopically, this is predicted to manifest in the heterostructure's Meissner screening profile with a distinct bipartite form [21], which was recently confirmed experimentally for $Nb_{1-x}Ti_xN$(50 nm to 160 nm)/Nb samples [5]. A weaker Meissner screening current is observed, which, as a corollary, provides enhanced protection against

flux nucleation (see, e.g., [18]). While the $\mu_0 H_{\mathrm{vp}} \approx \mu_0 H_{\mathrm{sh}}$ we observe is in good agreement with this prediction, the theory also suggests that $\mu_0 H_{\mathrm{vp}}$ can be improved further still through optimizing the Nb_3Sn coating's thickness. This enhancement is achievable by ensuring a flux-free surface layer and enabling superheating in both the surface and substrate layers. Achieving this involves precise adjustments to the thickness of the surface layer and the presence of an interface barrier at the SS boundary for the substrate layer. For an SS structure, the optimum thickness of the surface layer $d_{\mathrm{s}}^{\mathrm{opt}}$ is defined by Equation (3.17) [18]: where λ_i and H_{sh}^{i} denote the magnetic penetration depth and superheating field for the surface (i = s) and substrate (i = sub) layers. Using literature values for these quantities ($\lambda_{\mathrm{Nb_3Sn}} = 173(32)\,\mathrm{nm}$ [99, 119]; $B_{\mathrm{sh}}^{\mathrm{Nb_3Sn}} = 430(110)\,\mathrm{mT}$ [99, 119]; $\lambda_{\mathrm{Nb}} = 29.01(10)\,\mathrm{nm}$ [145]; and $B_{\mathrm{sh}}^{\mathrm{Nb}} = 237(29)\,\mathrm{mT}$ [119, 133]), Equation (3.17) yields $d_{\mathrm{s}}^{\mathrm{opt}} = 210(60)\,\mathrm{nm}$ or, equivalently, $\sim 1.2\lambda_{\mathrm{Nb_3Sn}}$. Similar predictions have been made for $Nb_{1-x}Ti_xN$/Nb [5]. It would be interesting to test these explicitly, for example, using the experimental formalism employed in this work. Investigating this phenomena in closely related superconductor-insulator-superconductor (SIS) heterostructures would also be fruitful, as they offer similar means of enhancing $\mu_0 H_{\mathrm{vp}}$ [18].

As a close to our discussion of the Nb_3Sn/Nb bilayer, it is interesting to consider its synthesis. We note that in our sample, as is common for heterostructures prepared by thermal diffusion, the composition of the Nb_3Sn/Nb interface deviates appreciably from each layer's respective "bulk" [212, 225]. Specifically, within the first few hundred nanometers from the heterojunction, a localized Sn deficiency (enhancement) is present in the Nb_3Sn (Nb) layers, with the former known to lower Nb_3Sn's T_{c}, making the region a poor superconductor [212, 225]. The presence of such inhomogeneities, however, do not meaningfully impact $\mu_0 H_{\mathrm{vp}}$, as indicated by it's agreement with Nb's $\mu_0 H_{\mathrm{sh}}$. Testing the extent in which this remains true, for example, on samples with extended defect regions, would be interesting. Similarly,

these nanoscale inhomogeneities at the SS interface could be examined directly using a depth-resolved technique such as LE-μSR [192, 205], with the caveat that the Nb_3Sn layer thickness must be compatible with the technique's spatial sensitivity (i.e., subsurface depths typically <150 nm). Finally, given the presence of a secondary energy barrier at the SS interface, we suggest that incorporating SS bilayers into SRF cavity structures holds great promise for surpassing the inherent limitations of current Nb cavity technology (i.e., enabling higher accelerating gradients and enhanced performance in particle accelerators).

We now turn our attention to the 120 °C LTB treatment [11], which is well-known in SRF applications for its ability to alleviate the so-called high field Q slope (HFQS) "problem" [2, 10], where a rapid decrease in a cavity's quality factor (Q_0) occurs as the peak surface magnetic field exceeds ~100 mT.[7] True to this fashion, our finding of $\mu_0 H_{\mathrm{vp}}$s in excess of Nb's $\mu_0 H_{\mathrm{c1}}$ underscores its utility in this domain; however, the treatment's depth-dependent $\mu_0 H_{\mathrm{vp}}$ and relatively large $\Delta_{\mathrm{vp}}/\sigma_z$ make it unique among the comparison treatments reported here. As mentioned above, near-surface pinning of the flux-lines provides the most likely explanation for these facts. The observed delay in flux-penetration would then arise from the pinning centers acting as "supplementary barriers," impeding the movement of vortices from the edges of the sample to the center [132]. The relatively large Meissner-vortex transition "widths" observed here also support this interpretation. It has been suggested by others that material inhomogeneities, such as interstitial oxygen or hydrogen precipitates, may dominate the pinning mechanism [226]. For further insight into the matter, it is instructive to consider some of the treatment's finer details, which we do below.

During LTB, the heat treatment induces changes to Nb's superfluid density in its outermost nanoscale region through the dissolution and diffusion of oxygen

[7] Note that, in regards to HFQS mitigation, the most effective LTB treatments generally include an electropolishing (EP) step in place of the BCP used in this work.

originating from the metal's native surface oxide [11].[8] This alteration is believed to result in a "dirty" region localized near Nb's surface (i.e., the first ∼50 nm), as explained by an oxygen diffusion model [219]. This length scale aligns well other work, including an experiment that used repeat hydrofluoric HF "rinses" to remove the topmost ∼50 nm and (essentially) restore the HFQS following LTB [230]. Similarly, an increase of the ratio of the upper and surface critical fields after baking was explained by the presence of an impurity layer of thickness smaller than Nb's coherence length [231], which is of similar magnitude. Other work on related treatments have also found similar results [221, 232], and the first ∼10 nm may be particularly enriched with interstitial oxygen [233]. It has been suggested that the LTB effect (i.e., HFQS mitigation) is due to the strong suppression of hydride precipitation [102], as oxygen efficiently traps interstitial (or "free") hydrogen that has accumulated during standard chemical treatments, such as BCP or EP [102, 232, 234]. Indeed, LTB has been linked to changes in the vacancy structure in Nb's near-surface region [235, 236], supporting the prevailing idea that nanoscale niobium hydrides cause the HFQS [102]. These works all point to the importance of surface defects, especially those closest to the surface.

Within the ∼50 nm "dirty" region, it is expected that quantities sensitive to the density of (nonmagnetic) scattering centers (e.g., the carrier mean-free-path, the magnetic penetration depth, etc.) be altered from their (clean-limit) "bulk" values. As the doping is likely inhomogeneous over this length scale, a similar character may be imparted on dependent quantities. Early experimental results seemed to favor this possibility [206], with other authors suggesting a strong likeness of LTB Nb to an "effective" SS bilayer [18]. Subsequent experiments, however, have shown that such a distinction is far from clear, with both a recent a commentary [209] and a separate LE-μSR experiment [145] showing that the

[8] The microscopic mechanisms underlying these changes remain an active topic of investigation. Proposed explanations include limited oxygen diffusion at 120 °C, reorganization of the metal–oxide interface, and the formation or dissociation of suboxide phases; see Refs. [227–229].

effects are homogeneous over subsurface depths spanning ∼10 nm to ∼160 nm. Such a finding was rather surprising, given the aforementioned related work [219, 230, 231] and that doping from the closely related nitrogen infusion treatment [13] yields inhomogeneous superconducting properties over the same length scale [208]. We point out, however, that the observed electromagnetic response for LTB [145, 209] is consistent with the absence of an interface energy barrier preventing flux-penetration [207, 208], in line with our present findings.

As alluded above, the "dirty" nature of LTB provides an ample environment for pinning centers, which can serve as seeds for flux penetration. While other experiments are clear on their surface proximity, their ∼50 nm localization is quite different from the micrometer depth-dependence we observe for $\mu_0 H_{\mathrm{vp}}$, which warrants further consideration. As is shown in Figure 5.6(a), LTB's $\mu_0 H_{\mathrm{vp}}$ varies approximately linearly in $\langle z \rangle$. From a fit to a function of the form

$$\mu_0 H_{\mathrm{vp}}(\langle z \rangle) \approx A + B\langle z \rangle,$$

we parameterize this trend, but postulate that Nb's $\mu_0 H_{\mathrm{c1}}$ acts as the floor for $\mu_0 H_{\mathrm{vp}}$. Upon equating the two relations, we find that $\mu_0 H_{\mathrm{vp}}(\langle z \rangle) \approx \mu_0 H_{\mathrm{c1}}$ when $\langle z \rangle \approx 14\,\mu\mathrm{m}$. Clearly, this scale is considerably larger than the "dirty" region's extent [219, 230, 231]. We argue that, despite the LTB effect being confined to the very near surface, this "layer" could introduce pinning over a µm length scale in an ellipsoidal geometry. This is a consequence of the fact that, even if flux lines penetrate further into the material, they must both enter and exit through the "dirty" region. The pinning strength is directly influenced by the flux line's path length through this volume, which in the case of an ellipsoid is minimized for the straight path along its equator, but maximized for a (curved) trajectory close to the surface (see Figure 5.1). Indeed, magnetometry studies demonstrate that LTB can significantly alter the pinning characteristics in this geometry [47]. We emphasize that an ellipsoidal geometry is the ideal means for probing intrinsic pinning effects,

as opposed to other sample forms (e.g., rectangular prisms) where additional geometric effects are present [216]. In line with the generally accepted view that LTB changes the concentration of pinning centers (i.e., from the redistribution of near-surface defects) [221, 230, 237, 238], our identification of a length scale associated with flux pinning may prove useful in further refining their microscopic distribution. In the future, it would be interesting to use this finding as a constraint for simulations of flux-entry in ellipsoidal geometries (see, e.g., Ref. [239]).

In terms of SRF cavity performance, it is important to highlight that our investigation on the LTB "dirty" layer cannot explain situations where cavities in radio frequency (RF) operation exhibit $\mu_0 H_{\mathrm{vp}}$s above $\mu_0 H_{\mathrm{c1}}$, reaching values as high as ~190 mT [226, 240], equivalent to accelerating gradients of ~45 MV m^{-1} [2]. Recall that, if the Meissner state of any (type-II) material persists above $\mu_0 H_{\mathrm{c1}}$, it must do so in a *metastable* state. For DC fields, flux penetration can only be prevented by an energy barrier [24], generally anticipated for defect-free surfaces. From the delineations above, it is clear that LTB results in surfaces that are anything but defect-free and any prospect for achieving such high $\mu_0 H_{\mathrm{vp}}$ fields during RF operation depends on the interplay between the time needed for the vortex core formation and the RF period. In such cases, maintaining a flux-free state above $\mu_0 H_{\mathrm{c1}}$ necessitates the time required for vortex penetration to exceed the operating RF period (i.e., the inverse RF frequency) of the cavity [85]. Comparing this study with $\mu_0 H_{\mathrm{vp}} \sim 190$ mT [226, 240], we suggest that LTB cavities need a longer flux nucleation time than the RF period to sustain the Meissner state. Alternatively, SS bilayers can maintain that up to its $\mu_0 H_{\mathrm{vp}} \sim 235$ mT, even in the DC flux penetration case, offering a more robust approach for achieving higher accelerating gradients than LTB.

Considering the above details, it is apparent that LTB Nb differs fundamentally from that of an SS bilayer in both its composition and mechanism for impeding flux entry. Concerning the latter, our present findings, in conjunction with related

work [47, 132], support the notion that LTB does not create a supplemental energy barrier, but instead postpones vortex penetration above $\mu_0 H_{c1}$ due to pinning. While it remains an open question as to if this behavior could be further engineered to benefit SRF applications, it is apparent that careful control over the near-surface doping is crucial. Advances in this area are already apparent [221]. In future work, it would be interesting to test these ideas on related LTB treatments [12–14], as well as the recently discovered "mid-T" treatments that are known to produce very small surface resistances [241, 242].

5.5 Conclusion

Using μSR, we measured the depth-dependence (on the µm scale) of the vortex penetration field in Nb ellipsoids that received either a LTB surface-treatment or a 2 µm coating of Nb_3Sn. In each sample, the measured field of first-flux-entry is greater than Nb's lower critical field of ~170 mT, suggesting their applicability for SRF cavities. In the coated sample, we find a depth-independent $\mu_0 H_{vp}$ = 234.5(35) mT, consistent with Nb's superheating field and the presence of interface energy barrier preventing flux penetration. Conversely, in LTB Nb, its $\mu_0 H_{vp}$ is only moderately larger than Nb's $\mu_0 H_{c1}$, increasing slightly with increasing depths below the surface. The latter observation, in conjunction with the increased span of the Meissner-vortex transition, suggests pinning from surface-localized defects. Our findings confirm that the introduction of a thin superconducting overlayer on Nb can effectively push the onset of vortex penetration up the superheating field, but rules out LTB as a means of achieving this. We suggest that its success is rather due to effects specific to the operation under RF fields, such as the time required for vortex nucleation. These findings validate the potential of employing superconducting bilayers to achieve a flux-free Meissner state up to the superheating field of the substrate.

Chapter 6

Evidence for current suppression in superconductor-superconductor bilayers

6.1 Introduction

A large accelerating gradient (E_{acc}) (i.e., energy gain per unit length) is required for high energy accelerators to limit their length and therefore their cost [1, 10]. Currently, the highest E_{acc} values are achieved using normal conducting radio frequency (RF) cavities, some exceeding $100\,\mathrm{MV\,m^{-1}}$ [243, 244]. In the case of field-emission-free superconducting radio frequency (SRF) cavities, the maximum E_{acc} is proportional to the highest sustainable vortex-free surface magnetic field, which is presently achieved by cavities made from niobium sheets. Some of these cavities have produced E_{acc} values as high as $\approx 49\,\mathrm{MV\,m^{-1}}$ [14], corresponding to surface magnetic fields on the order of $\sim 210\,\mathrm{mT}$, exceeding "clean" Nb's lower critical field (B_{c1}) $\approx 170\,\mathrm{mT}$ at $2\,\mathrm{K}$ [7, 245]. While this achievement is commendable, it remains below the ultimate limit for bulk Nb, which is set by its superheating field (B_{sh}) $\approx 240\,\mathrm{mT}$ [89]. While Nb cavity operating conditions continue to approach this material limit, substantial advances in accelerator technology necessitate finding alternative materials.

6.1.1 SRF materials beyond niobium

One possibility to achieve surface magnetic fields beyond B_{sh} of Nb is to use a different superconducting material with a greater B_{sh} (e.g., Nb_3Sn or $Nb_{1-x}Ti_xN$) [94]; however, there is no viable replacement with a B_{c1} exceeding that of Nb. This is problematic, as all *real* SRF cavities possess both surface defects and topographic imperfections, facilitating vortex penetration below B_{sh}. Vortices that penetrate at these "weak points" often evolve into a thermomagnetic flux avalanche, quenching superconductivity at SRF cavity operating temperatures ($T \lesssim 4\,\mathrm{K}$) [18, 22, 23].

To overcome this, a different approach has been proposed, wherein superconducting *multilayers* are used to push the field of first-flux penetration beyond Nb's intrinsic B_{sh} (see e.g., [18, 20–22]). Gurevich [20] was the first to suggest the use of multilayer structures as a means of preventing thermomagnetic avalanches induced by vortex penetration at defects before they become predominant. The approach is to coat a conventional Nb cavity with several thin superconducting and insulating layers, the simplest version of which is one superconducting and one insulating layer on Nb, referred to as a superconductor-insulator-superconductor (SIS) structure. The insulating layer decouples the superconducting layers and if the layers are thinner than the London penetration depth (λ_{L}) of their material, nucleation of parallel vortices will only become energetically favorable at larger fields than B_{c1} of layer material. Kubo [18] suggested that a simpler structure containing only a single superconducting layer with a larger penetration depth on top of a Nb cavity can also increase the vortex penetration field (B_{vp}) due to the presence of an energy barrier at the superconductor-superconductor (SS) interface analogous to the vacuum-superconductor interface (i.e., the Bean-Livingston (BL) barrier [24]). Experimental evidence for this interface barrier has been reported in Ref. [133].

In summary, the maximum field (B_{max}) depends on the thickness and superconducting properties of all individual layers in a correlated way. This is a direct

consequence of Maxwell's equations with continuity conditions enforced at interface boundaries [18].

6.1.2 Magnetic screening and current in superconducting heterostructures

Recall that, for a bulk superconductor in the "local" London limit (see e.g., [246]) with an ideal flat surface, the Meissner screening profile, $B(z)$, is given by Equation (2.14), where B_0 is the (effective) applied magnetic field, z is the depth below the superconductor's surface, and λ_{L} is the London penetration depth. Equation (2.14) is well-known for its applicability to semi-infinite superconductors; however we are interested in SS bilayers comprised of dissimilar layers whose materials have different screening properties (i.e., λ_{L}s). Considering a naive exponential London decay in each component of the SS bilayer by treating the screening properties independently, the field screening profile is given by:

$$B(z) = B_0 \times \begin{cases} 1, & z < 0, \\ \exp\left(-\dfrac{z}{\lambda_{\mathrm{s}}}\right), & 0 \le z < d_{\mathrm{s}}, \\ \exp\left(-\dfrac{d_{\mathrm{s}}}{\lambda_{\mathrm{s}}}\right) \exp\left(-\dfrac{z - d_{\mathrm{s}}}{\lambda_{\mathrm{sub}}}\right), & z \ge d_{\mathrm{s}}, \end{cases} \tag{6.1}$$

where d_{s} is the thickness of the top superconducting layer, and the λ_i denote the penetration depth in the surface ($i = \mathrm{s}$) and substrate ($i = \mathrm{sub}$) layers, respectively. While Equation (6.1) is both conceptually simple and qualitatively correct in its form, it does not consider any "coupling" between the adjacent layers. Notably, the substrate layer significantly influences the screening properties of the surface layer superconductor when their penetration depths differ. This occurs because an SS bilayer's electromagnetic (EM) response depends on satisfying the boundary and continuity criteria for both the magnetic field and vector potential. Recently, it has been predicted that this coupling depends also on the surface layer's thickness

and is most effective when $d_s \sim \lambda_s$ [21]. For example, when the surface layer penetration depth is larger than the substrate's (i.e., $\lambda_s > \lambda_{sub}$), the Meissner current in the surface layer is suppressed by the substrate layer's counter-current (i.e., a counterflow current generated by the substrate in a multilayer superconductor [18, 19, 22, 23]) to satisfy the boundary and continuity condition at the interface. This results in a higher B-field for vortex entry in the outer layer with a correspondingly a reduced shielding of the substrate (higher field at the substrate interface). This effect is expected for all superconducting heterostructures with and without insulting interlayers. Quantitatively, the field screening considering counter-current-flow induced by the substrate is derived by solving the relation between the applied field, B_0 and current density, J (or equivalently vector potential, A). For a SS structure this yields Equation (3.8) [18, 19, 21, 22].

The current density distribution, $J(z)$ can be obtained from the field screening profiles using Equation (3.9). Both Equations (3.8) and (6.1) are essentially forms of exponential decay; however, the screening behavior is significantly modified in the surface layer. Figure 6.1 presents a comparison of the magnetic field profiles and current density distributions, with (a) showing normalized field screening behavior and (b) representing normalized current density distributions. In both figures, the solid red curve describes the London screening behavior in the absence of a "coupling" between the superconducting layers [Equation (6.1)], whereas the blue dashed curve corresponds to screening according to Kubo's counter-current-flow model [Equation (3.8)]. Here, the SS bilayer is $Nb_{1-x}Ti_xN$ (50 nm)/Nb with assumed penetration depths of $\lambda_{Nb_{1-x}Ti_xN} = 200$ nm and $\lambda_{Nb} = 50$ nm for $Nb_{1-x}Ti_xN$ and Nb, respectively. As alluded to above, the two models have qualitatively similar behavior; $B(z)$'s decay rate in the Nb substrate is identical, with the two curves differing only in their amplitudes at the SS boundary. This similarity is also observed in the decay rate of $J(z)$ in the Nb substrate. Conversely, a notable difference is apparent in the top $Nb_{1-x}Ti_xN$ layer, where the decay rate is

substantially reduced in Kubo's model. This is the effect of the reduced current in the surface layer as seen in Figure 6.1(b) due to the counter-current induced by the substrate.

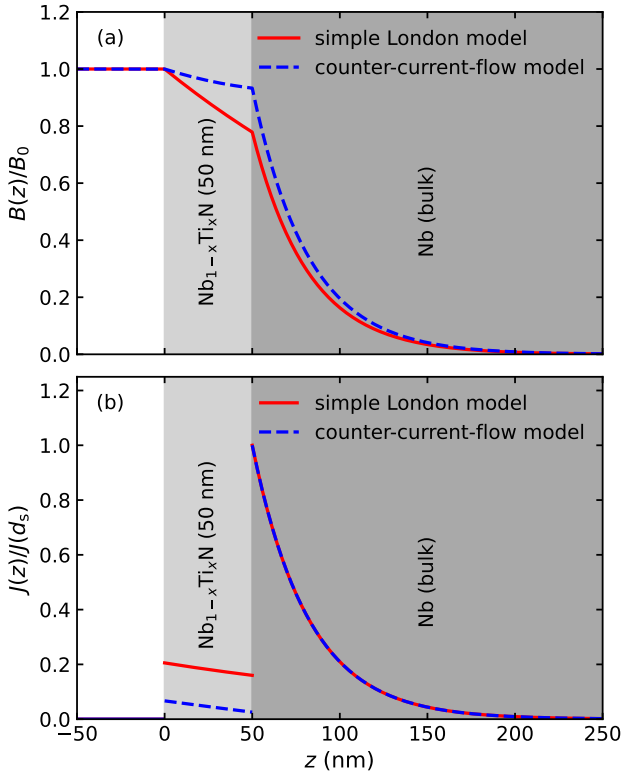

Figure 6.1: Magnetic field profiles given by Equations (3.8) and (6.1) in (a) and the current density distributions of those equations normalized to the current density at interface in (b). The used magnetic penetration depths are $\lambda_{Nb_{1-x}Ti_xN} = 200\,nm$ and $\lambda_{Nb} = 50\,nm$ for the $Nb_{1-x}Ti_xN$ and Nb layers, respectively. The thickness of the $Nb_{1-x}Ti_xN$ layer is 50 nm. Comparing the two field profiles in (a), the strongest effect on field screening is observed in the $Nb_{1-x}Ti_xN$ layer due to the suppressed Meissner current in the $Nb_{1-x}Ti_xN$ layer as seen in (b).

In order to observe the effect of counter-current in SS bilayers, it is necessary to investigate the field screening profiles experimentally and quantify the penetration depths using an appropriate model. Perhaps the best way of achieving this through low energy muon spin rotation (LE-μSR) [145, 247–250], which uses implanted positive muons to probe the sub-surface field distributions in the material under investigation. The key feature of this approach is the ability to control the energy at which the muons are implanted, conferring *depth-resolution* to the measurements.

This is in contrast to other surface-sensitive techniques (e.g., Magnetic force microscopy (MFM) [41–45], scanning tunnelling microscopy (STM) [39, 40], etc.), which provide *lateral* resolution across the surface, but lack the depth sensitivity to directly view the Meissner screening profile across a buried interface.

To this end, we measured the Meissner screening profile and observed suppression of screening current in the surface layer in $Nb_{1-x}Ti_xN$/Nb samples with different alloy thicknesses using the LE-μSR technique. These measurements were conducted under applied fields ($15 \lesssim B_0 \lesssim 25$) mT. By globally fitting the field profiles of all the samples, we quantitatively determined the common magnetic penetration depths of $Nb_{1-x}Ti_xN$, $\lambda_{Nb_{1-x}Ti_xN}$, and Nb, λ_{Nb}. This quantitative assessment involves comparing Kubo's counter-current-flow model (i.e., London theory with appropriate boundary and continuity conditions) with a simple London model without appropriate boundary conditions. The resultant comparison highlights the significant suppression of the Meissner current in the surface $Nb_{1-x}Ti_xN$ layer in $Nb_{1-x}Ti_xN$/Nb samples with film thicknesses shorter but close to the London penetration depth of $Nb_{1-x}Ti_xN$.

6.2 Experiment

6.2.1 The LE-μSR technique

LE-μSR experiments were performed at the Paul Scherrer Institute's (PSI) Swiss Muon Source located in Villingen, Switzerland, using the μE4 beamline [141]. In the beamline a thin film of condensed noble gas [167] is used to reduce the energy of a "surface" muon beam of ~4 MeV down to around 15 eV. Following that, the muons are accelerated to create a beam with an adjustable energy $E \leq 30$ keV which corresponds to an implantation depth of $\lesssim 150$ nm in Nb and Nb-based alloys. These low energy positive muons (μ^+) are ~100 % spin-polarized. The μ^+ are implanted into a sample one at a time using a (quasi-)continuous

beam [192], wherein they quickly thermalize in the target and their spins precess around the local magnetic field at the Larmor frequency, ω_μ permitting depth-resolved measurements of the field screening profile in surface-parallel applied fields up to ~30 mT [146].

When a μ^+ decays, it emits a positron preferentially along its spin direction at the moment of decay. The emitted positrons are detected as a function of time in a set of positron detectors symmetrically placed surrounding the sample. This allows for the temporal evolution of the muon's spin orientation to be deduced, and consequently, the properties of the magnetic fields it experiences.

In this experiment, the *asymmetry* of μ^+ decay is determined in a transverse field arrangement wherein a magnetic field is applied perpendicular to the initial direction of muon spin-polarization and parallel to the sample surface. The positron event rate in one (or more) "counters" i (expressed as $\pm$), is given by Equation (4.26), where $\tau_\mu = 2.2\,\mu$s is the muon lifetime, $N_{0,i}$ represents the total number of "good" decay events (i.e., decays from muons stopped in the sample), b_i is the time-independent rate from uncorrelated "background" events, and $A_0(t)$ represents the time-evolution of the muon ensemble asymmetry by Equation (4.24), where A_0 is the experimental decay asymmetry and $P(t)$ is expressed as $P_\mu(t)$ is the polarization of the muon ensemble.

In a transverse-field experiment, the time-evolution of $P_\mu(t)$ is given by Equation (4.36), where $p(B)$ is the internal magnetic field distribution sensed by the muons, $\gamma_\mu = 2\pi \times 135.54\,\text{MHz}\,\text{T}^{-1}$ is the gyromagnetic ratio of the muon, B is the magnitude of the local magnetic field at the muon site, t is the time after implantation, and ϕ is the phase factor (i.e., angle between the initial muon spin-polarization and the effective symmetry axis of a positron detector).

6.2.2 Muon Stopping Profiles

As mentioned in Section 6.2.1, LE-μSR has the ability to explore the local field in a depth resolved manner. Muons of a particular energy stop over a specific range distribution when implanted into a sample. In this experiment, a range of implantation energies (~2 keV to ~30 keV) were used (see Figure 6.2), providing depth-resolution on the nm scale (i.e., ~10 nm to ~150 nm).

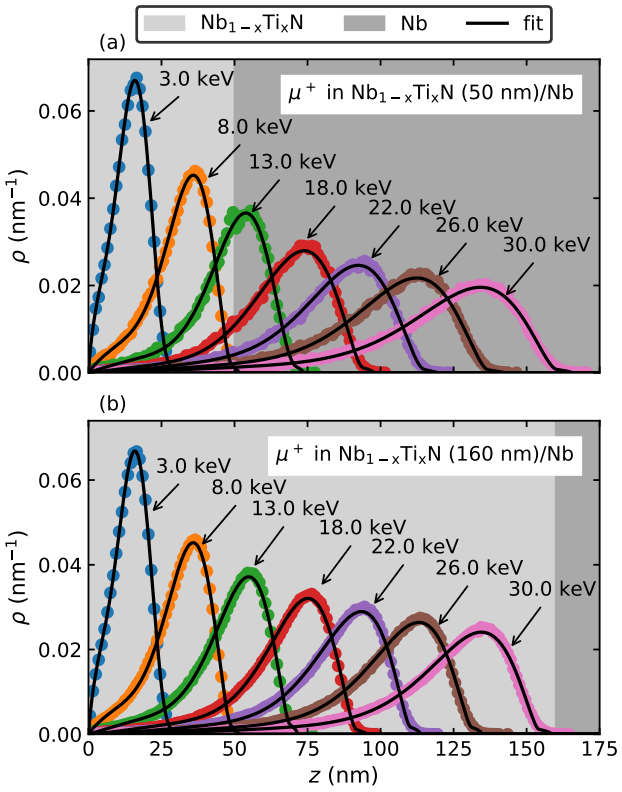

Figure 6.2: Typical stopping profiles for μ^+ implanted in (a) $Nb_{1-x}Ti_xN$ (50 nm)/Nb, and (b) $Nb_{1-x}Ti_xN$(160 nm)/Nb SS bilayer, simulated using the Monte Carlo code TRIM.SP [184]. The densities of $Nb_{1-x}Ti_xN$ and Nb are 6.6223 g cm^{-3}, and 8.57 g cm^{-3}, respectively. The light gray color in the first 50 nm of figure (a) and 160 nm of figure (b) refers to the $Nb_{1-x}Ti_xN$ film thickness on bulk Nb substrate (i.e., dark gray color). The normalized stopping distribution ρ of μ^+ is plotted against the depth z below the surface. The black solid curves are fits to the stopping profile (represented as a histogram) using Equations (6.2) and (6.3). These fits clearly capture all features of the stopping profiles.

The stopping profile of muons can be accurately simulated [145, 186, 205] using the TRIM.SP code (a Monte Carlo code) [184], which treats all collisions

within the target using the binary collision approximation. Simulation results for μ^+ implanted in a $Nb_{1-x}Ti_xN$(50 nm)/Nb, and a $Nb_{1-x}Ti_xN$(160 nm)/Nb SS bilayer are shown in Figure 6.2, illustrating LE-μSR's typical range of spatial sensitivity. For our analysis (see Section 6.3), it was convenient to have the ability to describe these profiles at arbitrary E, which can be accomplished by fitting the simulated profiles and interpolating their "shape" parameters [145]. Empirically, we found the μ^+ stopping probability, $\rho(z)$, at a given E can be described by:

$$\rho(z) = \sum_i^m f_i p_i(z), \tag{6.2}$$

where $p_i(z)$ is a probability density function, $f_i \in [0, 1]$ is the i^{th} stopping fraction, constrained such that

$$\sum_i^m f_i \equiv 1,$$

and z is the depth below the surface. For our SS bilayers, the stopping data are well-described using $m = 2$ and a $p(z)$ is given by a modified beta distribution. Explicitly,

$$p(z) = \begin{cases} 0, & \text{for } z < 0, \\ \dfrac{(z/z_0)^{\alpha-1}\,(1 - z/z_0)^{\beta-1}}{z_0\,B(\alpha,\beta)}, & \text{for } 0 \le z \le z_0, \\ 0, & \text{for } z > z_0, \end{cases} \tag{6.3}$$

where $z \in [0, z_0]$ is the depth below the surface and $B(\alpha, \beta)$ is the beta function:

$$B(\alpha,\beta) \equiv \frac{\Gamma(\alpha)\Gamma(\beta)}{\Gamma(\alpha+\beta)},$$

with $\Gamma(s)$ denoting the gamma function. Further details of the stopping profile simulation can be found elsewhere [145, 186].

6.2.3 Sample Preparation

Table 6.1: Superconducting properties of $Nb_{1-x}Ti_xN$ films from several literatures [94, 251–256]. Here, T_c is the critical temperature, B_c is the thermodynamic critical field, B_{c1} is the lower critical field, B_{sh} is the superheating field, B_{c2} is the upper critical field, λ is the penetration depth, and ξ is the BCS [57] coherence length.

Sample	T_c (K)	B_c (mT)	B_{c1} (mT)	B_{sh} (mT)	B_{c2} (mT)	λ (nm)	ξ (nm)	Ref.
$Nb_{1-x}Ti_xN/Nb$	15.97		35					[251]
$Nb_{1-x}Ti_xN/Al_2O_3$	17.3		30		15 000	150 – 200		[94]
$Nb_{1-x}Ti_xN/Al_2O_3$	15.8		25	186		208		[252]
$Nb_{0.62}Ti_{0.38}N/Si$	~15.0						2.4(3)	[253]
$Nb_{1-x}Ti_xN/MgO$	~15.0							[254]
$Nb_{1-x}Ti_xN/Al_2O_3$	~13.1							[255]
$Nb_{0.62}Ti_{0.38}N/Si$	~16.0					200(20)		[256]

In this study, $Nb_{1-x}Ti_xN$/Nb SS bilayer samples were prepared by growing thin films of $Nb_{1-x}Ti_xN$ on "bulk" Nb substrates using direct current (DC) magnetron reactive sputtering (R-DCMS) in a vacuum chamber with a base pressure of low 1×10^{-10} mbar. The sputtering target consisted of 80/20 (wt %) Nb/Ti alloy, was used within an Ar and N_2 (P_{N_2}/P_{Ar}) gas mixture at a pressure of 2×10^{-3} mbar. Films with nominal thicknesses of 50 nm, 80 nm, and 160 nm were deposited at 450 °C on 3 mm thick bulk Nb substrates, with respective T_c values of 15.8 K, 16.3 K and 16.3 K.[1] Following standard practice for preparing the surface of a Nb SRF cavity, the substrates were prepared by mechanical polishing (MP) followed by 5 µm cold electropolishing (EP) or by 50 µm buffered chemical polishing (BCP) (see e.g., Ref. [217]). Specifically, the 50 nm sample was prepared using EP and the others using BCP. Prior to film growth, the substrates were baked at 600 °C for 24 h under vacuum and the $Nb_{1-x}Ti_xN$ films were annealed at 450 °C after deposition. The typical surface roughness of the $Nb_{1-x}Ti_xN$ layer is similar to the original substrate roughness (1 nm for MP+EP substrates and microns for BCP

[1] Based on the measurements of T_c carried out for other samples prepared using identical methods with dissimilar thicknesses of $Nb_{1-x}Ti_xN$.

substrates).[2] All film depositions were performed at Thomas Jefferson National Accelerator Facility (JLab) and further details on deposition technique can be found in Ref. [251]. Note that, unlike the elemental superconductors, the magnitude of superconducting properties (such as the penetration depth and the coherence length) of $Nb_{1-x}Ti_xN$ are not robust. This is due to the fact that $Nb_{1-x}Ti_xN$ is not a "natural" compound [251]. Therefore, the superconducting properties of some $Nb_{1-x}Ti_xN$ films prepared using different target stoichiometries, deposition techniques, and preparation methods have been reviewed from the literature and are listed in Table 6.1 for reference. Although the tabulated values for various samples show considerable variation, the attributes derived from all reviewed research are in fair agreement with one another. These will be used to compare our measured penetration depths in Section 6.3 as well as for the prediction of critical fields in Section 6.4.1.

6.3 Results

Typical muon spin-precession signals are shown in Figure 6.3(a) for the normal conducting state (20 K) and in Figure 6.3(b-f) for the Meissner state (2.7 K) in $Nb_{1-x}Ti_xN$ (50 nm)/Nb. In the normal state, there is no substantial energy dependence to the time evolution of the muon ensemble polarization. This means muons implanted at different depths experience almost the same local field. By contrast, in the Meissner state the temporal evolution of $A(t)$ varies as the implantation energy increases, wherein the μ^+ spin-precession rate is greatly reduced, and the signal is more strongly damped at high implantation energies.

Figure 6.4 shows the Fourier amplitude (i.e., $\sqrt{(\text{Fourier power})}$ [257]) of the LE-μSR time spectra depicted in Figure 6.3 in the $Nb_{1-x}Ti_xN$ (50 nm)/Nb sample as a function of field (note $\omega_\mu = \gamma_\mu B$), in the normal (20 K) and Meissner (2.7 K)

[2] We note that while a smoother surface is advantageous for the BL barrier, the larger surface roughness of the BCP treated substrates does not inhibit characterization of the Meissner screening profiles in the SS bilayers.

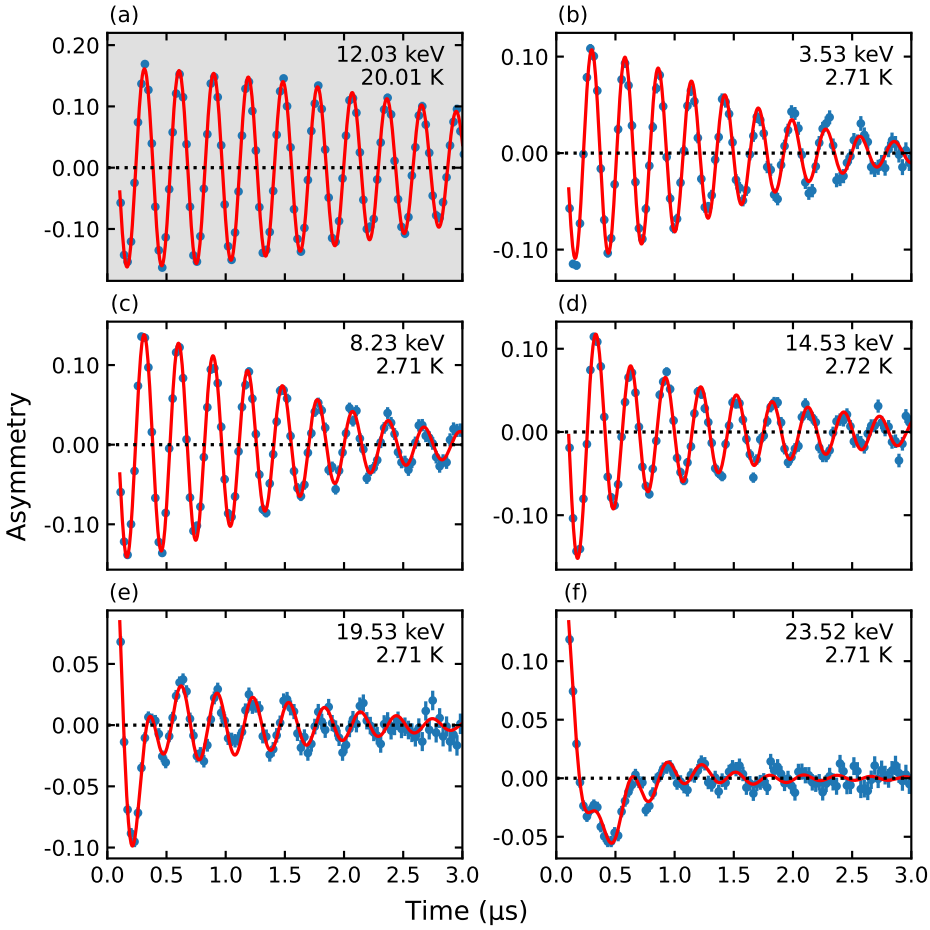

Figure 6.3: Asymmetry as a function of time for different implantation energies (given in the panel's inset) in $Nb_{1-x}Ti_xN$ (50 nm)/Nb in both the normal (20 K) and Meissner state (2.7 K) at an applied magnetic field of ~25 mT parallel to the sample surface. In the normal state (gray shaded background panel), there is no substantial energy dependence to the time evolution of the muon ensemble polarization, meaning the implanted muons experience the same local field. By contrast, it is evident that the temporal evolution of $A(t)$ varies in the Meissner state (plain white background panels). As the implantation energy increases, the μ^+ spin-precession frequency is reduced, and the signal is more strongly damped. The solid red lines denote fits to *all* of the data (i.e., a global fit) using Equations (6.6) to (6.8). Clearly, the model captures all the data's main features.

state. In the Fourier transform of the data, it is evidenced that a large damping rate in the time domain signal corresponds to a wider distribution of frequencies (i.e., local fields) [see Figure 6.4(b-f)]. For energies above ~14.5 keV, the Fourier spectra show two distinct peaks, implying at least two unique field regions are sensed, consistent with the different materials in the SS bilayer.

The measured internal field distribution, $p(B)$, in the Meissner state depends on energy via the muon implantation depth profile and the magnetic screening due to the Meissner current. We will now consider how to approximate $p(B)$ in Equation (4.36) for our analysis. In the Meissner state, the applied field decays to zero monotonically below the sample surface and the field screening is expected to be intrinsically asymmetric. For the $Nb_{1-x}Ti_xN$/Nb samples, it is found that a sum of two skewed Gaussian (SKG) components (i.e., one for each material) gives a good fit describing the data in all measurement conditions. Because each layer in the SS has a different screening properties, the SKG distribution function is defined as [258]:

$$P_{\mathrm{SKG}}(B) = \sqrt{\frac{2}{\pi}} \frac{\gamma_\mu}{(\sigma_+ + \sigma_-)} \times \begin{cases} \exp\left[-\frac{1}{2}\frac{(B-B_\mathrm{p})^2}{(\sigma_+/\gamma_\mu)^2}\right], & B \geq B_\mathrm{p}, \\ \exp\left[-\frac{1}{2}\frac{(B-B_\mathrm{p})^2}{(\sigma_-/\gamma_\mu)^2}\right], & B < B_\mathrm{p}, \end{cases} \tag{6.4}$$

where B_p is the "peak" field (i.e., *not* the mean) and $\sigma_\pm$ denotes the distribution's "width" on either side of B_p.

By substituting Equation (6.4) into Equation (4.36) for $p(B)$, the polarization formula can be written as:

$$P_{\mathrm{SKG}}(t) = P^+_{\mathrm{SKG}}(t) + P^-_{\mathrm{SKG}}(t), \tag{6.5}$$

where

$$\begin{aligned} P^\pm_{\mathrm{SKG}}(t) = &\left(\frac{\sigma_\pm}{\sigma_+ + \sigma_-}\right) \exp\left(-\frac{\sigma_\pm^2 t^2}{2}\right) \\ &\left[\cos(\gamma_\mu B_\mathrm{p} t + \phi) \mp \sin(\gamma_\mu B_\mathrm{p} t + \phi)\, \mathrm{erfi}\left(\frac{\sigma_\pm t}{\sqrt{2}}\right)\right], \end{aligned} \tag{6.6}$$

where erfi(x) is the imaginary error function. Therefore, the total asymmetry signal $A(t)$ yields:

$$A(t) = A_0 \sum_{i=1}^{n} k_i P_{\mathrm{SKG},i}(t), \tag{6.7}$$

where k reflects the fraction of muons stopping in each component of the SS bilayer, constrained such that

$$\sum_{i=1}^{n} k_i \equiv 1. \tag{6.8}$$

To fit the data, the program *musrfit* was used [193]. The red lines in Figure 6.3 are fits to *all* the data (i.e., a global fit) of the 50 nm sample using Equations (6.4) to (6.8), where the phase, ϕ is shared as a common parameter. The imposition of this restriction is necessary because in situations where $A(t)$ is significantly damped at high implantation energies in the Meissner state, the phase becomes poorly defined, and only a few complete precession periods can be resolved. The fit was constrained such that for $E \leq 14.5$ keV (i.e., mean stopping depths ≤ 50 nm) we assumed $n = 1$ in Equation (6.7) and used $n = 2$ at higher implantation energies. This choice gave the best fit to the data at all measurement conditions, as evidenced by the goodness of fit criterion (i.e., reduced-$\chi^2 = 1.06$).

In order to construct the Meissner screening profile in the $Nb_{1-x}Ti_xN$ (50 nm)/Nb sample, the mean field, $\langle B \rangle$, needs to be derived from $p(B)$ for each implantation energy E. The $\langle B \rangle$ is a convenient means of encapsulating the $p(B)$'s shift to lower fields as the E increases. The $\langle B \rangle$ is derived using the fit parameters $B_{\mathrm{p},i}$, $\sigma_{+,i}$, and $\sigma_{-,i}$ (see Section 6.6) of Equation (6.7):

$$\langle B \rangle = \sum_{i=1}^{n} k_i \left[B_{\mathrm{p},i} + \sqrt{\frac{2}{\pi}} \left(\frac{\sigma_{+,i} - \sigma_{-,i}}{\gamma_\mu} \right) \right]. \tag{6.9}$$

The field screening profile of $Nb_{1-x}Ti_xN$ (50 nm)/Nb at an applied field of $B_0 \sim 25$ mT as a function of energy E (bottom scale) and corresponding mean

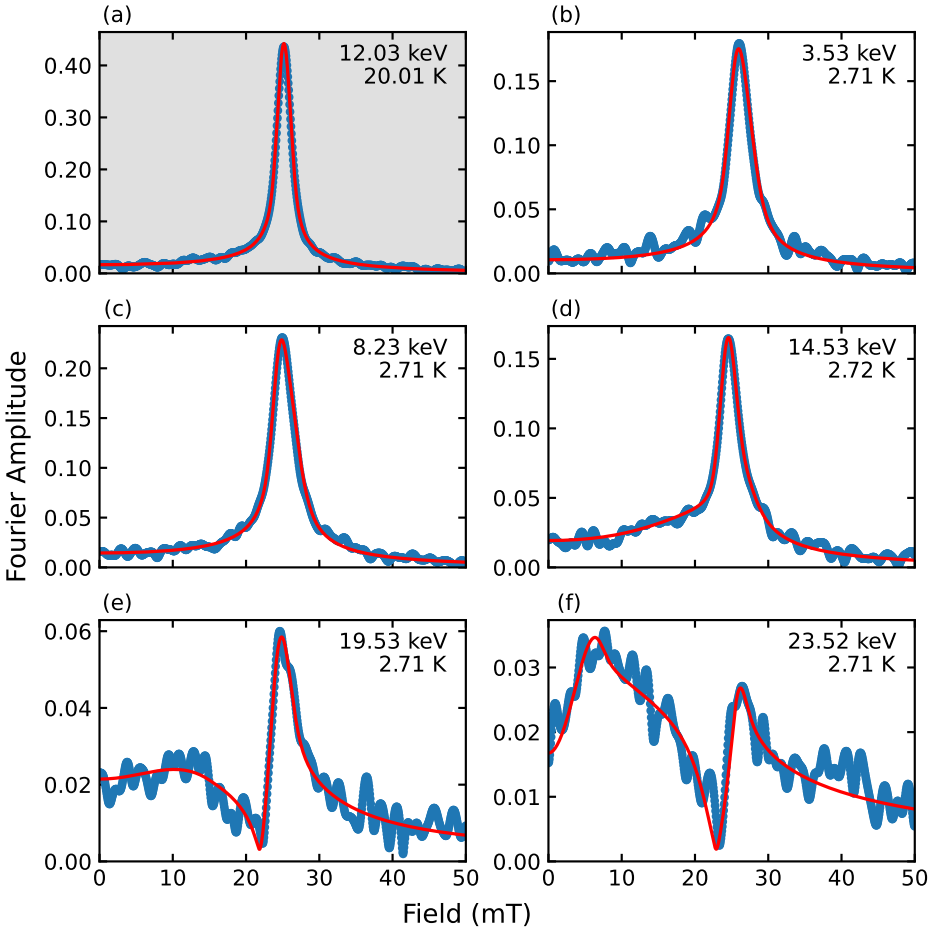

Figure 6.4: Fourier amplitude of the LE-μSR data (shown in Figure 6.3) in $Nb_{1-x}Ti_xN$ (50 nm)/Nb as a function of field (note $\omega_\mu = \gamma_\mu B$), in the normal (20 K) and Meissner (2.7 K) state with an applied magnetic field of ~25 mT. The red lines are skewed Gaussian fits corresponding to the field distribution described by Equations (6.6) to (6.8). Above ~14.5 keV two distinct peaks are observed indicating that muons of a single implantation energy sense the field in both layers of the SS bilayer.

implantation depth $\langle z \rangle$ (top scale) in the Meissner ($T = 2.7$ K) and normal state ($T = 20$ K) is shown in Figure 6.5. The closed circles and open squares in Figure 6.5(a) and (b) represent the mean field $\langle B \rangle$ of the same data. In the normal state the $\langle B \rangle$ is not screened and in the Meissner state $\langle B \rangle$ decays with increasing E as expected.

In order to fit $\langle B \rangle$, we shall consider a model that describes all essential features of the data. In Equations (4.36) and (6.4) to (6.9), $\langle B \rangle$ is derived by fitting a field

distribution $p(B)$ at a given energy E. At specific E, muons sample over a range of depths (i.e., distribution) which is simulated and quantified by $\rho(z)$ as discussed in Section 6.2.2. The quantities $\rho(z)$ and $p(B)$ are both energy dependent. Hence, $\langle B \rangle$ depends on the Meissner screening and the μ^+ implantation distribution $\rho(z)$. The mean field $\langle B \rangle$ as a function of E is therefore:

$$\langle B \rangle(E) = \int_0^\infty B(z)\rho(E,z)\,\mathrm{d}z, \tag{6.10}$$

where the dependence on E is accounted for *implicitly* by $\rho(E,z)$ which is predetermined from fits to simulated implantation profiles (see Figure 6.2). The screening profile $B(z)$ is derived from Equations (3.8) and (6.1). Note that the applied magnetic field, B_{applied} in both Equations (3.8) and (6.1) is enhanced in the Meissner state due to the sample geometry, which needs to be accounted. This is done by using:

$$B_0 = B_{\text{applied}} \times \frac{1}{(1-N)}, \tag{6.11}$$

where the demagnetization factor N depends on the geometry of the sample [132, 136, 259]. To compare our measured penetration depths with literature values (see Table 6.1), the T dependence of λ was assumed to follow the phenomenological power law by Equation (2.16) where $n = 4$ [123].

The fits to the normal state data in Figure 6.5 are represented by dashed red curves. The solid red curves denote fits to the Meissner state data using Equation (6.10) and one of the screening models introduced in Section 6.1.2 (i.e., counter-current-flow or simple London model). Figure 6.5(a) is fitted with a simple London model (Equation (6.1)), and the counter-current-flow model field distribution (Equation (3.8)) is used to fit the data in Figure 6.5(b). It can be seen that both models capture all physically meaningful details of the data and give excellent fits. The fit parameters for both models are tabulated in Table 6.2. The values of the extracted parameters N, λ_{Nb}, and $d_{\text{Nb}_{1-x}\text{Ti}_x\text{N}}$ are almost identical in the

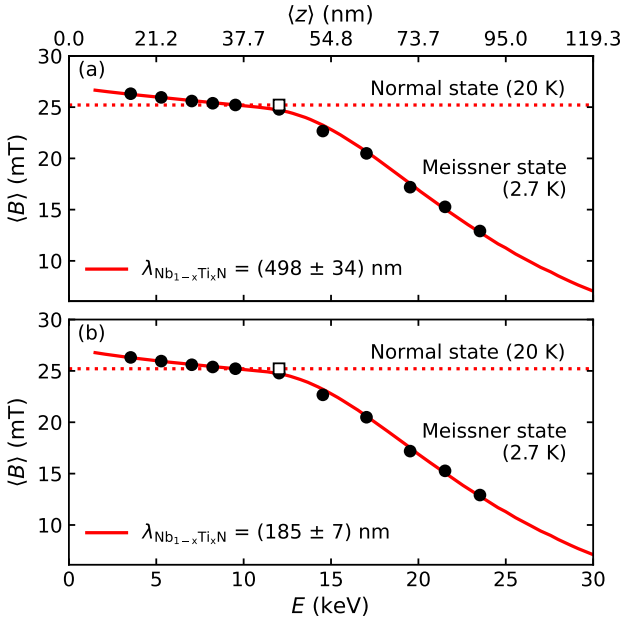

Figure 6.5: $Nb_{1-x}Ti_xN$ (50 nm)/Nb field profile: Plot of the mean magnetic field, $\langle B \rangle$, sensed by μ^+ at different implantation energies, E, in a $Nb_{1-x}Ti_xN$ (50 nm)/Nb sample at an applied field ($B_0 \sim 25$ mT) parallel to the sample surface in the Meissner ($T = 2.7$ K) and normal state ($T = 20$ K). The closed circles and open squares are the data points in the Meissner state and normal state, respectively. The implantation energy E is related to the mean implantation depth $\langle z \rangle$ as shown in the top x-axis. The solid red lines are fits to the data in the Meissner state and the dashed red lines are fits to the normal state data. Both figures represent the same data points fitted to different models. In the Meissner state $\langle B \rangle$ decays with increasing E as expected. The fit to Figure 6.5(a) represents the field screening using Equation (6.1) i.e., a simple London model with fit parameters $\lambda_{Nb_{1-x}Ti_xN} = 498(34)$ nm and $\lambda_{Nb} = 42.9(30)$ nm. Figure 6.5(b) is fitted with the Equation (3.8) which considers counter-current-flow induced by the substrate layer and the extracted fit parameters are $\lambda_{Nb_{1-x}Ti_xN} = 185(7)$ nm and $\lambda_{Nb} = 43.6(29)$ nm.

Table 6.2: Fit results of the $Nb_{1-x}Ti_xN$ (50 nm)/Nb bilayer with a counter-current-flow (i.e., Equation (3.8)) and a naive bi-exponential model (i.e., Equation (6.1)). Here, $B_{applied}$ is the applied magnetic field, N is the demagnetization factor, $d_{Nb_{1-x}Ti_xN}$ is the thickness of $Nb_{1-x}Ti_xN$ layer, and $\lambda_{Nb_{1-x}Ti_xN}$, λ_{Nb} are the penetration depths of $Nb_{1-x}Ti_xN$ and Nb at 0 K.

Model	$B_{applied}$ (mT)	N	$d_{Nb_{1-x}Ti_xN}$ (nm)	$\lambda_{Nb_{1-x}Ti_xN}$ (nm)	λ_{Nb} (nm)
counter-current-flow	25.209(31)	0.079(5)	58.5(13)	185(7)	43.6(29)
simple London	25.209(31)	0.070(4)	59.0(15)	498(34)	42.9(30)

two models. However, a large discrepancy exists between the determined values of $\lambda_{Nb_{1-x}Ti_xN}$. The simple London model gives $\lambda_{Nb_{1-x}Ti_xN} = 498(34)$ nm, while Kubo's counter-current-flow model gives $\lambda_{Nb_{1-x}Ti_xN} = 185(7)$ nm. Interestingly,

the value determined using Kubo's counter-current-flow model [Equation (3.8)] is in good agreement with literature estimates (see Table 6.1), whereas the expression in Equation (6.1) overestimates $\lambda_{Nb_{1-x}Ti_xN}$ by a factor of ~2.5. This observation strongly supports the predictions of the counter-current-flow theory [18] and suggests that Equation (6.1) is not appropriate for quantifying $B(z)$ in superconducting heterostructures.

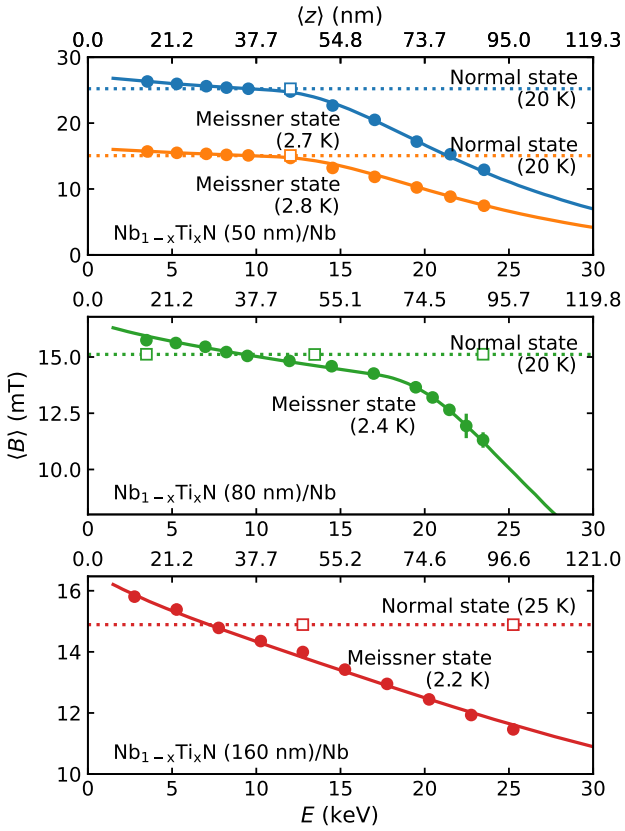

Figure 6.6: Plot of the mean magnetic field, $\langle B \rangle$, sensed by μ^+ at different implantation energies, E, in $Nb_{1-x}Ti_xN$/Nb samples with different $Nb_{1-x}Ti_xN$ thicknesses (i.e., 50 nm, 80 nm, and 160 nm) at applied fields of $15.0 \lesssim B_0 \lesssim 25.0$ mT, parallel to the sample surface in the Meissner state ($T \leq 2.8$ K) and normal state ($T \geq 20$ K). The mean implantation depth $\langle z \rangle$ corresponding to E of each sample is shown in the top x-axis on each panel. The colored closed circles and open squares are the data derived from the LE-μSR measurements. The solid and dashed lines represent a (global) fit to the data using Equation (6.10) where $B(z)$ is the field screening formula, i.e., Equation (3.8). In the normal state, there is no energy or depth dependence to $\langle B \rangle$, which represents the strength of the applied magnetic field. However, in the Meissner state, $\langle B \rangle$ decays with increasing E. The apparent difference in $\langle B \rangle$ at $E \sim 0$ keV between the Meissner and normal state is due to the field "enhancement" in the Meissner state. The fit parameters are shown in the Table 6.3.

Table 6.3: Individual parameters derived from a global fit to the counter-current-flow model of three $Nb_{1-x}Ti_xN$/Nb samples. The magnetic penetration depths at 0 K of the $Nb_{1-x}Ti_xN$ layer and the Nb substrate were derived as global fit parameters, using the analysis approach described in Section 6.3. Here, $B_{applied}$ is the strength of the magnetic field applied parallel to the sample surface, N is the demagnetization factor, and $d_{Nb_{1-x}Ti_xN}$ is the thickness of the $Nb_{1-x}Ti_xN$ layer.

Sample	$B_{applied}$ (mT)	N	$d_{Nb_{1-x}Ti_xN}$ (nm)	$\lambda_{Nb_{1-x}Ti_xN}$ (nm)	λ_{Nb} (nm)
$Nb_{1-x}Ti_xN$ (50 nm)/Nb	15.058(29)	0.0801(22)	57.5(9)	182.5(31)	43.3(19)
	25.214(29)				
$Nb_{1-x}Ti_xN$ (80 nm)/Nb	15.115(20)	0.0977(35)	84.0(9)		
$Nb_{1-x}Ti_xN$ (160 nm)/Nb	14.89(5)	0.115(7)	168 (fixed)		

To be more conclusive about this observation, we measured the field screening profile in three samples with different $Nb_{1-x}Ti_xN$ thicknesses (50 nm, 80 nm, and 160 nm) deposited on Nb substrates, see Figure 6.6. Using the counter-current-flow model, the field screening profiles were fitted simultaneously (i.e., global fit) with the penetration depth values at 0 K of $Nb_{1-x}Ti_xN$ and Nb as shared fit parameters, this is justified by the fact that when the profiles for each sample were fit separately, identical λ values were obtained. Other fit parameters were the thickness of each film and individual demagnetization factors. The thickness of the $Nb_{1-x}Ti_xN$ (160 nm)/Nb sample cannot be determined from the fit as all muons are stopped in the $Nb_{1-x}Ti_xN$ layer, see Figure 6.2(b). This parameter was therefore directly measured using transmission electron microscopy (TEM) and found to be 168 nm [100].

The best fit parameters were determined to be: $\lambda_{Nb_{1-x}Ti_xN}(0\,K) = 182.5(31)$ nm (using T_c of $Nb_{1-x}Ti_xN$ mentioned in Section 6.2.3) and $\lambda_{Nb}(0\,K) = 43.3(19)$ nm (using $T_c = 9.25$ K for Nb [7]). All fit parameters can be found in Table 6.3. Although the magnetic screening is very different for each sample, the fact that the global fit gives excellent agreement with the entire data, with the penetration depths of the layer and the substrate as common fit parameters, further confirms the applicability of the counter-current-flow model to the data.

6.4 Discussion

From Figure 6.6, it is obvious that in both the 50 nm and 80 nm samples the decay of $B(z)$ is weaker in the $Nb_{1-x}Ti_xN$ layers, whereafter it is attenuated strongly in the Nb substrate. This bipartite screening represents the presence of two distinct penetration depths (i.e., $\lambda_{Nb_{1-x}Ti_xN}$ and λ_{Nb}), each associated with a distinct region in the SS bilayer. This spatially segregated response is directly resolved by the raw LE-μSR data, as evidenced by the Fourier spectra in Figure 6.4. Note that a low-temperature baked [11] Nb was considered an "effective" bilayer due to the anomalous Meissner screening [206] near the surface, however, more recent analysis evidenced that this bipartite screening profiles is absent (i.e., there is no evidence for an effective SS bilayer) [145]. The analysis shown in Figure 6.6, gives λ values that are independent of the particular sample used and measurement conditions, implying that the measured quantities are intrinsic to the individual materials (originating from this batch of "stocks" and the coating procedure). The experimentally obtained $\lambda_{Nb_{1-x}Ti_xN}$ in Table 6.3 agree with the literature values shown in Table 6.1, highlighting the suppression of the Meissner current in the surface layer. The obtained $\lambda_{Nb} = 43.3(19)$ nm exceeds the average literature estimate of Nb's penetration depth in the "clean" limit $\lambda = 28.0(15)$ nm [145, 250]. We propose that this increased λ_{Nb} is due to the suppression of the electron mean free path, ℓ. There might be some impurity added to the Nb substrate due to the material "doping" while exposing its surface to the Ar/N_2 mixture during sputtering at 450 °C. Commonly, low temperature baking of Nb in N_2 reduce ℓ [15, 260, 261] and consequently increase λ based on the Pippard's approximation [262].

Note that, Pippard's nonlocal electrodynamics [262] were not considered in describing the superconducting properties of Nb. Our previous LE-μSR investigation on "bare" and "N_2 doped" Nb samples [145] have shown that the London model sufficiently describes these properties, suggesting that the effects of nonlocal

electrodynamics could be even more prominent in higher purity samples [263].

Regarding the field screening in the $Nb_{1-x}Ti_xN$ (160 nm)/Nb sample the field decays far more rapidly in the first few nanometers than in the other samples, but the whole data can be fitted with a single $\lambda_{Nb_{1-x}Ti_xN}$ value. Agreement of the film thicknesses extracted as fit parameters with the nominal thicknesses of the films for different measurement conditions further confirm that the counter-current-flow model can very well describe the material properties. Also, the different magnitude of B_{applied} for the 50 nm sample does not have any effect on the other fit parameters.

An (apparent) difference in applied fields, B_{applied} for measurements in the normal and Meissner state is observed in Figure 6.6. B_{applied} is used as a shared fit parameter between Meissner and normal state data for all the samples, while for the Meissner state the magnetic field enhancement is accounted for by the demagnetization factor, N as an individual fit parameter (see Equation (6.11)). From the fit, the extracted value of B_{applied} agrees with the nominal applied fields of the samples.

We also find that a non-superconducting layer (i.e., "dead layer") at the surface is absent in our model. While such feature is often found in "real" superconductors, its absence here is not unexpected, given the surface roughness of our samples and the chemical stability of $Nb_{1-x}Ti_xN$. The 50 nm sample is mirrored surface finished and others are prepared by BCP however, we did not observe any effect of surface roughness in the field screening profile. The surface of $Nb_{1-x}Ti_xN$ oxidizes on exposure to the ambient atmosphere (forming NbO_x and TiO_x), with the thickness of the oxide layer saturating quickly to ~1.3 nm [264]. This layer is too thin for observation by LE-μSR at the implantation energies used here. Thus, while we can not completely rule out the existence of a thin ~1 nm non-superconducting region at the surface of our samples, we assert that such a feature is too small to meaningfully impact the material quantities reported here.

6.4.1 Predictions of critical fields

As discussed in Sections 6.1 and 6.3, the counter-current-flow model predicts that multilayer superconductors can maximize the field of first-flux entry beyond the individual superheating field of its layers and substrate. For a *crude* estimate of this quantity, the superheating field, B_{sh} and Ginzburg-Landau (GL) parameter, $\kappa \equiv \lambda/\xi_{GL}$ (i.e., the ratio between the magnetic penetration depth λ and the GL coherence length ξ_{GL}), of each layer are required, which we consider below.

Through linear stability analysis using GL theory (strictly valid at $T \simeq T_c$) B_{sh} for $\kappa > 1.1495$ was derived to be Equation (2.54), where B_c is the thermodynamic critical field. Following that, κ is calculated for each material from experimentally measured penetration depth with the literature value of the London penetration depth λ_L and Bardeen-Cooper-Schrieffer (BCS) [57] coherence length ξ_0 [55, 99]:

$$\kappa = \frac{\lambda}{\xi_{GL}} = \frac{2\sqrt{3}}{\pi}\frac{\lambda^2}{\xi_0 \lambda_L}, \tag{6.12}$$

using the fact that ξ_0 and ξ_{GL} both are correlated to the magnetic flux quantum Φ_0 [55]. Here, λ_L and ξ_0 are the fundamental properties of the metal defined by the clean stoichiometric material.

The next quantity is the lower critical field B_{c1}, which is calculated for both materials using Equation (2.44) where $\alpha = 0.497$.[3] Now, B_c of Equation (2.54) needs to be determined, which is well-defined for Nb [7]. However, since $Nb_{1-x}Ti_xN$ is not a natural compound B_c is not readily available from the literature, which we can be self-consistently evaluated when B_{c1} is known, by re-arranging Equation (2.43) [55]. To summarize the results of these calculations, the values of κ, B_{c1}, B_c, and B_{sh} for $Nb_{1-x}Ti_xN$ and Nb are presented in Table 6.4.

Finally, the maximum field for which the SS bilayer can remain in the Meissner state B_{max} is derived by solving the relation between applied field and screening

[3] This approximation is valid for $\kappa \gg 1$, as discussed in Section 2.5.2, which holds well for $Nb_{1-x}Ti_xN$. However, it is also applied to Nb ($\kappa \sim 1$) to provide a rough estimate.

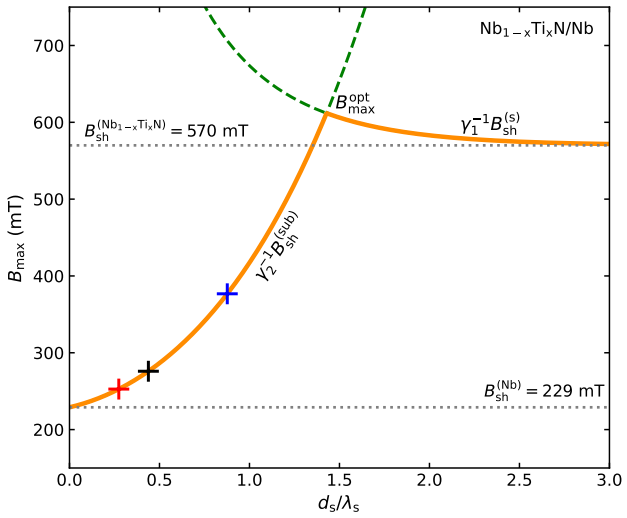

Figure 6.7: Prediction of the maximum applied field B_{max} where the Meissner state can be sustained for an SS bilayer as a function of thickness of the top $Nb_{1-x}Ti_xN$ superconducting layer, d_s (i.e., $d_{Nb_{1-x}Ti_xN}$) in $Nb_{1-x}Ti_xN$/Nb. The orange curve starting from the left represents B_{max} of the substrate Nb layer and the curve starting at right corresponds to the surface $Nb_{1-x}Ti_xN$ layer. Here the measured penetration depths of $\lambda_s = \lambda_{Nb_{1-x}Ti_xN} = 182.5(31)$ nm and $\lambda_{sub} = \lambda_{Nb} = 43.3(19)$ nm were used to find the magnitude of γ_1 and γ_2 using Equations (3.12) and (3.14). The predicted values of the superheating field of $Nb_{1-x}Ti_xN$ and Nb are $B_{sh}^{(s)} = B_{sh}^{(Nb_{1-x}Ti_xN)} = 570(40)$ mT and $B_{sh}^{(sub)} = B_{sh}^{(Nb)} = 229(6)$ mT, respectively. The +, + and + are the position of maximum fields for each of the 50 nm, 80 nm, and 160 nm samples.

Table 6.4: Superconducting parameters GL parameter κ, thermodynamic critical field B_c, lower critical field B_{c1}, and superheating field B_{sh} were calculated from the measured penetration depths of $\lambda_{Nb_{1-x}Ti_xN} = 182.5(31)$ nm and $\lambda_{Nb} = 43.3(19)$ nm. B_c for Nb and ξ_0 for both materials are taken from literature.

Material	λ_L (nm)	ξ_0 (nm)	κ	B_{c1} (mT)	B_c (mT)	B_{sh} (mT)
$Nb_{1-x}Ti_xN$	150 [94]	2.4(3) [253]	102(17)	22.9(11)	710(40)	570(40)
Nb	28.0(15) [145, 250]	40.3(35) [145]	1.83(25)	74(11)*	199(1) [7]	229(6)

* The B_{c1} value for Nb obtained from Equation (2.44) with $\alpha = 0.497$ (valid for $\kappa \gg 1$) is an underestimate, as Nb has $\kappa \sim 1$. A more accurate evaluation using Equations (2.44) and (2.45) yields $B_{c1} = 132(14)$ mT.

current density in the London model, with appropriate boundary and continuity conditions by Equation (3.15) [18, 19, 22], where $B_{sh}^{(s)}$ and $B_{sh}^{(sub)}$ are the superheating fields of the surface and substrate layers, respectively, and the terms γ_1 and γ_2 arise as coefficients while solving the relation for B_{max} (see Ref. [18] for details). Explicitly, the γ_is are Equations (3.12) and (3.14).

In Equation (3.15), the term $\gamma_1^{-1}B_{sh}^{(s)}$ is related to the maximum applied field for the surface layer, whereas the term $\gamma_2^{-1}B_{sh}^{(sub)}$ corresponds to the substrate. As B_{max} is a function of the surface layer thickness, d_s, there exists an optimum where its value is maximized expressed by Equation (3.18) [18, 19, 22].

B_{max} is plotted in Figure 6.7 as a function of d_s, wherein the entire $Nb_{1-x}Ti_xN$/Nb SS structure remains in the Meissner state. The predicted maximum applied fields for our different film thicknesses (50 nm, 80 nm, and 160 nm) were found to be 253(5) mT, 276(5) mT and, 377(5) mT, indicated in Figure 6.7 by "plus" (+, +, and +) symbols, respectively. Clearly, these values exceed the intrinsic field limit of the Nb substrate. The orange curve in Figure 6.7 represents the criteria for the surface and substrate layer to remain in the Meissner state. For zero film thickness, the substrate can sustain its Meissner state up to the superheating field of the substrate B_{sh} (229(6) mT for our Nb substrates). Upon increasing the d_s, B_{max} is initially increased, as the applied field is shielded by the surface superconductor before it reaches the SS interface. B_{max} reaches its optimum (i.e., $B_{max}^{opt} = 610(40)$ mT) for a surface layer thickness, $d_m \sim 1.4\lambda_s = 261(14)$ nm according to Equation (3.18).

Note that a surface layer thicker than λ_s can only remain in the Meissner state above B_{c1} in the presence of a BL barrier [24] just like a bulk superconductor of same material. The strong suppression of the screening current by the counter-current-flow between substrate and surface layers therefore suggests that multilayer structures with several interlayers to stop vortices are necessary in order to achieve largest B_{max}^{opt}.

6.5 Summary

In conclusion, the depth-dependent field screening profile in SS bilayers composed of $Nb_{1-x}Ti_xN$ films (50 nm, 80 nm, and 160 nm) deposited on Nb substrates were measured using LE-μSR. A fit of the magnetic screening profile to a counter-

current-flow model yielded a penetration depth for $Nb_{1-x}Ti_xN$ of 182.5(31) nm in agreement with literature values. This is contrasted by fits to a naive biexponential model, which was found to overestimate λ by a factor of ~2.5. For the Nb substrates, a common λ of 43.3(19) nm was found. This comparison highlights the pronounced suppression of the Meissner current within the surface layer and serves as an experimental validation of the counter-current-flow model. Using these quantities, the optimum maximum field that can be sustained before first-flux entry by a $Nb_{1-x}Ti_xN$/Nb heterostructure with these material properties was predicted to be 610(40) mT. This study emphasizes that the samples tested can collectively be well described by a London model with appropriate boundary conditions.

6.6 Appendix

6.6.1 Fit parameters of LE-μSR time spectra data of $Nb_{1-x}Ti_xN$ (50 nm)/Nb sample

Figure 6.8 shows fit parameters of the Meissner state (2.7 K) data of the $Nb_{1-x}Ti_xN$ (50 nm)/Nb sample presented in Figure 6.3. The size of the error bars in the fit parameters signifies the robustness of the skewed Gaussian approach to present the field distribution.

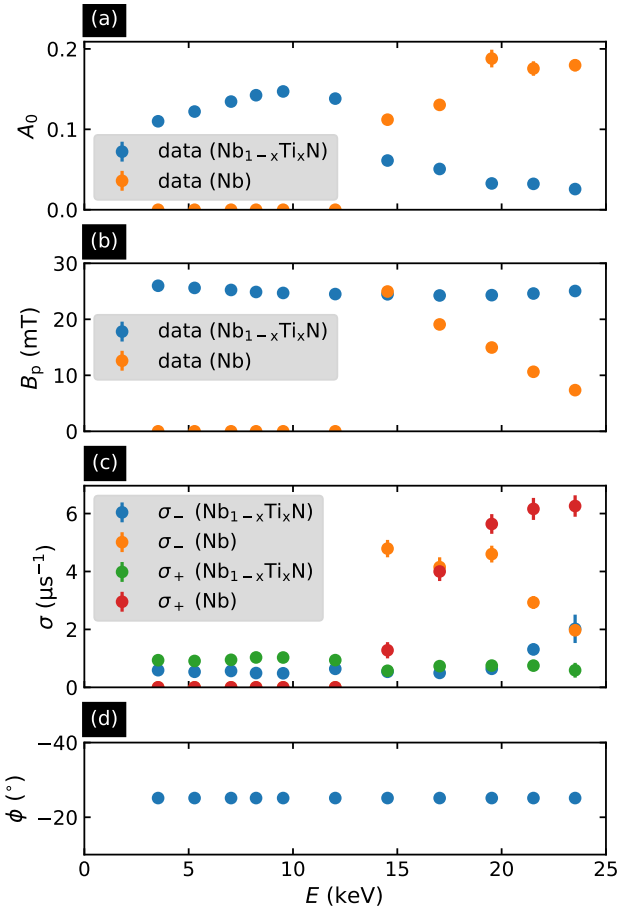

Figure 6.8: Plot of the fit parameters A_0, B_p, $\sigma_\pm$, and ϕ of Equations (6.4) to (6.8) as a function of E in $Nb_{1-x}Ti_xN$ (50 nm)/Nb in the Meissner state (2.7 K) at an applied magnetic field of ~25 mT. For $E \leq 14.5$ keV the fit is constrained such that $n = 1$ in Equation (6.7) indicating the μ^+ sample is only implanted in the $Nb_{1-x}Ti_xN$ layer. (a) The blue and orange closed circles are the asymmetry, A_0 data points corresponding to the $Nb_{1-x}Ti_xN$ and Nb layer, respectively. (b) the peak field, B_p of $Nb_{1-x}Ti_xN$ and Nb layer are denoted by the blue and orange closed circles, (c) the distribution's "width" on either side of B_p, $\sigma_\pm$ is plotted for both $Nb_{1-x}Ti_xN$ and Nb layers indicated by colored closed circles shown in the figure inset, and (d) represents the shared parameter, phase ϕ.

Chapter 7

Superconducting properties of thin film $Nb_{1-x}Ti_xN$ studied via the NMR of implanted ^8Li

7.1 Introduction

$Nb_{1-x}Ti_xN$ is a ternary alloy with a cubic $B1$ (rocksalt) crystal structure (see Figure 7.1), derived from Group IV and Group V transition metal nitrides [265, 266]. It forms a fully miscible, quasi-binary solid solution with its end members TiN and NbN over the entire $0 \leq x \leq 1$ composition range [254, 267], with structural details that closely follow Vegard's law [268, 269]. Similar to its end members, the alloy is a type-II superconductor with a relatively high critical temperature T_c (up to 17 K [270, 271]). Thanks to the alloy's facile synthesis in the form of thin films [255, 265, 272, 273], $Nb_{1-x}Ti_xN$ finds use in numerous technical applications that employ superconducting coatings (e.g., tunnel junctions [274, 275], THz receivers [276, 277] and mixers [278, 279], etc.). In particular, the alloy has emerged as a promising candidate [94] for coating conventional Nb superconducting radio frequency (SRF) cavities — common components of modern particle accelerators [203] — which we consider in detail below.

SRF cavities accelerate charged particle beams via the electric fields created under resonant radio frequency (RF) excitation. Essential for maintaining a high quality factor Q_0 is low electrical resistivity of the cavity material, making superconductors like Nb ideal [203]. The performance of Nb cavities is ultimately

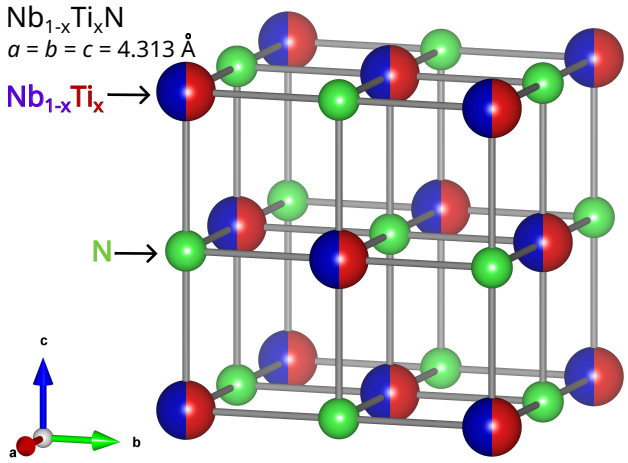

Figure 7.1: Crystal structure of cubic $B1$ (rocksalt) $Nb_{1-x}Ti_xN$ (space group $Fm\bar{3}m$, number 225). The metal atoms Nb and Ti atoms (blue and red spheres) randomly occupy the Wyckoff $4a$ site, which forms an FCC sublattice. Similarly, the N atoms (green spheres) occupy the Wyckoff $4b$ site, can be viewed as filling the octahedral "intersticies" of the FCC metal sublattice. The gray bonds highlight the octahedral coordination environment of each equilibrium position. Lattice constants a, b, c for the x = 0.25 stoichiometry are indicated in the inset. The structures were drawn using VESTA [280].

limited by the element's so-called superheating field $B_{sh} \approx 240\,\text{mT}$ [119, 133], beyond which vortex penetration occurs and resistive losses cause Q_0 to plummet. To address this limitation, coatings with superconductors having higher T_c and superheating field B_{sh} than Nb (e.g., Nb_3Sn, $Nb_{1-x}Ti_xN$) have been proposed [18, 20, 21]. Such coatings (with or without an insulating "buffer" layer) are predicted [18–22] to allow such devices to operate in field regimes beyond the capabilities of "bare" Nb cavities, a claim supported by recent experiments [4, 5, 126, 129, 133, 281]. Central to modelling the *macroscopic* behavior of these heterostructures, however, is knowledge of the coating film's *microscopic* superconducting properties, which are not well-established for $Nb_{1-x}Ti_xN$.

Part of the uncertainty in $Nb_{1-x}Ti_xN$'s intrinsic properties stems from their compositional "tunability", with a transition temperature T_c that can be tuned with stoichiometry. For instance, a $T_c \approx 17\,\text{K}$ has been reported for x = 0.34 [282, 283], while a slightly lower value of ∼15 K is observed for $x \lesssim 0.5$ [251, 252, 265, 266].

As $x \rightarrow 1$, T_c decreases further to approximately 4 K [252, 284]. This trend may be attributed to the properties of the end-member compositions, where NbN exhibits $T_c \gtrsim 16\,\mathrm{K}$ [285, 286], while TiN has a significantly lower $T_c \approx 4\,\mathrm{K}$ [287, 288]. Less well characterized is how stoichiometry affects its other superconducting properties. For example, measurements indicate a magnetic penetration depth $\lambda \gtrsim 150\,\mathrm{nm}$ [5, 100, 252, 256, 279, 289, 290] for $x \leq 0.46$, a Ginzburg-Landau (GL) coherence length $\xi_{GL} \approx 4\,\mathrm{nm}$ [253, 255, 267, 291], a lower critical field $B_{c1} \approx 30\,\mathrm{mT}$ [251, 292, 293], and an upper critical field $B_{c2} \gtrsim 15\,\mathrm{T}$ [265, 267, 272, 284, 291, 294, 295]. Similarly, the alloy's superconducting energy gap Δ is also known to vary with x, with gap ratios $2\Delta(0\,\mathrm{K})/k_B T_c(0\,\mathrm{T})$ ranging from 3.53 to 5.0 [274–279, 289, 290, 296–298]. This complexity can be further compounded by their variability with other factors such as film thickness, substrate material, and post-deposition annealing [48, 254, 255, 273, 299–301].

As $Nb_{1-x}Ti_xN$ films are most important for technical applications — particularly in form of superconductor-insulator-superconductor (SIS) structures (e.g., $Nb_{1-x}Ti_xN$/AlN/Nb), which are widely used in tunnel junctions, THz mixers, and SRF cavities — we focus our attention on this material class. One means of elucidating its properties is through the study of the superconductor's internal magnetic field distribution $p(B)$ in the vortex state [56, 70]. Techniques such as nuclear magnetic resonance (NMR) [302, 303] and muon spin rotation (μSR) [53, 75] are effective approaches for bulk superconductors, but are less suited for thin films or layered heterostructures. On the other hand, closely related techniques based on low-energy implanted spin-probes like low energy muon spin rotation (LE-μSR) [146, 205] and β-detected nuclear magnetic resonance (βNMR) [142, 304] are well-suited to such a situation, enabling spatially resolved measurements at subsurface depths $\lesssim 150\,\mathrm{nm}$.

In this work, we investigate the superconducting and normal-state properties of thin film $Nb_{1-x}Ti_xN$ using ^{8}Li βNMR spectroscopy [142, 304]. Specifically,

we report measurements in the normal and vortex states of a $Nb_{0.75}Ti_{0.25}N$(91 nm) /AlN(4 nm)/Nb heterostructure under a 4.1 T field applied normal to its surface. Resonance measurements find wide ^{8}Li lineshapes that (symmetrically) broaden below the film's T_c due to the formation of vortex field lines. Spin-lattice relaxation (SLR) data reveal distinct T-dependent behavior, with a Korringa response [305] below ∼100 K that displays a Hebel-Slichter coherence peak [306, 307] below T_c, and relaxation that is dominated by thermally activated fluctuations at higher-T. From an analysis of these features, we quantify the parameters governing the film's superconducting properties and compare them against literature values. Our findings provide key insight into the superconducting behavior of $Nb_{1-x}Ti_xN$ thin films in an SIS arrangement.

7.2 Experiment

βNMR [142, 304] experiments were conducted at TRIUMF's isotope separator and accelerator (ISAC) facility in Vancouver, BC, Canada. The local spin probe ^{8}Li (nuclear spin $I = 2$, radioactive lifetime $\tau_{^8\mathrm{Li}} = 1.21$ s (half-life 848 ms), gyromagnetic ratio $\gamma_{^8\mathrm{Li}}/(2\pi) = 6.301\,98(8)$ MHz T^{-1}, nuclear electric quadrupole moment $Q = +32.6$ mb, and mass $m_{^8\mathrm{Li}} = 8.023$ u) was introduced into the sample by ion-implantation using a beam of ^{8}Li$^+$. The incident ion beam had a typical flux of ∼10^6 ions s^{-1} over a beam spot ∼3 mm in diameter, with a beam implantation energy $E = 4.85$ keV, corresponding to a mean stopping depth $\langle z \rangle \sim 21$ nm, as calculated by the Stopping and Range of Ions in Matter (SRIM) [183] Monte Carlo code (see Figure 7.2). Prior to implantation, the probe was spin-polarized in-flight by collinear optical pumping with circularly polarized laser light [308], achieving a polarization $P \approx 70\,\%$ [173]. All βNMR measurements were performed in an applied field $B_0 = 4.1$ T perpendicular to the sample's surface.

During the measurements, ^{8}Li's P, defined by Equation (4.22). In this process, an electron is preferentially emitted opposite to the direction of the nuclear

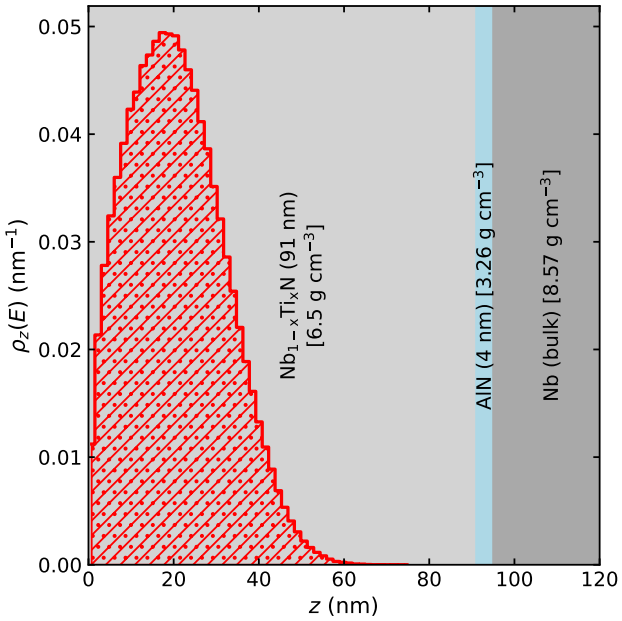

Figure 7.2: Simulated stopping profile for 10^6 $^8Li^+$ implanted in $Nb_{0.75}Ti_{0.25}N$(91 nm)/AlN(4 nm) /Nb at energy $E = 4.85$ keV, obtained using the SRIM Monte Carlo code [183]. The target's layer thicknesses and material densities are indicated in the inset. The stopping profile $\rho_z(E)$ (i.e., the distribution of implantation depths z) is represented as a histogram, whose mean implantation depth $\langle z \rangle \approx 21$ nm and straggle (i.e., standard deviation) $\sigma_z \approx 11$ nm.

polarization at the time of decay. This was done using a pair of fast plastic scintillation counters positioned 180° apart with respect to each other along the beam axis [142, 178]. During the data acquisition, the handedness of the laser polarization used during optical pumping was periodically alternated to control the $^8Li^+$ beam's helicity (i.e., positive and negative) [142], with data recorded separately for each polarization sense ±. The four-counter method was used to form the β-decay asymmetry $\mathscr{A}$, which is proportional to P by Equation (4.40).[1]

In this work, two types of experiments were conducted (i) resonance measurements, where the steady-state (i.e., time-integral) spin-polarization was monitored as a function of the frequency of the small RF magnetic field B_1, which is used to map the (static) local field distribution; and (ii) SLR measurements, where the

[1]Forming the asymmetry in this manner has the advantage of implicitly removing select detection systematics (e.g., different detector efficiencies).

temporal decay of P caused by stochastic fluctuations in the probe's local field is monitored both during and following implantation. In the former, a continuous $^{8}Li^{+}$ beam was used with the frequency of the small transverse RF field stepped slowly near ^{8}Li's Larmor frequency by Equation (4.5), where γ is the gyromagnetic magnetic ratio of ^{8}Li.

On resonance, the ^{8}Li spin precesses rapidly due to the RF field, resulting in a loss of the time-averaged asymmetry. Multi-frequency techniques were also used to search for small "quadrupolar" features (see, e.g., Refs. [309, 310]). For the SLR measurement, a pulsed $^{8}Li^{+}$ beam was used with a typical duration $\Delta \sim 4\,\mathrm{s}$. As the initial state of the probe nuclei are *very* far from thermal equilibrium, no RF field is required to measure SLR, unlike conventional NMR. During the pulse, the polarization approaches a dynamic equilibrium value, while afterward it relaxes to ~0. Notably, data acquired in this manner has a characteristic bipartite form with (statistical) error bars that are governed by Poisson statistics. This uncertainty is minimized near the pulse's trailing edge, but increases exponentially with the ^{8}Li lifetime afterward (see, e.g., [304]). In the present study, the typical duration of either measurement was ~15 min to ~30 min.

7.2.1 Sample Preparation

First, flat Nb substrates were prepared by cutting fine-grain Nb stock sheets (Wah Chang Corporation) with a residual-resistivity ratio (RRR) > 150 and machining them into flat plates approximately 12 mm by 8 mm by 0.5 mm. Following machining, the samples underwent buffered chemical polishing (BCP) (see, e.g., [217]) to remove the topmost ~100 μm of material from the surface. Subsequently, the samples were annealed at 1400 °C for 5 h to relieve any remaining mechanical stresses in the metal. After annealing, an additional round of BCP was performed to remove the topmost ~10 μm of material from the surface, effectively eliminating any contaminants introduced during the annealing process.

The $Nb_{1-x}Ti_xN$/AlN bilayer was deposited on a Nb substrate using thermal atomic layer deposition (ALD) in a custom-built reactor at CEA Saclay [311]. The AlN layer was grown using a standard process with $AlCl_3$ and NH_3 precursors [312], while the $Nb_{1-x}Ti_xN$ film was deposited at 450 °C by alternating NbN and TiN cycles. Its composition can be controlled by adjusting the number of TiN and NbN cycles [48, 300, 301]. In this work, each $Nb_{1-x}Ti_xN$ supercycle consisted of 4 ($TiCl_4$ + NH_3) cycles followed by 1 ($NbCl_5$ + NH_3) cycle, as the subsequent $NbCl_5$ pulse etches surface Ti in the form of volatile $TiCl_4$. NH_3 was pulsed for 0.5 s, $TiCl_4$ for 2.5 s, and $NbCl_5$ for 1 s, with 10 s purges after each step. This yielded a Ti/Nb ratio of 0.25 (x = 0.25), confirmed by x-ray photoelectron spectroscopy (XPS) [48]. Excess nitrogen incorporated during deposition was effectively removed by high-vacuum annealing at 900 °C [48]. Further discussion on the annealing process, along with additional characterization, can be found in Section 7.6.1 of the Supplemental Material Section 7.6.

The film's characteristic superconducting transition temperature T_c was determined to be ∼15 K using a vibrating sample magnetometer (VSM). Point contact tunneling (PCT) [313, 314] measurements on a similarly prepared sample show a spatial variation in the density of states near the Fermi level, which is encapsulated by an energy gap $\Delta = 2.49(29)$ meV and a Dynes-like [66] broadening parameter $\Gamma_D = 0.10(6)$ meV. Full characterization details, along with complementary measurements on similarly prepared samples, are presented in Section 7.6.2 of the Supplemental Material Section 7.6.

7.3 Results and analysis

7.3.1 Resonance Spectra

Typical resonance spectra in $Nb_{0.75}Ti_{0.25}N$ are presented in Figure 7.3. At all temperatures, the lineshape consists of a single, broad resonance whose ampli-

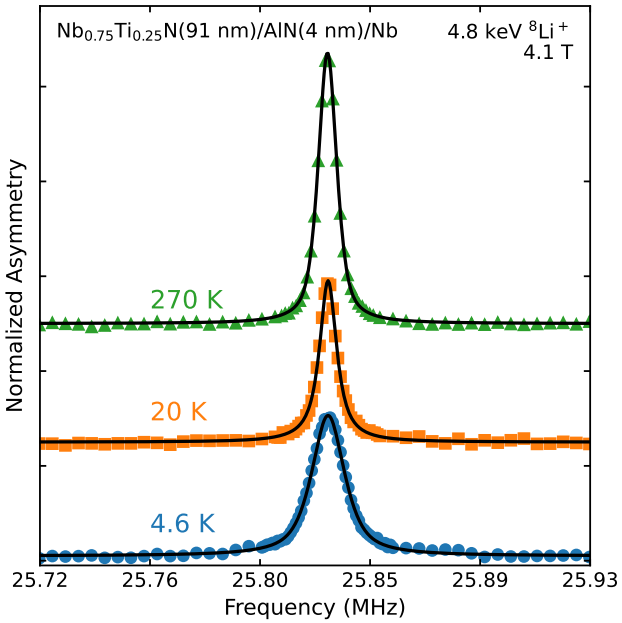

Figure 7.3: Typical ^{8}Li NMR lineshapes in $Nb_{0.75}Ti_{0.25}N$(91 nm)/AlN(4 nm)/Nb, measured in an applied field $B_0 = 4.1$ T perpendicular to the sample's surface, at select temperatures T (indicated in the figure) above and below the film's critical temperature $T_c \approx 15$ K. For $T > T_c$, the resonance linewidth remains roughly T-independent, but broadens by up to a factor of ~2 at lower temperatures. The solid black lines represent fits to the data using Equation (7.1).

tude decreases with decreasing temperature. The simplicity of this spectral shape suggests that all implanted $^8Li^+$ stop in high-symmetry lattice positions where the local electric field gradients (EFGs) is vanishing.[2] These sites are likely the tetrahedral interstitial positions (e.g., (1/4, 1/4, 1/4) in Figure 7.1), which are vacant in the ideal rocksalt structure. Such a site assignment aligns with the cubic symmetry of $Nb_{1-x}Ti_xN$ (see Figure 7.1), as well as with observations in isostructural compounds like MgO [315]. In the film's normal state, the resonance's width is approximately temperature-independent, with a full width at half maximum (FWHM) of 8.126(18) kHz. This large width is likely due to the high natural abundance of spin-active isotopes that make up the film's elemental composition (see Table 7.1), and is consistent with values predicted from dipolar broadening

[2]To confirm the absence of any (static) non-zero EFGss, we also performed frequency comb measurements (see, e.g., Refs. [309, 310]), which greatly amplifies the sensitivity to such features. No evidence for any finite EFGss was found at all measured temperatures.

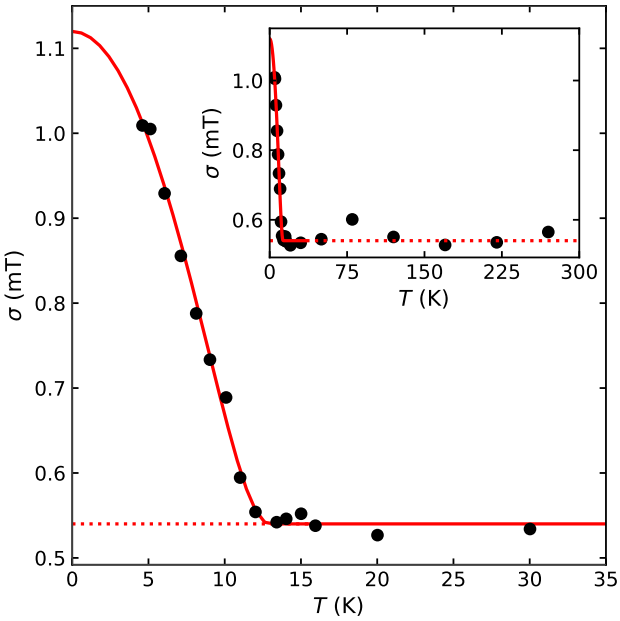

Figure 7.4: Temperature T dependence of the Gaussian component σ of the resonance linewidth $Nb_{0.75}Ti_{0.25}N(91\,nm)/AlN(4\,nm)/Nb$ in an applied field of $B_0 = 4.1\,T$ perpendicular to its surface. Note that the parameter σ is expressed as a magnetic field in units of mT. The solid red line represents a fit to the data for $T < 35\,K$ using the model given by Equations (2.41), (2.49), (7.2) and (7.3) and Equation (2.16) with $n = 2$, capturing the line broadening below the superconducting transition temperature T_c, with the T-independent (normal state) contribution highlighted as a dotted line. Measured values at temperatures up to 270 K are shown in the inset, where (apart from some small scatter) σ's T-independence is evident.

by host nuclear spins for the likely interstitial or substitutional sites in an ideal, unperturbed host lattice. Below T_c, the resonance broadens substantially, with the linewidth gradually increasing by a factor ~2. Such a broadening is typical of a superconductor upon formation of the vortex state's flux-line lattice (FLL) [82].

To quantify these features, the resonances were fitted using a phenomenological pseudo-Voigt (pV) function:

$$pV(\nu) = \mathcal{A}\left[\alpha G(\nu) + (1-\alpha)L(\nu)\right], \tag{7.1}$$

which represents a linear combination of Gaussian (G) and Lorentzian (L) com-

Table 7.1: Stable spin-active nuclei present in $Nb_{1-x}Ti_xN$. Here, n_A is the natural isotopic abundance, I is the nuclear spin, γ is the gyromagnetic ratio, and Q is the electric quadrupole moment. For comparison, properties of our βNMR probe ^{8}Li are also listed. Inapplicable properties are marked by an asterisk (*).

Isotope	n_A (%)	I	$\gamma/(2\pi)$ (MHz T^{-1})	Q (mb)
^{14}N	99.58	1	3.077 71	+20.44
^{15}N	0.42	1/2	−4.317 27	*
^{47}Ti	7.44	5/2	−2.404 10	+302
^{49}Ti	5.41	7/2	−2.404 75	+247
^{93}Nb	100	9/2	10.439 56	−320
^{8}Li	*	2	6.301 98	+32.6

ponents:

$$G(\nu) \equiv \exp\left(-\frac{(\nu-\nu_0)^2}{2\sigma^2}\right),$$
$$L(\nu) \equiv \frac{\Gamma_L^2}{(\nu-\nu_0)^2+\Gamma_L^2}.$$

and it mimics features of the true Voigt function which is a convolution of the two, and provides a good description of the data. Here, $\mathcal{A}$ is the resonance amplitude, $\alpha \in [0,1]$ is a mixing term that defining the lineshape's Gaussian fraction, ν_0 is the resonance frequency, $\sigma = \Gamma/(2\sqrt{2\ln 2})$ is the Gaussian width parameter, $\Gamma_L = \Gamma/2$ defines the Lorentzian width, and Γ denotes the line's (common) FWHM. Consistent with the qualitative description above, the T-dependence of the line's FWHM remains its most salient feature. Assuming the Lorentzian contribution to the line is systematic (i.e., "power broadening" from the single-tone continuous wave (CW) technique described in Section 7.2),[3] we encapsulate this broadening by σ's T-dependence, which is shown in Figure 7.4. Although some scatter is evident, σ remains approximately constant above T_c, but increases monotonically below the superconducting transition.

[3]Which is nearly T-independent in the film's normal state but decreases monotonically below T_c.

To understand this broadening, we consider the following model. In the normal conducting (nc) state, the Gaussian width σ can be approximated by a T-independent constant, whereas in the vortex state the measured value consists of a convolution of the superconducting (sc) and nc contributions:

$$\sigma^2 = \begin{cases} \sigma_{\mathrm{sc}}^2 + \sigma_{\mathrm{nc}}^2, & T < T_{\mathrm{c}}, \\ \sigma_{\mathrm{nc}}^2, & T \geq T_{\mathrm{c}}. \end{cases} \tag{7.2}$$

In an isotropic type-II superconductor with GL parameter $\kappa \gg 1$, σ_{sc} is related to the material's effective magnetic penetration depth λ_{eff} by replacing λ_{L} in Equation (2.41) [74, 82], where $\Phi_0 = 2.068 \times 10^{-15}$ Wb is the magnetic flux quantum.[4] In thin-film superconductors subjected to a magnetic field normal to their surface, when the film thickness d is smaller than the material's (bulk) penetration depth λ, λ_{eff} is given by the Pearl length [316]:

$$\lambda_{\mathrm{eff}}(T) = \frac{\lambda^2(T)}{d}, \tag{7.3}$$

where we account for λ's T-dependence using the analytic approximation by Equation (2.16) with $n = 2$,[5] where $\lambda(0\,\mathrm{K})$ is the penetration depth at 0 K and $T_{\mathrm{c}}(B_0)$ accounts for the suppression of the transition temperature in an applied field.[6] We treat this suppression empirically by inverting an analytic approximation for the simplest solution to the Werthamer-Helfand-Hohenberg (WHH) [318] expression for B_{c2} by Equation (2.49) [83], where, $t \equiv T_{\mathrm{c}}(B)/T_{\mathrm{c}}(0\,\mathrm{T})$. Further details are given in Section 7.6.3 of the Supplemental Material Section 7.6. We note that WHH theory has been used describe the T-dependence of B_{c2} in $Nb_{1-x}Ti_xN$ [265, 295] and related materials (e.g., NbTi [317] and Nb_3Sn [83]), implying the correctness of

[4] As $Nb_{1-x}Ti_xN$ alloys exhibit small coherence lengths [253, 255, 267, 291] and large magnetic penetration depths [5, 100, 252, 256, 279, 289, 290], which together imply a large GL parameter.

[5] The form of Equation (2.16) with $n = 2$ closely approximates the T-dependence predicted by Bardeen-Cooper-Schrieffer (BCS) theory (see, e.g., [53]).

[6] Note that the exponent in Equation (2.16) is 2 here, unlike its more common value of 4 found in the two-fluid model. This choice is intentional, as it better describes $\lambda(T)$ in $Nb_{1-x}Ti_xN$ [290] and NbTi [317].

this choice here, where fitting our data to this expression yields $B_{c2}(0\,\mathrm{K}) = 18(4)$ T.

A fit of Equations (2.41), (2.49), (7.2) and (7.3) and Equation (2.16) with $n = 2$ to the $\sigma(T)$ data is shown in Figure 7.4. In the fit, both the film thickness $d = 91$ nm and the applied field $B_0 = 4.1$ T were fixed to their known values (see Section 7.2), with all other parameters left free. The fit is in good agreement with the data, with the optimal values for the free parameters summarized in Table 7.2. At this juncture, we note the good agreement of the extracted T_c with the value identified by magnetometry measurements (see Section 7.2.1), as well as the $\lambda(0\,\mathrm{K})$ measured in other films [5]. We shall consider these results further in Section 7.4.1.

Table 7.2: Fit parameters describing the temperature dependence of resonance linewidth's Gaussian component σ (shown in Figure 7.4) using Equations (2.41), (2.49), (7.2) and (7.3) and Equation (2.16) with $n = 2$. Here, $d_{Nb_{0.75}Ti_{0.25}N}$ is the thickness of the $Nb_{0.75}Ti_{0.25}N$ thin film, $T_c(0\,\mathrm{T})$ is the critical temperature at 0 T, $\lambda(0\,\mathrm{K})$ is the penetration depth at 0 K, σ_{nc} is the Gaussian width in the normal conducting state, B_0 is the applied magnetic field, and $B_{c2}(0\,\mathrm{K})$ represents the upper critical field at 0 K. Both $d_{Nb_{0.75}Ti_{0.25}N}$ and B_0 were determined independently and fixed during fitting.

Parameter	Value	Unit	Comment
$d_{Nb_{0.75}Ti_{0.25}N}$	91	nm	fixed (from Section 7.2.1)
$T_c(0\,\mathrm{T})$	15.4(7)	K	
$\lambda(0\,\mathrm{K})$	180.57(30)	nm	
σ_{nc}	540.1(19)	μT	
B_0	4.1	T	fixed (from Section 7.2)
$B_{c2}(0\,\mathrm{K})$	18(4)	T	

Besides the changes to the resonance lineshape induced by the superconducting transition, we also quantified ^{8}Li's NMR shift K^c in the film. Using the resonance position in single crystal MgO with $B_0 \parallel (100)$ at 295 K as a reference [315], K^c (in ppm) is obtained using the expression (see, e.g., [319]):

$$K^c = 10^6 \left(\frac{\nu_0/\zeta_0 - \nu_{MgO}/\zeta_{MgO}}{\nu_{MgO}/\zeta_{MgO}} \right), \tag{7.4}$$

where the factor

$$\zeta_i = 1 + \left(\frac{1}{3} - N_i\right)\chi_i \tag{7.5}$$

corrects for contributions from demagnetization,[7] with N_i denoting the demagnetization factor and χ_i denoting the material's volume susceptibility. While details of the full calculation can be found in Section 7.6.4 of the Supplemental Material Section 7.6, we summarize the main results below. We find that K^{c} varies between +15 ppm to +35 ppm over the measured T-ranges. This magnitude is typical of ^{8}Li in many materials [142, 304], but as is common with small NMR shifts, corrections for demagnetization are a dominant contribution (+25.4 ppm here).[8] This range of K^{c} is small compared to other metals (see, e.g., [320]), suggesting weak hybridization with the ternary alloy's conduction band. We shall consider this quantity further in Section 7.4.1.

7.3.2 SLR Spectra

Representative time-differential SLR data at various temperatures are shown in Figure 7.5. At low temperatures the relaxation is very slow, approaching the limit of what is measurable by ^{8}Li due to its radioactive lifetime [142]. As the temperature is raised, so too does the relaxation, though it remains slow compared to other cubic metals (e.g., Ag [177] and Nb [321]), but comparable to other metallic compounds where the probe's hybridization with the conduction band is weak [322–324]. Interestingly, this increase in relaxation is non-monotonic with temperature, with a local maximum observed near ∼140 K. At all temperatures, the SLR is non-exponential, as might be expected for a host with an abundance of spin-active nuclei (see Table 7.1) and three-dimensional (3D) disorder (see, e.g., [325]). We note that even in the absence of structural disorder from alloying,

[7] Note that the form of Equation (7.4) correctly accounts for the general case when both the sample and reference have different magnetic susceptibilities and demagnetization factors.

[8] The "raw" (i.e., uncorrected) ^{8}Li NMR shifts were measured to range from −10 ppm to +10 ppm.

^{93}Nb NMR of the end member NbN also displays non-exponential SLR [326], suggesting the behaviour may be intrinsic.

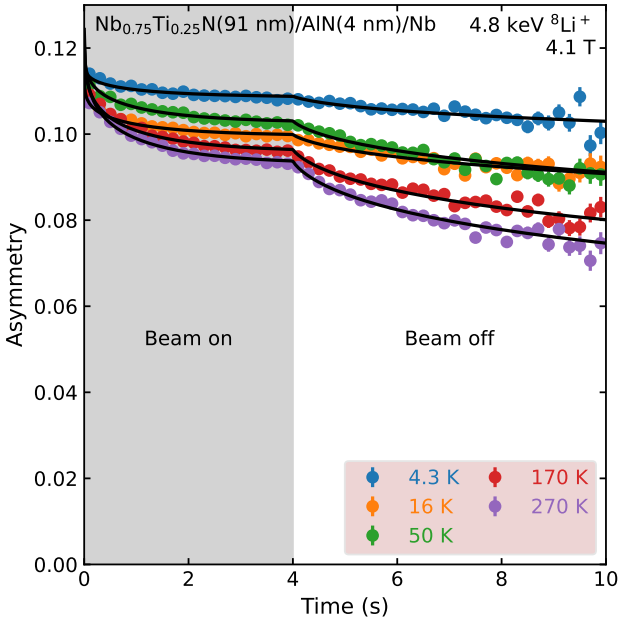

Figure 7.5: ^{8}Li SLR data at various temperatures T in $Nb_{0.75}Ti_{0.25}N$(91 nm)/AlN(4 nm)/Nb, measured under a perpendicular applied field of $B_0 = 4.1$ T. The shaded region indicates the duration of the $^{8}Li^{+}$ beam pulse (4 s). The data exhibit T-dependent relaxation that is non-monotonic with temperature, with a significant non-relaxing or very slow-relaxing component. The solid black lines represent fits to a stretched exponential [Equation (7.6)] convoluted with the $^{8}Li^{+}$ beam pulse using a common stretching exponent β (described in Section 7.3.2). The displayed data have been binned by a factor of 20 for clarity.

To quantify these observations, we adopt a phenomenological approach used to analyze other disordered metal-like compounds [323, 324] and fit the SLR data using a stretched exponential model. Explicitly, for an ^{8}Li ion implanted at time t', the spin polarization at a later time $t > t'$ is given by:

$$P(t,t') = \exp\left(-\left[\frac{(t-t')}{T_1}\right]^{\beta}\right), \tag{7.6}$$

where $1/T_1$ is the SLR rate (i.e., the reciprocal of the signal decays to $1/e$ of its initial value) and $0 < \beta \leq 1$ is the stretching exponent. This model provides a simple yet effective fit to the data, while minimizing the number of free parameters.

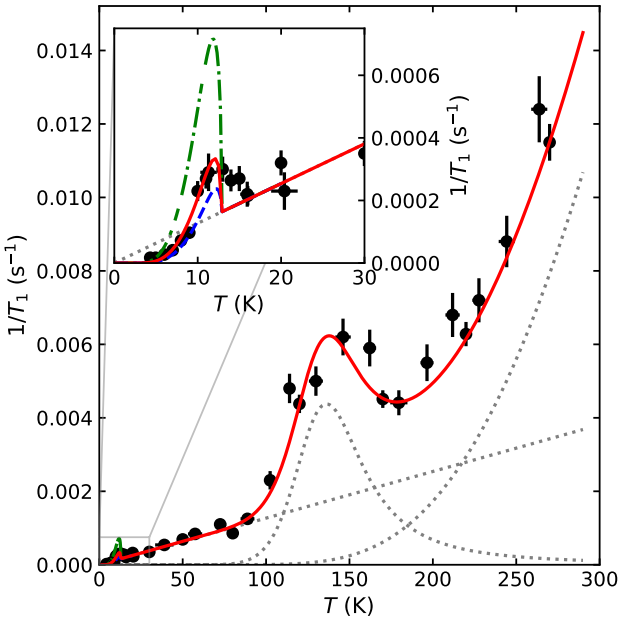

Figure 7.6: Temperature T-dependence of the ^{8}Li SLR rate $1/T_1$ in $Nb_{0.75}Ti_{0.25}N$(91 nm)/AlN (4 nm)/Nb at $B_0 = 4.1$ T. $1/T_1$ varies nonmonotonically with temperature, with T-linear behavior below ~100 K that is modified by a Hebel-Slichter coherence peak below the film's T_c (see inset for a detailed view). Near ~140 K, a BPP peak is observed, while at higher temperatures $1/T_1$ increases exponentially with increasing T. The solid red line shows the fit to Equations (2.32), (2.49) and (7.7) to (7.14) (described in Section 7.3.2), with the individual contributions from the linear slope, BPP peak, and exponential rise shown as dotted lines. The green dash-dotted and blue dashed curves show the expected Hebel-Slichter coherence peak for fixed $\Gamma_D = 0$ and 0.1 meV, respectively, using the same fit parameters.

To further avoid overparameterization, all SLR data were fit simultaneously using Equation (7.6) convoluted with the 4 s beam pulse and a shared $\beta = 0.216(6)$.[9] While this approach yields an excellent fit (reduced $\chi^2 \approx 1.02$), as pointed out by others [327, 328], this choice has the caveat of imparting some temperature dependence to A_0. We assert that this choice does not impede the quantitation of $1/T_1$ and that this model provides a simple, accurate fit across all measured conditions.[10] We note that the small β indicates a very broad distribution of rates, and the relaxation could also be modeled as a sum of exponentials. However,

[9]This suggests a significant fraction of ^{8}Li relax much more slowly than the fitted $1/T_1$, likely due to weak coupling to the electronic system in low-density or poorly metallic regions, beyond simple site-to-site Korringa variation.

[10]For example, sharing A_0 instead of β yields a very similar fit, with a virtually identical T-dependence to $1/T_1$.

the extra parameters required to define this relaxation lead to overparametrization. The resulting $1/T_1$ values in both normal and superconducting states are shown in Figure 7.6.

Consistent with the above observations, the T-dependence of $1/T_1$ exhibits a rich assortment of behavior. At temperatures below ~100 K, $1/T_1$ varies linearly with T, typical of metallic systems [305]. Near the film's T_c, this linear proportionality is modified, revealing a small Hebel-Slichter coherence peak [306, 307] that decays exponentially to zero for $T \ll T_c$. Such a feature is expected for an s-wave BCS superconductor, but a rare observation by ^{8}Li βNMR (see, e.g., [185]). Above ~100 K, additional relaxation contributions appear superimposed on the T-linear contribution. At ~140 K, $1/T_1$ goes through a local maximum, reminiscent of a Bloembergen-Purcell-Pound (BPP) peak [329]. At higher temperature, the peak vanishes and $1/T_1$ increases exponentially, suggesting another distinct contribution to the SLR.

With these qualitative features in mind, we now consider a quantitative model to describe them. We postulate that the distinct T-dependencies of $1/T_1$ correspond to the presence of distinct relaxation mechanisms, with the measured SLR rate corresponding to their sum. We make the *ansatz* that the rate contributions can be added linearly:

$$\frac{1}{T_1} = \left(\frac{1}{T_1}\right)_{\mathrm{e}} + \left(\frac{1}{T_1}\right)_{\mathrm{BPP}} + \left(\frac{1}{T_1}\right)_{\mathrm{exp}}, \tag{7.7}$$

where each $(1/T_1)_i$ term represents a specific contribution i. Here, we assign $i = \mathrm{e}$ to relaxation due to conduction electrons, $i = \mathrm{BPP}$ to the BPP peak, and, $i = \mathrm{exp}$ to the exponential takeoff at high-T. We now consider the detailed form of each mechanism.

The SLR in metallic systems is governed by spin-flip scattering "collisions" between conduction electrons and the probe nuclear spins. The magnitude of this contribution is proportional to the density of states (DOS) at the Fermi level E_F,

as well as the probe's hybridization with the host's conduction band, yielding a relaxation rate that varies linearly with T [305]. In BCS superconductors below T_c, the condensation of Cooper pairs along with the opening of a gap in the DOS at E_F modifies this linearity, producing a coherence peak [306, 307] just below T_c and exponential decay of $(1/T_1)_e$ to zero as $T \to 0\,\mathrm{K}$ (i.e., due to the freezing-out of all cross-gap thermal excitations). Quantitatively, this can be described by (see, e.g., [302, 330, 331]):

$$\left(\frac{1}{T_1}\right)_e = \begin{cases} mT, & T > T_c \\ mT \times \dfrac{2}{k_B T} \displaystyle\int_0^\infty f(E)[1 - f(E')][N_s(E)N_s(E') + M_s(E)M_s(E')]dE, & T \leq T_c \end{cases} \tag{7.8}$$

where m is the so-called Korringa slope [305], E and $E' = E + \hbar\omega_0$ are the superconducting quasiparticle energies in their initial and final scattering states (the latter defined by the NMR probe's Larmor frequency), $f(E)$ is Fermi function:

$$f(E) = \frac{1}{\exp\left[E/(k_B T)\right] + 1},$$

k_B is the Boltzmann constant, $N_s(E)$ denotes the superconducting DOS, and $M_s(E)$ refers to the anomalous quasiparticle density arising from the coherence factor [302, 332]. These latter two quantities can be expressed as:

$$N_s(E) = \mathrm{Re}\left\{(E - i\Gamma_D)/[(E - i\Gamma_D)^2 - \Delta^2]^{1/2}\right\}, \tag{7.9}$$

$$M_s(E) = \mathrm{Re}\left\{\Delta/[(E - i\Gamma_D)^2 - \Delta^2]^{1/2}\right\}, \tag{7.10}$$

where Δ is the superconducting energy gap by Equation (2.32) [64] where $\Delta(0\,\mathrm{K})$ is the gap's value at $0\,\mathrm{K}$, and Γ_D is an empirical broadening parameter (e.g., accounting for finite quasiparticle lifetimes) [66]. Additionally, the dependence of T_c under an applied magnetic field follows the same relationship as described in Equation (2.49), and also quantifies the B_{c2} independently.

We now consider the SLR contribution from the BPP peak. Quite generally, a local maximum in the SLR rate manifests when the correlation rate τ_c^{-1} of the fluctuating interaction causing the relaxation matches the probe's Larmor frequency [see Equation (4.5)]. Far away from this "resonance," the contribution to the relaxation is negligible, leaving a "peak" that is superimposed atop the other SLR contributions. Explicitly, this contribution can be described by [329, 333]:

$$\left(\frac{1}{T_1}\right)_{\text{BPP}} = c(J_1 + 4J_2) \tag{7.11}$$

where c is a coupling constant proportional to the mean-squared transverse fluctuating field, and J_n is the n-quantum NMR spectral density function [333]:

$$J_n = \frac{\tau_c}{1 + (n\omega_0\tau_c)^2}. \tag{7.12}$$

As ω_0 is fixed in the measurements, the temperature dependence of Equation (7.11) arises from τ_c^{-1}, which we assume follows an Arrhenius form:

$$\tau_c^{-1} = \tau_0^{-1} \exp\left[-E_A/(k_B T)\right], \tag{7.13}$$

where τ_0^{-1} is the attempt frequency, and E_A is the activation energy. Note that these expressions are agnostic the source of the (thermally activated) dynamics causing the relaxation "peak."

Finally, we consider a model for the growth of the SLR observed for $T \gtrsim 200$ K. Recalling the exponential-like take-off noted above, we describe this behavior empirically using:

$$\left(\frac{1}{T_1}\right)_{\text{exp}} \approx g \exp\left[-E_{\text{exp}}/(k_B T)\right], \tag{7.14}$$

where g is a prefactor, E_{exp} is the activation energy. Note that the form of Equation (7.14) is identical to Equations (7.11) to (7.13) in the "slow fluctuating" limit (i.e., when $\tau_c^{-1} \ll \omega_0$).

Combining the above models [Equations (2.32), (2.49) and (7.7) to (7.14)], we fit the $1/T_1$ vs. T data shown in Figure 7.6. For consistency with the lineshape analysis in Section 7.3.1, we fixed both $T_c(0\,\mathrm{T})$ and $B_{c2}(0\,\mathrm{K})$ at the values listed in Table 7.2. Similarly, we fixed Γ_D at 0.02 meV to mitigate its strong correlation with $\Delta(0\,\mathrm{K})$ (i.e., the present data lacks to the precision to simultaneously identify both quantities).[11] We note that this value small compared to what is expected from PCT (see Section 7.2.1); however, it is consistent with the range reported by others [298, 334, 335]. This (empirical) restriction notwithstanding, our approach enables a robust description of $1/T_1$'s T-dependence across both $Nb_{1-x}Ti_xN$'s normal and superconducting states, with the resulting fit in good agreement with the data (see Figure 7.6). Values of the extracted fit parameters are summarized in Table 7.3. We will return to considering these results in Section 7.4.2.

7.4 Discussion

The ^{8}Li βNMR data presented in Section 7.3 display a rich range of behavior. At temperatures below $\sim$100 K, the NMR response is metallic, with the most salient features occurring at or below the superconducting transition, where significant lineshape broadening coincides with a coherence peak in the SLR. At higher temperatures, the lineshape remains T-insensitive, while the SLR is dominated by additional sources of relaxation, deviating significantly from the T-linear Korringa response. Following this dichotomy, we divide our discussion into two parts. First, we consider the low-T metallic behavior in Section 7.4.1, followed by the dynamics observed at higher temperatures in Section 7.4.2.

[11] Alternatively, Γ_D can be determined by fixing $\Delta(0) = 2.49(29)$ meV, as obtained from PCT, yielding $\Gamma_D = 0.039(12)$ meV. The consistency of both parameters—regardless of which is fixed—demonstrates the robustness of the fit and agreement with independent PCT results.

Table 7.3: Fit parameters describing the temperature dependence of the SLR rate $1/T_1$ (shown in Figure 7.6) using Equations (2.32), (2.49) and (7.7) to (7.14). Here, $\Delta(0\,\mathrm{K})$ represents the superconducting gap at 0 K, $T_c(0\,\mathrm{T})$ is the critical temperature at 0 T, $\hbar\omega_0$ corresponds to the final scattering state associated with the ^{8}Li NMR frequency, Γ_D is the broadening parameter, m is the Korringa slope, B_0 is the applied magnetic field, $B_{c2}(0\,\mathrm{K})$ is the upper critical field at 0 K, τ_0^{-1} and E_A are the Arrhenius prefactor and activation energy from Equation (7.13), c is a coupling constant, while g and E_{exp} are the prefactor and activation energy from Equation (7.14). The values of $\hbar\omega_0$, B_0, $T_c(0\,\mathrm{T})$ and $B_{c2}(0\,\mathrm{K})$ are fixed, as the first two quantities are known independently, while the latter two are determined from resonance linewidth analysis (Table 7.2).

Parameter	Value	Unit	Comment
$\Delta(0\,\mathrm{K})$	2.60(12)	meV	
$T_c(0\,\mathrm{T})$	15.4	K	fixed (from Table 7.2)
$\hbar\omega_0$	1.1×10^{-4}	meV	fixed (from Section 7.2)
Γ_D	0.02	meV	fixed (from Refs. [298, 334, 335])
m	$12.7(6) \times 10^{-6}$	$\mathrm{s^{-1}\,K^{-1}}$	
B_0	4.1	T	fixed (from Section 7.2)
$B_{c2}(0\,\mathrm{K})$	18	T	fixed (from Table 7.2)
c	$0.50(5) \times 10^6$	$\mathrm{s^{-2}}$	
τ_0^{-1}	1×10^{12}	$\mathrm{s^{-1}}$	fixed (see Section 7.4.2)
E_A	0.0968(14)	eV	
g	0.6	$\mathrm{s^{-1}}$	fixed (see Section 7.4.2)
E_{exp}	0.1011(15)	eV	

7.4.1 Metallic & Superconducting Response

To start this section, we proceed with a discussion of the resonance lineshapes, whose salient feature is a broadening upon transition to the vortex state below T_c. From the analysis in Section 7.3.1, we find that $\lambda(0\,\mathrm{K}) = 180.57(30)$ nm for our film, in excellent agreement with a direct measurement using LE-μSR [5] and comparable to a crude estimate made for different $Nb_{1-x}Ti_xN$ stoichiometries [252]. Other studies have reported values where $\lambda \gtrsim 200$ nm [256, 279, 289, 290], suggesting that our measurement is likely closer to the alloy's *intrinsic* value (i.e., its London penetration depth $\lambda_L \sim 150$ nm [94]). While λ_L value is not well-defined, we may use it to estimate the GL parameter κ for our film via Equation (6.12) [55, 336], which makes use of the relationship between Φ_0 and the coherence lengths within BCS (ξ_0) and GL theory. Using the values for $\lambda(0\,\mathrm{K})$ and λ_L noted above,

along with $\xi_0 = 2.4(3)$ nm [253], Equation (6.12) yields $\kappa = 100(12)$, placing our film in the extreme type-II limit. While a value on this order is typical of $Nb_{1-x}Ti_xN$, we note that it justifies our use of Equation (2.41), which requires $\kappa \gtrsim 70$.

Similar to λ, the extracted critical temperature $T_c(0) = 15.4(7)$ K from the lineshape analysis agrees with the magnetometry measurements (see Section 7.2.1 and Section 7.6.2 of the Supplemental Material Section 7.6) and range expected for our film's stoichiometry [251, 252, 265, 266]. Given $Nb_{1-x}Ti_xN$'s variability in properties, particularly with synthesis and form (see Section 7.1), this level of agreement is encouraging. Unique to our analysis approach though, is using T_c's suppression by B_0 to make an estimate of our film's upper critical field $B_{c2}(0\,\mathrm{K})$. This value turned out to be 18(4) T, which has a high relative uncertainty (~22 %), largely due to B_{c2}'s strong correlation with $T_c(0\,\mathrm{T})$. Nonetheless, its value is consistent with the range reported by others [267, 291, 294, 295]. To further validate this estimate, we calculate the ξ_{GL} by re-arranging Equation (2.46) [55], which yields $\xi_{GL}(0\,\mathrm{K}) = 4.3(5)$ nm, in excellent agreement with prior reports [253, 267, 291], further suggesting the reliability of our analysis approach.

We now turn our attention to the Knight shifts K^c extracted from the resonance data. As noted in Section 7.3.1, K^c is small and positive, ranging from +15 ppm to +35 ppm over the measured temperature range. The observed shift arises from a (presumably isotropic) contact hyperfine interaction, stemming from the hybridization of $^8Li^+$'s vacant $2s$ orbital with $Nb_{1-x}Ti_xN$'s conduction band. This weak coupling is a general feature of ^{8}Li βNMR, and similar observations have been noted for other cubic metals (see, e.g., [320]). While this static (i.e., time-average) contribution of the contact interaction gives rise to the resonance shift, its dynamic (i.e., time-dependent) component dominates ^{8}Li's low-T SLR, which we consider below.

The T-linear relaxation observed below ~100 K is one of the hallmarks of the

metallic state probed by NMR [152, 305]. Over this temperature range, a linear fit with zero intercept yields a slope $m = 12.7(6) \times 10^{-6}\,\mathrm{s}^{-1}\,\mathrm{K}^{-1}$. This value is surprisingly small and at least an order of magnitude less than in other cubic metals (cf. [320]). From relaxation in metals, this slope may be written as [152, 305]:

$$m \equiv \frac{1}{T_1 T} = \frac{2\pi k_B}{\hbar} A^2 \rho_e(E)^2, \tag{7.15}$$

where k_B is the Boltzmann constant, $\hbar$ is the reduced Planck constant, A is the hyperfine coupling (in units of energy), and $\rho_e(E)$ is the electronic DOS. It follows from Equation (7.15) that two sources can contribute to a small m: a small A or a small $\rho_e(E)$ (or both). Given the metallic nature of $\mathrm{Nb_{1-x}Ti_xN}$ [267, 292], the implication of this means that a small hyperfine coupling is the most probable source for the small m, but note that a small A is also unexpected given $\mathrm{Nb_{1-x}Ti_xN}$'s structure (see Figure 7.1). That is, in the rocksalt structure there are a limited number of sites for implanted $^8\mathrm{Li}^+$ that could facilitate this (cf. the van der Waals gap in layered chalcogenides [322–324]). Noting the absence of quadrupolar splittings to our resonance data (see Figure 7.3), symmetry constrains the possible candidates. We suggest the most plausible interstitial position to be the Wyckoff 8*c* site i.e., the tetrahedral interstitial sites in the face-centred cubic (FCC) lattice, situated in the center of the sub-cubes within the alloy's unit cell (see Figure 7.1), but note that $^8\mathrm{Li}^+$ may simply be substitutional for Nb/Ti in Wyckoff site 4*a*. The small m is even more surprising when one considers the (intrinsic) disorder present in the film, which generally *increases* its value [337, 338].

Further insight into the film's metallic behavior can be inferred from considering K^c and m in unison. Following a so-called Korringa analysis, we compute the (dimensionless) Korringa ratio [152, 321]:

$$\mathcal{K} \equiv \frac{(K^\mathrm{c})^2 T_1 T}{\mathcal{S}}, \tag{7.16}$$

where $\mathcal{S}$ is a constant specific to the NMR probe nucleus ($\mathcal{S} \approx 1.20 \times 10^{-5}$ s K for ^{8}Li). Using our measured value for m, along with $K^{c}(270\,\mathrm{K}) = 14.0(13)$ ppm, we obtain $\mathcal{K} = 1.29(25)$.[12] In the limit that the conduction electrons are non-interacting, one expects $\mathcal{K} = 1$; however, deviations from this can indicate (anti)ferromagnetic electronic correlations and are often encountered for weakly interacting systems [152] (see, e.g., [320]). Alternatively, a $\mathcal{K} > 1$ may be understood in terms of an enhancement factor η resulting from disorder [337, 338]:

$$\mathcal{K}_{\mathrm{measured}} = \mathcal{K}\eta,$$

caused by, for example, an increased residence time of the conduction electrons at the probe's site. Assuming electronic correlations in our film are negligible, an $\eta \approx 1.3$ at 270 K is implied. While this is quite modest on the scale of (disordered) conductors, it agrees with predictions (see, e.g., the "Warren plot" in Ref. [337]) based on our film's conductivity inferred from measured resistivity using four-point probe method (see Section 7.6.1 of the Supplemental Material Section 7.6). Despite the film's intrinsic disorder, the above suggests that its electronic behavior is consistent with nearly-free electrons, but close to the crossover to diffusive transport.

Having discussed the metallic SLR in the film's normal state, we now consider its modification below the superconducting transition, whose main feature is the Hebel-Slichter coherence peak [306, 307] below T_c (see the inset in Figure 7.6). While such an observation is rare for βNMR (see, e.g., ^{8}Li SLR in $NbSe_2$ [185]), its presence is not unexpected. For example, such a feature is also observed in the ^{93}Nb NMR of the alloy's end member NbN [326, 339]. One might anticipate that $Nb_{1-x}Ti_xN$'s intrinsic disorder may suppress such a feature, but given the alloy's modest enhancement factor η (see above), any suppression is likely minimal [340,

[12] If different values were chosen, such as $K^{c}(20\,\mathrm{K}) = 22.5(14)$ ppm or $K^{c}(120\,\mathrm{K}) = 20.3(13)$ ppm, the corresponding Korringa ratios would be $\mathcal{K} = 3.4(5)$ and $\mathcal{K} = 2.7(4)$, respectively.

341]. While our data is in good qualitative agreement with the theoretical description outlined in Section 7.3.2, it does not provide a perfect match. Notably, a rise in $1/T_1$ is observed above the onset of film's (average) T_c. Indeed, transport measurements of a similarly prepared sample on an Al_2O_3 substrate show a sharp transition at approximately 15 K, but with a small deviation beginning earlier around ~16 K [48], suggesting a range of T_c values. While the relaxation model captures the most prominent T_c, the SLR data appear much more sensitive to this distribution of transition temperatures than the resonance measurements (see Section 7.3.1). The precise reason for this is unclear; however, we remark that these deviations are small and that the SLR model does an excellent job of describing the data below the film's "characteristic" T_c. As will be clear below, this aberration does affect our ability to quantify parameters governing the coherence peak.

Following Equations (2.32) and (7.8) to (7.10), the magnitude of the Hebel-Slichter coherence peak is dictated primarily by two quantities: a zero-temperature gap $\Delta(0\,\mathrm{K}) = 2.60(12)\,\mathrm{meV}$,[13] and a Dynes [66] broadening parameter $\Gamma_D = 0.02\,\mathrm{meV}$. The extracted gap agrees with PCT measurements on similarly prepared samples (see Section 7.2.1). In contrast, the smaller Γ_D value inferred from βNMR differs from the PCT value of 0.10(6) meV, which is too large to account for the magnitude of the coherence peak (see Figure 7.6). This discrepancy could reflect differences in each technique's spatial sensitivity [PCT is only sensitive to depths up to ~10 nm, but has micrometer lateral resolution; βNMR has sensitivity to depths up to ~60 nm (see Figure 7.2), but averages over lateral distances on the order of millimeters (i.e., the $^8Li^+$ beam's spot size)]. The βNMR value of Γ_D agrees with the 0.015 meV to 0.02 meV range reported for $Nb_{1-x}Ti_xN$ thin-film coplanar waveguide resonators, where a Dynes broadening parameter Γ_D was required in Mattis-Bardeen [342] fits to microwave transmission measurements at

[13] This value reflects a spatial average over many vortex unit cells within the ~3 mm βNMR beam spot. Given the short GL coherence length $\xi_{GL} = 4.3(5)$ nm, the vortex cores occupy a negligible volume fraction, so the spatial variation of Δ in the mixed state can be neglected.

100 mK [298, 334, 335]. We note that without the broadening term (i.e., $\Gamma_D = 0$) the coherence peak is much too sharp relative to the data (see Figure 7.6).

Using the values of Γ_D and $\Delta(0\,\mathrm{K})$, the dimensionless ratio $\Gamma_D/\Delta(0\,\mathrm{K}) = 7.68(34) \times 10^{-3}$ was obtained, serving as a sensitive metric for quantifying disorder within the superconducting film. This value is consistent with tunneling studies on disordered films of $Nb_{1-x}Ti_xN$'s end members NbN [343] and TiN [344], and implies small disorder in the crystal lattice. The film's room temperature resistivity of 124 μΩ cm (see Supplemental Material Section 7.6 Section 7.6.1) further supports this, exceeding the >100 μΩ cm threshold for disorder reported in [299]. A corresponding $\Gamma_D/\Delta(0\,\mathrm{K}) = 0.040(24)$ extracted from PCT measurements, appears larger due to its higher absolute Γ_D, but still overlaps with the βNMR result. These results suggest that Γ_D at the surface is higher compared to that in the bulk of the film. The modest peak suppression and the overall agreement with the relaxation model [Equations (2.32) and (7.8) to (7.10)] is suggestive of *s*-wave symmetry of the Cooper pairs, consistent with other reports [299]. Returning to the zero-temperature gap, upon combining $\Delta(0\,\mathrm{K})$ with the $T_c(0\,\mathrm{T})$ determined from the resonance lineshape analysis we obtain a gap ratio $2\Delta(0\,\mathrm{K})/k_B T_c(0\,\mathrm{T}) = 3.92(25)$. This value aligns well with the 3.53 to 5 range reported in the literature [274–279, 289, 290, 296–298], and matches with values observed for films of similar stoichiometry [277]. This ratio is also consistent with the BCS strong-coupling limit, as well as other reports on $Nb_{1-x}Ti_xN$ [289, 297]. Overall, our measured parameters—including $T_c(0\,\mathrm{T})$, $\lambda(0\,\mathrm{K})$, $B_{c2}(0\,\mathrm{K})$, $\Delta(0\,\mathrm{K})$, and Γ_D—show good agreement with independent measurements detailed in the Supplemental Material Section 7.6 and the literature reviewed in Section 7.1.

With the alloy's superconducting properties established, it would be interesting in the future to study how they translate into preventing magnetic-flux-nucleation in SIS heterostructures.[14] Similar ^{8}Li βNMR measurements have been done on

[14] Particularly in ellipsoidal samples, which prevent field penetration from both sides of the superconducting layers and ensure a uniform magnetic response, making them a relevant proxy for SRF cavities.

"bare" and "baked" Nb [147] using a purpose-built βNMR spectrometer [3]. Such measurements would complement the findings of Ref. [5], but under conditions closer to those of state-of-the-art accelerator cavities [203].

7.4.2 High-T Dynamics

Similar to Section 7.4.1, we first discuss the ^{8}Li resonance at high temperatures. Above T_c, the lineshape is approximately T-independent, characterized by a field distribution width $\sigma_n = 540.1(19)\,\mu$T (see Figures 7.3 and 7.4). The absence of any pronounced linewidth reduction at elevated temperatures (i.e., "motional narrowing" [152]) immediately rules out long-range translational dynamics as the source of the dominant SLR contributions above ~100 K. While it is difficult to be conclusive about their origin, we consider some possibilities below.

To begin, we consider the BPP at ~140 K (see Figure 7.6). The fit of this peak to the model given by Equations (7.11) to (7.13) is characterized by three main terms: a coupling constant $c = 0.50(5) \times 10^6\,\mathrm{s}^{-2}$, an activation barrier $E_A = 0.0968(14)\,\mathrm{eV}$, and an assumed attempt frequency $\tau_0^{-1} = 10^{12}\,\mathrm{s}^{-1}$ (see Table 7.3), the latter being comparable to optical phonon frequencies. Consistent with the absence of "motional narrowing," the small E_A is incompatible with ^{8}Li$^+$ diffusion, which is typically characterized by a larger energy barrier (in all but the most exceptional lithium-ion conductors). This is reasonable based on $Nb_{1-x}Ti_xN$'s structure (see Figure 7.1), and the (nominal) ionic valence of its atomic constituents. Thus, the kinetic process causing relaxation must be *highly localized*. We shall hold off on speculating its origin for the time being, but note that the magnitude of the coupling term c is also rather small. This is surprising given $Nb_{1-x}Ti_xN$'s dense spin concentration (see Table 7.1); however, the dynamic component of the local field may have an origin distinct from the static component (cf. the ^{8}Li βNMR in Bi [345]).

We now consider the monotonic increase in $1/T_1$ above ~200 K, which is

empirically described by an Arrhenius-like relation [Equation (7.14)]. As noted in Section 7.3.2, Equations (7.11) to (7.13) reduce to this expression in the limit that $\tau_c^{-1} \ll \omega_0$, emphasizing its similarity with the BPP peak. This SLR component is governed by an activation energy $E_{exp} = 0.1011(15)$ eV and a fixed prefactor $g = 0.6\,s^{-1}$ (assigned empirically). The similarity of E_{exp} to E_A is remarkable and possibly suggests a connection between the two. Much like E_A, E_{exp}'s magnitude is suggestive of a localized kinetic process. A closer comparison with the former's kinetic details is, however, hampered by our ability to precisely identify g, which is only correct to an order-of-magnitude. This is often the case for fits in the "slow fluctuating" limit, where the coupling term is inseparable from the (apparent) prefactor. A crude calculation using c's magnitude suggests the g is equivalent to a τ_0^{-1} on the order of $\sim 10^6\,s^{-1}$, which is too low to be physical. While the kinetic process' true prefactor remains uncertain, we may infer that the coupling term for this likely exceeds c by several orders-of-magnitude.

Having discussed the high-T relaxation details, we now consider their possible origin. The observed relaxation may plausibly arise from several distinct microscopic processes. One possibility is from annealing of damage caused by $^8Li^+$ implantation, which creates Frenkel pairs (i.e., a vacancy and an interstitial defect) that may induce local atomic rearrangements, potentially involving a site-change transition of the probe ion. Another is the implantation-induced displacement of residual nitrogen atoms, leading to the formation of molecular N_2 whose thermally activated rotational or vibrational modes could weakly couple to the ^8Li spin system. A further possibility is the annealing of Ti/Nb interstitials, whose thermally activated migration to vacant 4*a* sites is supported by similar activation energies, reflecting their comparable ionic sizes and charges. Identifying the dominant origin among these possibilities is beyond the scope of this work, and further experimental studies are required to test these ideas. Additional SLR measurements at different applied fields may help refine our parameterization of the

underlying kinetic processes. Central to this may be identifying ^{8}Li's stopping site, which, for a dense spin system like $Nb_{1-x}Ti_xN$, may be accomplished by searching for avoided level-crossing resonances (ALCRs) over a wide range of applied fields (see, e.g., [346]). A recently upgraded βNMR spectrometer at TRIUMF is well-suited for this purpose [3].

7.5 Conclusion

Using implanted-ion ^{8}Li βNMR as a local space probe, we investigated the superconducting and normal-state properties of a $Nb_{0.75}Ti_{0.25}N$(91 nm)/AlN(4 nm)/Nb thin film between $4.6\,\mathrm{K} \leq T \leq 270\,\mathrm{K}$ in a 4.1 T field perpendicular to its surface. Resonance measurements revealed a broad lineshape in the normal state that (symmetrically) broadens below T_c due to FLL formation in the vortex state. From a fit to a broadening model, we find a superconducting transition temperature $T_c(0\,\mathrm{T}) = 15.4(7)\,\mathrm{K}$, an upper critical field $B_{c2}(0\,\mathrm{K}) = 18(4)\,\mathrm{T}$, and a magnetic penetration depth $\lambda(0\,\mathrm{K}) = 180.57(30)\,\mathrm{nm}$, in good agreement with independent measurements and estimates from the literature. SLR measurements find a metallic response at low-T with a Korringa slope $m = 12.6(6) \times 10^{-6}\,\mathrm{s^{-1}\,K^{-1}}$, which is modified by below T_c by a Hebel-Slichter coherence peak characterized by a superconducting gap $\Delta(0\,\mathrm{K}) = 2.60(12)\,\mathrm{meV}$ and a Dynes broadening parameter $\Gamma_D = 0.02\,\mathrm{meV}$. These findings yield a gap ratio $2\Delta(0\,\mathrm{K})/k_BT_c(0\,\mathrm{T}) = 3.92(25)$, consistent with strong-coupling behavior for the ternary alloy. These superconducting properties measured in thin films (not accessible by conventional NMR) are relevant for technological applications. In the future, it would be interesting to test explicitly how these properties translate into preventing magnetic-flux penetration in SIS heterostructures (e.g., for SRF cavity applications).

7.6 Supplemental

7.6.1 Structural and Thin Film Characterization

The $Nb_{1-x}Ti_xN$/AlN bilayer was deposited on a Nb substrate using thermal ALD in a custom-built reactor at CEA Saclay. ALD is a chemical-phase film deposition technique based on sequential, self-limiting gas-surface reactions, enabling atomic-scale thickness control. During this process, two or more chemical precursors are introduced to the surface separately, one at a time, following a cyclic sequence [311].

As mentioned in Section II A, the film stoichiometry is x = 0.25, corresponding to $Nb_{0.75}Ti_{0.25}N$. The optimization of film properties was characterized using a similarly prepared $Nb_{0.75}Ti_{0.25}N$ (50 nm)/AlN (∼10 nm)/Al_2O_3 sample [48], as summarized here. The thickness was determined by x-ray reflection (XRR) using a Rigaku Smartlab diffractometer with Cu K-α radiation. The as-deposited film exhibited a normal-state resistivity of ∼225 μΩ cm and a critical temperature $T_c \approx 7$ K, measured via the standard four-point probe method. This T_c is significantly lower than the typical value of ∼15 K, consistent with a reduced lattice constant $a \approx 4.25$ Å (measured by Grazing incidence x-ray diffraction (GIXRD)) and density 6.5 g cm^{-3} (measured by XRR). These reduced values are attributed to a nitrogen-rich growth environment, where $TiCl_4$ and $NbCl_5$ react with NH_3 [48], resulting in excess nitrogen, lattice distortion, and reduced crystallinity. Annealing improves crystallinity and superconducting properties of nitride films [347, 348]. By removing excess nitrogen, annealing resulted in lower resistivity ∼100 μΩ cm, higher $T_c \approx 14$ K, increased lattice constant $a \approx 4.31$ Å, and density of 6.6 g cm^{-3}.

The optimal annealing protocol involved heating to 800 °C at 6 °C min^{-1}, then to 900 °C at 18 °C min^{-1}, followed by immediate cooling using the same ramps without holding at 900 °C. This procedure was applied to fabricate our $Nb_{0.75}Ti_{0.25}N$ (91 nm)/AlN(4 nm)/Nb sample. Further film properties were characterized on a

witness $Nb_{0.75}Ti_{0.25}N$ (91 nm)/AlN(4 nm)/Al_2O_3 sample. Figure 7.7 represents fitting the XRR measurements yielded a $Nb_{0.75}Ti_{0.25}N$ density of 6.5 g cm^{-3} and an AlN thickness of 4 nm with a density of 3.26 g cm^{-3}. GIXRD confirmed a cubic $B1$ structure with lattice parameter $a = 4.313$ Å, as shown in Figure 7.8. The resistivity of the $Nb_{0.75}Ti_{0.25}N$ film was measured to be 124 μΩ cm on the same witness sample using a standard four-point probe method.

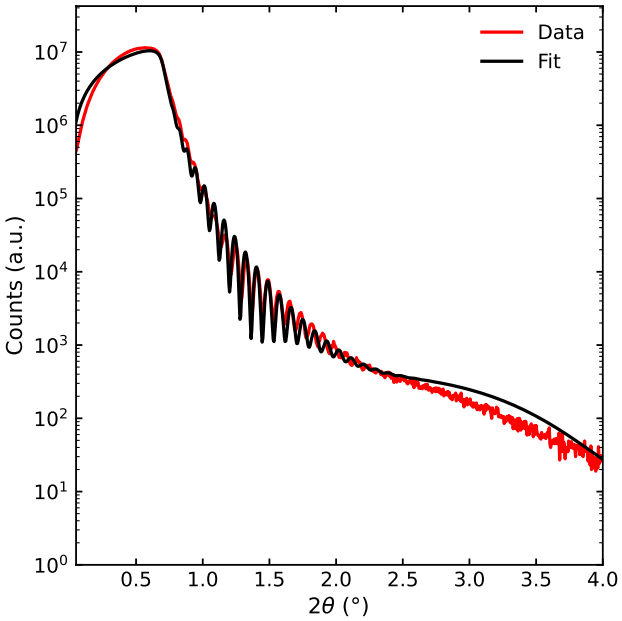

Figure 7.7: XRR measurement of the $Nb_{0.75}Ti_{0.25}N$(91 nm)/AlN(4 nm)bilayer deposited on an Al_2O_3 substrate. Experimental data (red curve) and the corresponding fit model (black curve) are shown.

7.6.2 Superconducting Properties Characterization

The superconducting critical temperature T_c was measured using VSM, which detects the "bulk" magnetization as a function of temperature, identifying T_c by the sharp drop in magnetization as the sample enters the Meissner state. For the $Nb_{0.75}Ti_{0.25}N$(91 nm)/AlN(4 nm)/Al_2O_3 sample, a clear superconducting transition was observed at approximately 15 K (see Figure 7.9(a)). In contrast, the $Nb_{0.75}Ti_{0.25}N$(91 nm)/AlN(4 nm)/Nb multilayer exhibited two distinct transitions:

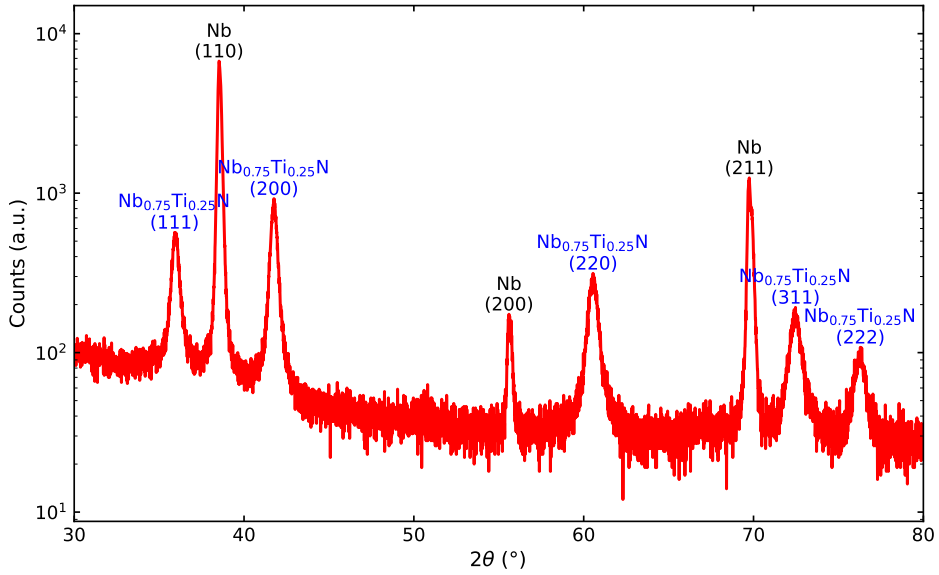

Figure 7.8: GIXRD pattern of the $Nb_{0.75}Ti_{0.25}N$/AlN/Nb multilayer structure. From the measured diffraction peak positions, the lattice parameter was determined to be $a = 4.313$ Å. The diffraction peaks corresponding to the $Nb_{0.75}Ti_{0.25}N$ film (shown in blue) indexed according to the cubic $B1$ NaCl-type structure. The prominent reflections appear at positions consistent with the (111), (200), (220), (311), and (222) planes of $Nb_{0.75}Ti_{0.25}N$. Peaks corresponding to the Nb substrate (shown in black) indexed as (110), (200), and (211) reflections, confirming FCC structure of the space group $Fm\bar{3}m$ as expected. The logarithmic intensity scale highlights both strong and weak reflections across the range of 2θ values from 30° to 80°.

a first at 15 K, attributed to the $Nb_{0.75}Ti_{0.25}N$ layer, and a second at 9.3 K, corresponding to the Nb substrate, as shown in Figure 7.9(b).

The surface superconducting properties were characterized on similarly prepared $Nb_{0.75}Ti_{0.25}N$(50 nm)/AlN(6 nm)/Nb multilayer structure using PCT, following the methodology described in Ref. [313]. This technique is a powerful and sensitive probe of the DOS in superconducting materials and has recently been applied in SRF contexts to reveal metallic inclusions and crystalline inhomogeneities in niobium surfaces [314]. In our setup, junctions were formed by approaching the sample surface with an Al tip, creating a superconductor-insulator-normal (SIN) junction where the insulator is the oxide layer on the sample surface. The PCT system used in this study is capable of measuring junction resistances spanning from a quasi-ohmic regime (a few hundred Ω) to a tunneling regime (up to 1 GΩ),

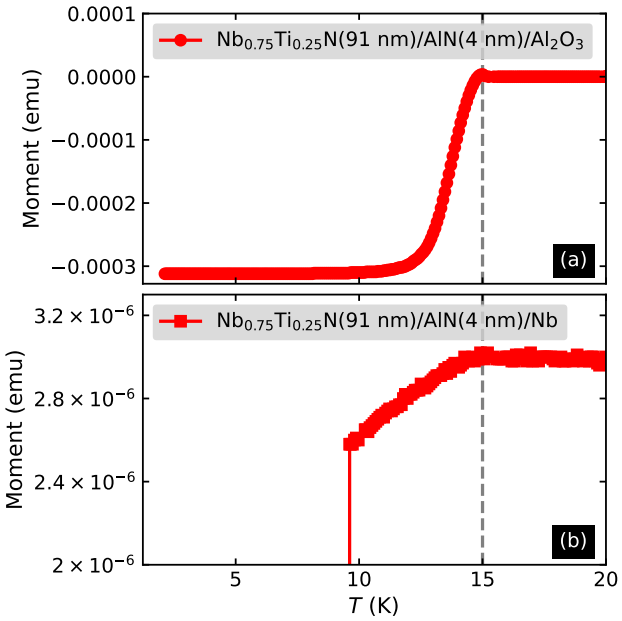

Figure 7.9: Superconducting transition temperature T_c measurements using VSM for (a) the $Nb_{0.75}Ti_{0.25}N$(91 nm)/AlN(4 nm)/Al_2O_3 sample, showing a single transition at 15 K, and (b) the $Nb_{0.75}Ti_{0.25}N$(91 nm)/AlN(4 nm)/Nb sample, displaying two transitions at 15 K and 9.3 K. The dashed lines indicate the corresponding T_c values in each plot.

while enabling lateral mapping of superconducting properties over areas ranging from tens of μm^2 to several mm^2. In the tunneling regime, the current I_{ns} flowing between a normal (n) metal electrode (in this case, an Al tip) and a superconducting (s) sample (e.g., a $Nb_{0.75}Ti_{0.25}N$ film) through an insulator (i.e., the oxide layer on the surface which is thin and formed during deposition) is measured as a function of the applied bias voltage V. The resulting PCT spectra provide information about the superconducting DOS. To quantitatively interpret these measurements, the data were analyzed using the standard expression for the differential tunneling conductance, expressed as:

$$\frac{dI_{ns}(V)}{dV} \propto \int_{-\infty}^{\infty} N_s(E) \left(-\frac{\partial f(E+eV)}{\partial (eV)} \right) dE, \tag{7.17}$$

where $N_s(E)$ is the superconducting DOS, and $f(E)$ is the Fermi-Dirac distribution function. Here the superconducting DOS, $N_s(E)$, was modeled using the Dynes

formula [66] given by Equation (2.34).

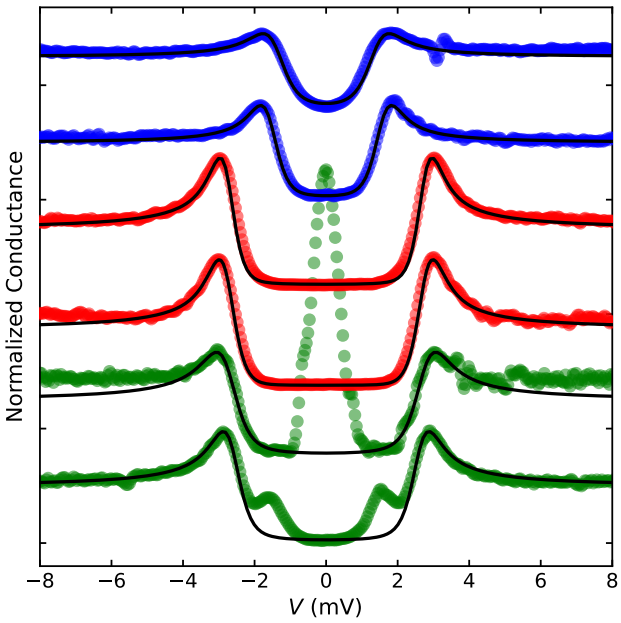

Figure 7.10: Representative tunneling conductance spectra measured on the $Nb_{0.75}Ti_{0.25}N$(46 nm) /AlN(8 nm)/Nb multilayer sample at 1.8 K within a 100 µm × 100 µm area. Closed circles are measured data points, while solid lines represent fit to the data using Equations (2.34) and (7.17). The data illustrate the range of junction behaviors observed: two with smaller superconducting gaps (top), two characteristic of ideal $Nb_{0.75}Ti_{0.25}N$ spectra (middle), and two exhibiting enhanced subgap conductance (bottom). Solid lines represent fits to the Dynes formula. The extracted parameters (Δ, Γ_D) in meV, from top to bottom, are: (1.44, 0.25), (1.56, 0.10), (2.74, 0.02), (2.75, 0.06), (2.74, 0.19), and (2.61, 0.143).

A total of approximately 100 junctions were measured within a 100 µm×100 µm area at 1.8 K. Representative tunneling conductance spectra alongside Dynes fits are presented in Figure 7.10. The data reveal a range of junction behaviors: some with smaller superconducting gaps (two top curves), some consistent with ideal $Nb_{0.75}Ti_{0.25}N$ spectra (middle two curves), and others showing subgap conductance features (bottom two curves), which may arise from magnetic impurities or local stoichiometric fluctuations within the $Nb_{0.75}Ti_{0.25}N$ film.

The statistical distributions of Δ and Γ_D, extracted from Dynes fits, along with their spatial maps, are shown in Figure 7.11. The histogram of Δ values was fitted with a Gaussian function (solid line in Figure 7.11(a)), yielding a distribution

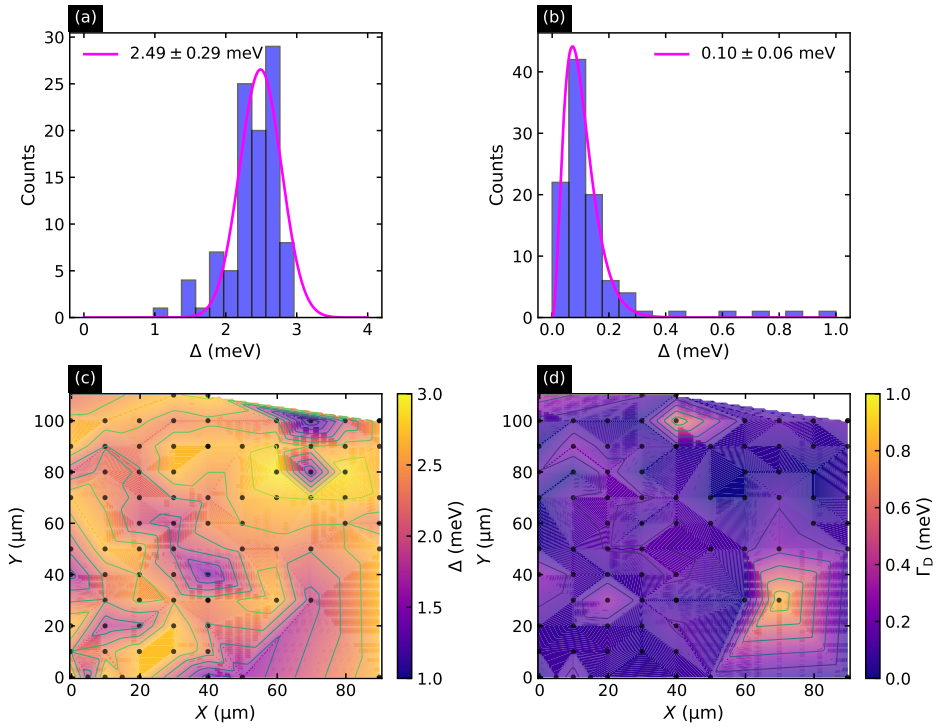

Figure 7.11: Statistics of the superconducting gap Δ and Dynes broadening parameter Γ_D were extracted from fits to tunneling conductance spectra measured at 1.8 K. (a) Histogram of the Δ, with a Gaussian fit (solid line) giving a mean value of $\Delta = 2.49(29)$ meV. (b) Histogram of Γ_D, fitted with a Gamma distribution (solid line), yielding a mean value of 0.10(6) meV. (c) Spatial map of Δ and (d) spatial map of Γ_D across the sample surface. Black dots indicate the positions of individual tunnel junctions. The color bars reflect the local values of Δ and Γ_D, revealing the spatial distribution.

centered at 2.49(29) meV. Similarly, the distribution of Γ_D values was fitted with a Gamma distribution (solid line in Figure 7.11(b)), resulting in a mean value of 0.10(6) meV. The corresponding spatial maps of Δ and Γ_D (shown in Figure 7.11(c, d)) reveal some local variations of superconducting properties.

Additionally, temperature-dependent measurements of the superconducting energy gap $\Delta(T)$ were performed at two distinct locations on the sample, as displayed in Figure 7.12. In both cases, the temperature evolution of the gap closely follows the expected BCS behavior, yielding $2\Delta(0\,\mathrm{K})/k_B T_c(0\,\mathrm{T}) = 4.5(13)$ in Figure 7.12(a) and $2\Delta(0\,\mathrm{K})/k_B T_c(0\,\mathrm{T}) = 3.8(5)$ in Figure 7.12(b) confirming conventional *s*-wave superconductivity in the $Nb_{0.75}Ti_{0.25}N$ layer.

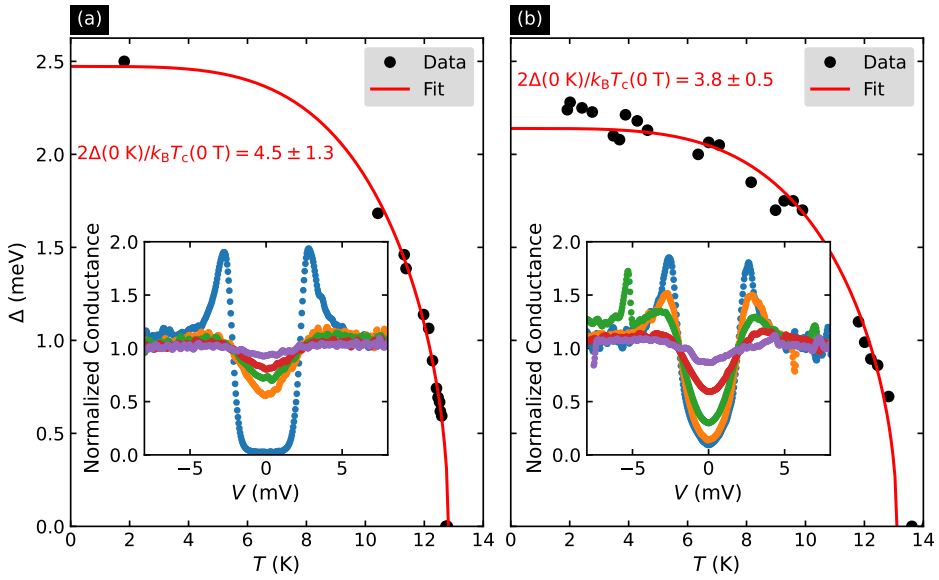

Figure 7.12: T dependence of the Δ measured by PCT spectroscopy on the $Nb_{0.75}Ti_{0.25}N$/AlN /Nb multilayer sample at two different locations. Black circles represent the extracted $\Delta(T)$ values obtained by fitting the differential conductance spectra at each temperature using Equations (2.34) and (7.17). The solid red lines correspond to fits using Equation (2.32) of the main text, yielding $2\Delta(0\,\mathrm{K})/k_B T_c(0\,\mathrm{T}) = 4.5(13)$ in (a) and $3.8(5)$ in (b), indicating slight spatial variations. The insets show representative normalized tunneling conductance spectra at select temperatures, highlighting the superconducting gap and coherence peaks.

7.6.3 Magnetic Field Suppression of T_c

Key to our analysis of the ^{8}Li βNMR data is accounting for the well-known suppression of the superconducting transition temperature T_c in a static magnetic field B_0. As mentioned in Section III A, we treat this quantitatively by inverting an empirical expression for B_{c2} derived from WHH theory [83, 318], with explicit steps given below.

Starting from Equation (9) of the main text, we re-arrange it into the form of a depressed quartic expression:

$$u^4 + pu^2 - qu + rb = 0, \tag{7.18}$$

where we have used the substitutions:

$$\begin{aligned} u &\equiv 1 - t, \\ b &\equiv \frac{B_0}{B_{c2}(0)}, \\ p &\equiv \frac{-0.153}{-0.152}, \\ q &\equiv \frac{1}{-0.152}, \\ r &\equiv \frac{-0.693}{-0.152}. \end{aligned}$$

To solve Equation (7.18), we first write it as:

$$u^4 = -pu^2 + qu - rb,$$

whereafter we introduce an auxiliary term y that makes both sides of this expression perfect squares. While the left-hand side may be rewritten using:

$$(u^2 + y)^2 - (2y - p)u^2 - qu - (y^2 - rb) = 0,$$

for the right-hand side to be a perfect square the condition:

$$y^2 - rb = \frac{q^2}{4(2y - p)}$$

must hold. Upon substitution, it can be shown that:

$$(u^2 + y)^2 - \left(u\sqrt{2y - p} + \frac{q}{2\sqrt{2y - p}} \right)^2 = 0.$$

This leads to four possible solutions for u:

$$u_{1\pm} = \frac{1}{2}\left(-\sqrt{2y-p} \pm \sqrt{2y-p-4y-\frac{2q}{\sqrt{2y-p}}}\right)$$
$$u_{2\pm} = \frac{1}{2}\left(\sqrt{2y-p} \pm \sqrt{2y-p-4y+\frac{2q}{\sqrt{2y-p}}}\right)$$

Among these, only

$$u_{2-} = \frac{1}{2}\left(\sqrt{2y-p} - \sqrt{2y-p-4y+\frac{2q}{\sqrt{2y-p}}}\right) \tag{7.19}$$

is physically meaningful, based on the criterion that $u \in [0,1]$ (i.e., ensuring a real and positive T_c).

To determine u_{2-}, we solve the corresponding cubic equation for y:

$$2y^3 - py^2 - 2rby + \left(prb - \frac{1}{4}q^2\right) = 0.$$

Its solution is:

$$y = \frac{p}{6} + v - \frac{x}{3v}, \tag{7.20}$$

where

$$v = \sqrt[3]{-\frac{w}{2} + \sqrt{\frac{w^2}{4} + \frac{x^3}{27}}}, \tag{7.21}$$
$$x = -\frac{p^2}{12} - rb, \tag{7.22}$$
$$w = -\frac{p^3}{108} + \frac{prb}{3} - \frac{q^2}{8}. \tag{7.23}$$

Substituting the known values of m, n, p, and b into Equations (7.20) to (7.23) provides the explicit solution for y, which in turn determines u_{2-} and ultimately

T_c's dependence on B_0 using Equation (7.19).

7.6.4 Knight Shift Calculation

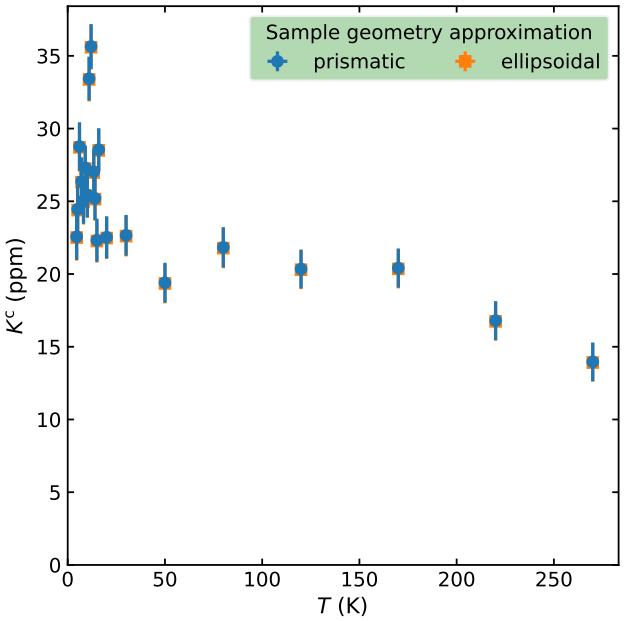

Figure 7.13: Temperature T-dependence of the (corrected) ^{8}Li Knight shift K^c in the $Nb_{0.75}Ti_{0.25}N$ thin film. The data are presented for two different sample geometry approximations: prismatic (blue circles) and ellipsoidal (orange squares). Both geometries yield nearly identical values across the measured temperature range.

As described in Section III A, correcting for demagnetization contributions to the resonance position are crucial for quantifying the Knight shift, which can be calculated using Equations (10) and (11) of the main text for the case when both the sample and reference have different geometries (see, e.g., [319]). Necessary for the computation are knowledge of each component's demagnetization factor N and (volume) magnetic susceptibility χ. Below, we detail our estimates for these quantities.

For thin films, the demagnetization factor $N = 1$ [349], which applies to our 91 nm $Nb_{0.75}Ti_{0.25}N$ thin film sample. For the reference compound MgO, with dimensions $10 \times 8 \times 0.5\,\mathrm{mm}^3$, the N was calculated assuming both prismatic

and ellipsoidal geometries [136]. These calculations yielded consistent values of $N \approx 0.9$ ($N = 0.922$ for a prism and $N = 0.917$ for an ellipsoid), confirming the minor geometric dependence. The centimetre-gram-second system of units (CGS) volume magnetic susceptibility of $Nb_{0.75}Ti_{0.25}N$ χ_0 was calculated from the molar susceptibilities of its components, NbN (31×10^{-6} emu mol^{-1}) and TiN (38×10^{-6} emu mol^{-1}) [270, 350], using their molar masses (106.913 g mol^{-1}) and (61.874 g mol^{-1}) [351], respectively. Assuming our sample stoichiometry $x = 0.25$ and incorporating the measured density of the $Nb_{0.75}Ti_{0.25}N$ (6.5 g cm^{-3}), χ_0 was estimated to be 2.23×10^{-6}. For MgO, the molar susceptibility $\chi^{\text{mol}}_{\text{MgO}} = -10.2 \times 10^{-6}$ emu mol^{-1} [351] is typical of weakly diamagnetic solids. This was converted into a volume susceptibility $\chi_{\text{MgO}} = -9.11 \times 10^{-6}$ using its density (3.6 g cm^3 [351]) and its molar mass (40.3044 g mol^{-1} [351]). Inserting these values into Equations (10) and (11) of the main text along with the measured ν_0s, we obtain the corrected (Knight) shift K^{c}, which varied between +15 ppm to +35 ppm over the measured T-range (see Figure 7.13), with the correction for demagnetization (+25.4 ppm) being the dominant contribution.

Chapter 8

Summary & outlook

8.1 Summary

This thesis presents a comprehensive investigation of Meissner-current suppression, first-flux penetration, and the superconducting properties of coated Nb heterostructures relevant to next-generation superconducting radio frequency (SRF) applications. The insight gained into these domains was made possible through the use of "exotic" ion-implanted β-detected spin spectroscopies, including muon spin rotation (μSR), low energy muon spin rotation (LE-μSR), and β-detected nuclear magnetic resonance (βNMR). In the following, we summarize the main findings of these experiments.

In Chapter 5, μSR measurements revealed the µm-scale dependence of the vortex-penetration field in Nb ellipsoids subjected to low-temperature baking (LTB) or coated with 2 µm Nb_3Sn. Both treatments yielded vortex penetration field ($\mu_0 H_{vp}$) values exceeding the Nb lower critical field ($\mu_0 H_{c1}$) ($\sim$170 mT), highlighting their potential for SRF cavity enhancement. The Nb_3Sn-coated sample exhibited a depth-independent $\mu_0 H_{vp} = 234.5(35)$ mT, consistent with Nb's superheating field ($\mu_0 H_{sh}$) and indicative of an interfacial barrier in a superconductor-superconductor (SS) structure [18]. In contrast, the LTB treatment produced only a modest increase above $\mu_0 H_{c1}$, with a weak depth dependence consistent with defect-induced pinning. These results show unambiguously that a thin supercon-

ducting overlayer can elevate the vortex-entry field to $\mu_0 H_{\mathrm{sh}}$, while LTB baked Nb lacks this feature.

Depth-resolved magnetic screening in SS $Nb_{1-x}Ti_xN$/Nb bilayers (50, 80, and 160 nm) was examined using LE-μSR in Chapter 6. Fits to the counter-current-flow model [18] for a SS bilayer yielded penetration depths of $Nb_{1-x}Ti_xN$ $\lambda_{Nb_{1-x}Ti_xN}$ = 182.5(31) nm and "dirty" Nb $\lambda_{\mathrm{Nb}} = 43.3(19)$ nm, the former is in agreement with estimates by others, whereas naive biexponential fits overestimated $\lambda_{Nb_{1-x}Ti_xN}$ by a factor ~ 2.5. These findings confirm strong suppression of the Meissner current in the surface layer and provide experimental validation of the counter-current model in the Meissner state. The parameters derived from the analysis predict a maximum sustainable field of 610(40) mT before flux entry, exceeding the superheating field (B_{sh}) of the individual layers. These results emphasize the potential for how, through careful selection of the thicknesses used in a superconducting multilayer, the first-flux-entry field may be maximized.

Superconducting and normal-state properties of a $Nb_{0.75}Ti_{0.25}N$(91 nm)/AlN (4 nm)/Nb superconductor-insulator-superconductor (SIS) heterostructure were characterized using implanted-ion ^{8}Li βNMR in Chapter 7 under a 4.1 T perpendicular field between 4.6 K and 270 K. Below the film's critical temperature (T_c), the spectra showed symmetric broadening from flux-line lattice (FLL) formation. Fits yielded $T_c(0\,\mathrm{T}) = 15.4(7)$ K, $B_{c2}(0\,\mathrm{K}) = 18(4)$ T, and $\lambda(0\,\mathrm{K}) = 180.57(30)$ nm, consistent with other studies in the literature. Spin-lattice relaxation (SLR) data revealed metallic Korringa behavior below ~100 K, which was modified below T_c by a Hebel-Slichter coherence peak. This peak was characterized by a superconducting gap $\Delta(0\,\mathrm{K}) = 2.60(12)$ meV, Dynes broadening parameter $\Gamma_D = 0.02$ meV, and a gap ratio $2\Delta/k_B T_c = 3.92(25)$, confirming strong-coupling superconductivity in the alloy. Above ~100 K, SLR was dominated by thermally activated dynamics. While further field-dependent SLR measurements are suggested to clarify the underlying kinetic processes, this characterization sets the stage for future βNMR

measurements aimed at *directly* identifying the first-flux-penetration field at the *nanoscale* in similar SIS heterostructures.

Together, the results on the SS bilayers confirm the prediction of Section 3.3 that a single-layer Nb coating provides two key advantages: suppression of the Meissner screening current in the surface layer and the creation of an interface barrier at the SS junction. These findings demonstrate that superconducting coatings can enhance flux penetration fields beyond the intrinsic limits of individual materials, highlighting multilayer architectures with interlayers that impede vortex entry as a promising pathway to maximize the vortex penetration field.

Building on this, vortex penetration studies in SIS heterostructures are essential to validate the role of interlayers. A necessary precursor to such measurements is the characterization of the coated superconducting layer, which has been achieved through the βNMR study in Chapter 7. This study quantified the superconducting properties of the $Nb_{0.75}Ti_{0.25}N$ surface layer in a $Nb_{0.75}Ti_{0.25}N$(91 nm)/AlN(4 nm) /Nb SIS heterostructure with applied magnetic field (B_0) applied perpendicular to the surface, providing a foundation for future vortex penetration experiments. The following outlook discusses these forthcoming measurements and broader directions for advancing superconducting heterostructure research.

8.2 Outlook

A logical next step is to carry out depth-resolved βNMR studies of the Meissner-to-vortex transition in a $Nb_{0.75}Ti_{0.25}N$(91 nm)/AlN(4 nm)/Nb SIS heterostructure with B_0 applied parallel to the surface. These measurements would directly determine the maximum sustainable field in each layer. This is particularly important because, as shown in Section 3.4, magnetization measurements with a vibrating sample magnetometer (VSM) suggested enhanced performance, whereas radio frequency (RF) tests on $Nb_{0.75}Ti_{0.25}N$/AlN-coated Nb cavities did not. A likely explanation is that the $Nb_{0.75}Ti_{0.25}N$ layer enters a vortex state prematurely, while the Nb

substrate remains protected up to the superheating field by the interface barrier. Conventional "bulk" VSM measurements cannot resolve layer-specific magnetic responses, which makes βNMR indispensable for depth-resolved studies of the Meissner-to-vortex transition.

Recent advances in beamline and spectrometer design [3], enabling βNMR measurements up to ~200 mT parallel to the sample surface, have already been applied to study this transition in "bare" and "baked" Nb [147]. In these studies, depth-dependent SLR measurements as a function of B_0 were employed, since the SLR rate is inversely proportional to B_0 [101, 147, 185]. However, SLR studies are challenging because spin dynamics at low fields are complex [101], and extracting the transition requires careful parametric modeling of both the magnetic field profile and the implantation distribution of the ^{8}Li probe [147].

An alternative and potentially simpler approach is to measure the field dependence of the ^{8}Li resonance, which directly probes the internal field distribution. In the Meissner state, the distribution is expected to skew asymmetrically towards zero field, whereas in the vortex state it should be centered on the applied field and broadened by the FLL, with the linewidth reflecting flux-line lattice symmetry. In practice, such measurements require a highly symmetric ^{8}Li stopping site to avoid quadrupolar contributions, which complicate the lineshape and reduce the measurement's signal-to-noise ratio. This condition is not met in Nb, where quadrupole splitting of ^{8}Li is observed below 70 K [321]. By contrast, at all temperatures (4.6 K to 270 K) in $Nb_{0.75}Ti_{0.25}N$ the resonance appears as a single, broad line whose amplitude decreases with decreasing temperature, as shown in Chapter 7. Owing to this simpler spectral shape, we propose resonance-based measurements of the Meissner-to-vortex transition to determine the layer-specific maximum sustainable fields in SIS heterostructures and to assess how coating strategies can suppress magnetic-flux nucleation and enhance cavity performance.

Future work may also include flux penetration studies of thicker surface layers,

aimed at realizing the optimum thickness predicted in Section 6.4.1, but now within an SIS heterostructure. Similarly, optimizing the insulating-layer thickness is crucial, as the current 4 nm AlN layer may not sufficiently decouple the surface and substrate. This could be pursued through bulk magnetization measurements using a VSM; however, if flux penetration occurs earlier under RF excitation, such bulk measurements would not capture that behavior, as discussed in Section 3.4. Therefore, depth-resolved techniques remain the most suitable approach. Beyond thickness optimization, exploring SIS multilayers with alternative superconductors and insulators could yield valuable insights. Potential superconductors include NbN, Nb_3Sn, MgB_2, V_3Si and even more exotic Fe-based pnictides, while candidate insulators include MgO, AlN, and Al_2O_3. Furthermore, systematic flux penetration studies of multilayered Nb stacks incorporating alternating superconducting and insulating layers would directly probe the effectiveness of multilayers in enhancing field limits. Overall, the prognosis for enhancing SRF cavity performance through the use of superconducting multilayers remains promising.

Chapter 9

Additional Information

9.1 Spin-$\frac{1}{2}$ precession

A significant component of this thesis is dedicated to investigating static magnetic field distributions using muon spin rotation (μSR) and low energy muon spin rotation (LE-μSR). Therefore, it is instructive to outline the Larmor precession of a spin-$\frac{1}{2}$ particle in a magnetic field oriented at an arbitrary angle relative to the quantization axis. The following discussion, which largely follows Ref. [352], provides the necessary quantum mechanical framework.

Quantum mechanical treatment

In quantum mechanics the spin operator $\boldsymbol{S}$ for a spin-$\frac{1}{2}$ particle is given by

$$\boldsymbol{S} = \frac{\hbar}{2}\boldsymbol{\sigma}, \tag{9.1}$$

where $\boldsymbol{\sigma} = (\sigma_x, \sigma_y, \sigma_z)$ is the vector of Pauli matrices, which represent the intrinsic spin components along the Cartesian axes:

$$\sigma_x = \begin{pmatrix} 1 & 0 \\ 0 & 1 \end{pmatrix}, \sigma_y = \begin{pmatrix} 0 & -i \\ i & 0 \end{pmatrix}, \sigma_z = \begin{pmatrix} 1 & 0 \\ 0 & -1 \end{pmatrix}. \tag{9.2}$$

The eigenstates of σ_z have the quantum numbers $s = \frac{1}{2}$ and $m_s = \pm\frac{1}{2}$. These eigenstates can be used as a basis to describe the spin$-\frac{1}{2}$ wave function $|\psi\rangle$:

$$\begin{aligned} |\psi\rangle &= \alpha|s = 1/2, m_s = 1/2\rangle + \beta|s = 1/2, m_s = -1/2\rangle, \\ &= \alpha|\uparrow\rangle + \beta|\downarrow\rangle, \\ &= \alpha \begin{pmatrix} 1 \\ 0 \end{pmatrix} + \beta \begin{pmatrix} 0 \\ 1 \end{pmatrix} = \begin{pmatrix} \alpha \\ \beta \end{pmatrix}, \end{aligned} \tag{9.3}$$

where different common notations for this spinor have been recalled. The coefficients α and β are complex numbers obeying the normalization condition

$$|\alpha|^2 + |\beta|^2 = 1. \tag{9.4}$$

In order to arrive at a "spatial representation" of this spinor, the spin direction should be given by $\hat{\boldsymbol{n}} = (\cos\phi\sin\theta,\ \sin\phi\sin\theta,\ \cos\theta)$, where ϕ and θ are the standard spherical coordinate angles. Therefore, the combination of the spin operator $\boldsymbol{\sigma}$ and the projection onto this direction must yield the same spinor. Mathematically, this means that $\begin{pmatrix} \alpha \\ \beta \end{pmatrix}$ is an eigenvector of $\hat{\boldsymbol{n}} \cdot \boldsymbol{\sigma}$ with the eigenvalue 1:

$$\hat{\boldsymbol{n}} \cdot \boldsymbol{\sigma} \begin{pmatrix} \alpha \\ \beta \end{pmatrix} = \begin{pmatrix} \alpha \\ \beta \end{pmatrix}. \tag{9.5}$$

Combining Equation (9.4) and Equation (9.5) yields $|\alpha| = \cos(\theta/2)$ and $|\beta| = \sin(\theta/2)$, as well as a phase difference of ϕ between α and β. Taking into account the 2-dimensional special unitary operator SU(2) relation that a rotation of $|\psi\rangle$ by 2π gives $-|\psi\rangle$ and only a rotation by 4π returns $|\psi\rangle$, one arrives at the following

representation (up to a constant phase):

$$|\psi\rangle = \begin{pmatrix} \exp\left(-i\frac{\phi}{2}\right) & \cos\left(\frac{\theta}{2}\right) \\ \exp\left(i\frac{\phi}{2}\right) & \sin\left(\frac{\theta}{2}\right) \end{pmatrix}. \tag{9.6}$$

The interaction of the magnetic moment $\boldsymbol{\mu}$ of a spin$-\frac{1}{2}$ particle in the presence of a magnetic field $\boldsymbol{B}$ is given by:

$$\begin{aligned} \boldsymbol{\mu} &= \gamma \boldsymbol{S} \\ &= \gamma\hbar\frac{\boldsymbol{\sigma}}{2}, \end{aligned} \tag{9.7}$$

where γ is the gyromagnetic ratio of the respective particle carrying the spin. The time evolution of a spin system can be described by the Zeeman Hamiltonian $\mathcal{H}$:

$$\begin{aligned} \mathcal{H} &= -\boldsymbol{\mu} \cdot \boldsymbol{B}, \\ &= -\gamma\hbar\frac{\boldsymbol{\sigma}}{2} \cdot \boldsymbol{B}. \end{aligned} \tag{9.8}$$

In the case that only a static magnetic field is considered, $\mathcal{H}$ is time-independent and therefore, the time evolution of the wave function is obtained by the unitary operator $U(t)$:

$$\begin{aligned} U(t) &= \exp\left(-\frac{i}{\hbar}\mathcal{H}t\right), \\ &= \exp\left(\frac{i}{2}\gamma\boldsymbol{\sigma} \cdot \boldsymbol{B}t\right). \end{aligned} \tag{9.9}$$

Assuming the magnetic field is directed along the z direction ($\boldsymbol{B} = B_0\hat{\boldsymbol{z}}$), then $U(t)$

simplifies to:

$$\begin{aligned} U(t) &= \exp\left(\frac{i}{2}\gamma\sigma_z B_0 t\right), \\ &= \begin{pmatrix} \exp\left(\frac{i}{2}\gamma B_0 t\right) & 0 \\ 0 & \exp\left(\frac{i}{2}\gamma B_0 t\right) \end{pmatrix}. \end{aligned} \tag{9.10}$$

Finally, the propagator of Equation (9.10) describing the time evolution of the initial wave function of Equation (9.6) can be obtained:

$$\begin{aligned} |\psi(t)\rangle &= U(t)|\psi(0)\rangle, \\ &= \begin{pmatrix} \exp\left(\frac{i}{2}\gamma B_0 t\right) & 0 \\ 0 & \exp\left(\frac{i}{2}\gamma B_0 t\right) \end{pmatrix} \begin{pmatrix} \exp\left(-i\frac{\phi}{2}\right) & \cos\left(\frac{\theta}{2}\right) \\ \exp\left(i\frac{\phi}{2}\right) & \sin\left(\frac{\theta}{2}\right) \end{pmatrix}, \\ &= \begin{pmatrix} \exp\left(-\frac{i}{2}(\phi - \gamma B_0 t)\right) & \cos\left(\frac{\theta}{2}\right) \\ \exp\left(\frac{i}{2}(\phi - \gamma B_0 t)\right) & \sin\left(\frac{\theta}{2}\right) \end{pmatrix}. \end{aligned} \tag{9.11}$$

When comparing Equation (9.11) and Equation (9.6), it is obvious that after a time interval t, the spin gets rotated by $\gamma B_0 t$ about the direction of the field; this is known as *Larmor precession*, whose angular frequency is:

$$\omega_0 = \gamma B_0. \tag{9.12}$$

Thus, the time evolution of the spin state is fully characterized by the Larmor frequency, which determines the fundamental precession rate of the system. In experiments such as μSR, LE-μSR, and β-detected nuclear magnetic resonance (βNMR), the observable quantity is not the motion of an individual spin but rather the ensemble-averaged expectation value of the spin operator along the

quantization axis. The resulting precession of this ensemble polarization occurs at the Larmor frequency, corresponding directly to the experimentally observed precession signal.

9.2 Nb ellipsoidal sample specifications and characterization

The ellipsoidal sample used for the study described in Section 5.2.1 was fabricated from a fine-grain Nb ingot procured from the Wah Chang Corporation, with a nominal residual-resistivity ratio (RRR) > 150. Figure 9.1 compares the upper limits of impurity concentrations in the as-received Nb ingot with the TESLA cavity specifications summarized in Ref. [17]. While TESLA cavities are specified to have a RRR of $\geq$ 300 to ensure high thermal conductivity and stable operation at high accelerating gradients, the ellipsoidal sample produced from the Nb ingot exhibits a lower and spatially varying RRR. The values range from approximately 168 at the top to approximately 310 at the bottom of the ingot, where "top" and "bottom" refer to the physical positions within the ingot at which the measurements were taken during fabrication.

The impurity levels in the Nb ingot—including both interstitial impurities (H, C, N, O) and metallic impurities (Si, P, Ti, Fe, Ni, Zr, Mo, Hf, Ta, W)—are generally comparable to those specified for TESLA cavities, but are higher in the case of interstitial impurities (see Figure 9.1). These differences likely reflect variations in impurity incorporation during ingot fabrication. Interstitial elements such as C, N, and O are known to strongly influence the electron mean free path and therefore reduce the RRR of Nb [1, 17]. Similar correlations between impurity content and RRR have been reported in the production of Nb by Tokyo Denkai Co., Ltd. for superconducting radio frequency (SRF) cavity applications [353].

Following baking treatments at 1400 °C and 120 °C, the sample underwent further microstructural analysis using scanning electron microscope (SEM)/energy dispersive X-ray spectroscopy (EDX) and secondary ion mass spectrometry (SIMS),

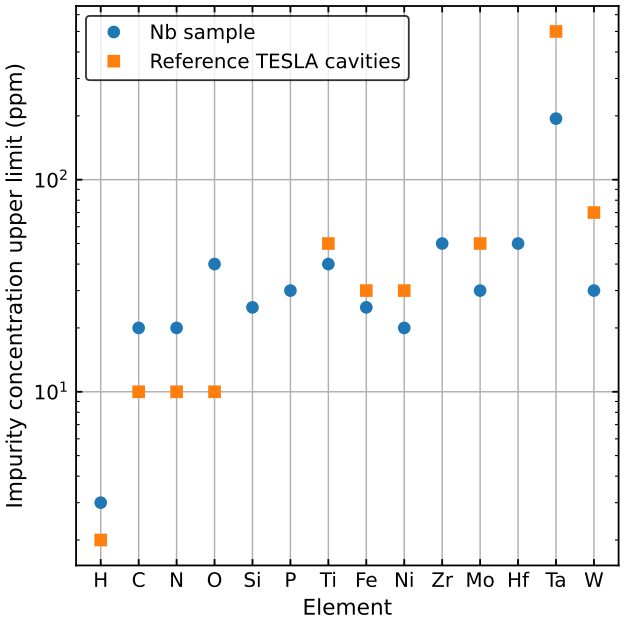

Figure 9.1: Comparison of impurity concentration upper limits (in ppm) for the Nb to make ellipsoidal sample described in Section 5.2.1 with the TESLA cavity specifications reported in Ref. [17]. The elements considered include interstitial impurities (H, C, N, O) and metallic impurities (Si, P, Ti, Fe, Ni, Zr, Mo, Hf, Ta, W). The TESLA specification showed the concentration of interstitial impurities slightly lower values then the used sample, with an overall high RRR $\geq$ 300 compared to the sample RRR > 150.

as shown in Figure 9.2. The SEM/EDX analysis revealed no unexpected features or contamination, consistent with observations typically reported for high-RRR Nb exposed to air [218] (see, for example, Figures 9.2a and 9.2b). Following the 120 °C baking treatment, an increase in oxygen concentration was observed using SIMS within the near-surface region, extending to depths of approximately 20 nm. This behavior is consistent with predictions from oxygen diffusion models [219–221] (see Figure 9.2c). While the average RRR of the ellipsoidal sample is lower, the near-surface composition and microstructural properties relevant to the present study remain comparable to those of RRR $\geq$ 300 Nb commonly used for SRF cavity fabrication.

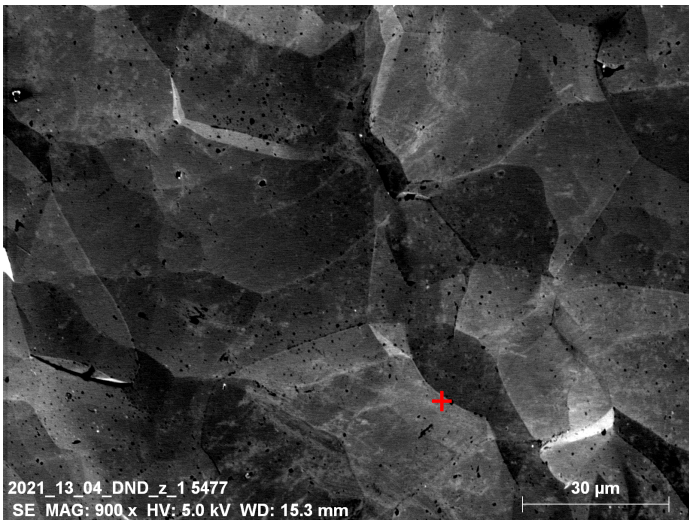

(a) SEM image of 1400 °C Nb.

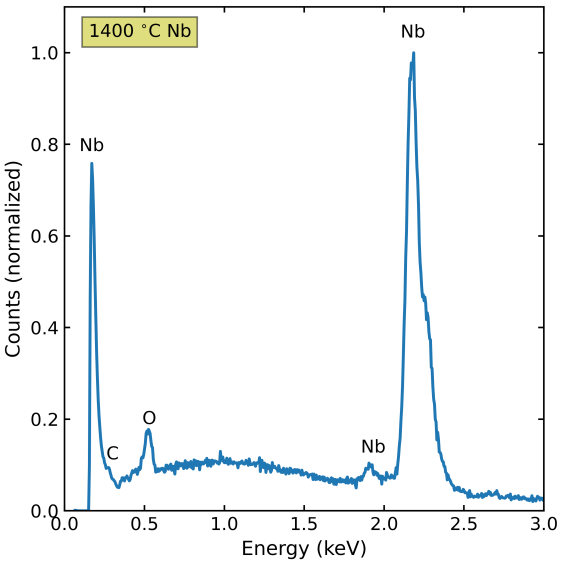

(b) EDX measurement of 1400 °C Nb.

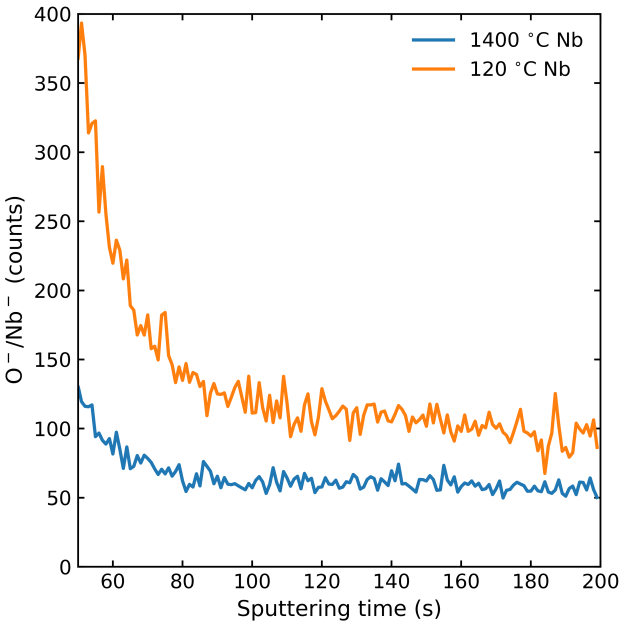

(c) SIMS measurement of 1400 °C and 120 °C Nb.

Figure 9.2: (a) SEM imaging of 1400 °C annealed Nb followed by (b) EDX analysis of the samples reveals no chemical residue or subparticles in the samples. (c) SIMS plot of O^-/Nb^- showing the area under the oxide layer. An increased oxygen concentration is observed for 120 °C Nb. A sputter time of 200 s roughly corresponds to a depth of 20 nm.

Bibliography

[1] H. Padamsee, J. Knobloch, and T. Hays, *RF Superconductivity for Accelerators*, 2nd ed. (Wiley, Weinheim, 2008) (Cited on pages iii, 35, 36, 39, 95, 117, 191).

[2] H. Padamsee, *RF Superconductivity: Science, Technology, and Applications*, Rf Superconductivity (Wiley-VCH Verlag GmbH & Co. KGaA, Weinheim, May 2009) (Cited on pages iii, 1, 23, 36, 38, 95, 112, 115).

[3] E. Thoeng, R. M. L. McFadden, S. Saminathan, G. D. Morris, P. Kolb, B. Matheson, M. Asaduzzaman, R. Baartman, S. R. Dunsiger, D. Fujimoto, T. Junginger, V. L. Karner, S. Kiy, R. Li, M. Stachura, J. O. Ticknor, R. F. Kiefl, W. A. MacFarlane, and R. E. Laxdal, "A new high parallel-field spectrometer at TRIUMF's β-NMR facility", Rev. Sci. Instrum. **94**, 023305 (2023) (Cited on pages v, 56, 59, 85–87, 168, 170, 185).

[4] M. Asaduzzaman, R. M. L. McFadden, E. Thoeng, R. E. Laxdal, and T. Junginger, "Measurements of the first-flux-penetration field in surface-treated and coated Nb: distinguishing between near-surface pinning and an interface energy barrier", Supercond. Sci. Technol. **37**, 085006 (2024) (Cited on pages lii, 58, 144).

[5] M. Asaduzzaman, R. M. L. McFadden, A.-M. Valente-Feliciano, D. R. Beverstock, A. Suter, Z. Salman, T. Prokscha, and T. Junginger, "Evidence for current suppression in superconductor–superconductor bilayers", Supercond. Sci. Technol. **37**, 025002 (2023) (Cited on pages liii, 58, 110, 111, 144, 145, 153, 154, 162, 168).

[6] M. Asaduzzaman, R. M. L. McFadden, E. Thoeng, Y. Kalboussi, I. Curci, T. Proslier, S. R. Dunsiger, W. Andrew MacFarlane, G. D. Morris, R. Li, J. O. Ticknor, R. E. Laxdal, and T. Junginger, "Superconducting properties of thin film $Nb_{1-x}Ti_xN$ studied via the NMR of implanted ^{8}Li", J. Phys.: Condens. Matter **37**, 395701 (2025) (Cited on pages liii, 58).

[7] D. K. Finnemore, T. F. Stromberg, and C. A. Swenson, "Superconducting Properties of High-Purity Niobium", Phys. Rev. **149**, 231–243 (1966) (Cited on pages 1, 43, 107, 117, 135, 138, 139).

[8] A. Gurevich, "Superconducting Radio-Frequency Fundamentals for Particle Accelerators", Rev. Accel Sci. Technol. **05**, 119–146 (2012) (Cited on pages 1, 43).

[9] A. Grassellino, C. Beard, P. Kolb, R. Laxdal, N. S. Lockyer, D. Longuevergne, and J. E. Sonier, "Muon spin rotation studies of niobium for superconducting rf applications", Phys. Rev. ST Accel. Beams **16**, 062002 (2013) (Cited on pages 1, 97, 101).

[10] H. Padamsee, "50 years of success for SRF accelerators—a review", Supercond. Sci. Technol. **30**, 053003 (2017) (Cited on pages 1, 35, 36, 41, 112, 117).

[11] G. Ciovati, "Effect of low-temperature baking on the radio-frequency properties of niobium superconducting cavities for particle accelerators", J. Appl. Phys. **96**, 1591–1600 (2004) (Cited on pages 2, 40, 95, 96, 103, 112, 113, 136).

[12] A. Grassellino, A. Romanenko, D. Sergatskov, O. Melnychuk, Y. Trenikhina, A. Crawford, A. Rowe, M. Wong, T. Khabiboulline, and F. Barkov, "Nitrogen and argon doping of niobium for superconducting radio frequency cavities: a pathway to highly efficient accelerating structures", Supercond. Sci. Technol. **26**, 102001 (2013) (Cited on pages 2, 40, 95, 116).

[13] A. Grassellino, A. Romanenko, Y. Trenikhina, M. Checchin, M. Martinello, O. S. Melnychuk, S. Chandrasekaran, D. A. Sergatskov, S. Posen, A. C. Crawford, S. Aderhold, and D. Bice, "Unprecedented quality factors at accelerating gradients up to 45 MV m^{-1} in niobium superconducting resonators via low temperature nitrogen infusion", Supercond. Sci. Technol. **30**, 094004 (2017) (Cited on pages 2, 40, 95, 114, 116).

[14] A. Grassellino, A. Romanenko, D. Bice, O. Melnychuk, A. C. Crawford, S. Chandrasekaran, Z. Sung, D. A. Sergatskov, M. Checchin, S. Posen, M. Martinello, and G. Wu, *Accelerating fields up to* 49 MV m^{-1} *in TESLA-shape superconducting RF niobium cavities via* 75 °C *vacuum bake*, June 2018, arXiv:1806.09824 [physics.acc-ph] (Cited on pages 2, 40, 42, 95, 96, 116, 117).

[15] P. Dhakal, S. Chetri, S. Balachandran, P. J. Lee, and G. Ciovati, "Effect of low temperature baking in nitrogen on the performance of a niobium superconducting radio frequency cavity", Phys. Rev. Accel. Beams **21**, 032001 (2018) (Cited on pages 2, 42, 136).

[16] D. Bafia, A. Grassellino, O. Melnychuk, A. Romanenko, Z.-H. Sung, and J. Zasadzinski, "Gradients of 50 MV m^{-1} in TESLA Shaped Cavities via Modified Low Temperature Bake", in Proc. SRF'19, International Conference on RF Superconductivity 19 (Aug. 2019), pp. 586–591 (Cited on pages 2, 42).

[17] B. Aune, R. Bandelmann, D. Bloess, B. Bonin, A. Bosotti, M. Champion, C. Crawford, G. Deppe, B. Dwersteg, D. A. Edwards, H. T. Edwards, M. Ferrario, M. Fouaidy, P.-D. Gall, A. Gamp, A. Gössel, J. Graber, D. Hubert, M. Hüning, M. Juillard, T. Junquera, H. Kaiser, G. Kreps, M. Kuchnir, R. Lange, M. Leenen, M. Liepe, L. Lilje, A. Matheisen, W.-D. Möller, A. Mosnier, H. Padamsee, C. Pagani, M. Pekeler, H.-B. Peters, O. Peters, D. Proch, K. Rehlich, D. Reschke, H. Safa, T. Schilcher, P. Schmüser, J. Sekutowicz, S. Simrock, W. Singer, M. Tigner, D. Trines, K. Twarowski, G. Weichert, J. Weisend, J. Wojtkiewicz, S. Wolff, and K. Zapfe, "Superconducting TESLA cavities", Phys. Rev. ST Accel. Beams **3**, 092001 (2000) (Cited on pages 2, 38, 102, 191, 192).

[18] T. Kubo, "Multilayer coating for higher accelerating fields in superconducting radio-frequency cavities: a review of theoretical aspects", Supercond. Sci. Technol. **30**, 023001 (2016) (Cited on pages 2, 40, 42, 44–47, 49–51, 96, 107, 110, 111, 113, 118–120, 134, 139, 140, 144, 182, 183).

[19] T. Kubo, "Superheating fields of semi-infinite superconductors and layered superconductors in the diffusive limit: structural optimization based on the microscopic theory", Supercond. Sci. Technol. **34**, 045006 (2021) (Cited on pages 2, 44, 45, 120, 139, 140, 144).

[20] A. Gurevich, "Enhancement of rf breakdown field of superconductors by multilayer coating", Appl. Phys. Lett. **88**, 012511 (2006) (Cited on pages 2, 40, 42, 118, 144).

[21] T. Kubo, Y. Iwashita, and T. Saeki, "Radio-frequency electromagnetic field and vortex penetration in multilayered superconductors", Appl. Phys. Lett. **104**, 032603 (2014) (Cited on pages 2, 45, 107, 110, 118, 120, 144).

[22] T. Kubo, "Optimum multilayer coating of superconducting particle accelerator cavities and effects of thickness dependent material properties of thin films", Jpn. J. Appl. Phys. **58**, 088001 (2019) (Cited on pages 2, 42, 44, 45, 49, 118, 120, 139, 140, 144).

[23] A. Gurevich, "Maximum screening fields of superconducting multilayer structures", AIP Adv. **5**, 017112 (2015) (Cited on pages 2, 42, 118, 120).

[24] C. P. Bean and J. D. Livingston, "Surface barrier in Type-II superconductors", Phys. Rev. Lett. **12**, 14–16 (1964) (Cited on pages 2, 29, 45, 96, 97, 107, 110, 115, 118, 140).

[25] F. Colauto, D. do Carmo, A. M. H. de Andrade, A. A. M. Oliveira, W. A. Ortiz, Y. M. Galperin, and T. H. Johansen, "Anisotropic Flux Penetration in Superconducting Nb Films With Frozen-in In-plane Magnetic Fields", IEEE Trans. Appl. Supercond. **29**, 1–5 (2019) (Cited on page 3).

[26] S. Ooi, M. Tachiki, T. Konomi, T. Kubo, A. Kikuchi, S. Arisawa, H. Ito, and K. Umemori, "Observation of intermediate mixed state in high-purity cavity-grade Nb by magneto-optical imaging", Phys. Rev. B **104**, 064504 (2021) (Cited on page 3).

[27] A. A. Polyanskii, P. J. Lee, A. Gurevich, Z.-H. Sung, and D. C. Larbalestier, "Magneto-Optical Study High-Purity Niobium for Superconducting RF Application", AIP Conf. Proc. **1352**, 186–202 (2011) (Cited on page 3).

[28] J. Köszegi, O. Kugeler, D. Abou-Ras, J. Knobloch, and R. Schäfer, "A magneto-optical study on magnetic flux expulsion and pinning in high-purity niobium", J. Appl. Phys. **122**, 173901 (2017) (Cited on page 3).

[29] S. Balachandran, A. Polyanskii, S. Chetri, P. Dhakal, Y.-F. Su, Z.-H. Sung, and P. J. Lee, "Direct evidence of microstructure dependence of magnetic flux trapping in niobium", Sci. Rep. **11**, 5364 (2021) (Cited on page 3).

[30] F. Barkov, A. Romenko, A. Grassellino, and L. Y. Vinnikov, "Bitter decoration studies of magnetic flux penetration into cavity cutouts.", in 16th International Conference on RF Superconductivity (Sept. 2013) (Cited on page 3).

[31] G. J. Dolan, F. Holtzberg, C. Feild, and T. R. Dinger, "Anisotropic vortex structure in $Y_1Ba_2Cu_3O_7$", Phys. Rev. Lett. **62**, 2184–2187 (1989) (Cited on page 3).

[32] P. L. Gammel, D. J. Bishop, G. J. Dolan, J. R. Kwo, C. A. Murray, L. F. Schneemeyer, and J. V. Waszczak, "Observation of Hexagonally Correlated Flux Quanta In $YBa_2Cu_3O_7$", Phys. Rev. Lett. **59**, 2592–2595 (1987) (Cited on page 3).

[33] Y. Fasano, J. Herbsommer, and F. de la Cruz, "Superficial Periodic Pinning Induced by Bitter Decoration Applied to the Study of Vortex Structure Nucleation and Growth", physica status solidi (b) **215**, 563–571 (1999) (Cited on page 3).

[34] G. J. Dolan, G. V. Chandrashekhar, T. R. Dinger, C. Feild, and F. Holtzberg, "Vortex Structure in $YBa_2Cu_3O_7$ and Evidence for Intrinsic Pinning", Phys. Rev. Lett. **62**, 827–830 (1989) (Cited on page 3).

[35] S. Okayasu, T. Nishio, Y. Hata, J. Suzuki, I. Kakeya, K. Kadowaki, and V. Moshchalkov, "Vortex imaging in microscopic superconductors with a scanning SQUID microscope", IEEE Trans. Appl. Supercond. **15**, 696–698 (2005) (Cited on page 3).

[36] E. M. Lechner, B. D. Oli, J. Makita, G. Ciovati, A. Gurevich, and M. Iavarone, "Electron Tunneling and X-Ray Photoelectron Spectroscopy Studies of the Superconducting Properties of Nitrogen-Doped Niobium Resonator Cavities", Phys. Rev. Appl. **13**, 044044 (2020) (Cited on page 3).

[37] T. Nishizaki, A. Troyanovski, G. van Baarle, P. Kes, and J. Aarts, "STM imaging of vortex structures in NbN thin films", Physica C **388-389**, 777–778 (2003) (Cited on page 3).

[38] H. Suderow, I. Guillamón, J. G. Rodrigo, and S. Vieira, "Imaging superconducting vortex cores and lattices with a scanning tunneling microscope", Supercond. Sci. Technol. **27**, 063001 (2014) (Cited on page 3).

[39] J. Brisbois, B. Raes, J. Van de Vondel, V. V. Moshchalkov, and A. V. Silhanek, "Determination of the magnetic penetration depth in a superconducting Pb film", J. Appl. Phys. **115**, 103906 (2014) (Cited on pages 3, 122).

[40] A. Oral, S. J. Bending, R. G. Humphreys, and M. Henini, "Microscopic measurement of penetration depth in thin films by scanning Hall probe microscopy", Supercond. Sci. Technol. **10**, 17 (1997) (Cited on pages 3, 122).

[41] J. Kim, L. Civale, E. Nazaretski, N. Haberkorn, F. Ronning, A. S. Sefat, T. Tajima, B. H. Moeckly, J. D. Thompson, and R. Movshovich, "Direct measurement of the magnetic penetration depth by magnetic force microscopy", Supercond. Sci. Technol. **25**, 112001 (2012) (Cited on pages 3, 122).

[42] E. Nazaretski, J. P. Thibodaux, I. Vekhter, L. Civale, J. D. Thompson, and R. Movshovich, "Direct measurements of the penetration depth in a superconducting film using magnetic force microscopy", Appl. Phys. Lett. **95**, 262502 (2009) (Cited on pages 3, 122).

[43] J. T. Zhang, J. Kim, M. Huefner, C. Ye, S. Kim, P. C. Canfield, R. Prozorov, O. M. Auslaender, and J. E. Hoffman, "Single-vortex pinning and penetration depth in superconducting $NdFeAsO_{1-x}F_x$", Phys. Rev. B **92**, 134509 (2015) (Cited on pages 3, 122).

[44] L. Luan, O. M. Auslaender, T. M. Lippman, C. W. Hicks, B. Kalisky, J.-H. Chu, J. G. Analytis, I. R. Fisher, J. R. Kirtley, and K. A. Moler, "Local measurement of the penetration depth in the pnictide superconductor $Ba(Fe_{0.95}Co_{0.05})_2As_2$", Phys. Rev. B **81**, 100501 (2010) (Cited on pages 3, 122).

[45] L. Luan, T. M. Lippman, C. W. Hicks, J. A. Bert, O. M. Auslaender, J.-H. Chu, J. G. Analytis, I. R. Fisher, and K. A. Moler, "Local measurement of the superfluid density in the pnictide superconductor $Ba(Fe_{1-x}CO_x)As_2$ across the superconducting dome", Phys. Rev. Lett. **106**, 067001 (2011) (Cited on pages 3, 122).

[46] M. Konczykowski, L. I. Burlachkov, Y. Yeshurun, and F. Holtzberg, "Evidence for surface barriers and their effect on irreversibility and lower-critical-field measurements in Y-Ba-Cu-O crystals", Phys. Rev. B **43**, 13707–13710 (1991) (Cited on page 3).

[47] D. A. Turner, G. Burt, and T. Junginger, "No interface energy barrier and increased surface pinning in low temperature baked niobium", Sci. Rep. **12**, 5522 (2022) (Cited on pages 3, 95, 96, 103, 108, 114, 116).

[48] Y. Kalboussi, "Nano hetero-structures for improving performances of superconductors under high fields", PhD thesis (Université Paris-Saclay, Mar. 2023) (Cited on pages 3, 53–56, 145, 149, 166, 171).

[49] M. Yethiraj, H. A. Mook, G. D. Wignall, R. Cubitt, E. M. Forgan, D. M. Paul, and T. Armstrong, "Small-angle neutron scattering study of flux line lattices in twinned $YBa_2Cu_3O_7$", Phys. Rev. Lett. **70**, 857–860 (1993) (Cited on page 3).

[50] W. Meissner and R. Ochsenfeld, "Ein neuer Effekt bei Eintritt der Supraleitfähigkeit", Naturwissenschaften **21**, 787–788 (1933) (Cited on page 5).

[51] F. London and H. London, "The Electromagnetic Equations of the Supraconductor", Proc. R. Soc. London, Ser. A **149**, 71–88 (1935) (Cited on pages 6, 8).

[52] C. J. Gorter, *Paramagnetic relaxation* (Elsevier Publishing Company, 1947) (Cited on page 9).

[53] A. Amato and E. Morenzoni, *Introduction to muon spin spectroscopy: applications to solid state and material sciences*, 1st ed., Lecture Notes in Physics (Springer Cham, 2024) (Cited on pages 10, 145, 153).

[54] L. D. Landau and V. L. Ginzburg, "On the theory of superconductivity", Zh. Eksp. Teor. Fiz. **20**, 1064 (1950) (Cited on pages 11, 23).

[55] M. Tinkham, *Introduction to superconductivity*, 2nd ed., International Series in Pure and Applied Physics (McGraw-Hill, New York, 1996) (Cited on pages 12, 16, 17, 22, 25, 138, 162, 163).

[56] A. A. Abrikosov, "On the magnetic properties of superconductors of the second group", Sov. Phys. JETP **5**, 1174–1182 (1957) (Cited on pages 14, 26, 145).

[57] J. Bardeen, L. N. Cooper, and J. R. Schrieffer, "Microscopic Theory of Superconductivity", Phys. Rev. **106**, 162–164 (1957) (Cited on pages 15, 18, 126, 138).

[58] J. Bardeen, L. N. Cooper, and J. R. Schrieffer, "Theory of Superconductivity", Phys. Rev. **108**, 1175–1204 (1957) (Cited on pages 15, 18).

[59] P. G. De Gennes, *Superconductivity of metals and alloys* (CRC Press, Mar. 2018) (Cited on page 16).

[60] L. N. Cooper, "Bound Electron Pairs in a Degenerate Fermi Gas", Phys. Rev. **104**, 1189–1190 (1956) (Cited on page 16).

[61] P. Phillips, "Superconductivity in metals", in *Advanced solid state physics* (Cambridge University Press, 2012), pp. 189–257 (Cited on page 17).

[62] C. Kittel and P. McEuen, *Introduction to Solid State Physics* (John Wiley & Sons, 2015) (Cited on pages 17, 60).

[63] A. Carrington and F. Manzano, "Magnetic penetration depth of MgB_2", Physica C **385**, 205–214 (2003) (Cited on page 18).

[64] T. P. Sheahen, "Rules for the Energy Gap and Critical Field of Superconductors", Phys. Rev. **149**, 368–370 (1966) (Cited on pages 18, 159).

[65] B. Mühlschlegel, "Die thermodynamischen funktionen des supraleiters", Z. Physik **155**, 313–327 (1959) (Cited on pages 18, 19).

[66] R. C. Dynes, V. Narayanamurti, and J. P. Garno, "Direct Measurement of Quasiparticle-Lifetime Broadening in a Strong-Coupled Superconductor", Phys. Rev. Lett. **41**, 1509–1512 (1978) (Cited on pages 20, 149, 159, 166, 175).

[67] R. C. Dynes, J. P. Garno, G. B. Hertel, and T. P. Orlando, "Tunneling Study of Superconductivity near the Metal-Insulator Transition", Phys. Rev. Lett. **53**, 2437–2440 (1984) (Cited on page 20).

[68] E. Wigner and F. Seitz, "On the Constitution of Metallic Sodium", Phys. Rev. **43**, 804–810 (1933) (Cited on page 23).

[69] R. Parks, *Superconductivity: in two parts: volume 2*, 1st, Superconductivity (Taylor & Francis, New York, 1969) (Cited on page 24).

[70] E. H. Brandt, "The flux-line lattice in superconductors", Rep. Prog. Phys. **58**, 1465–1594 (1995) (Cited on pages 24, 101, 145).

[71] E. H. Brandt, "Magnetic field density of perfect and imperfect flux line lattices in type II superconductors. I. Application of periodic solutions", J. Low Temp. Phys. **73**, 355–390 (1988) (Cited on page 24).

[72] E. H. Brandt, "The vortex lattice in type-II superconductors: Ideal or distorted, in bulk and films", Phys. Status Solidi B **248**, 2305–2316 (2011) (Cited on pages 24, 25).

[73] T. M. Riseman and J. H. Brewer, "Modified London model for the determination of λ and ξ in a high κ superconductor", Hyperfine Interact. **86**, 597–602 (1994) (Cited on pages 24, 25).

[74] E. H. Brandt, "Flux distribution and penetration depth measured by muon spin rotation in high-T_c superconductors", Phys. Rev. B **37**, 2349–2352 (1988) (Cited on pages 24, 153).

[75] J. E. Sonier, J. H. Brewer, and R. F. Kiefl, "μSR studies of the vortex state in type-II superconductors", Rev. Mod. Phys. **72**, 769–811 (2000) (Cited on pages 24, 145).

[76] E. H. Brandt, "Muon spin rotation and the vortex lattice in superconductors", Physica B **404**, 695–699 (2009) (Cited on page 24).

[77] Z. Salman, R. F. Kiefl, K. H. Chow, M. D. Hossain, T. A. Keeler, S. R. Kreitzman, C. D. P. Levy, R. I. Miller, T. J. Parolin, M. R. Pearson, H. Saadaoui, J. D. Schultz, M. Smadella, D. Wang, and W. A. MacFarlane, "Near-Surface Structural Phase Transition of $SrTiO_3$ Studied with Zero-Field β-Detected Nuclear Spin Relaxation and Resonance", Phys. Rev. Lett. **96**, 147601 (2006) (Cited on pages 25, 89).

[78] C.-R. Hu, "Numerical Constants for Isolated Vortices in Superconductors", Phys. Rev. B **6**, 1756–1760 (1972) (Cited on page 26).

[79] M. Hein, *High-Temperature-Superconductor Thin Films at Microwave Frequencies*, Vol. 155, Springer Tracts in Modern Physics (Springer Berlin Heidelberg, 1999) (Cited on page 26).

[80] J. Harden and V. Arp, "The lower critical field in the Ginzburg-Landau theory of superconductivity", Cryogenics **3**, 105–108 (1963) (Cited on pages 26, 27).

[81] L. Neumann and L. Tewordt, "The structure of a vortex line and the lower critical field in superconducting alloys", Z. Physik **189**, 55–66 (1966) (Cited on pages 26, 27).

[82] E. H. Brandt, "Properties of the ideal Ginzburg-Landau vortex lattice", Phys. Rev. B **68**, 054506 (2003) (Cited on pages 26, 101, 151, 153).

[83] T. Baumgartner, M. Eisterer, H. W. Weber, R. Flükiger, C. Scheuerlein, and L. Bottura, "Effects of neutron irradiation on pinning force scaling in state-of-the-art Nb_3Sn wires", Supercond. Sci. Technol. **27**, 015005 (2013) (Cited on pages 28, 153, 177).

[84] T. Yogi, G. J. Dick, and J. E. Mercereau, "Critical rf Magnetic Fields for Some Type-I and Type-II Superconductors", Phys. Rev. Lett. **39**, 826–829 (1977) (Cited on page 30).

[85] A. Gurevich, "Tuning microwave losses in superconducting resonators", Supercond. Sci. Technol. **36**, 063002 (2023) (Cited on pages 30, 115).

[86] D. B. Liarte, S. Posen, M. K. Transtrum, G. Catelani, M. Liepe, and J. P. Sethna, "Theoretical estimates of maximum fields in superconducting resonant radio frequency cavities: stability theory, disorder, and laminates", Supercond. Sci. Technol. **30**, 033002 (2017) (Cited on pages 30–33).

[87] J. R. Schrieffer, *Theory of Superconductivity* (CRC Press, Mar. 2018) (Cited on page 31).

[88] P. de Gennes, "Vortex nucleation in type II superconductors", Solid State Commun. **3**, 127–130 (1965) (Cited on page 32).

[89] M. K. Transtrum, G. Catelani, and J. P. Sethna, "Superheating field of superconductors within Ginzburg-Landau theory", Phys. Rev. B **83**, 094505 (2011) (Cited on pages 32, 117).

[90] N. Kopnin, *Theory of Nonequilibrium Superconductivity* (Oxford University Press, May 2001) (Cited on page 33).

[91] G. Eilenberger, "Transformation of Gorkov's equation for type II superconductors into transport-like equations", Z. Physik **214**, 195–213 (1968) (Cited on page 33).

[92] G. Catelani and J. P. Sethna, "Temperature dependence of the superheating field for superconductors in the high-κ London limit", Phys. Rev. B **78**, 224509 (2008) (Cited on page 33).

[93] F. P.-J. Lin and A. Gurevich, "Effect of impurities on the superheating field of type-II superconductors", Phys. Rev. B **85**, 054513 (2012) (Cited on page 33).

[94] A.-M. Valente-Feliciano, "Superconducting RF materials other than bulk niobium: a review", Supercond. Sci. Technol. **29**, 113002 (2016) (Cited on pages 33, 39, 40, 118, 126, 139, 143, 162).

[95] N. Valles and M. Liepe, "The Superheating Field of Niobium: Theory and Experiment", International Conference on RF Superconductivity (Proc. SRF'11), 293–301 (2011) (Cited on page 33).

[96] A. Gurevich, "Theory of RF superconductivity for resonant cavities", Supercond. Sci. Technol. **30**, 034004 (2017) (Cited on pages 35, 36, 39, 40).

[97] A. Gurevich and T. Kubo, "Surface impedance and optimum surface resistance of a superconductor with an imperfect surface", Phys. Rev. B **96**, 184515 (2017) (Cited on pages 36, 39).

[98] S. Posen, "Understanding and overcoming limitation mechanisms in Nb_3Sn superconducting RF cavities", PhD thesis (Cornell University, 2015) (Cited on page 40).

[99] S. Keckert, T. Junginger, T. Buck, D. Hall, P. Kolb, O. Kugeler, R. Laxdal, M. Liepe, S. Posen, T. Prokscha, Z. Salman, A. Suter, and J. Knobloch, "Critical fields of Nb_3Sn prepared for superconducting cavities", Supercond. Sci. Technol. **32**, 075004 (2019) (Cited on pages 40, 111, 138).

[100] T. Junginger, T. Prokscha, Z. Salman, A. Suter, and A.-M. Valente-Feliciano, "Critical fields of SRF materials", in Proceedings of IPAC'18, International Particle Accelerator Conference 9 (TRIUMF, June 2018), pp. 3921–3924 (Cited on pages 40, 135, 145, 153).

[101] R. M. L. McFadden, M. Asaduzzaman, T. J. Buck, D. L. Cortie, M. H. Dehn, S. R. Dunsiger, R. F. Kiefl, R. E. Laxdal, C. D. P. Levy, W. A. MacFarlane, G. D. Morris, M. R. Pearson, E. Thoeng, and T. Junginger, "Depth-resolved measurement of the Meissner screening profile in a niobium thin film from spin-lattice relaxation of the implanted β-emitter ^{8}Li", J. Appl. Phys. **134**, 163902 (2023) (Cited on pages 40, 58, 92, 185).

[102] A. Romanenko, F. Barkov, L. D. Cooley, and A. Grassellino, "Proximity breakdown of hydrides in superconducting niobium cavities", Supercond. Sci. Technol. **26**, 035003 (2013) (Cited on pages 41, 113).

[103] P. Kneisel, D. Mansen, G. Müller, H. Piel, J. Pouryamout, and R. Roeth, "Nb_3Sn Layers on High-Purity Nb Cavities with Very High Quality Factors and Accelerating Gradients", in Proc. EPAC'96 (1996) (Cited on page 42).

[104] S. Posen, J. Lee, D. N. Seidman, A. Romanenko, B. Tennis, O. S. Melnychuk, and D. A. Sergatskov, "Advances in Nb_3Sn superconducting radiofrequency cavities towards first practical accelerator applications", Supercond. Sci. Technol. **34**, 025007 (2021) (Cited on page 42).

[105] J. Lee, S. Posen, Z. Mao, Y. Trenikhina, K. He, D. L. Hall, M. Liepe, and D. N. Seidman, "Atomic-scale analyses of Nb_3Sn on Nb prepared by vapor diffusion for superconducting radiofrequency cavity applications: a correlative study", Supercond. Sci. Technol. **32**, 024001 (2018) (Cited on page 42).

[106] S. Posen and M. Liepe, "Advances in development of Nb_3Sn superconducting radiofrequency cavities", Phys. Rev. ST Accel. Beams **17**, 112001 (2014) (Cited on pages 42, 103).

[107] S. Posen, M. Liepe, and D. L. Hall, "Proof-of-principle demonstration of Nb_3Sn superconducting radiofrequency cavities for high Q applications", Appl. Phys. Lett. **106**, 082601 (2015) (Cited on pages 42, 103).

[108] J. Lee, Z. Mao, K. He, Z. H. Sung, T. Spina, S.-I. Baik, D. L. Hall, M. Liepe, D. N. Seidman, and S. Posen, "Grain-boundary structure and segregation in Nb_3Sn coatings on Nb for high-performance superconducting radiofrequency cavity applications", Acta Mater. **188**, 155–165 (2020) (Cited on page 42).

[109] G. Eremeev, W. Clemens, K. Macha, C. E. Reece, A. M. Valente-Feliciano, S. Williams, U. Pudasaini, and M. Kelley, "Nb_3Sn multicell cavity coating system at Jefferson Lab", Rev. Sci. Instrum. **91**, 073911 (2020) (Cited on page 42).

[110] N. S. Sitaraman, M. M. Kelley, R. D. Porter, M. U. Liepe, T. A. Arias, J. Carlson, A. R. Pack, M. K. Transtrum, and R. Sundararaman, "Effect of the density of states at the Fermi level on defect free energies and superconductivity: A case study of Nb_3Sn", Phys. Rev. B **103**, 115106 (2021) (Cited on page 42).

[111] U. Pudasaini, G. V. Eremeev, C. E. Reece, J. Tuggle, and M. J. Kelley, "Initial growth of tin on niobium for vapor diffusion coating of Nb_3Sn", Supercond. Sci. Technol. **32**, 045008 (2019) (Cited on page 42).

[112] U. Pudasaini, G. V. Eremeev, J. W. Angle, J. Tuggle, C. E. Reece, and M. J. Kelley, "Growth of Nb_3Sn coating in tin vapor-diffusion process", J. Vac. Sci. Technol. **37**, 051509 (2019) (Cited on page 42).

[113] Q. Chen, Y. Zong, Z. Wang, S. Xing, J. Wu, P. Dong, M. Zhao, X. Wu, J. Rong, and J. Chen, "First Results of Nb_3Sn Coated Cavity by Vapor Diffusion Method at SARI", Coatings **14**, 10.3390/coatings14050581 (2024) (Cited on page 42).

[114] N. A. Stilin, A. Holic, M. Liepe, R. D. Porter, J. Sears, and Z. Sun, "RF and thermal studies on conduction cooled Nb_3Sn SRF cavity", Eng. Res. Express **5**, 025078 (2023) (Cited on page 42).

[115] G. Jiang, S. Wu, Z. Yang, Y. He, Y. Ye, H. Guo, C. Li, P. Xiong, L. Li, S. Huang, A. Wu, F. Qiu, J. Zhang, X. Niu, Q. Huang, Z. Qin, T. Tan, Z. Wang, S. Zhang, H. Zhao, and W. Zhan, "Understanding and optimization of the coating process of the radio-frequency Nb_3Sn thin film superconducting cavities using tin vapor diffusion method", Appl. Surf. Sci. **643**, 158708 (2024) (Cited on page 42).

[116] E. Viklund, D. N. Seidman, S. Posen, B. M. Tennis, and G. Eremeev, "Healing gradient degradation in Nb_3Sn SRF cavities using a recoating method", APL Mater. **12**, 071106 (2024) (Cited on page 42).

[117] C. Dong, Z. Lin, P. Sha, B. Liu, L. Ye, and X. He, "Preliminary Research of Niobium Cavity Coating with Nb_3Sn Film at IHEP", Physica C **600**, 1354107 (2022) (Cited on page 42).

[118] G. Wang, S. Quan, L. Lin, M. Ren, J. Hao, F. Wang, F. Jiao, F. Zhu, S. Huang, X. Yan, and K. Zhu, "Nb_3Sn Cavities Coated by Tin Vapor Diffusion Method at Peking University", Appl. Sci. **13**, 10.3390/app13158618 (2023) (Cited on page 42).

[119] S. Posen, N. Valles, and M. Liepe, "Radio Frequency Magnetic Field Limits of Nb and Nb_3Sn", Phys. Rev. Lett. **115**, 047001 (2015) (Cited on pages 42, 95, 96, 106, 107, 110, 111, 144).

[120] R. D. Porter, "Advancing the Maximum Accelerating Gradient of Niobium-3 Tin Superconducting Radiofrequency Accelerator Cavities: RF Measurements, Dynamic Temperature Mapping, and Material Growth", PhD thesis (Cornell University, 2021) (Cited on page 42).

[121] A. Abrikosov, "On the lower critical field of thin layers of superconductors of the second group", Soviet Physics JETP **19**, 988–991 (1964) (Cited on page 43).

[122] G. Stejic, A. Gurevich, E. Kadyrov, D. Christen, R. Joynt, and D. C. Larbalestier, "Effect of geometry on the critical currents of thin films", Phys. Rev. B **49**, 1274–1288 (1994) (Cited on page 43).

[123] C. Poole Jr, H. Farach, R. Creswick, and R. Prozorov, *Superconductivity, (2007)*, 1st ed. (Academic press, Amsterdam, 2007) (Cited on pages 44, 132).

[124] C. Z. Antoine, S. Berry, S. Bouat, J.-F. Jacquot, J.-C. Villegier, G. Lamura, and A. Gurevich, "Characterization of superconducting nanometric multilayer samples for superconducting rf applications: First evidence of magnetic screening effect", Phys. Rev. ST Accel. Beams **13**, 121001 (2010) (Cited on page 52).

[125] C. Z. Antoine, S. Berry, M. Aurino, J.-F. Jacquot, J.-C. Villegier, G. Lamura, and A. Andreone, "Characterization of Field Penetration in Superconducting Multilayers Samples", IEEE Trans. Appl. Supercond. **21**, 2601–2604 (2011) (Cited on page 52).

[126] C. Z. Antoine, M. Aburas, A. Four, F. Weiss, Y. Iwashita, H. Hayano, S. Kato, T. Kubo, and T. Saeki, "Optimization of tailored multilayer superconductors for rf application and protection against premature vortex penetration", Supercond. Sci. Technol. **32**, 085005 (2019) (Cited on pages 52, 144).

[127] C. Z. Antoine, J.-C. Villegier, and G. Martinet, "Study of nanometric superconducting multilayers for RF field screening applications", Appl. Phys. Lett. **102**, 102603 (2013) (Cited on page 52).

[128] W. M. Roach, D. B. Beringer, Z. Li, C. Clavero, and R. A. Lukaszew, "Magnetic Shielding Larger Than the Lower Critical Field of Niobium in Multilayers", IEEE Trans. Appl. Supercond. **23**, 8600203–8600203 (2013) (Cited on page 52).

[129] T. Tan, M. A. Wolak, X. X. Xi, T. Tajima, and L. Civale, "Magnesium diboride coated bulk niobium: a new approach to higher acceleration gradient", Sci. Rep. **6**, 35879 (2016) (Cited on pages 52, 53, 144).

[130] D. B. Beringer, C. Clavero, T. Tan, X. X. Xi, W. M. Roach, and R. A. Lukaszew, "Thickness Dependence and Enhancement of H_{c1} in Epitaxial MgB_2 Thin Films", IEEE Trans. Appl. Supercond. **23**, 7500604–7500604 (2013) (Cited on page 53).

[131] T. Tan, M. A. Wolak, N. Acharya, A. Krick, A. C. Lang, J. Sloppy, M. L. Taheri, L. Civale, K. Chen, and X. X. Xi, "Enhancement of lower critical field by reducing the thickness of epitaxial and polycrystalline MgB_2 thin films", APL Mater. **3**, 041101 (2015) (Cited on page 53).

[132] T. Junginger, S. H. Abidi, R. D. Maffett, T. Buck, M. H. Dehn, S. Gheidi, R. Kiefl, P. Kolb, D. Storey, E. Thoeng, W. Wasserman, and R. E. Laxdal, "Field of first magnetic flux entry and pinning strength of superconductors for rf application measured with muon spin rotation", Phys. Rev. Accel. Beams **21**, 032002 (2018) (Cited on pages 53, 58, 96, 97, 101, 102, 107–110, 112, 116, 132).

[133] T. Junginger, W. Wasserman, and R. E. Laxdal, "Superheating in coated niobium", Supercond. Sci. Technol. **30**, 125012 (2017) (Cited on pages 53, 58, 95–97, 101, 102, 107, 108, 110, 111, 118, 144).

[134] I. Senevirathne, D. Beverstock, J. Delayen, A. Gurevich, and A.-M. Valente-Feliciano, "Investigation of the Multilayer Shielding Effect through NbTiN-AlN Coated Bulk Niobium", in Proc. 21th Int. Conf. RF Supercond. (SRF'23), International Conference on RF Superconductivity 21 (Sept. 2023), pp. 311–315 (Cited on page 53).

[135] Y. Kalboussi, A. four, B. Delatte, C. Antoine, D. Longuevergne, O. Hryhoenko, D. Dragoe, J. Leroy, S. Tusseau-Nenez, Y. Zheng, D. Hrabovsky, A. Gentils, S. J. Leclerc, F. Miserque, M. Belhaj, and T. Proslier, "ALD-deposited multilayer to improve the superconducting performances of RF cavities", in 10th International Workshop on Thin Films and New Ideas for Pushing the Limits of RF Superconductivity, Thin films and new ideas for SRF (Sept. 2022) (Cited on page 53).

[136] R. Prozorov and V. G. Kogan, "Effective Demagnetizing Factors of Diamagnetic Samples of Various Shapes", Phys. Rev. Applied **10**, 014030 (2018) (Cited on pages 54, 132, 181).

[137] S. Keckert, J. Knobloch, O. Kugeler, D. Tikhonov, and A.-M. Valente-Feliciano, "RF Characterization of an S-I-S' Multilayer Sample", in Proc. SRF'19, International Conference on RF Superconductivity 19 (Aug. 2019), pp. 800–806 (Cited on page 55).

[138] D. Tikhonov, E. Chyhyrynets, S. Keckert, J. Knobloch, O. Kugeler, S. Leith, C. Pira, and M. Vogel, "Investigation of SIS Multilayer Films at HZB", in Proc. 20th International Conference on RF Superconductivity (SRF'21), International Conference on RF Superconductivity 20 (Oct. 2022), pp. 72–76 (Cited on page 55).

[139] S. R. Kreitzman and G. D. Morris, "TRIUMF MuSR and βNMR research facilities", JPS Conf. Proc. **21**, 011056 (2018) (Cited on pages 57, 59, 85, 97, 99).

[140] D. J. Arseneau, B. Hitti, S. R. Kreitzman, and E. Whidden, "The TRIUMF μSR facility", Hyperfine Interact. **106**, 277–282 (1997) (Cited on page 57).

[141] T. Prokscha, E. Morenzoni, K. Deiters, F. Foroughi, D. George, R. Kobler, A. Suter, and V. Vrankovic, "The new μE4 beam at PSI: a hybrid-type large acceptance channel for the generation of a high intensity surface-muon beam", Nucl. Instrum. Methods Phys. Res., Sect. A **595**, 317–331 (2008) (Cited on pages 57, 122).

[142] W. MacFarlane, "Implanted-ion βNMR: A new probe for nanoscience", Solid State Nucl. Magn. Reson. **68-69**, 1–12 (2015) (Cited on pages 57, 58, 145–147, 155).

[143] E. Tiesinga, P. J. Mohr, D. B. Newell, and B. N. Taylor, "CODATA recommended values of the fundamental physical constants: 2018", Rev. Mod. Phys. **93**, 025010 (2021) (Cited on page 58).

[144] P. D. Group, P. A. Zyla, R. M. Barnett, J. Beringer, O. Dahl, D. A. Dwyer, D. E. Groom, C. .-. Lin, K. S. Lugovsky, E. Pianori, D. J. Robinson, C. G. Wohl, W. .-. Yao, K. Agashe, G. Aielli, B. C. Allanach, C. Amsler, M. Antonelli, E. C. Aschenauer, D. M. Asner, H. Baer, S. Banerjee, L. Baudis, C. W. Bauer, J. J. Beatty, V. I. Belousov, S. Bethke, A. Bettini, O. Biebel, K. M. Black, E. Blucher, O. Buchmuller, V. Burkert, M. A. Bychkov, R. N. Cahn, M. Carena, A. Ceccucci, A. Cerri, D. Chakraborty, R. S. Chivukula, G. Cowan, G. D'Ambrosio, T. Damour, D. de Florian, A. de Gouvêa, T. DeGrand, P. de Jong, G. Dissertori, B. A. Dobrescu, M. D'Onofrio, M. Doser, M. Drees, H. K. Dreiner, P. Eerola, U. Egede, S. Eidelman, J. Ellis, J. Erler, V. V. Ezhela, W. Fetscher, B. D. Fields, B. Foster, A. Freitas, H. Gallagher, L. Garren, H. .-. Gerber, G. Gerbier, T. Gershon, Y. Gershtein, T. Gherghetta, A. A. Godizov, M. C. Gonzalez-Garcia, M. Goodman, C. Grab, A. V. Gritsan, C. Grojean, M. Grünewald, A. Gurtu, T. Gutsche, H. E. Haber, C. Hanhart, S. Hashimoto, Y. Hayato, A. Hebecker, S. Heinemeyer, B. Heltsley, J. J. Hernández-Rey, K. Hikasa, J. Hisano, A. Höcker, J. Holder, A. Holtkamp, J. Huston, T. Hyodo, K. F. Johnson, M. Kado, M. Karliner, U. F. Katz, M. Kenzie, V. A. Khoze, S. R. Klein, E. Klempt, R. V. Kowalewski, F. Krauss, M. Kreps, B. Krusche, Y. Kwon, O. Lahav, J. Laiho, L. P. Lellouch, J. Lesgourgues, A. R.

Liddle, Z. Ligeti, C. Lippmann, T. M. Liss, L. Littenberg, C. Lourengo, S. B. Lugovsky, A. Lusiani, Y. Makida, F. Maltoni, T. Mannel, A. V. Manohar, W. J. Marciano, A. Masoni, J. Matthews, U. .-. Meißner, M. Mikhasenko, D. J. Miller, D. Milstead, R. E. Mitchell, K. Mönig, P. Molaro, F. Moortgat, M. Moskovic, K. Nakamura, M. Narain, P. Nason, S. Navas, M. Neubert, P. Nevski, Y. Nir, K. A. Olive, C. Patrignani, J. A. Peacock, S. T. Petcov, V. A. Petrov, A. Pich, A. Piepke, A. Pomarol, S. Profumo, A. Quadt, K. Rabbertz, J. Rademacker, G. Raffelt, H. Ramani, M. Ramsey-Musolf, B. N. Ratcliff, P. Richardson, A. Ringwald, S. Roesler, S. Rolli, A. Romaniouk, L. J. Rosenberg, J. L. Rosner, G. Rybka, M. Ryskin, R. A. Ryutin, Y. Sakai, G. P. Salam, S. Sarkar, F. Sauli, O. Schneider, K. Scholberg, A. J. Schwartz, J. Schwiening, D. Scott, V. Sharma, S. R. Sharpe, T. Shutt, M. Silari, T. Sjöstrand, P. Skands, T. Skwarnicki, G. F. Smoot, A. Soffer, M. S. Sozzi, S. Spanier, C. Spiering, A. Stahl, S. L. Stone, Y. Sumino, T. Sumiyoshi, M. J. Syphers, F. Takahashi, M. Tanabashi, J. Tanaka, M. Taševský, K. Terashi, J. Terning, U. Thoma, R. S. Thorne, L. Tiator, M. Titov, N. P. Tkachenko, D. R. Tovey, K. Trabelsi, P. Urquijo, G. Valencia, R. Van de Water, N. Varelas, G. Venanzoni, L. Verde, M. G. Vincter, P. Vogel, W. Vogelsang, A. Vogt, V. Vorobyev, S. P. Wakely, W. Walkowiak, C. W. Walter, D. Wands, M. O. Wascko, D. H. Weinberg, E. J. Weinberg, M. White, L. R. Wiencke, S. Willocq, C. L. Woody, R. L. Workman, M. Yokoyama, R. Yoshida, G. Zanderighi, G. P. Zeller, O. V. Zenin, R. .-. Zhu, S. .-. Zhu, F. Zimmermann, J. Anderson, T. Basaglia, V. S. Lugovsky, P. Schaffner, and W. Zheng, "Review of Particle Physics", Prog. Theor. Exp. Phys. **2020**, 083C01 (2020) (Cited on page 58).

[145] R. M. L. McFadden, M. Asaduzzaman, T. Prokscha, Z. Salman, A. Suter, and T. Junginger, "Depth-resolved measurements of the meissner screening profile in surface-treated Nb", Phys. Rev. Appl. **19**, 044018 (2023) (Cited on pages 58, 92, 93, 96, 103, 111, 113, 114, 121, 124, 125, 136, 139).

[146] S. J. Blundell, R. De Renzi, T. Lancaster, and F. L. Pratt, "Low energy μSR", in *Muon Spectroscopy: An Introduction* (Oxford University Press, Nov. 2021) (Cited on pages 59, 78, 123, 145).

[147] E. Thoeng, M. Asaduzzaman, P. Kolb, R. M. L. McFadden, G. D. Morris, J. O. Ticknor, S. R. Dunsiger, V. L. Karner, D. Fujimoto, T. Junginger, R. F. Kiefl, W. A. MacFarlane, R. Li, S. Saminathan, and R. E. Laxdal, "Depth-resolved characterization of Meissner screening breakdown in surface treated niobium", Sci. Rep. **14**, 21487 (2024) (Cited on pages 59, 168, 185).

[148] T. Junginger, R. Laxdal, W. A. MacFarlane, and A. Suter, "SRF material research using muon spin rotation and beta-detected nuclear magnetic resonance", Front. Electron. Mater. **4**, 10.3389/femat.2024.1346235 (2024) (Cited on page 59).

[149] S. Blundell, *Magnetism in Condensed Matter*, Oxford Master Series in Condensed Matter Physics 4 (OUP Oxford, 2001) (Cited on page 60).

[150] B. Cowan, *Nuclear Magnetic Resonance and Relaxation* (Cambridge University Press, 1997) (Cited on page 60).

[151] F. Bloch, "Nuclear Induction", Phys. Rev. **70**, 460–474 (1946) (Cited on page 64).

[152] C. P. Slichter, *Principles of Magnetic Resonance* (Springer Berlin Heidelberg, 1990) (Cited on pages 65, 164, 165, 168).

[153] A. Abragam, *The Principles of Nuclear Magnetism*, International series of monographs on physics 32 (Clarendon Press, 1961) (Cited on page 65).

[154] T. D. Lee and C. N. Yang, "Question of Parity Conservation in Weak Interactions", Phys. Rev. **104**, 254–258 (1956) (Cited on page 66).

[155] C. S. Wu, E. Ambler, R. W. Hayward, D. D. Hoppes, and R. P. Hudson, "Experimental Test of Parity Conservation in Beta Decay", Phys. Rev. **105**, 1413–1415 (1957) (Cited on page 66).

[156] R. L. Garwin, L. M. Lederman, and M. Weinrich, "Observations of the Failure of Conservation of Parity and Charge Conjugation in Meson Decays: the Magnetic Moment of the Free Muon", Phys. Rev. **105**, 1415–1417 (1957) (Cited on page 66).

[157] W. F. Dudziak, R. Sagane, and J. Vedder, "Positron Spectrum from the Decay of the μ Meson", Phys. Rev. **114**, 336–358 (1959) (Cited on page 69).

[158] A. Yaouanc and P. Dalmas de Réotier, *Muon spin rotation, relaxation, and resonance: applications to condensed matter*, Vol. 147, International Series of Monographs on Physics (Oxford University Press, Oxford, 2011) (Cited on pages 70, 78, 96, 101).

[159] J. Sonier, "Muon spin rotation/relaxation", Resonance brochure (2002) (Cited on pages 73, 75).

[160] S. Lee, S. Kilcoyne, R. Cywinski, and P. Osborne, *Muon Science: Muons in Physics, Chemistry and Materials*, English, Publisher Copyright: © 1999 The Scottish Universities Summer School in Physics. (CRC Press, Jan. 2017) (Cited on page 74).

[161] R. Kubo and T. Toyabe, "A stochastic model for low field resonance and relaxation", in *Magnetic resonance and relaxation*, edited by R. Blinc (North-Holland, Amsterdam, 1967), pp. 810–823 (Cited on pages 75, 101).

[162] R. S. Hayano, Y. J. Uemura, J. Imazato, N. Nishida, T. Yamazaki, and R. Kubo, "Zero-and low-field spin relaxation studied by positive muons", Phys. Rev. B **20**, 850–859 (1979) (Cited on pages 75, 77, 101, 104).

[163] D. R. Harshman, A. P. Mills, J. L. Beveridge, K. R. Kendall, G. D. Morris, M. Senba, J. B. Warren, A. S. Rupaal, and J. H. Turner, "Generation of slow positive muons from solid rare-gas moderators", Phys. Rev. B **36**, 8850–8853 (1987) (Cited on page 79).

[164] E. Morenzoni, F. Kottmann, D. Maden, B. Matthias, M. Meyberg, T. Prokscha, T. Wutzke, and U. Zimmermann, "Generation of very slow polarized positive muons", Phys. Rev. Lett. **72**, 2793–2796 (1994) (Cited on pages 79, 80).

[165] Z. Salman, T. Prokscha, P. Keller, E. Morenzoni, H. Saadaoui, K. Sedlak, T. Shiroka, S. Sidorov, A. Suter, V. Vrankovic, and H.-P. Weber, "Design and Simulation of a Spin Rotator for Longitudinal Field Measurements in the Low Energy Muons Spectrometer", Physics Procedia **30**, 55–60 (2012) (Cited on page 79).

[166] L.-P. Zhou, X.-J. Ni, Z. Salman, A. Suter, J.-Y. Tang, V. Vrankovic, and T. Prokscha, "Simulation studies for upgrading a high-intensity surface muon beamline at Paul Scherrer Institute", Phys. Rev. Accel. Beams **25**, 051601 (2022) (Cited on page 79).

[167] T. Prokscha, E. Morenzoni, C. David, A. Hofer, H. Glückler, and L. Scandella, "Moderator gratings for the generation of epithermal positive muons", Appl. Surf. Sci. **172**, 235–244 (2001) (Cited on pages 80, 122).

[168] E. Morenzoni, T. Prokscha, A. Hofer, B. Matthias, M. Meyberg, T. Wutzke, H. Glückler, M. Birke, J. Litterst, C. Neidermayer, and G. Schatz, "Characteristics of condensed gas moderators for the generation of very slow polarized muons", J. Appl. Phys. **81**, 3340–3347 (1997) (Cited on page 80).

[169] E. Morenzoni, H. Glückler, T. Prokscha, H. Weber, E. Forgan, T. Jackson, H. Luetkens, C. Niedermayer, M. Pleines, M. Birke, A. Hofer, J. Litterst, T. Riseman, and G. Schatz, "Low-energy μSR at PSI: present and future", Physica B **289-290**, 653–657 (2000) (Cited on page 80).

[170] T. Griffy and L. Biedenharn, "Beta decay involving the $Be^{8*}(2^+)$ state", Nucl. Phys. **15**, 636–645 (1960) (Cited on page 82).

[171] J. Dilling, R. Krücken, and G. Ball, "ISAC overview", Hyperfine Interact. **225**, 1–8 (2013) (Cited on page 83).

[172] I. Bylinskii and M. K. Craddock, "The TRIUMF 500 MeV cyclotron: the driver accelerator", Hyperfine Interact. **225**, 9–16 (2013) (Cited on page 83).

[173] C. Levy, A. Hatakeyama, Y. Hirayama, R. Kiefl, R. Baartman, J. Behr, H. Izumi, D. Melconian, G. Morris, R. Nussbaumer, M. Olivo, M. Pearson, R. Poutissou, and G. Wight, "Polarized radioactive beam at ISAC", Nucl. Instrum. Methods Phys. Res., Sect. B **204**, 689–693 (2003) (Cited on pages 84, 85, 146).

[174] W. A. MacFarlane, C. D. P. Levy, M. R. Pearson, T. Buck, K. H. Chow, A. N. Hariwal, R. F. Kiefl, F. H. McGee, G. D. Morris, and D. Wang, "The Initial State of Optically Polarized $^{8}Li^{+}$ from the β-NMR in Bismuth", J. Phys. Conf. Ser. **551**, 012059 (2014) (Cited on page 85).

[175] C. Levy, R. Baartman, K. Jayamanna, R. Kiefl, T. Kuo, M. Olivo, G. Wight, D. Yuan, and A. Zelenski, "A polarized beams project at ISAC", Nucl. Phys. A **701**, 5th International Conference on Radioactive Nuclear Beams, 253–258 (2002) (Cited on page 85).

[176] J. Dilling and R. Krücken, "The experimental facilities at ISAC", Hyperfine Interact. **225**, 111–114 (2014) (Cited on page 85).

[177] G. D. Morris, W. A. MacFarlane, K. H. Chow, Z. Salman, D. J. Arseneau, S. Daviel, A. Hatakeyama, S. R. Kreitzman, C. D. P. Levy, R. Poutissou, R. H. Heffner, J. E. Elenewski, L. H. Greene, and R. F. Kiefl, "Depth-Controlled β-NMR of ^{8}Li in a Thin Silver Film", Phys. Rev. Lett. **93**, 157601 (2004) (Cited on pages 85, 155).

[178] G. D. Morris, "β-NMR", Hyperfine Interact. **225**, 173–182 (2014) (Cited on pages 85, 147).

[179] Z. Salman, E. P. Reynard, W. A. MacFarlane, K. H. Chow, J. Chakhalian, S. R. Kreitzman, S. Daviel, C. D. P. Levy, R. Poutissou, and R. F. Kiefl, "β-detected nuclear quadrupole resonance with a low-energy beam of $^{8}Li^{+}$", Phys. Rev. B **70**, 104404 (2004) (Cited on page 85).

[180] Z. Salman, K. H. Chow, M. D. Hossain, R. F. Kiefl, C. D. P. Levy, T. J. Parolin, M. R. Pearson, H. Saadaoui, D. Wang, and W. A. MacFarlane, "β-detected nuclear quadrupole resonance and relaxation of $^{8}Li^{+}$ in sapphire", J. Phys. Conf. Ser. **551**, 012034 (2014) (Cited on page 87).

[181] D. Jimenez-Rey, B. Zurro, K. J. McCarthy, G. Garcia, and A. Baciero, "The response of a radiation resistant ceramic scintillator (Al_2O_3:Cr) to low energy ions (-60 keV)", Rev. Sci. Instrum. **79**, 10E516 (2008) (Cited on page 87).

[182] H. Ackermann, P. Heitjans, and H.-J. Stöckmann, "β Emitters and Isomeric Nuclei as Probes in Condensed Matter", in *Hyperfine interactions of radioactive nuclei* (Springer Berlin Heidelberg, 1983), pp. 291–361 (Cited on page 89).

[183] J. F. Ziegler, J. P. Biersack, and M. D. Ziegler, *SRIM — The Stopping and Range of Ions in Matter*, 7th ed. (SRIM Co., Chester, 2008) (Cited on pages 92, 98, 100, 146, 147).

[184] W. Eckstein, *Computer Simulation of Ion-Solid Interactions*, Vol. 10, Springer Series in Materials Science (Springer, Berlin, 1991) (Cited on pages 92, 124).

[185] M. D. Hossain, Z. Salman, D. Wang, K. H. Chow, S. Kreitzman, T. A. Keeler, C. D. P. Levy, W. A. MacFarlane, R. I. Miller, G. D. Morris, T. J. Parolin, M. Pearson, H. Saadaoui, and R. F. Kiefl, "Low-field cross spin relaxation of ^{8}Li in superconducting $NbSe_2$", Phys. Rev. B **79**, 144518 (2009) (Cited on pages 92, 158, 165, 185).

[186] E. Morenzoni, H. Glückler, T. Prokscha, R. Khasanov, H. Luetkens, M. Birke, E. M. Forgan, C. Niedermayer, and M. Pleines, "Implantation studies of keV positive muons in thin metallic layers", Nucl. Instrum. Methods Phys. Res., Sect. B **192**, 254–266 (2002) (Cited on pages 92, 124, 125).

[187] M. J. Berger, M. Inokuti, H. H. Andersen, H. Bichsel, D. Powers, S. . M. Seltzer, D. . Thwaites, and D. E. Watt, "Report 49", Journal of the ICRU **os25**, NP–NP (2016) (Cited on page 93).

[188] M. V. Moro, P. Bauer, and D. Primetzhofer, "Experimental electronic stopping cross section of transition metals for light ions: Systematics around the stopping maximum", Phys. Rev. A **102**, 022808 (2020) (Cited on page 93).

[189] P. Bauer and D. Semrad, "Stopping of hydrogen ions in chemically active metal targets, characterized by AES and RBS", Nucl. Instrum. Methods Phys. Res., Sect. B **13**, 201–206 (1986) (Cited on page 93).

[190] E. Sirotinin, A. Tulinov, V. Khodyrev, and V. Mizgulin, "Proton energy loss in solids", Nucl. Instrum. Methods Phys. Res., Sect. B **4**, 337–345 (1984) (Cited on page 93).

[191] C. Varelas and J. Biersack, "Reflection of energetic particles from atomic or ionic chains in single crystals", Nucl. Instrum. Methods **79**, 213–218 (1970) (Cited on page 93).

[192] P. Bakule and E. Morenzoni, "Generation and applications of slow polarized muons", Contemp. Phys. **45**, 203–225 (2004) (Cited on pages 93, 96, 112, 123).

[193] A. Suter and B. M. Wojek, "Musrfit: A Free Platform-Independent Framework for μSR Data Analysis", Phys. Proc. **30**, 69–73 (2012) (Cited on pages 93, 130).

[194] R. Brun and F. Rademakers, "ROOT — An object oriented data analysis framework", Nucl. Instrum. Methods Phys. Res., Sect. A **389**, New Computing Techniques in Physics Research V, 81–86 (1997) (Cited on page 93).

[195] F. James and M. Roos, "Minuit - a system for function minimization and analysis of the parameter errors and correlations", Comput. Phys. Commun. **10**, 343–367 (1975) (Cited on page 94).

[196] M. Hatlo, F. James, P. Mato, L. Moneta, M. Winkler, and A. Zsenei, "Developments of mathematical software libraries for the LHC experiments", IEEE Trans. Nucl. Sci. **52**, 2818–2822 (2005) (Cited on page 94).

[197] C. R. Harris, K. J. Millman, S. J. van der Walt, R. Gommers, P. Virtanen, D. Cournapeau, E. Wieser, J. Taylor, S. Berg, N. J. Smith, R. Kern, M. Picus, S. Hoyer, M. H. van Kerkwijk, M. Brett, A. Haldane, J. F. del Río, M. Wiebe, P. Peterson, P. Gérard-Marchant, K. Sheppard, T. Reddy, W. Weckesser, H. Abbasi, C. Gohlke, and T. E. Oliphant, "Array programming with NumPy", Nature **585**, 357–362 (2020) (Cited on page 94).

[198] P. Virtanen, R. Gommers, T. E. Oliphant, M. Haberland, T. Reddy, D. Cournapeau, E. Burovski, P. Peterson, W. Weckesser, J. Bright, S. J. van der Walt, M. Brett, J. Wilson, K. J. Millman, N. Mayorov, A. R. J. Nelson, E. Jones, R. Kern, E. Larson, C. J. Carey, İ. Polat, Y. Feng, E. W. Moore, J. VanderPlas, D. Laxalde, J. Perktold, R. Cimrman, I. Henriksen, E. A. Quintero, C. R. Harris, A. M. Archibald, A. H. Ribeiro, F. Pedregosa, P. van Mulbregt, and SciPy 1.0 Contributors, "SciPy 1.0: Fundamental Algorithms for Scientific Computing in Python", Nat. Methods **17**, 261–272 (2020) (Cited on page 94).

[199] H. Dembinski and P. O. et al., "Scikit-hep/iminuit", `10.5281/zenodo.3949207` (2020) (Cited on page 94).

[200] D. Fujimoto, "bfit: A Python Application For Beta-Detected NMR", J. Open Source Softw. **6**, 3598 (2021) (Cited on page 94).

[201] D. Fujimoto, "Digging Into MUD With Python: mudpy, bdata, and bfit", arXiv e-prints, arXiv:2004.10395 (2020), arXiv:`2004.10395 [physics.data-an]` (Cited on page 94).

[202] J. D. Hunter, "Matplotlib: A 2D graphics environment", Comput. Sci. Eng. **9**, 90–95 (2007) (Cited on page 94).

[203] H. Padamsee, *Superconducting Radiofrequency Technology for Accelerators: State of the Art and Emerging Trends* (Wiley, Weinheim, 2023) (Cited on pages 95, 143, 168).

[204] W. Singer, S. Aderhold, A. Ermakov, J. Iversen, D. Kostin, G. Kreps, A. Matheisen, W.-D. Möller, D. Reschke, X. Singer, K. Twarowski, H. Weise, and H.-G. Brokmeier, "Development of large grain cavities", Phys. Rev. ST Accel. Beams **16**, 012003 (2013) (Cited on page 96).

[205] E. Morenzoni, T. Prokscha, A. Suter, H. Luetkens, and R. Khasanov, "Nano-scale thin film investigations with slow polarized muons", J. Phys.: Condens. Matter **16**, S4583–S4601 (2004) (Cited on pages 96, 112, 124, 145).

[206] A. Romanenko, A. Grassellino, F. Barkov, A. Suter, Z. Salman, and T. Prokscha, "Strong meissner screening change in superconducting radio frequency cavities due to mild baking", Appl. Phys. Lett. **104**, 072601 (2014) (Cited on pages 96, 113, 136).

[207] V. Ngampruetikorn and J. A. Sauls, "Effect of inhomogeneous surface disorder on the superheating field of superconducting RF cavities", Phys. Rev. Res. **1**, 012015(R) (2019) (Cited on pages 96, 114).

[208] M. Checchin and A. Grassellino, "High-field Q-slope mitigation due to impurity profile in superconducting radio-frequency cavities", Appl. Phys. Lett. **117**, 032601 (2020) (Cited on pages 96, 114).

[209] R. M. L. McFadden, M. Asaduzzaman, and T. Junginger, "Comment on "Strong Meissner screening change in superconducting radio frequency cavities due to mild baking" [Appl. Phys. Lett. 104, 072601 (2014)]", Appl. Phys. Lett. **124**, 086101 (2024) (Cited on pages 96, 113, 114).

[210] A. D. Hillier, S. J. Blundell, I. McKenzie, I. Umegaki, L. Shu, J. A. Wright, T. Prokscha, F. Bert, K. Shimomura, A. Berlie, H. Alberto, and I. Watanabe, "Muon spin spectroscopy", Nat. Rev. Methods Primers **2**, 4 (2022) (Cited on page 96).

[211] A. Godeke, "A review of the properties of Nb_3Sn and their variation with A15 composition, morphology and strain state", Supercond. Sci. Technol. **19**, R68–R80 (2006) (Cited on page 97).

[212] S. Posen and D. L. Hall, "Nb_3Sn superconducting radiofrequency cavities: fabrication, results, properties, and prospects", Supercond. Sci. Technol. **30**, 033004 (2017) (Cited on pages 97, 103, 111).

[213] J. F. Ziegler and J. M. Manoyan, "The stopping of ions in compounds", Nucl. Instrum. Methods Phys. Res., Sect. B **35**, 215–228 (1988) (Cited on page 98).

[214] E. B. Karlsson, "The positive muon implanted in metals — a story full of surprises", Eur. Phys. J. H **39**, 303–323 (2014) (Cited on page 101).

[215] T. Junginger, S. Calatroni, A. Sublet, G. Terenziani, T. Prokscha, Z. Salman, A. Suter, T. Proslier, and J. Zasadzinski, "A low energy muon spin rotation and point contact tunneling study of niobium films prepared for superconducting cavities", Supercond. Sci. Technol. **30**, 125013 (2017) (Cited on page 101).

[216] E. H. Brandt, "Superconductors in realistic geometries: geometric edge barrier versus pinning", Physica C **332**, 99–107 (2000) (Cited on pages 102, 115).

[217] G. Ciovati, H. Tian, and S. G. Corcoran, "Buffered electrochemical polishing of niobium", J. Appl. Electrochem. **41**, 721–730 (2011) (Cited on pages 102, 126, 148).

[218] C. Antoine, *Materials and surface aspects in the development of SRF Niobium cavities*, Vol. 12, EuCARD editorial series on accelerator science (2012) (Cited on pages 103, 192).

[219] G. Ciovati, "Improved oxygen diffusion model to explain the effect of low-temperature baking on high field losses in niobium superconducting cavities", Appl. Phys. Lett. **89**, 022507 (2006) (Cited on pages 103, 113, 114, 192).

[220] E. M. Lechner, J. W. Angle, A. D. Palczewski, F. A. Stevie, M. J. Kelley, and C. E. Reece, "Oxide dissolution and oxygen diffusion scenarios in niobium and implications on the Bean-Livingston barrier in superconducting cavities", J. Appl. Phys. **135**, 133902 (2024) (Cited on pages 103, 192).

[221] E. M. Lechner, J. W. Angle, F. A. Stevie, M. J. Kelley, C. E. Reece, and A. D. Palczewski, "RF surface resistance tuning of superconducting niobium via thermal diffusion of native oxide", Appl. Phys. Lett. **119**, 082601 (2021) (Cited on pages 103, 113, 115, 116, 192).

[222] E. Saur and J. Wurm, "Präparation und Supraleitungseigenschaften von Niobdrahtproben mit Nb_3Sn-Überzug", Naturwiss. **49**, 127–128 (1962) (Cited on page 103).

[223] G. Arnolds and D. Proch, "Measurement on a Nb_3Sn structure for linear accelerator application", IEEE Trans. Magn. **13**, 500–503 (1977) (Cited on page 103).

[224] G. Eremeev, M. Kelley, U. Kelley M.J.Pudasaini, C. Reece, and J. Tuggle, "Progress With Multi-Cell Nb_3Sn Cavity Development Linked With Sample Materials Characterization", in Proc. of International Conference on RF Superconductivity (SRF2015), Whistler, BC, Canada, Sept. 13-18, 2015, 17 (JACoW, Dec. 2015), pp. 505–511 (Cited on page 103).

[225] Y. Trenikhina, S. Posen, A. Romanenko, M. Sardela, J.-M. Zuo, D. L. Hall, and M. Liepe, "Performance-defining properties of Nb_3Sn coating in SRF cavities", Supercond. Sci. Technol. **31**, 015004 (2017) (Cited on page 111).

[226] A. S. Dhavale, P. Dhakal, A. A. Polyanskii, and G. Ciovati, "Flux pinning characteristics in cylindrical niobium samples used for superconducting radio frequency cavity fabrication", Supercond. Sci. Technol. **25**, 065014 (2012) (Cited on pages 112, 115).

[227] Q. Ma, P. Ryan, J. W. Freeland, and R. A. Rosenberg, "Thermal effect on the oxides on Nb(100) studied by synchrotron-radiation x-ray photoelectron spectroscopy", J. Appl. Phys. **96**, 7675–7680 (2004) (Cited on page 113).

[228] G. D. L. Semione, A. D. Pandey, S. Tober, J. Pfrommer, A. Poulain, J. Drnec, G. Schütz, T. F. Keller, H. Noei, V. Vonk, B. Foster, and A. Stierle, "Niobium near-surface composition during nitrogen infusion relevant for superconducting radio-frequency cavities", Phys. Rev. Accel. Beams **22**, 103102 (2019) (Cited on page 113).

[229] A. Zaidman, V. Vonk, G. K. Deyu, R. Zierold, R. Blick, W. Hillert, M. Wenskat, and A. Stierle, "Influence of an Al_2O_3 capping layer on the thermal reduction of the native niobium oxide: An in situ x-ray reflectivity study", Phys. Rev. Mater. **9**, 094806 (2025) (Cited on page 113).

[230] A. Romanenko, A. Grassellino, F. Barkov, and J. P. Ozelis, "Effect of mild baking on superconducting niobium cavities investigated by sequential nanoremoval", Phys. Rev. ST Accel. Beams **16**, 012001 (2013) (Cited on pages 113–115).

[231] S. Casalbuoni, E. A. Knabbe, J. Kötzler, L. Lilje, L. von Sawilski, P. Schmüser, and B. Steffen, "Surface superconductivity in niobium for superconducting RF cavities", Nucl. Instrum. Methods Phys. Res., Sect. A **538**, 45–64 (2005) (Cited on pages 113, 114).

[232] A. Romanenko, D. Bafia, A. Grassellino, M. Martinello, and Y. Trenikhina, "First Direct Imaging and Profiling TOF-SIMS Studies on Cutouts from Cavities Prepared by State-of-the-Art Treatments", in Proc. SRF'19, International Conference on RF Superconductivity 19 (Aug. 2019), pp. 866–870 (Cited on page 113).

[233] M. Delheusy, A. Stierle, N. Kasper, R. P. Kurta, A. Vlad, H. Dosch, C. Antoine, A. Resta, E. Lundgren, and J. Andersen, "X-ray investigation of subsurface interstitial oxygen at Nb/oxide interfaces", Appl. Phys. Lett. **92**, 101911 (2008) (Cited on page 113).

[234] D. C. Ford, L. D. Cooley, and D. N. Seidman, "Suppression of hydride precipitates in niobium superconducting radio-frequency cavities", Supercond. Sci. Technol. **26**, 105003 (2013) (Cited on page 113).

[235] A. Romanenko, C. J. Edwardson, P. G. Coleman, and P. J. Simpson, "The effect of vacancies on the microwave surface resistance of niobium revealed by positron annihilation spectroscopy", Appl. Phys. Lett. **102**, 232601 (2013) (Cited on page 113).

[236] Y. Trenikhina, A. Romanenko, J. Kwon, J.-M. Zuo, and J. F. Zasadzinski, "Nanostructural features degrading the performance of superconducting radio frequency niobium cavities revealed by transmission electron microscopy and electron energy loss spectroscopy", J. Appl. Phys. **117**, 154507 (2015) (Cited on page 113).

[237] G. Ciovati, G. Myneni, F. Stevie, P. Maheshwari, and D. Griffis, "High field Q slope and the baking effect: Review of recent experimental results and new data on Nb heat treatments", Phys. Rev. ST Accel. Beams **13**, 022002 (2010) (Cited on page 115).

[238] M. Wenskat, J. Čižek, M. O. Liedke, M. Butterling, C. Bate, P. Haušild, E. Hirschmann, A. Wagner, and H. Weise, "Vacancy-Hydrogen Interaction in Niobium during Low-Temperature Baking", Sci. Rep. **10**, 8300 (2020) (Cited on page 115).

[239] E. H. Brandt, "Computer simulation of vortex pinning in type II superconductors. I. Two-dimensional simulation", J. Low Temp. Phys. **53**, 41–70 (1983) (Cited on page 115).

[240] A. S. Dhavale, G. Ciovati, and G. R. Myneni, "Effect of Electropolishing and Low-Temperature Baking on the Superconducting Properties of Large-Grain Niobium", AIP Conf. Proc. **1352**, 119–130 (2011) (Cited on page 115).

[241] S. Posen, A. Romanenko, A. Grassellino, O. Melnychuk, and D. Sergatskov, "Ultralow Surface Resistance via Vacuum Heat Treatment of Superconducting Radio-Frequency Cavities", Phys. Rev. Appl. **13**, 014024 (2020) (Cited on page 116).

[242] H. Ito, H. Araki, K. Takahashi, and K. Umemori, "Influence of furnace baking on Q-E behavior of superconducting accelerating cavities", Prog. Theor. Exp. Phys. **2021**, 071G01 (2021) (Cited on page 116).

[243] W. Wuensch, C. Achard, S. Dobert, H. Braun, I. Syratchev, M. Taborelli, and I. Wilson, "Demonstration of high-gradient acceleration", in Proceedings of the 2003 Particle Accelerator Conference, Vol. 1 (2003), 495–497 Vol.1 (Cited on page 117).

[244] E. I. Simakov, V. A. Dolgashev, and S. G. Tantawi, "Advances in high gradient normal conducting accelerator structures", Nucl. Instrum. Methods Phys. Res., Sect. A **907**, 221–230 (2018) (Cited on page 117).

[245] K. Watanabe, S. Noguchi, E. Kako, K. Umemori, and T. Shishido, "Development of the superconducting rf 2-cell cavity for cERL injector at KEK", Nucl. Instrum. Methods Phys. Res., Sect. A **714**, 67–82 (2013) (Cited on page 117).

[246] M. Dressel, "Electrodynamics of Metallic Superconductors", Adv. Condens. Matter Phys. **2013**, 1–25 (2013) (Cited on page 119).

[247] R. F. Kiefl, M. D. Hossain, B. M. Wojek, S. R. Dunsiger, G. D. Morris, T. Prokscha, Z. Salman, J. Baglo, D. A. Bonn, R. Liang, W. N. Hardy, A. Suter, and E. Morenzoni, "Direct measurement of the london penetration depth in $YBa_2Cu_3O_{6.92}$ using low-energy μSR", Phys. Rev. B **81**, 180502 (2010) (Cited on page 121).

[248] T. Riseman, T. Jackson, M. Long, E. Forgan, E. Morenzoni, H. Glückler, T. Prokscha, H.-P. Weber, C. Niedermayer, A. Hofer, M. Pleines, G. Schatz, J. Litterst, H. Luetkens, and A. Schatz, "Measurements of the penetration depth of an $YBa_2Cu_3O_{7-\delta}$ thin film with low-energy muons", Physica B **289-290**, 334–337 (2000) (Cited on page 121).

[249] T. J. Jackson, T. M. Riseman, E. M. Forgan, H. Glückler, T. Prokscha, E. Morenzoni, M. Pleines, C. Niedermayer, G. Schatz, H. Luetkens, and J. Litterst, "Depth-Resolved Profile of the Magnetic Field beneath the Surface of a Superconductor with a Few nm Resolution", Phys. Rev. Lett. **84**, 4958–4961 (2000) (Cited on page 121).

[250] A. Suter, E. Morenzoni, N. Garifianov, R. Khasanov, E. Kirk, H. Luetkens, T. Prokscha, and M. Horisberger, "Observation of nonexponential magnetic penetration profiles in the meissner state: a manifestation of nonlocal effects in superconductors", Phys. Rev. B **72**, 024506 (2005) (Cited on pages 121, 136, 139).

[251] M. C. Burton, M. R. Beebe, K. Yang, R. A. Lukaszew, A.-M. Valente-Feliciano, and C. Reece, "Superconducting NbTiN thin films for superconducting radio frequency accelerator cavity applications", J. Vac. Sci. Technol. A **34**, 021518 (2016) (Cited on pages 126, 127, 144, 145, 163).

[252] R. Di Leo, A. Nigro, G. Nobile, and R. Vaglio, "Niboium-titanium nitride thin films for superconducting rf accelerator cavities", J. Low Temp. Phys. **78**, 41–50 (1990) (Cited on pages 126, 144, 145, 153, 162, 163).

[253] L. Yu, N. Newman, and J. M. Rowell, "Measurement of the coherence length of sputtered $Nb_{0.62}Ti_{0.38}N$ thin films", IEEE Trans. Appl. Supercond. **12**, 1795–1798 (2002) (Cited on pages 126, 139, 145, 153, 163).

[254] L. Zhang, W. Peng, L. X. You, and Z. Wang, "Superconducting properties and chemical composition of NbTiN thin films with different thickness", Appl. Phys. Lett. **107**, 122603 (2015) (Cited on pages 126, 143, 145).

[255] D. Hazra, N. Tsavdaris, A. Mukhtarova, M. Jacquemin, F. Blanchet, R. Albert, S. Jebari, A. Grimm, A. Konar, E. Blanquet, F. Mercier, C. Chapelier, and M. Hofheinz, "Superconducting properties of NbTiN thin films deposited by high-temperature chemical vapor deposition", Phys. Rev. B **97**, 144518 (2018) (Cited on pages 126, 143, 145, 153).

[256] L. Yu, R. K. Singh, H. Liu, S. Y. Wu, R. Hu, D. Durand, J. Bulman, J. M. Rowell, and N. Newman, "Fabrication of niobium titanium nitride thin films with high superconducting transition temperatures and short penetration lengths", IEEE Trans. Appl. Supercond. **15**, 44–48 (2005) (Cited on pages 126, 145, 153, 162).

[257] T. M. Riseman, "μSR measurement of the magnetic penetration depth and coherence length in the high-T_c superconductor $YBa_2Cu_3O_{6.95}$", PhD thesis (University of British Columbia, Canada, May 1993) (Cited on page 127).

[258] A. Suter, *The Skewed Gaussian*, Memorandum (Paul Scherrer Institut, Villigen, Dec. 2008) (Cited on page 129).

[259] D.-X. Chen, E. Pardo, and A. Sanchez, "Fluxmetric and magnetometric demagnetizing factors for cylinders", J. Magn. Magn. Mater. **306**, 135–146 (2006) (Cited on page 132).

[260] P. Dhakal, "Nitrogen doping and infusion in SRF cavities: A review", Phys. Open **5**, 100034 (2020) (Cited on page 136).

[261] D. Gonnella, J. Kaufman, and M. Liepe, "Impact of nitrogen doping of niobium superconducting cavities on the sensitivity of surface resistance to trapped magnetic flux", J. Appl. Phys. **119**, 073904 (2016) (Cited on page 136).

[262] A. B. Pippard and W. L. Bragg, "An experimental and theoretical study of the relation between magnetic field and current in a superconductor", Proc. R. Soc. London, Ser. A **216**, 547–568 (1953) (Cited on page 136).

[263] R. Prozorov, M. Zarea, and J. A. Sauls, "Niobium in the clean limit: An intrinsic type-I superconductor", Phys. Rev. B **106**, L180505 (2022) (Cited on page 137).

[264] L. Zhang, L. You, L. Ying, W. Peng, and Z. Wang, "Characterization of surface oxidation layers on ultrathin NbTiN films", Phys. C: Supercond. Appl. **545**, 1–4 (2018) (Cited on page 137).

[265] J. R. Gavaler, D. W. Deis, J. K. Hulm, and C. K. Jones, "Superconducting Properties of Niobium-Titanium-Nitride Thin Films", Appl. Phys. Lett. **15**, 329–331 (1969) (Cited on pages 143–145, 153, 163).

[266] C. Benvenuti, P. Chiggiato, L. Parrini, and R. Russo, "Production of niobium-titanium nitride coatings by reactive diffusion for superconducting cavity applications", Nucl. Instrum. Methods Phys. Res., Sect. B **124**, 106–111 (1997) (Cited on pages 143, 144, 163).

[267] P. Pratap, L. Nanda, K. Senapati, R. P. Aloysius, and V. Achanta, "Optimization of the superconducting properties of NbTiN thin films by variation of the N_2 partial pressure during sputter deposition", Supercond. Sci. Technol. **36**, 085017 (2023) (Cited on pages 143, 145, 153, 163, 164).

[268] G. M. Matenoglou, L. E. Koutsokeras, C. E. Lekka, G. Abadias, C. Kosmidis, G. A. Evangelakis, and P. Patsalas, "Structure, stability and bonding of ternary transition metal nitrides", Surf. Coat. Technol. **204**, 911–914 (2009) (Cited on page 143).

[269] K. Vasu, M. G. Krishna, and K. A. Padmanabhan, "Effect of Nb concentration on the structure, mechanical, optical, and electrical properties of nano-crystalline $Ti_{1-x}Nb_xN$ thin films", J. Mater. Sci. **47**, 3522–3528 (2012) (Cited on page 143).

[270] L. Toth, *Transition Metal Carbides and Nitrides* (Academic Press, 2012) (Cited on pages 143, 181).

[271] S. Kikkawa, T. Yamamoto, K. Ohta, M. Takahashi, and F. Kanamaru, "Transition metal-based double nitrides", in *The chemistry of transition metal carbides and nitrides*, edited by S. T. Oyama (Springer, Dordrecht, 1996) Chap. 9, pp. 175–190 (Cited on page 143).

[272] J. Zbasnik, L. E. Toth, Y. M. Shy, and E. Maxwell, "Superconducting Critical Fields and Currents of Nb–Ti–N Thin Films in Continuous Magnetic Fields to 175 kG", J. Appl. Phys. **40**, 2147–2152 (1969) (Cited on pages 143, 145).

[273] K. Makise, H. Terai, M. Takeda, Y. Uzawa, and Z. Wang, "Characterization of NbTiN Thin Films Deposited on Various Substrates", IEEE Trans. Appl. Supercond. **21**, 139–142 (2011) (Cited on pages 143, 145).

[274] M. Cyberey, T. Farrahi, J. Lu, A. Kerr, R. M. Weikle, and A. W. Lichtenberger, "NbTiN /AlN/NbTiN SIS Junctions Realized by Reactive Bias Target Ion Beam Deposition", IEEE Trans. Appl. Supercond. **29**, 1–6 (2019) (Cited on pages 143, 145, 167).

[275] M. Cyberey, S. Hinton, C. Moore, R. M. Weikle, and A. W. Lichtenberger, "SuperGaN: Synthesis of NbTiN/GaN/NbTiN Tunnel Junctions", IEEE Trans. Appl. Supercond. **34**, 1–4 (2024) (Cited on pages 143, 145, 167).

[276] E. S. Zhukova, B. P. Gorshunov, L. S. Kadyrov, K. V. Zhivetev, A. V. Terentiev, A. M. Chekushkin, F. V. Khan, A. V. Khudchenko, N. V. Kinev, and V. P. Koshelets, "Impact of the Buffer Layers and Anodization on Properties of NbTiN Films for THz Receivers", IEEE Trans. Appl. Supercond. **34**, 1–5 (2024) (Cited on pages 143, 145, 167).

[277] Y. Uzawa, Y. Fujii, A. Gonzalez, K. Kaneko, M. Kroug, T. Kojima, A. Miyachi, K. Makise, S. Saito, H. Terai, and Z. Wang, "Tuning Circuit Material for Mass-Produced Terahertz SIS Receivers", IEEE Trans. Appl. Supercond. **25**, 1–5 (2015) (Cited on pages 143, 145, 167).

[278] M. P. Westig, S. Selig, K. Jacobs, T. M. Klapwijk, and C. E. Honingh, "Improved Nb SIS devices for heterodyne mixers between 700 GHz and 1.3 THz with NbTiN transmission lines using a normal metal energy relaxation layer", J. Appl. Phys. **114**, 124504 (2013) (Cited on pages 143, 145, 167).

[279] F. V. Khan, E. S. Zhukova, B. P. Gorshunov, L. S. Kadyrov, A. M. Chekushkin, A. V. Khudchenko, and V. P. Koshelets, "Characterization of Microwave Properties of Superconducting NbTiN Films Using TDS", IEEE Trans. Terahertz Sci. Technol. **13**, 627–632 (2023) (Cited on pages 143, 145, 153, 162, 167).

[280] K. Momma and F. Izumi, "*VESTA3* for three-dimensional visualization of crystal, volumetric and morphology data", J. Appl. Cryst. **44**, 1272–1276 (2011) (Cited on page 144).

[281] W. M. Roach, D. B. Beringer, Z. Li, C. Clavero, and R. A. Lukaszew, "Magnetic Shielding Larger Than the Lower Critical Field of Niobium in Multilayers", IEEE Trans. Appl. Supercond. **23**, 8600203–8600203 (2013) (Cited on page 144).

[282] G. D. Cody and R. E. Miller, "Magnetic Transitions of Superconducting Thin Films and Foils. I. Lead", Phys. Rev. **173**, 481–493 (1968) (Cited on page 144).

[283] H. Bell, Y. M. Shy, D. E. Anderson, and L. E. Toth, "Superconducting Properties of Reactively Sputtered Thin-Film Ternary Nitrides, Nb–Ti–N and Nb–Zr–N", J. Appl. Phys. **39**, 2797–2803 (1968) (Cited on page 144).

[284] C. M. Yen, L. E. Toth, Y. M. Shy, D. E. Anderson, and L. G. Rosner, "Superconducting H_c–J_c and T_c Measurements in the Nb–Ti–N, Nb–Hf–N, and Nb–V–N Ternary Systems", J. Appl. Phys. **38**, 2268–2271 (1967) (Cited on page 145).

[285] V. Pan, V. Gorishnyak, E. Rudenko, V. Shaternik, M. Belous, S. Koziychuk, and F. Korzhinsky, "Investigation of the properties of superconducting niobium nitride films", Cryogenics **23**, 258–262 (1983) (Cited on page 145).

[286] S. Isagawa, "rf superconducting properties of reactively sputtered NbN", J. Appl. Phys. **52**, 921–927 (1981) (Cited on page 145).

[287] A. Torgovkin, S. Chaudhuri, A. Ruhtinas, M. Lahtinen, T. Sajavaara, and I. J. Maasilta, "High quality superconducting titanium nitride thin film growth using infrared pulsed laser deposition", Supercond. Sci. Technol. **31**, 055017 (2018) (Cited on page 145).

[288] M. R. Vissers, J. Gao, J. S. Kline, M. Sandberg, M. P. Weides, D. S. Wisbey, and D. P. Pappas, "Characterization and in-situ monitoring of sub-stoichiometric adjustable superconducting critical temperature titanium nitride growth", Thin Solid Films **548**, 485–488 (2013) (Cited on page 145).

[289] F. Khan, A. V. Khudchenko, A. M. Chekushkin, and V. P. Koshelets, "Characterization of the Parameters of Superconducting NbN and NbTiN Films Using Parallel Plate Resonator", IEEE Trans. Appl. Supercond. **32**, 1–5 (2022) (Cited on pages 145, 153, 162, 167).

[290] T. Hong, K. Choi, K. Ik Sim, T. Ha, B. Cheol Park, H. Yamamori, and J. Hoon Kim, "Terahertz electrodynamics and superconducting energy gap of NbTiN", J. Appl. Phys. **114**, 243905 (2013) (Cited on pages 145, 153, 162, 167).

[291] M. Sidorova, A. D. Semenov, H.-W. Hübers, S. Gyger, S. Steinhauer, X. Zhang, and A. Schilling, "Magnetoconductance and photoresponse properties of disordered NbTiN films", Phys. Rev. B **104**, 184514 (2021) (Cited on pages 145, 153, 163).

[292] I. González Díaz-Palacio, M. Wenskat, G. K. Deyu, W. Hillert, R. H. Blick, and R. Zierold, "Thermal annealing of superconducting niobium titanium nitride thin films deposited by plasma-enhanced atomic layer deposition", J. Appl. Phys. **134**, 035301 (2023) (Cited on pages 145, 164).

[293] A.-M. Valente-Feliciano, M. Burton, G. Eremeev, R. Lukaszew, C. Reece, and J. Spradlin, "Growth and Characterization of Multi-Layer NbTiN Films", in Proc. of International Conference on RF Superconductivity (SRF2015), Whistler, BC, Canada, Sept. 13-18, 2015, International Conference on RF Superconductivity 17 (Dec. 2015), pp. 516–520 (Cited on page 145).

[294] K. Hechler, G. Horn, G. Otto, and E. Saur, "Measurements of critical data for some type II superconductors and comparison with theory", J. Low Temp. Phys. **1**, 29–43 (1969) (Cited on pages 145, 163).

[295] S. R. Nieto, J. Hofer, M. Sirena, and N. Haberkorn, "Flexible NbTiN thin films for superconducting electronics", Physica C **607**, 1354241 (2023) (Cited on pages 145, 153, 163).

[296] N. R. Groll, J. A. Klug, C. Cao, S. Altin, H. Claus, N. G. Becker, J. F. Zasadzinski, M. J. Pellin, and T. Proslier, "Tunneling spectroscopy of superconducting MoN and NbTiN grown by atomic layer deposition", Appl. Phys. Lett. **104**, 092602 (2014) (Cited on pages 145, 167).

[297] B. N. R. Lap, A. Khudchenko, R. Hesper, K. I. Rudakov, P. Dmitriev, F. Khan, V. P. Koshelets, and A. M. Baryshev, "Characterization of superconducting NbTiN films using a dispersive Fourier transform spectrometer", Appl. Phys. Lett. **119**, 152601 (2021) (Cited on pages 145, 167).

[298] R. Barends, N. Vercruyssen, A. Endo, P. J. de Visser, T. Zijlstra, T. M. Klapwijk, and J. J. A. Baselmans, "Reduced frequency noise in superconducting resonators", Appl. Phys. Lett. **97**, 033507 (2010) (Cited on pages 145, 161, 162, 167).

[299] E. F. C. Driessen, P. C. J. J. Coumou, R. R. Tromp, P. J. de Visser, and T. M. Klapwijk, "Strongly Disordered TiN and NbTiN *s*-Wave Superconductors Probed by Microwave Electrodynamics", Phys. Rev. Lett. **109**, 107003 (2012) (Cited on pages 145, 167).

[300] T. Proslier, J. Klug, N. C. Becker, J. W. Elam, and M. Pellin, "(Invited) Atomic Layer Deposition of Superconductors", ECS Trans. **41**, 237 (2011) (Cited on pages 145, 149).

[301] Y. Kalboussi, C. Antoine, S. Bira, B. Delatte, D. Dragoe, J. Leroy, D. Longuevergne, T. Proslier, and S. Tusseau-Nenez, "Material Engineering of ALD- Deposited Multilayer to Improve the Superconducting Performances of RF Cavities Under Intense Fields", in, International Conference on RF Superconductivity, presented at SRF'21 in East Lansing, MI, USA, unpublished (Oct. 2022) (Cited on pages 145, 149).

[302] D. E. MacLaughlin, "Magnetic Resonance in the Superconducting State", in , Vol. 31, edited by H. Ehrenreich, F. Seitz, and D. Turnbull, Solid State Physics (Academic Press, 1976), pp. 1–69 (Cited on pages 145, 159).

[303] R. E. Walstedt, "Introduction to NMR studies of metals, metallic compounds, and superconductors", in *The NMR probe of high-T_c materials*, Vol. 228, Springer Tracts in Modern Physics (Springer, Berlin, 2008) Chap. 2, pp. 13–65 (Cited on page 145).

[304] W. A. MacFarlane, "Status and progress of ion-implanted βNMR at TRIUMF", Z. Phys. Chem. **236**, 757–798 (2022) (Cited on pages 145, 146, 148, 155).

[305] J. Korringa, "Nuclear magnetic relaxation and resonnance line shift in metals", Physica **16**, 601–610 (1950) (Cited on pages 146, 158, 159, 164).

[306] L. C. Hebel and C. P. Slichter, "Nuclear Relaxation in Superconducting Aluminum", Phys. Rev. **107**, 901–902 (1957) (Cited on pages 146, 158, 159, 165).

[307] L. C. Hebel and C. P. Slichter, "Nuclear Spin Relaxation in Normal and Superconducting Aluminum", Phys. Rev. **113**, 1504–1519 (1959) (Cited on pages 146, 158, 159, 165).

[308] C. D. P. Levy, M. R. PPearson, R. F. Kiefl, E. Mané, G. D. Morris, and A. Voss, "Laser polarization facility", Hyperfine Interact. **225**, 165–172 (2013) (Cited on page 146).

[309] T. Minamisono, T. Ohtsubo, S. Fukuda, I. Minami, Y. Nakayama, M. Fukuda, K. Matsuta, and Y. Nojiri, "New nuclear quadrupole resonance technique in β-NMR", Hyperfine Interact. **80**, 1315–1319 (1993) (Cited on pages 148, 150).

[310] J. R. Adelman, D. Fujimoto, M. H. Dehn, S. R. Dunsiger, V. L. Karner, C. D. P. Levy, R. Li, I. McKenzie, R. M. L. McFadden, G. D. Morris, M. R. Pearson, M. Stachura, E. Thoeng, J. O. Ticknor, N. Ohashi, K. M. Kojima, and W. A. MacFarlane, "Nuclear magnetic resonance of ^{8}Li ions implanted in ZnO", Phys. Rev. B **106**, 035205 (2022) (Cited on pages 148, 150).

[311] V. Miikkulainen, M. Leskelä, M. Ritala, and R. L. Puurunen, "Crystallinity of inorganic films grown by atomic layer deposition: Overview and general trends", J. Appl. Phys. **113**, 021301 (2013) (Cited on pages 149, 171).

[312] V. Rontu, P. Sippola, M. Broas, G. Ross, T. Sajavaara, H. Lipsanen, M. Paulasto-Kröckel, and S. Franssila, "Atomic layer deposition of AlN from $AlCl_3$ using NH_3 and Ar/NH_3 plasma", J. Vac. Sci. Technol. A **36**, 021508 (2018) (Cited on page 149).

[313] N. Groll, M. J. Pellin, J. F. Zasadzinksi, and T. Proslier, "Point contact tunneling spectroscopy apparatus for large scale mapping of surface superconducting properties", Rev. Sci. Instrum. **86**, 095111 (2015) (Cited on pages 149, 173).

[314] Y. Kalboussi, I. Curci, F. Miserque, D. Troadec, N. Brun, M. Walls, G. Jullien, F. Eozenou, M. Baudrier, L. Maurice, Q. Bertrand, P. Sahuquet, and T. Proslier, "Crystallinity in niobium oxides: A pathway to mitigate two-level-system defects in niobium three-dimensional resonators for quantum applications", Phys. Rev. Appl. **23**, 044023 (2025) (Cited on pages 149, 173).

[315] W. A. MacFarlane, T. J. Parolin, D. L. Cortie, K. H. Chow, M. D. Hossain, R. F. Kiefl, C. D. P. Levy, R. M. L. McFadden, G. D. Morris, M. R. Pearson, H. Saadaoui, Z. Salman, Q. Song, and D. Wang, "^{8}Li^{+} β-NMR in the Cubic Insulator MgO", J. Phys. Conf. Ser. **551**, 012033 (2014) (Cited on pages 150, 154).

[316] J. Pearl, "Current distribution in superconducting films carrying quantized fluxoids", Appl. Phys. Lett. **5**, 65–66 (1964) (Cited on page 153).

[317] Y. Lee, J. Yun, C. Lee, M. Sirena, J. Kim, and N. Haberkorn, "Penetration depth and critical fields in superconducting NbTi thin films grown by co-sputtering at room temperature", Phys. Scr. **99**, 065963 (2024) (Cited on page 153).

[318] N. R. Werthamer, E. Helfand, and P. C. Hohenberg, "Temperature and Purity Dependence of the Superconducting Critical Field, H_{c2}. III. Electron Spin and Spin-Orbit Effects", Phys. Rev. **147**, 295–302 (1966) (Cited on pages 153, 177).

[319] R. M. L. McFadden, D. Szunyogh, N. Bravo-Frank, A. Chatzichristos, M. H. Dehn, D. Fujimoto, A. Jancsó, S. Johannsen, I. Kálomista, V. L. Karner, R. F. Kiefl, F. H. Larsen, J. Lassen, C. D. P. Levy, R. Li, I. McKenzie, H. McPhee, G. D. Morris, M. R. Pearson, S. P. A. Sauer, R. K. O. Sigel, P. W. Thulstrup, W. A. MacFarlane, L. Hemmingsen, and M. Stachura, "Magnesium(II)-ATP Complexes in 1-Ethyl-3-Methylimidazolium Acetate Solutions Characterized by ^{31}Mg β-Radiation-Detected NMR Spectroscopy", Angew. Chem. Int. Ed. **61**, e202207137 (2022) (Cited on pages 154, 180).

[320] T. J. Parolin, Z. Salman, K. H. Chow, Q. Song, J. Valiani, H. Saadaoui, A. O'Halloran, M. D. Hossain, T. A. Keeler, R. F. Kiefl, S. R. Kreitzman, C. D. P. Levy, R. I. Miller, G. D. Morris, M. R. Pearson, M. Smadella, D. Wang, M. Xu, and W. A. MacFarlane, "Erratum: High resolution β-NMR study of ^{8}Li^{+} implanted in gold [Phys. Rev. B 77, 214107 (2008)]", Phys. Rev. B **100**, 209904 (2019) (Cited on pages 155, 163–165).

[321] T. J. Parolin, J. Shi, Z. Salman, K. H. Chow, P. Dosanjh, H. Saadaoui, Q. Song, M. D. Hossain, R. F. Kiefl, C. D. P. Levy, M. R. Pearson, and W. A. MacFarlane, "Nuclear magnetic resonance study of Li implanted in a thin film of niobium", Phys. Rev. B **80**, 174109 (2009) (Cited on pages 155, 164, 185).

[322] D. Wang, M. Hossain, Z. Salman, D. Arseneau, K. Chow, S. Daviel, T. Keeler, R. Kiefl, S. Kreitzman, C. Levy, G. Morris, R. Miller, W. MacFarlane, T. Parolin, and H. Saadaoui, "β-detected NMR of ^{8}Li in the normal state of 2H-$NbSe_2$", Physica B **374-375**, 239–242 (2006) (Cited on pages 155, 164).

[323] R. M. L. McFadden, A. Chatzichristos, K. H. Chow, D. L. Cortie, M. H. Dehn, D. Fujimoto, M. D. Hossain, H. Ji, V. L. Karner, R. F. Kiefl, C. D. P. Levy, R. Li, I. McKenzie, G. D. Morris, O. Ofer, M. R. Pearson, M. Stachura, R. J. Cava, and W. A. MacFarlane, "Ionic and electronic properties of the topological insulator Bi_2Te_2Se investigated via β-detected nuclear magnetic relaxation and resonance of ^{8}Li", Phys. Rev. B **99**, 125201 (2019) (Cited on pages 155, 156, 164).

[324] R. M. L. McFadden, A. Chatzichristos, D. L. Cortie, D. Fujimoto, Y. S. Hor, H. Ji, V. L. Karner, R. F. Kiefl, C. D. P. Levy, R. Li, I. McKenzie, G. D. Morris, M. R. Pearson, M. Stachura, R. J. Cava, and W. A. MacFarlane, "Local electronic and magnetic properties of the

doped topological insulators Bi_2Se_3 : Ca and Bi_2Te_3 : Mn investigated using ion-implanted ^{8}Li β−NMR", Phys. Rev. B **102**, 235206 (2020) (Cited on pages 155, 156, 164).

[325] H.-J. Stöckmann and P. Heitjans, "Low-temperature nuclear spin-lattice relaxation in glasses — homogeneous and inhomogeneous averaging", J. Non-Cryst. Solids **66**, 501–509 (1984) (Cited on page 155).

[326] A. Lascialfari, A. Rigamonti, E. Bernardi, M. Corti, A. Gauzzi, and J. C. Villegier, "Superconducting properties of a textured NbN film from ^{93}Nb NMR relaxation and magnetization measurements", Phys. Rev. B **80**, 104505 (2009) (Cited on pages 156, 165).

[327] J. Sugiyama, I. Umegaki, T. Uyama, R. M. L. McFadden, S. Shiraki, T. Hitosugi, Z. Salman, H. Saadaoui, G. D. Morris, W. A. MacFarlane, and R. F. Kiefl, "Lithium diffusion in spinel $Li_4Ti_5O_{12}$ and $LiTi_2O_4$ films detected with ^{8}Li β-NMR", Phys. Rev. B **96**, 094402 (2017) (Cited on page 157).

[328] D. L. Cortie, T. Buck, M. H. Dehn, V. L. Karner, R. F. Kiefl, C. D. P. Levy, R. M. L. McFadden, G. D. Morris, I. McKenzie, M. R. Pearson, X. L. Wang, and W. A. MacFarlane, "β-NMR Investigation of the Depth-Dependent Magnetic Properties of an Antiferromagnetic Surface", Phys. Rev. Lett. **116**, 106103 (2016) (Cited on page 157).

[329] N. Bloembergen, E. M. Purcell, and R. V. Pound, "Relaxation Effects in Nuclear Magnetic Resonance Absorption", Phys. Rev. **73**, 679–712 (1948) (Cited on pages 158, 160).

[330] R. F. Kiefl, W. A. MacFarlane, K. H. Chow, S. Dunsiger, T. L. Duty, T. M. S. Johnston, J. W. Schneider, J. Sonier, L. Brard, R. M. Strongin, J. E. Fischer, and A. B. Smith, "Coherence peak and superconducting energy gap in Rb_3C_{60} observed by muon spin relaxation", Phys. Rev. Lett. **70**, 3987–3990 (1993) (Cited on page 159).

[331] H. Kotegawa, K. Ishida, Y. Kitaoka, T. Muranaka, and J. Akimitsu, "Evidence for Strong-Coupling *s*-Wave Superconductivity in MgB_2: ^{11}B NMR Study", Phys. Rev. Lett. **87**, 127001 (2001) (Cited on page 159).

[332] N. J. Curro, T. Caldwell, E. D. Bauer, L. A. Morales, M. J. Graf, Y. Bang, A. V. Balatsky, J. D. Thompson, and J. L. Sarrao, "Unconventional superconductivity in $PuCoGa_5$", Nature **434**, 622–625 (2005) (Cited on page 159).

[333] P. A. Beckmann, "Spectral densities and nuclear spin relaxation in solids", Phys. Rep. **171**, 85–128 (1988) (Cited on page 160).

[334] R. Barends, H. L. Hortensius, T. Zijlstra, J. J. A. Baselmans, S. J. C. Yates, J. R. Gao, and T. M. Klapwijk, "Noise in NbTiN, Al, and Ta Superconducting Resonators on Silicon and Sapphire Substrates", IEEE Trans. Appl. Supercond. **19**, 936–939 (2009) (Cited on pages 161, 162, 167).

[335] R. Barends, H. L. Hortensius, T. Zijlstra, J. J. A. Baselmans, S. J. C. Yates, J. R. Gao, and T. M. Klapwijk, "Contribution of dielectrics to frequency and noise of NbTiN superconducting resonators", Appl. Phys. Lett. **92**, 223502 (2008) (Cited on pages 161, 162, 167).

[336] T. Junginger, "Investigations of the surface resistance of superconducting materials", PhD thesis (University of Heidelberg, 2012) (Cited on page 162).

[337] W. Götze and W. Ketterle, "Nuclear spin relaxation in disordered conductors", Z. Phys. B: Condens. Matter **54**, 49–57 (1983) (Cited on pages 164, 165).

[338] B. S. Shastry and E. Abrahams, "What does the Korringa ratio measure?", Phys. Rev. Lett. **72**, 1933–1936 (1994) (Cited on pages 164, 165).

[339] H. Nishihara, Y. Furutani, S. Yokota, M. Ohyanagi, and Y. Kumashiro, "Nuclear spin-lattice relaxation of ^{93}Nb in a superconducting NbN synthesized by SHS", J. Alloys Compd. **383**, 308–312 (2004) (Cited on page 165).

[340] H. Bahlouli, "Nuclear spin relaxation rate in disordered superconductors", Phys. Lett. A **164**, 206–210 (1992) (Cited on page 165).

[341] T. P. Devereaux, "Nuclear spin relaxation in strongly disordered superconductors", Z. Phys. B: Condens. Matter **90**, 65–68 (1993) (Cited on page 165).

[342] D. C. Mattis and J. Bardeen, "Theory of the anomalous skin effect in normal and superconducting metals", Phys. Rev. **111**, 412–417 (1958) (Cited on page 166).

[343] S. P. Chockalingam, M. Chand, A. Kamlapure, J. Jesudasan, A. Mishra, V. Tripathi, and P. Raychaudhuri, "Tunneling studies in a homogeneously disordered *s*-wave superconductor: NbN", Phys. Rev. B **79**, 094509 (2009) (Cited on page 167).

[344] B. Sacépé, C. Chapelier, T. I. Baturina, V. M. Vinokur, M. R. Baklanov, and M. Sanquer, "Disorder-Induced Inhomogeneities of the Superconducting State Close to the Superconductor-Insulator Transition", Phys. Rev. Lett. **101**, 157006 (2008) (Cited on page 167).

[345] W. A. MacFarlane, C. B. L. Tschense, T. Buck, K. H. Chow, D. L. Cortie, A. N. Hariwal, R. F. Kiefl, D. Koumoulis, C. D. P. Levy, I. McKenzie, F. H. McGee, G. D. Morris, M. R. Pearson, Q. Song, D. Wang, Y. S. Hor, and R. J. Cava, "β-detected NMR of $^{8}Li^{+}$ in Bi, Sb, and the topological insulator $Bi_{0.9}Sb_{0.1}$", Phys. Rev. B **90**, 214422 (2014) (Cited on page 168).

[346] K. H. Chow, A. I. Mansour, I. Fan, R. F. Kiefl, G. D. Morris, Z. Salman, T. Dunlop, W. A. MacFarlane, H. Saadaoui, O. Mosendz, B. Kardasz, B. Heinrich, J. Jung, C. D. P. Levy, M. R. Pearson, T. J. Parolin, D. Wang, M. D. Hossain, Q. Song, and M. Smadella, "Detection and decoherence of level-crossing resonances of ^{8}Li in Cu", Phys. Rev. B **85**, 092103 (2012) (Cited on page 170).

[347] Y. M. Shy, L. E. Toth, and R. Somasundaram, "Superconducting properties, electrical resistivities, and structure of NbN thin films", J. Appl. Phys. **44**, 5539–5545 (1973) (Cited on page 171).

[348] I. G. Díaz-Palacio, R. Blick, W. Hillert, M. Wenskat, and R. Zierold, "ALD-Based NbTiN Studies for SIS R&D", in Proc. IPAC'21, International Particle Accelerator Conference 12 (Aug. 2021), pp. 4420–4421 (Cited on page 171).

[349] M. Xu, M. Hossain, H. Saadaoui, T. Parolin, K. Chow, T. Keeler, R. Kiefl, G. Morris, Z. Salman, Q. Song, D. Wang, and W. MacFarlane, "Proximal magnetometry in thin films using βNMR", J. Magn. Reson. **191**, 47–55 (2008) (Cited on page 180).

[350] H. Rietschel, H. Winter, and W. Reichardt, "Strong depression of superconductivity in VN by spin fluctuations", Phys. Rev. B **22**, 4284–4292 (1980) (Cited on page 181).

[351] W. M. Haynes, *CRC Handbook of Chemistry and Physics* (CRC Press, June 2016) (Cited on page 181).

[352] B. M. Wojek, "Superconductivity and magnetism in cuprate single crystals and thin-film heterostructures", PhD thesis (University of Zurich, 2011) (Cited on page 187).

[353] H. Umezawa, "Production of High Purity Niobium Material for SRF Cavities", in Asian school on superconductivity and cryogenics for accelerators, Presented December 10–17, 2017 (Tokyo Denkai Co., Ltd, Dec. 2017) (Cited on page 191).